ABSTRACT

Title of dissertation: OPTICAL AND QUANTUM INTERFERENCES IN STRONG FIELD IONIZATION AND OPTIMAL CONTROL

David B. Foote, Doctor of Philosophy, 2018

Dissertation directed by: Professor Wendell T. Hill, III
IPST, JQI, and Department of Physics

For decades, ultrafast laser pulses have been used to probe and control strong-field molecular dynamics, including in optimal control experiments. While these experiments successfully recover the optimal control pulses (OCPs), they have a limitation – it is generally unknown how the OCP guides the target system to its final state.

This thesis is concerned with "unpacking" OCPs to explain how they achieve their control goals. The OCPs that inspired this work consisted of pulse trains; a twin-peaked pulse (TPP) is the simplest example. Consequently, TPPs with variable interpeak delay and relative phase were employed in this work to study ionization, the first step in many control experiments. Two types of interference influence ionization from a TPP: optical interference (OI) between the electric fields of the two peaks, and quantum interference (QuI) between the electron wavepackets produced by the two peaks.

Two sets of experiments were performed to determine what roles OI and QuI

play in controlling ionization from a TPP and how they in turn influence subsequent molecular dynamics. The first set of experiments measured the total ionization yield induced by the TPPs. It was found that OI was principally responsible for changing the ion yield; QuI-induced oscillations were not observed. Small imperfections in the shape of the TPP (i.e., pedestals and subordinate peaks) were found to have a surprisingly large influence in the OI, highlighting the need for researchers in molecular control experiments to characterize the temporal profile of their pulses accurately.

A time-dependent perturbation theory simulation showed that the signatures of QuI in the ionic continuum vanish when measuring *total* electron yield, but appear in *energy-resolved* electron yields. The second set of experiments measured photoelectron energy distributions from a TPP with a velocity map imager to search for QuI. The experiments were performed at high intensities ($\sim 10^{14}$ W/cm^2) where the ponderomotive energy tends to wash out the fine energy structures of QuI. The thesis ends by proposing a modified, low-intensity experiment that will allow for the first unambiguous observation of QuI in non-resonant, multiphoton ionization.

OPTICAL AND QUANTUM INTERFERENCES IN STRONG FIELD IONIZATION AND OPTIMAL CONTROL

by

David B. Foote

Dissertation submitted to the Faculty of the Graduate School of the
University of Maryland, College Park in partial fulfillment
of the requirements for the degree of
Doctor of Philosophy
2018

Advisory Committee:
Professor Wendell T. Hill, III, Chair/Advisor
Adjunct Professor Charles Clark
Professor Ki-Yong Kim – Dean's Representative
Professor Howard Milchberg
Professor Amy Mullin

Acknowledgments

In the acknowledgements section of my undergraduate thesis, I wrote: "The accomplishments I have had over the past five years seem to me to be solely a result of the incredible support and encouragement I have received from countless individuals and have little to do with my own determination or skill." It does not feel that way this time around. This dissertation has been the result of many years of difficult and often discouraging work, and required a bit of skill and a whole lot of determination on my part. This makes me realize even more, though, how indebted I am to the countless people who have helped me along the way. I have so many people to thank, but unfortunately only have space for a few...

Of course, the first and foremost person I have to thank is my advisor, Professor Wendell Hill. Wendell has been a supportive and encouraging mentor, while at the same time demanding excellence in everything that I do. He has taught me to not take anything for granted in my work, and that by challenging what I assume to be true, I can uncover the deeper answers – and more questions. My future career in science is sure to benefit from his tutelage. I would also like to thank Professors Charles Clark, Ki-Yong Kim, Howard Milchberg, and Amy Mullin, for graciously agreeing to serve on my dissertation committee.

I have received a lot of support from the members of the lab during my time at Maryland: Jane Lee and Hyounguk Jang for training me and preparing me for my project in the first year, and Yingda Lin, Kevin Lehr, Zhenqian Jian, Angela Small, and Calvin He for giving me invaluable help during my dissertation research.

Kevin in particular gave me great help in modeling the electron trajectories in our VMI using the SIMION software. I would be remiss if I left out my research group from my undergraduate days, Tim Scarborough, Collin McAcy, and Professor Kees Uiterwaal, who helped me develop in my earliest years as a physicist and who have continued to give me guidance and encouragement during my graduate studies. I would also like to thank Professor Anthony Starace, Jean Marcel Ngoko Djiokap, and Liang-Wen Pi at the University of Nebraska for a very fruitful theory collaboration.

I owe a great debt of gratitude to Guan-Yeu Chen, who performed the optimal control experiments in CO_2 that form the basis of this work. My thesis would not have been possible without his unparalleled experimental prowess and tireless work in the lab. It is unfortunate we only worked together for a few brief months, because I am sure he would have had much more to teach me.

I have been lucky to work with some amazing people in the support staffs of the Departments of Physics and Chemistry, the Joint Quantum Institute, and the Institute for Physical Science and Technology, who have all helped my PhD work go as smoothly as possible. Among this group, special thanks go out to Debbie Jenkins and Stacey Bremerman, who over and over again helped me navigate the often confusing experience of being a graduate student on the interface of two departments.

I have been blessed with so many friends who have provided me with welcome distraction and emotional support during my education. I may not stay in touch with many of you nearly as much as I would like, but to Stephen, Nick, Alexandra, Brad, Jake, Nitz, Marcus, Rachel, Brian, Emilee, Clancie, Ben, Jessica, Amit, Andrew,

Carrie, and many others – thank you for being my friend. Particular thanks go out to my roommates, Luke, John, Mina, Prasoon, and Piyali, for putting up with me these past several years, and the members of my band, Will, Shannon, and Tom, for helping me to keep music a part of my life.

None of this would have been possible without the unwavering love and support of my family. My siblings and siblings-in-law, Katie and James, and Tim and Laura, have each been an inspiration to me in their own way, and have given me three wonderful nieces, Hailey, Rebecca, and Lydia, who bring joy to my life. My grandparents, though they are no longer here with me on Earth, each played a huge role in guiding me into becoming the man I am today. I also want to thank all of my aunts, uncles and cousins, especially my Aunt Amy and Uncle Will – even though I moved a thousand miles away, they made sure I was never more than half an hour's drive from home.

I have trouble finding any words to express how thankful I am for my parents, for everything they have done for me. I do not know where I would be right now if I did not have their lifelong guidance, support, and sacrifice, but I know it would be nowhere near where I am now. I love you, Mom and Dad.

Lastly, I give thanks to God, who granted me the courage, determination, and faith to see me through to where I am now. Psalm 27:13 – "I would have lost heart, unless I had believed that I would see the goodness of the Lord in the land of the living."

Contents

List of Tables

List of Figures

List of Abbreviations

ATI	above-threshold ionization
BASEX	basis set expansion
BBO	beta barium borate
CPA	chirped pulse amplification
CW	continuous wave
ER	electrostatic ring
FROG	frequency-resolved optical gating
FWHM	full width at half maximum
GA	genetic algorithm
GDD	group delay dispersion
GVD	group velocity dispersion
HHG	high harmonic generation
HWHM	half width at half maximum
MPI	multiphoton ionization
MZ	Mach-Zehnder interferometer
OCP	optimal control pulse
OI	optical interference
PES	photoelectron spectrum
PS	pulse shaper
QuI	quantum interference
QWP	quarter-wave plate
REMPI	resonance-enhanced multiphoton ionization
RMS	root mean square
SD-FROG	self-diffraction frequency-resolved optical gating
SHG	second harmonic generation

SLM	spatial light modulator
TDPT	time-dependent perturbation theory
TEM	tranverse electromagnetic
Ti:sapphire	titanium-doped sapphire
TOF	time of flight
TPP	twin-peaked pulse
TPP_{MZ}	twin-peaked pulse produced by the Mach-Zehnder interferometer
TPP_{PS}	twin-peaked pulse produced by the pulse shaper
VMI	velocity map imager

List of Symbols

A_{FROG}	area under FROG-measured temporal intensity $I_{FROG}(t)$
A_{eff}	effective beam area
c	speed of light in vacuum
d	distance
$d_{i \to j}$	$i \to j$ atomic transition dipole moment
e	elementary charge
$\mathcal{E}$	electric field (static)
$\mathcal{E}(t)$	electric field (time domain)
$\mathcal{E}_{sim}(t)$	simulated electric field
$\tilde{\mathcal{E}}(\omega)$	electric field (frequency domain)
$E(t)$	electric field complex amplitude (time domain)
$\tilde{E}(\omega)$	electric field complex amplitude (frequency domain)
f	focal length
f_{EC}	intensity modification due to energy correction
f_{OI}	intensity modification due to optical interference
f_{rep}	pulse repetition rate
F	Fourier transform operator
$\mathcal{F}$	fluence
F_p	ponderomotive force
h	Planck's constant
$\hbar$	reduced Planck's constant
$I(t)$	pulse intensity (time domain)
$I_{FROG}(t)$	FROG-measured pulse intensity (time domain)
$I^{(max)}$	maximum intensity
$I_{TPP}^{(max)}$	maximum intensity of an ideal twin-peaked pulse
I_{sim}	simulated pulse intensity
$\tilde{I}(\omega)$	pulse intensity (frequency domain)
I_p	ionization potential
J	Jacobian

k	wavenumber
l	Mach-Zehnder interferometer variable stage position
L	laser cavity length
m	multiphoton order
m_e	electron mass
n_0	refractive index
n_2	second-order nonlinear refractive index
$p^{(m)}$	m-photon ionization probability
P	power
P_{avg}	average beam power
$\mathcal{P}$	normalized power (P divided by power modulation envelope)
r	radius (cylindrical coordinates)
t	time
t_{op}	optical period
$t_{i\rightarrow j}$	lifetime of the $i \rightarrow j$ atomic transition
T	$\equiv \tau/\Delta t$, scaled TPP peak separation
$\mathcal{T}$	transmittance of vacuum chamber entrance window
U	energy
U_p	ponderomotive energy
V	voltage
$\mathcal{V}$	fringe visibility
w	beam radius ($1/e^2$)
w_f	beam radius ($1/e^2$) at waist
w_f^{DL}	beam radius ($1/e^2$) at waist for a diffraction-limited beam
$W^{(m)}$	m-photon ionization rate
Y	charged particle yield
z_R	Rayleigh length
α	polar angle (spherical coordinates)

β	ratio of pedestal field amplitude to main peak field amplitude
β_{MZ}	$\mathrm{TPP}_{\mathrm{MZ}}$ peak amplitude ratio (due to MZ imbalance)
β_s	ratio of subordinate peak field amplitude to main peak field amplitude
γ	Keldysh parameter
δl	change in l
$\Delta\phi$	relative phase between peaks of the twin-peaked pulse
$\Delta\phi_0^{(E)}$	phase offset of ion yield oscillations
$\Delta\phi_0^{(M)}$	phase offset of model intensity oscillations
$\Delta\lambda_{FWHM}$	wavelength bandwidth of pulse, full width at half maximum
$\Delta\nu_{FWHM}$	frequency bandwidth of pulse, full width at half maximum
Δt	sech^2 pulse duration ($= 0.568\Delta t_{FWHM}$)
Δt_{FWHM}	full width at half maximum pulse duration
$\delta\tau$	change in τ
$\Delta\omega$	sech^2 angular frequency bandwidth ($= 2\pi \cdot 0.568 \cdot \Delta\nu_{FWHM}$)
ϵ_0	vacuum permittivity
η_{BBO}	BBO conversion efficiency
θ	carrier envelope phase
λ	wavelength
λ_0	center wavelength of pulse
ν	frequency
ν_0	central frequency of the laser pulse
ρ	radius (spherical coordinates)
σ	standard deviation
σ_Y	standard deviation of charged particle yield
$\sigma^{(m)}$	m-photon generalized cross section
$\sigma^{[m]}$	m-photon cross section
τ	temporal delay between peak of the twin-peaked pulse
τ_s	temporal delay between a main peak and subordinate peak

ϕ	phase
ϕ_p	pedestal phase (relative to main peak)
φ	azimuthal angle (spherical and cylindrical coordinates)
χ	nonlinear susceptibility
ω	angular frequency
ω_0	central angular frequency of the pulse
$\Omega_{i\to j}$	Rabi frequency for the $i \to j$ atomic transition
∇	gradient operator

Chapter 1: Introduction

1.1 Motivation

For approximately thirty years, ultrafast lasers have captured the interest of scientists in many fields for their potential to image and control molecular dynamics [1–4]. These ultrafast pulses, with a temporal duration between 10^{-15} and 10^{-12} seconds, are sometimes referred to as "photonic reagents" due to their potential to guide chemical reactions to a final state.

Extremely high intensities are attainable in ultrafast experiments, even for modest pulse energies due to the short pulse duration[1], enabling processes such as multiphoton ionization [5], tunneling ionization [6–10], high harmonic generation (HHG) [11–13], and attosecond pulse generation [14–17]. At the same time, ultrafast pulses are uniquely suited to image and control chemical reactions because they can stimulate and probe dynamics on a femtosecond time scale. Figure 1.1 shows the

[1] For instance, a 3 mJ pulse of 50 fs duration, focused to a spot size of 10 μm, has a peak intensity approximately equal to the atomic unit of intensity ($\frac{1}{2}\frac{\epsilon_0 c e^2}{a_0^4} = 3.5 \times 10^{16}$ W/cm^2, where ϵ_0 is the vacuum permittivity, c is the speed of light, e is the unit charge, and $a_0 = 5.28 \times 10^{-11}$ m is the Bohr radius). In other words, the peak instantaneous electric field produced by such a pulse is comparable to the Coulomb field experienced by the electron in a hydrogen atom.

relevant time scales for selected physical, chemical, and biological processes in atoms and molecules [18]. Pulses of tens to hundreds of femtoseconds have a duration commensurate with the time scales of molecular dynamics such as vibration and rotation, as well as nuclear motion during chemical reactions.

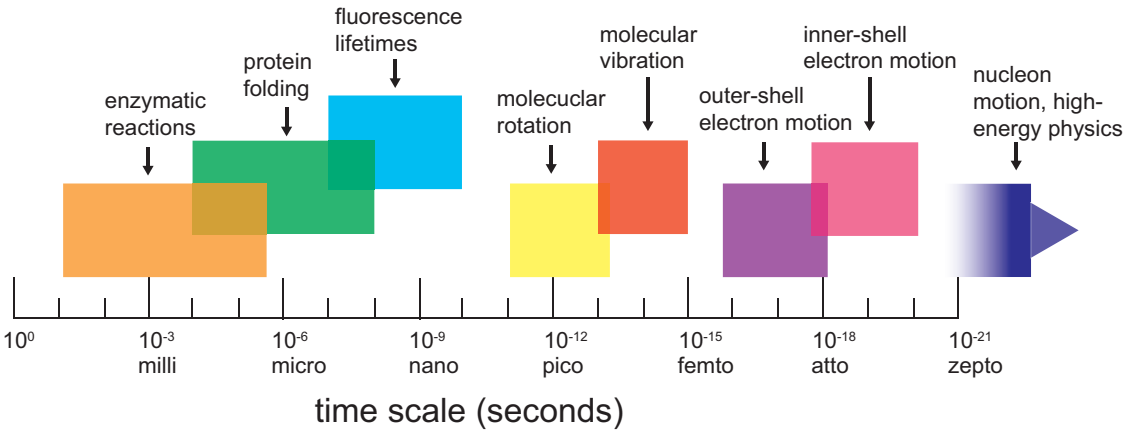

Fig. 1.1: Approximate time scales for a selection of processes in atoms and molecules. Ultrafast pulses, those with a duration of 10^{-15} to 10^{-12} seconds, allow investigation of molecular vibration, rotation, and chemical reaction dynamics. This figure has been modified from a figure in Ref. [18].

The unique applicability of ultrafast pulses to probing molecular dynamics led to the rapid and sustained growth of the field of femtochemistry, which seeks to either observe the evolution of chemical reactions and/or molecular dynamics (often referred to as a "molecular movie" [19–23]) or control their outcome. Coherent control of chemical reaction and molecular dynamics has been facilitated by successful applications of frequency-domain pulse shaping[2], in which the spectral profile of an ultrafast pulse (or combination of pulses) is changed in order to maximize a desired outcome of the target system. [3,4,24]. The complexity of molecules makes analytic

[2] One example of a pulse shaper is described in detail in Sec. 3.2.

determination of the optimal control pulse (OCP) exceedingly difficult.

Instead, the OCP can be determined by intelligent searches of the parameter space via a feedback algorithm, called closed-loop control [24–27]. In such an algorithm, a laser pulse interacts with a molecule, and a measurement related to the dynamics of interest is made. The value of this measurement, which depends on the shape of the applied pulse, is referred to as a fitness function(al). Based on how close the outcome is to the target value of the fitness functional, the pulse shape is changed, and the fitness functional is measured again. This process is repeated until an OCP is found and the fitness functional is maximized. Commonly, this feedback algorithm is a genetic algorithm (GA), in which a number of electric field "genes" are defined. These genes are subsequently mutated from generation to generation, with preference given to preserve those genes that improve the fitness functional [26, 28, 29].

Many experiments in ultrafast molecular dynamics have found great success in closed-loop control using a GA [24–26, 28, 29]. What is often not known, however, is why these OCPs are optimal – that is, how these pulses guide the molecule on the way to its end state. Deconstruction of OCPs has proven to be a difficult and arduous task. Efforts have involved studying the control landscape [28, 30, 31], the role of chirped pulses [32], and individual degrees of freedom [28, 30, 32, 33], all with limited success. Nevertheless, the goal of "unpacking" the OCP (that is, focusing on a small number of defining characteristics of the pulse shape to simplify the problem) represents the best hope one has of understanding how an OCP works. The research presented in this dissertation is primarily concerned with this goal, focusing on

the relative phase between components of an OCP – a prominent feature of many optimal pulses that has received comparatively little attention in the literature.

1.2 Research background

The study presented in this dissertation takes as its inspiration a previous set of experiments [28], which will be summarized briefly here[3]. In these experiments, a GA was used to find optimal pulses for maximizing the bending vibration amplitude of a CO_2^{6+} molecular ion prior to Coulomb explosion, a process in which a highly-charged molecular ion dissociates into individual atomic ions due to their mutual Coulomb repulsion [34, 35]. Several different OCPs were found, two of which are shown in Ref. [28]. These OCPs were compared with both transform-limited (TL) pulses[4] and phase-reversed counterparts (a phase-reversed counterpart is identical to its corresponding OCP except that the spectral phase has been reversed, $\phi(\omega) \rightarrow -\phi(\omega)$). It was found that the two optimal control pulses significantly enhanced the bending amplitude when compared with either a transform limited pulse at the same intensity or their respective phase-reversed counterparts.

[3] The findings of Ref. [28] will be visited in more detail in Chap. 5. There, the results of the "Ions" experiments described in Chaps. 3 and 4 will be related back to optimal control in the context of Ref. [28].

[4] A transform-limited pulse is a pulse which minimizes the time-bandwidth product $\Delta\nu_{FWHM}\Delta t_{FWHM}$, where $\Delta\nu_{FWHM}$ is the full width at half maximum (FWHM) of the optical frequency spectrum and Δt_{FWHM} is the FWHM pulse duration [36]. For a Gaussian frequency spectrum, $\Delta\nu_{FWHM}\Delta t_{FWHM} \geq 0.441$; for a hyperbolic secant frequency spectrum, $\Delta\nu_{FWHM}\Delta t_{FWHM} \geq 0.315$.

Both of the OCPs in Ref. [28] consisted of a sequence of peaks with well-defined relative phases. Sequences of peaks, referred to as pulse trains, are not uncommon in control experiments. Phase-locked pulse trains and pulse pairs have been studied for decades in the context of pump-probe experiments, see for example Refs. [37–40]More recently, pulse trains have been deliberately synthesized and used to control such processes as photoelectron angular distributions [41, 42], magnetization [43], and molecular vibration and rotation [44, 45]. Pulse trains have also appeared as solutions in optimal control experiments similar to Ref. [28], see for example Refs. [46–49].

Furthermore, optimal control experiments on other Coulomb explosion dynamics in CO_2 performed in this group have also found pulse train OCPs. Of particular interest here is an experiment that sought to maximize the Coulomb explosion branching ratio (221)/(222), where (lmn) refers to a $CO_2^{(l+m+n)+} \rightarrow O^{l+} + C^{m+} + O^{n+}$ Coulomb explosion event. This branching ratio can be trivially increased by decreasing the laser intensity – higher intensities are required, in general, to produce CO_2^{6+} than CO_2^{5+}. The OCP, shown in Fig. 1.2, enhanced the branching ratio beyond what was observed by simply lowering the intensity. This pulse presumably induced an optimally increased (221)/(222) branching ratio. The pulse shape is dominated by a pair of nearly-identical peaks with a well-defined relative phase and an approximately constant phase across each peak.

The influence of the relative phase on molecular dynamics has received little attention in experiments compared to more dominant features (e.g., intensity, pulse width, chirp), presumably because of the perceived limited dynamic range, $0 - 2\pi$

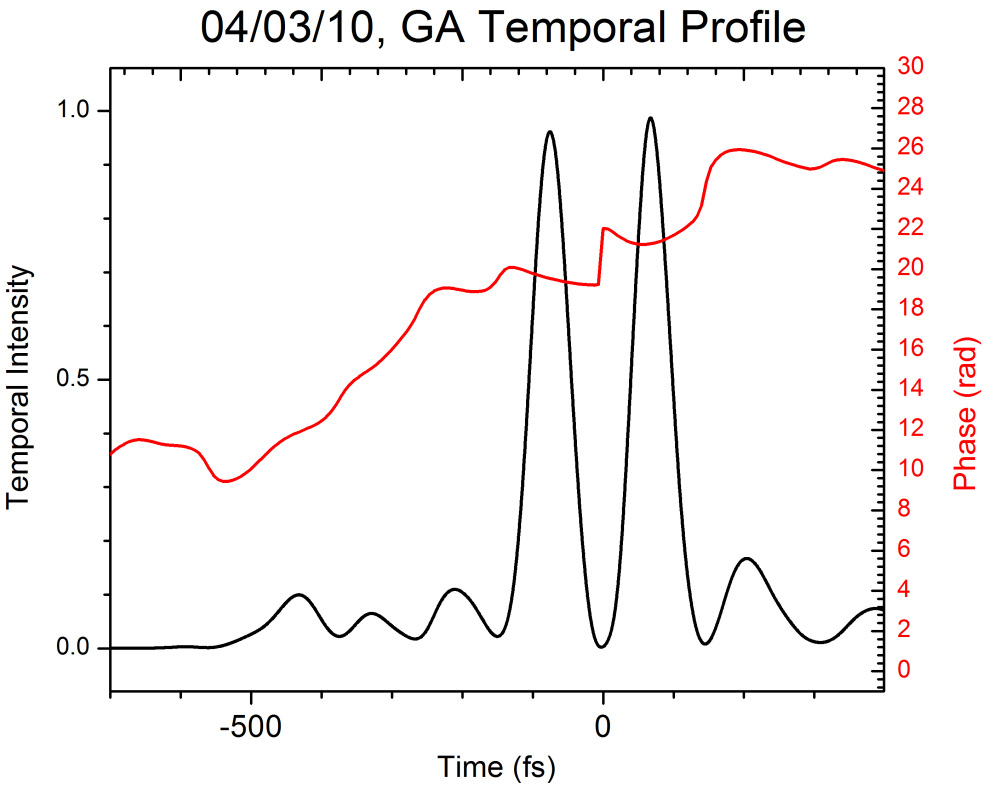

Fig. 1.2: Temporal intensity (black) and phase (red) of an OCP that controlled the branching ratio of CO_2 Coulomb explosion products. The shape of this OCP is dominated by a twin-peaked pulse, with several small satellite pulses before and after the main peaks. The small features are not likely to be simply noise, as determined in Sec. 4.1.2.

rad. To address this void, the relative phase between peaks was chosen to be the key feature around which to unpack the pulse-train OCPs of Ref. [28]. To make the study as quantitative and straightforward as possible, two further simplifications were made:

- The simplest case of a pulse train is considered, a pair of identical pulses.
- Only ionization, the first step of the dynamics in Ref. [28], is considered.

The first simplification takes the prohibitively large parameter space of an arbitrary OCP and reduces it to a single parameter – the relative phase between the two pulses. This pair of pulses will be referred to in this work as a twin-peaked pulse (TPP). The term "twin-peaked pulse" is used instead of "double pulse" or "pulse pair" to emphasize that the pulse is being treated as a single composite unit – a single pulse of complicated temporal structure.

While the second point may seem at first glance to be a drastic oversimplification of the problem at hand, the influence of pulse trains on ionization is of significant interest in strong-field optimal control. At intensities in excess of 10^{14} W/cm^2 at a wavelength near 1 μm, ionization will occur in almost every atomic and molecular species. Removal of multiple electrons occurs at intensities near or above 10^{15} W/cm^2 [5]. These intensities are common in strong-field control experiments, so ionization is usually involved as either an early step in the dynamics or concomitant with the dynamics of interest. Particularly, ionization is required in Ref. [28] to reach the high charge states of CO_2 to induce Coulomb explosion. To further simplify the experiment, ionization of an atom (Xe), will be considered along with ionization of CO_2.

In ionization with a TPP, interference will play a key role. Two types of interference are distinguished here: optical interference (OI), in which the electric fields of the individual peaks of the TPP interfere, leading to a variation in the energy and intensity of the composite pulse; and quantum interference (QuI), where the continuum electron wavepackets produced by each peak interfere. Quantum interference has been clearly observed between bound states, see for example, Ref. [50],

but it has not been unambiguously observed the continuum with linearly polarized light. As such, it remains an open question whether QuI could influence ionization and subsequent dynamics in strong-field control experiments like the one described in Ref. [28].

1.3 Contributions of this study

This dissertation considers two questions:

- What role does the relative phase play in controlling ionization from a TPP, and how does it in turn influence coherent control of molecular dynamics?
- Can quantum interference play any role in strong-field ionization and quantum control?

As mentioned above, these questions were explored over the limited, but well-defined domain associated with TPPs. Two separate sets of experiments were designed and performed on ionization with twin-peaked pulses to answer these two questions separately. The two sets are distinguished by the species of particle detected. In the first set of experiments, called the "Ions" experiments, atomic/molecular ions were detected after ionization using a time-of-flight mass spectrometer – this approach turned out only to address the first question, as will be explained later. In the second set of experiments, called the "Electrons" experiments, the photoelectron energy distributions were measured using a velocity map imager; these experiments supplemented the answer to the first question and provided an answer to the second question.

The manuscript is organized as follows. Chapter 2 provides a brief overview of laser-induced ionization and also considers optical and quantum interferences in ionization yields. The laser apparatus and design of the "Ions" experiments is described in Chap. 3; presentation and discussion of the results of these experiments is found in Chap. 4. The findings of the "Ions" experiments are related back to optimal control experiments, particularly Ref. [28], in Chap. 5, providing an answer to the first question from above. A simulation of quantum interference in ionization from TPPs, using time-dependent perturbation theory, is developed in Chap. 6. This simulation provides an answer as to why QuI is not observed in the "Ions" experiments and motivates the "Electrons" experiments. The design of the "Electrons" experiments is given in Chap. 7, and the results are the topic of Chap. 8. Chapter 9 proposes future "Electrons" experiments at lower intensities that will enable detection of QuI in ionization with a linearly-polarized TPP. Chapter 10 gives the conclusions of this work.

Chapter 2: Interference in Ionization

This chapter considers ionization of atoms and molecules under the influence of a TPP. A review of ionization in the multiphoton and tunneling regimes is given in Sec. 2.1. The mathematical definition of a TPP will be given in Sec. 2.2. Interference will play a key role in ionization induced by TPPs when the separation between peaks is small enough that the peaks partially overlap. This is often the case in strong-field control experiments, particularly in Ref. [28]. Optical interference, Sec. 2.3, and quantum interference, Sec. 2.4, are considered here.

2.1 Ionization regimes

Non-resonant light-induced ionization of atoms and molecules occurs in two different intensity regimes, broadly speaking. The working regime is determined by the Keldysh parameter γ [7],

$$\gamma = \sqrt{\frac{I_p}{2U_p}}, \tag{2.1}$$

where I_p is the ionization potential of the atom or molecule, U_p is the ponderomotive energy,

$$U_p = \frac{e^2 I}{2 m_e \omega_0^2 \epsilon_0 c}, \tag{2.2}$$

e is the elementary charge, m_e is the electron mass, ω_0 is the laser (central) frequency, ϵ_0 is the vacuum permittivity, c is the speed of light in vacuum, and I is the laser intensity[1].

The two regimes are shown in Fig. 2.1. The Keldysh parameter is equivalent to the ratio of the optical cycle time and the tunneling time, the time required for an electron to tunnel out of the deformed atomic/molecular potential. When $\gamma \gg 1$, the optical cycle time is much longer than the tunneling time. Multiphoton ionization (MPI) dominates, meaning that ionization proceeds by the sequential absorption of a number of photons that increase its energy above the ionization energy of the atom or molecule. The ionization can be treated perturbatively in this case [51–53]. The number of ions generated increases monotonically with the laser intensity I, going as I^m, where m is the number of photons required to ionize. The MPI regime with $\gamma \gg 1$ can be reached by lowering the intensity and/or increasing the laser frequency. If there is an intermediate state in the atom or molecule that is resonant with the absorption of q photons, where $q < m$, then resonance-enhanced multiphoton ionization (REMPI) occurs [54,55]. Ionization occurs much more readily in REMPI than in non-resonant MPI.

As γ decreases, the optical field distorts the atomic potential more strongly. Perturbation theory breaks down and intermediate states shift in and out of resonance, leading to a breakdown of the multiphoton treatment [7,9,56–58]. Eventually,

[1] The ponderomotive energy and ponderomotive force will be discussed in more detail in Sec. 6.3.

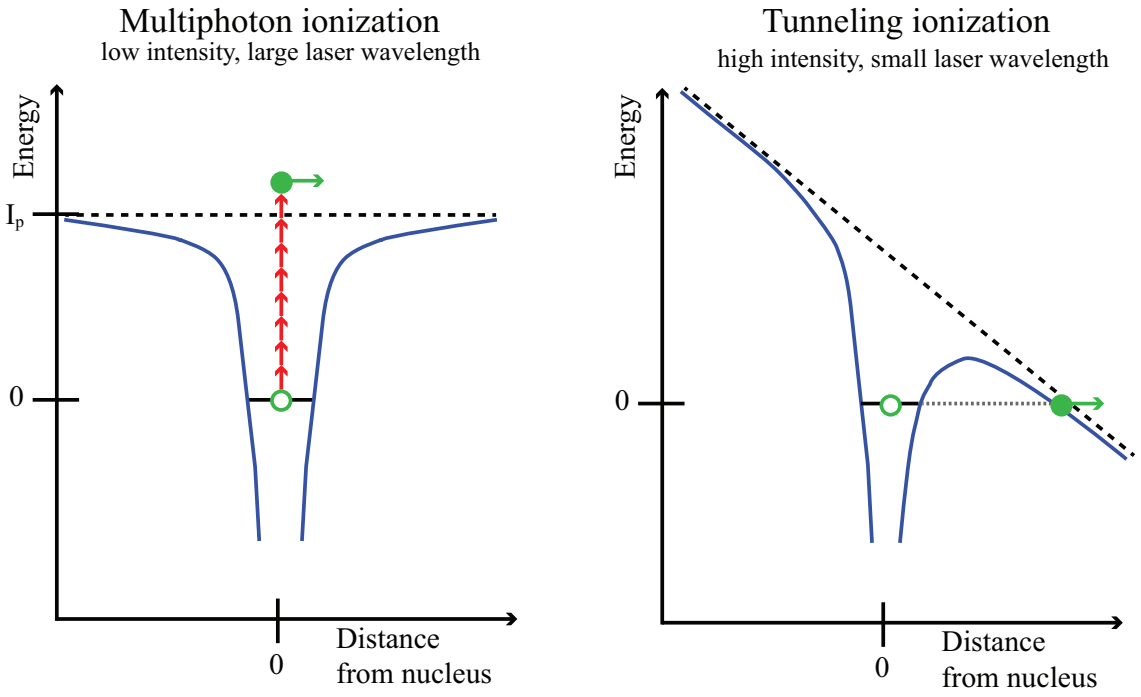

Fig. 2.1: Comparison of multiphoton (left) and tunneling (right) ionization of an atom. In both cases, the green hollow circle represents the initial (usually ground) state of the electron; the green filled circle is the free electron after ionization. The atomic potential is given by the solid blue curves. In multiphoton ionization, the optical field (dashed black line) does not distort the atomic potential very much and ionization proceeds by sequential absorption of a number of photons (red arrows) until the electron energy is larger than I_p (measured relative to the initial state indicated by the solid black line at 0 energy). In the tunneling regime, the much stronger optical field distorts the atomic potential to the point that the electron can tunnel out of the well.

the atomic potential distorts to the point than an electron can readily tunnel out within an optical cycle. This process is called tunneling ionization, and dominates when $\gamma \ll 1$. The tunneling ionization regime can be reached by increasing the laser intensity and/or lowering the laser frequency.

For $\gamma \simeq 1$, MPI and tunneling ionization are mixed; more exotic processes

tend to occur, e.g. above-threshold ionization [5]. The total number of ions generally increases monotonically with the laser intensity for all γ. At sufficiently high intensities, the ionization saturates[2] in the target population, which can cause a leveling-off or decrease in the ionization yield [55]. However, as the intensity increases, the volume in which ionization occurs increases as well, and so a monotonic increase in ion yield is typically observed over all intensities when collecting the ions over the entire focal volume [59, 60].

This monotonic increase is observed with TL pulses. More complex envelopes, such as the pulse trains considered in this work, do not always obey this trend [61], and therefore may induce ionization stabilization, a term used here to describe any effect where, in the absence of saturation, the ionization rate decreases with increasing pulse intensity [62–64]. Ionization stabilization received considerable experimental and theoretical interest in the past, see for example Refs. [65–76]. Quantum interference, if it changes the total ionization yield, would be considered a form of ionization stabilization.

2.2 Definition of a twin-peaked pulse (TPP)

An ideal TPP consists of two identical, transform-limited peaks. Assuming hyperbolic-secant shape for the individual peaks, the electric field of an ideal TPP is given by

[2] The saturation intensity is the intensity where the yield deviates from a straight line on a log-log plot.

$$\mathcal{E}_{TPP}(\tau, \Delta\phi; t) = \mathcal{E}_0 e^{-i(\omega_0 t - \phi_1)} \left[\text{sech}\left(\frac{t}{\Delta t}\right) + \text{sech}\left(\frac{t-\tau}{\Delta t}\right) e^{i\Delta\phi} \right] + \text{c.c.}, \tag{2.3}$$

where $\mathcal{E}_0$ is the electric field amplitude of a single peak, ω_0 ($= 2\pi\nu_0$) is the central frequency of the pulse spectrum, $1.76\Delta t = \Delta t_{FWHM}$ is the intensity full width at half maximum (FWHM) of each peak when the peaks are well separated in time, τ is the inter-peak delay, and $\Delta\phi \equiv \phi_2 - \phi_1$ is the relative phase between peaks; ϕ_1 (ϕ_2) is the phase of the earlier (later) peak, each measured relative to the maximum of the earlier peak envelope. The phase of a pulse is commonly defined as the phase of the electric field at the maximum of the envelope; this is called the carrier envelope phase (CEP). Taking the CEP of the earlier (later) peak to be θ_1 (θ_2), then

$$\phi_1 \equiv \theta_1, \;\; \phi_2 \equiv \theta_2 + \omega_0\tau \text{ and } \Delta\phi = \theta_2 - \theta_1 + \omega_0\tau. \tag{2.4}$$

The temporal intensity of the TPP is $I_{TPP}(\tau, \Delta\phi; t) = (c\epsilon_0 n_0/2)\,(\mathcal{E}(\tau, \Delta\phi; t))^2$, ϵ_0 is the vacuum permittivity, and n_0 is the refractive index. To simplify the expression for the temporal intensity, it is convenient to define the *complex envelope* of the electric field,

$$E_{TPP} = \mathcal{E}_0 \left[\text{sech}\left(\frac{t}{\Delta t}\right) + \text{sech}\left(\frac{t-\tau}{\Delta t}\right) e^{i\Delta\phi} \right]. \tag{2.5}$$

For a many-cycle pulse ($\Delta t \gg 1/\nu_0$), the envelope of Eq. 2.3 does not change appreciably over one optical period. In this case, one averages $(\mathcal{E}_{TPP}(\tau, \Delta\phi; t))^2$ over all ϕ_1 to determine the time-dependent intensity. This is known as the analytic

signal approximation [77, 78], and gives $I_{TPP}(\tau, \Delta\phi; t) \propto |E_{TPP}(\tau, \Delta\phi; t)|^2$. With Eq. 2.5, the intensity becomes

$$I_{TPP}(\tau, \Delta\phi; t) = I_0 \left[\text{sech}^2 \left(\frac{t}{\Delta t} \right) + \text{sech}^2 \left(\frac{t-\tau}{\Delta t} \right) + 2\text{sech} \left(\frac{t}{\Delta t} \right) \text{sech} \left(\frac{t-\tau}{\Delta t} \right) \cos(\Delta\phi) \right], \tag{2.6}$$

where $I_0 = (c\epsilon_0 n_0/2)\mathcal{E}_0^2$ is the single-peak intensity.

2.3 Optical interference (OI)

The total ionization yield induced by a TPP can change as a function of $\Delta\phi$ due to OI, the interference between individual peak electric fields when the peaks overlap. When the peaks are in phase ($\Delta\phi = 0$), the fields constructively interfere, so the maximum intensity (and energy) of the TPP increases. When the peaks are out of phase ($\Delta\phi = \pi$ rad), destructive interference causes the intensity and energy of the TPP to decrease. This can be seen directly by calculating $I_{TPP}^{(max)}$, the maximum intensity of the TPP, found by evaluating Eq. 2.6 at either $t = 0$ or $t = \tau$:

$$I_{TPP}^{(max)} = I_0 \left[1 + \text{sech}^2 \left(\frac{\tau}{\Delta t} \right) + 2\text{sech} \left(\frac{\tau}{\Delta t} \right) \cos(\Delta\phi) \right], \tag{2.7}$$

which exhibits sinusoidal oscillations in $\Delta\phi$, with the oscillation amplitude falling off with increasing $|\tau|$. The oscillation amplitude is also referred to as the *fringe visibility*, which will be defined in this context in Chap. 4. In the rest of this thesis, $I_{TPP}^{(max)}$ will be used to refer to the maximum intensity of this ideal TPP, while

$I^{(max)}$ will be used to refer to the maximum intensity of a pulse of arbitrary shape. The energy of the TPP can be found by integrating Eq. 2.6 over all time; it also oscillates sinusoidally. It is clear from Eq. 2.7 and 2.4 that the oscillation period of the intensity due to OI is equal to the optical period,

$$t_{opt} = \frac{2\pi}{\omega_0} = \frac{1}{\nu_0}. \tag{2.8}$$

As described in Sec. 2.1, the ionization yield is typically a monotonically-increasing function of the pulse intensity, so this periodic oscillation in the pulse intensity causes an oscillation (with the same period) in the ion yield.

2.4 Quantum interference (QuI)

In addition to the well-known OI, a more exotic quantum-mechanical interference can occur. For atomic ionization, there are at least three possible mechanisms through which QuI could arise.

2.4.1 Mechanism I

A two-level model atom illustrating QuI Mechanism I is shown in the left panel of Fig. 2.2. In this mechanism, the first peak of the TPP creates a superposition between the lower state $|g\rangle$ and the upper state $|e\rangle$ of the atom[3]. This superposition will result in a population oscillation (Rabi oscillations [79]) between these two states

[3] In a real atom, QuI Mechanism I occurs between any two states. In Ref. [50], the two states involved were the ground state and a pair of excited states, hence the state labels $|g\rangle$ and $|e\rangle$ in Fig. 2.2. If the upper state is the ionic continuum, Mechanism III applies instead.

on a timescale of h/U_{ge} where h is Planck's constant. The second peak of the TPP interacts with the superposition. This can cause an oscillation of the population in the $|e\rangle$ state with a period of h/U_{ge}. If the transition to the excited state is resonant with the absorption of m photons, the oscillation period is t_{opt}/m.

2.4.2 Mechanism II

A model atom that illustrates Mechanism II is shown in the middle panel of Fig. 2.2. In this model, a second excited state $|e'\rangle$ is added to the Mechanism I model atom. The two excited states are closely-spaced, close enough that the bandwidth of the pulse is sufficient to excite both bound states. In other words, the energy difference between $|e\rangle$ and $|e'\rangle$ is $U_{ee'} < h\Delta\nu_{FWHM}$. When multiple photons are required to reach the excited state, this further implies $U_{ee'} \ll U_{ge}$. In addition to the two Mechanism I population oscillations, a beat note occurs with a period $h/U_{ee'}$. Mechanisms I and II occur simultaneously. If more excited states are added, more beat notes occur [79].

Blanchet *et al.* [50] observed QuI and were able to distinguish Mechanisms I and II in a (2+1)-photon ionization of Cs through the $7^2D_{3/2}$ and $7^2D_{5/2}$ states with a 150 fs TPP at 768 nm (t_{opt} = 2.45 fs). The excited bound states were reached by a 2-photon transition. The population in the excited state was detected by observing Cs^+ ions that resulted from the absorption of an additional photon. Their ion signal showed the expected modulation with a period $t_{opt}/2$ (Mechanism I) with a beat note with a time scale set by the energy separation of the two excited states (Mechanism II). In addition, an oscillation with period t_{opt} also was observed

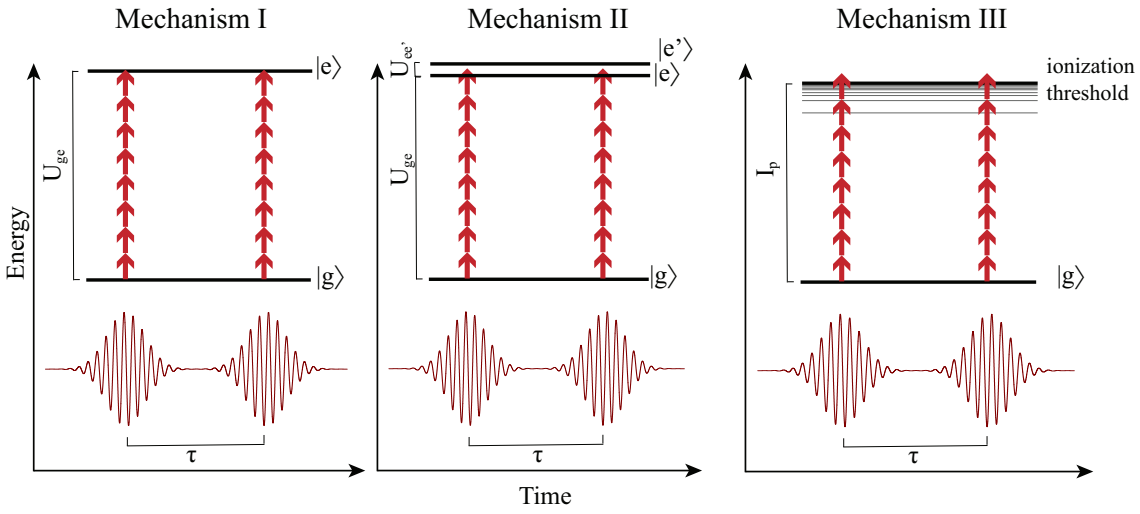

Fig. 2.2: Model atoms demonstrating the three different QuI Mechanisms. A TPP with temporal delay τ is shown in all three panels. Left panel: Mechanism I, in which the TPP probes interference in the multiphoton transition between a ground state $|g\rangle$ and an excited state $|e\rangle$. Middle panel: Mechanism II, similar to Mechanism I except that the multiphoton transition populates two closely-spaced excited states with energy separation $U_{ee'} \ll U_{ge}$. Right panel: Mechanism III, in which the interference occurs in the ionic continuum. If intermediate resonant states are present, Mechanisms I and II may occur simultaneously with Mechanism III.

when the peaks overlapped (due to OI). In contrast to the OI modulations, the QuI Mechanisms I and II oscillations continued well outside the temporal region where the peaks were overlapping, due to the comparatively long excited state lifetimes.

2.4.3 Mechanism III

A third QuI, Mechanism III, is shown schematically in the right panel of Fig. 2.2 and occurs in (multiphoton) transitions to the ionic continuum. It can be thought of as a limiting case of Mechanism II, when the density of excited states tends towards infinity, as described in Ref. [79]. In this mechanism, each peak of the

TPP generates a continuum electron wavepacket. The wavepackets interfere when they overlap spatially and temporally at the detector, resulting in a modulation of the photoelectron signal due to ambiguity in knowledge of which peak was responsible for the birth of the electron. This can be viewed as a temporal analogue to a Young's double slit arrangement. Much like Mechanism I, the oscillation period from an m-photon transition has a period t_{opt}/m in Mechanism III. However, unlike Mechanism I and II, the strength of Mechanism III follows that of OI[4]; as the peaks separate, the uncertainty in which peak was the electron progenitor is gradually lost and the oscillation amplitude decreases. In other words, the two photoelectron wavepackets must overlap at the detector in order to interfere.

One additional case worth mentioning is the case when an intermediate resonant state enhances the ionization. In this case, QuI Mechanism I, between the ground and resonant states, can occur simultaneously with QuI Mechanism III. If there are several intermediate resonant states, QuI Mechanism II can occur alongside Mechanisms I and III. This thesis is primarily concerned with ionization of Xe with 800 nm pulses ($h\nu_0 = 1.55$ eV, $t_{opt} = 2.35$ fs); there are no field-free intermediate resonances in Xe for this photon energy. However, there is a state approximately 0.3 eV below the energy corresponding to the absorption of seven photons. Depending on the field intensity, the ac-Stark effect could shift this state into a seven-photon resonance [57,58], which could leave excited state population less than 1.5 eV below the ionization threshold after the first peak. A (7+1)-photon ionization could lead to modulation of period $t_{opt}/7$ (Mechanism I) with the possibility of much longer beat

[4] This is shown in a simulation in Ch. 6.

notes due to two or more intermediate states being populated coherently (Mechanism II). Finally, a less direct QuI Mechanism III could occur resulting from a (7+1)-photon ionization from the first peak of the TPP and a single-photon ionization of the residual population in the excited state from the second peak. This indirect QuI Mechanism III will be referred to in this work as Mechanism III'. Because QuI Mechanisms III' results from a single-photon ionization, $m = 1$, it would have a period of t_{opt}.

Wollenhaupt *et al.* [80] interpreted their single-photon ionization of an incoherently pre-populated $5p$ state of K with a 790 nm fs TPP ($t_{opt} = 2.39$ fs) in terms of Mechanism III. However, it is difficult to separate OI and QuI Mechanism III in their experiment, as both decay as τ increases and both have the same oscillation period because $m = 1$. The authors in Ref. [80] recognize this, stating that the observed interference pattern "...might also be explained in terms of spectral [i.e., optical] interference projected onto the ionic continuum." The authors go on to say "...distinction between optical and wave packet interferences can be achieved with multiphoton transitions." In a multiphoton ionization, the periods of OI and QuI differ. Wollenhaupt *et al.* reference the work of Blanchet et al. [50,81] as an example of QuI in multiphoton ionization. However, these experiments differentiate OI from QuI in *bound state* transitions. Ionization was accomplished from a single-photon transition to the continuum, resulting in a Mechanism III' QuI with a period of t_{opt}. To the author's knowledge, no experiment showing QuI Mechanism III in non-resonant, multiphoton transitions to the continuum (and clearly distinguishing this interference from OI) has been done.

Chapter 3: Experiment 1, "Ions": Experimental Setup

This chapter describes the apparatus used in the first set of experiments, referred to as the "Ions" experiments [82]. A diagram of the experimental setup is shown in Fig. 3.1. Each component shown in Fig. 3.1 will be described in more detail in the following sections. The laser system, as well as the parameters of the pulses produced by the amplifier, will be described in Sec. 3.1. Twin-peaked pulses were produced with two distinct pulse shaping methodologies – with a spatial light modulator (SLM) and with a Mach-Zehnder interferometer (MZ). Both of these pulse shapers will be described in Sec. 3.2. Characterization of the temporal profile of the shaped and unshaped pulses is the topic of Sec. 3.3. Finally, the measurement of the atomic and molecular ions, including the vacuum chamber and time-of-flight mass spectrometer, will be described in Sec. 3.4.

3.1 Laser system

The femtosecond pulses used in the experiments are produced by a laser system composed of four individual lasers (see Fig. 3.1). Seed pulses are produced from an femtosecond oscillator (Kapteyn-Murnane Laboratories MTS) that is pumped by a continuous-wave (CW) pump laser (Coherent Verdi V-5). The seed pulses are

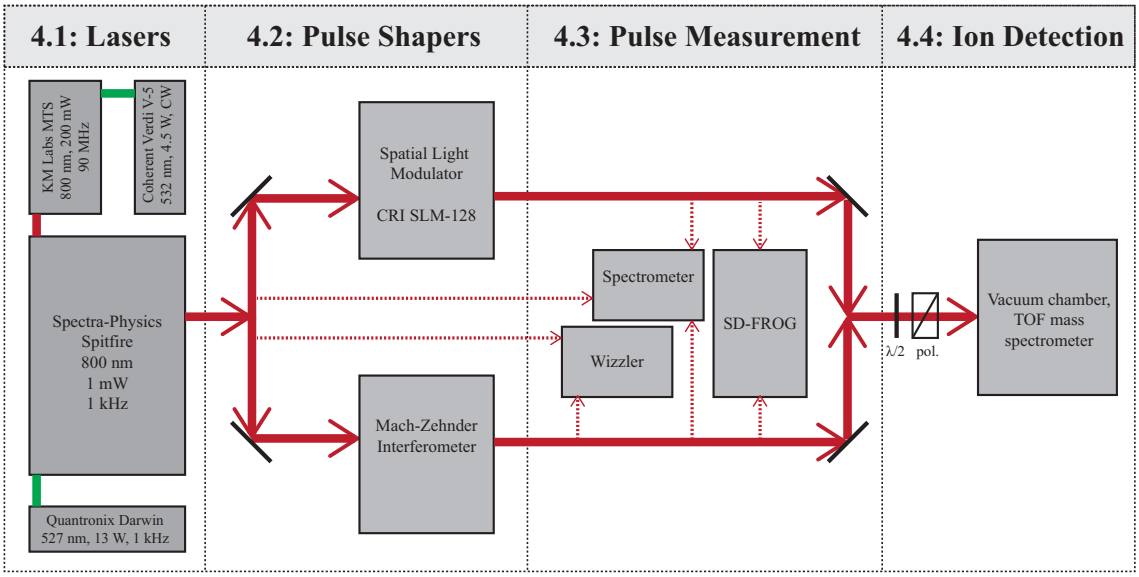

Fig. 3.1: High-level schematic of the "Ions" experiments. The experimental apparatus is divided into four sections, described in the four sections of this chapter.

amplified by a regenerative amplifier (Spectra-Physics Spitfire Pro40HP), which has its own pulsed pump laser (Quantronix Darwin-527). The oscillator and amplifier will be described in the following two subsections, followed by a description of the parameters of the amplified pulse.

3.1.1 Oscillator

The KM Labs oscillator provides weak seed pulses that can be amplified by the Spitfire. The gain medium inside the oscillator is a titanium-doped sapphire (Ti:sapphire) crystal. A simplified energy level diagram of Ti:sapphire, taken from Ref. [83] is shown in Fig. 3.2. The ground state is split into a pair of vibrationally-broadened levels. Absorption of 532 nm photons causes a transition of electron population from the ground state to an excited state. The excited state decays

to upper vibrational level of the ground state, causing fluorescence of 600-1000 nm photons. The oscillator is pumped by the Verdi, a diode-pumped, frequency-doubled Neodymium Vanadate (Nd:YVO_4) laser. The Verdi produces a CW beam at 532 nm (< 5 MHz RMS linewidth) [84].

Only the wavelengths λ that satisfy the boundary conditions of the cavity are amplified; this requires $L = j\lambda/2$, where L is the length of the cavity and j is a positive integer. The wavelengths that satisfy this condition are referred to as longitudinal modes; typically, only a few longitudinal mode survive (narrow bandwidth) and the oscillator operates in CW mode. It can be made to produce ultrashort pulses, however, by a technique known as mode-locking. A thorough discussion of mode-locking is given in reference [85]. When the oscillator cavity is mode-locked, many longitudinal modes oscillate together, with a well-defined relationship between the phases of different modes. The locked phase means that the modes only constructively interfere for a short amount of time, while destructively interfering at all others. This produces an ultrashort pulse, the exact duration of which is roughly determined by the bandwidth of supported longitudinal modes. The time between pulses is $2L/c$, the time for a pulse to make one round-trip in the oscillator cavity.

Mode-locking can be imposed on a laser cavity in many different ways, typically divided into two categories: active mode-locking, which will not be discussed here, and passive mode-locking. In passive mode-locking, a saturable absorber (an optical component that has a higher transmittance at high intensities than low intensities) is placed in the laser cavity. Pulses have a higher intensity than CW beams, because

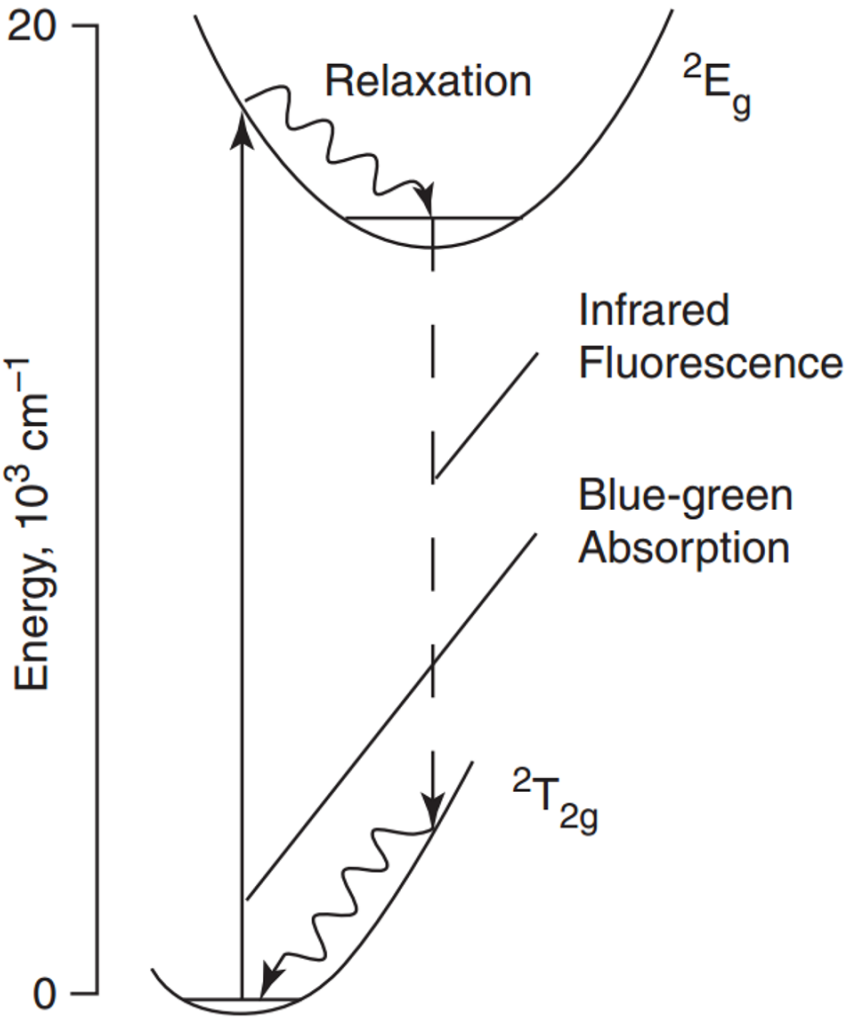

Fig. 3.2: Simplified energy-level diagram of Ti:sapphire, taken from Ref. [83]. Absorption of 532 nm photons promotes electrons to the excited state, which decay to an upper vibrational level of the ground state, leading to the fluorescence of near-infrared, 600-1000 nm photons.

the energy is concentrated in a short amount of time; therefore, the presence of a saturable absorber favors the production of ultrashort pulses in the laser cavity.

In the KM Labs oscillator used in this study, the Ti:sapphire crystal itself acts as the saturable absorber due to the optical Kerr effect. The optical Kerr effect is a third-order nonlinear effect that changes the index of refraction n due to the intensity of light I. The index of refraction is modified from its original value n_0 as $n(I) = n_0 + n_2 I$. The resulting spatially-dependent refractive index leads to a focusing of the pulses, a process known as self-focusing. The laser cavity is designed such that self-focusing leads to a better overlap of the pulsed beam with the pump (and consequently better amplification), compared to a CW beam. In this way, the Kerr medium acts as a saturable absorber, and mode-locked operation is favored [86].

The optical elements in the oscillator are dispersive, and so a spectral chirp is introduced into the pulse. Spectral chirp is a frequency-dependent group delay, which causes the pulse to broaden beyond the transform limit. In order to have the shortest possible mode-locked pulse, spectral chirp must be compensated. The chirp is compensated in the KM Labs oscillator by a prism pair [87].

The oscillator produces pulses at a repetition rate of 93.4 MHz, with an average power of $\sim$ 200 mW. This corresponds to $\sim$ 2.1 nJ per pulse. The pulses were observed to have a center wavelength of $\sim$ 805 nm. The FWHM bandwidth of the pulses was $\sim$ 25 nm. The duration of the pulses was not measured, but the minimum duration can be calculated from the time-bandwidth product for transform-limited hyperbolic secant pulses:

$$\Delta t_{FWHM}\Delta\nu_{FWHM} = \frac{c\Delta t_{FWHM}\Delta\lambda_{FWHM}}{\lambda_0^2} \geq 0.315, \tag{3.1}$$

where Δt_{FWHM} is the FWHM pulse duration, $\Delta\nu_{FWHM}$ and $\Delta\lambda_{FWHM}$ are the spectral FWHM bandwidths in frequency and wavelength, respectively, λ_0 is the center wavelength of the pulse, and c is the speed of light. Using the center wavelength and FWHM bandwidth above, the pulse duration was at least 27 fs.

3.1.2 Amplifier

The seed pulses produced by the oscillator were amplified in the Spectra-Physics Spitfire. The path of the seed pulses in the Spitfire is shown in Fig. 3.3 [83]. Amplifying the seed pulses directly is not feasible, because the high intensity of the amplified pulses would damage the optics in the amplifier cavity. Instead, the seed pulses were amplified through a process called chirped pulse amplification (CPA).

The seed pulse is first sent into a stretcher, where the pulse duration is broadened substantially (to approximately 100 ps). This is accomplished in the Spitfire by means of a series of diffraction gratings. The spectrum of the seed pulses is dispersed spatially by the first pair of gratings, and then the second pair of gratings undoes this spatial dispersion. By carefully selecting the geometry of the gratings, one can impose that the blue (lower wavelength) side of the spatially-dispersed pulse has a longer path in the stretcher than the red (higher wavelength) side – this is positive group velocity dispersion (GVD) [83]. The amount of GVD can be changed by changing the distance between the mirror grating pairs. For ease of alignment in the Spitfire, several fold mirrors (M1 and M2 in Fig. 3.3) are used so that the beam

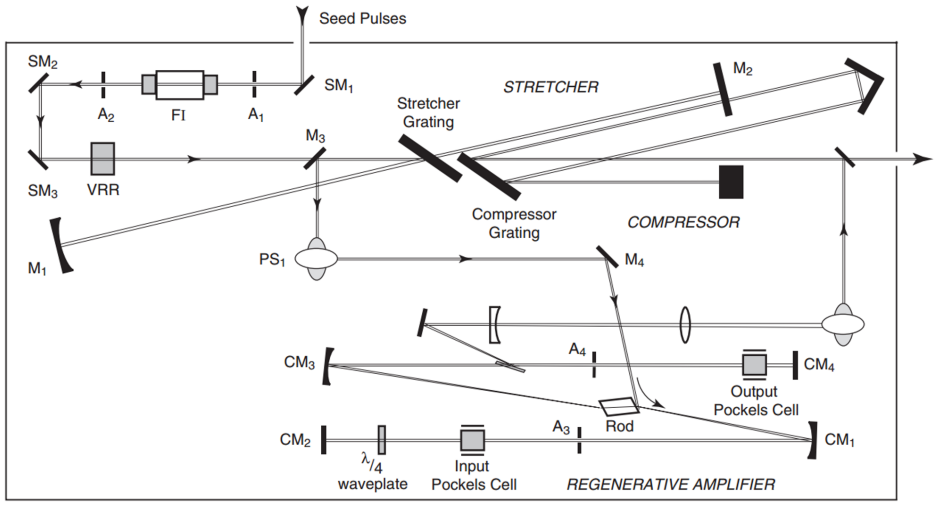

Fig. 3.3: Schematic of the seed pulses in the amplifier, taken from Ref. [83].

is incident on one grating four times, rather than four gratings one time each.

Next, the stretched pulses are sent into a regenerative amplifier, consisting of a gain medium (a Ti:sapphire crystal here) in an optical resonator. The stretched pulses are amplified by multiple passes through the gain medium in the optical resonator. The Ti:sapphire is pumped with the Darwin laser, which is a Q-switched, neodymium-doped yttrium lithium fluoride (Nd:YLF) laser with the following parameters: wavelength, 527 nm; repetition rate, 1 kHz; average power, 13 W; beam diameter, 2.5 mm [88]. As the repetition rate of the stretched seed pulses (93.5 MHz) is much larger than the repetition rate of the pump laser, only a small percentage of the seed pulses must be selected for amplification and the others discarded. This is accomplished in the Spitfire by placing two Pockels cells and a polarizer in the regenerative amplifier cavity. The Pockels cells act as voltage-controlled quarter waveplate (QWP); two passes through a Pockels cell that is "on" (i.e., has an ap-

plied voltage to put it in the QWP configuration) rotates the polarization of the pulse by 90 degrees. By selecting the "on" times of the two Pockels cells carefully, only one pulse every millisecond is amplified. The rest are discarded by the polarizer after one or fewer round trips in the cavity. The full details of the Pockels cell timing and cavity geometry are given in reference [83]. The pulses out of the amplifier have been increased in energy from the seed pulses by approximately a factor of 10^6 but are still on the order of hundreds of picoseconds long.

Finally, the amplified pulses are sent to the compressor. The compressor uses another combination of a grating and fold mirrors, set up in a geometry that introduces negative GVD to undo the positive GVD from the stretcher. The fold mirror is mounted on a motorized translation stage so that the amount of added GVD can be controlled, allowing for optimal recompression of the pulses.

3.1.3 Amplified pulse characteristics

Pulses were ejected from the Spitfire with a repetition rate of 1 kHz, with an energy of ~ 1 mJ per pulse. The nominal pulse duration was 70 fs–a full temporal characterization of the pulses will be given in Sec. 3.3. The pulses had a central wavelength of $\lambda_0 \sim 807 \pm 1$ nm (central frequency $\nu_0 = 0.372$ fs^{-1}, central angular frequency $\omega_0 \simeq 2.34$ rad/fs), with a FWHM bandwidth of ~ 20 nm (0.060 rad/fs angular frequency FWHM bandwidth). An example spectrum of an amplified pulse is given in Fig. 3.4.

In order to predict the focal intensity in ionization experiments, it is essential to be able to predict with some degree of accuracy the focal spot size of the beam

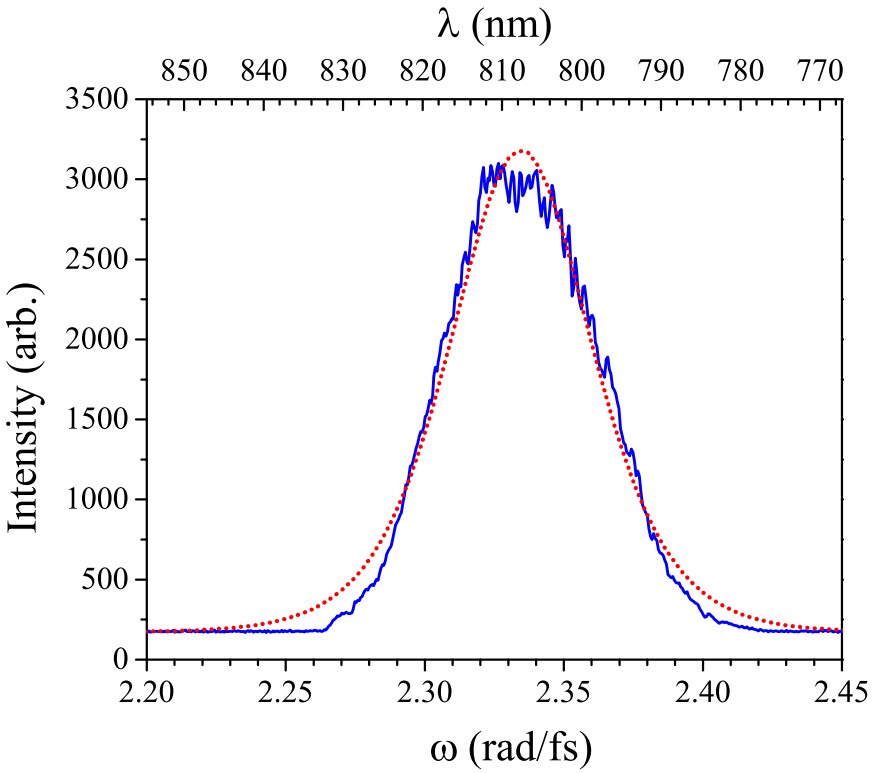

Fig. 3.4: (blue solid) Spectrum of the pulses directly after amplification (referred to as the *input pulses* for these experiments). (red dotted) A fit of the amplified spectrum to a sech^2 function, which finds $\omega_0 = 2.34$ rad/fs, $\Delta\omega_{FWHM} = 0.060$ rad/fs.

leaving the amplifier. For a beam with diffraction-limited divergence, the focused spot size is given as

$$w_f^{DL} = \frac{f\lambda_0}{\pi w_m}, \tag{3.2}$$

where f is the focal length of the lens, and w_m is the beam radius (at $1/e^2$ prior to the focusing element) [36]. The diffraction-limited spot size w_f^{DL} is also a $1/e^2$ radius. If the beam divergence is not diffraction-limited, the actual spot size will be larger than predicted by this equation.

In order to determine the beam divergence, the Spitfire output was focused using a concave mirror with a radius of curvature of 3 m (focal length $f = 1.5$ m). The input beam reflected off of the concave mirror with an angle of reflection of 2.8 degrees, which is small enough to be ignored here.

The beam radius was measured 10 in before hitting the concave mirror by knife-edging. The knife-edge measurement was done in both the horizontal and vertical directions to check the beam radius was the same in both directions. Knife-edging was accomplished by attaching a razor blade to a manual translation stage and incrementally blocking the beam. A Gaussian laser beam travelling in the $\hat{z}$ direction has a fluence (energy per unit area) distribution of

$$\mathcal{F}(x,y) = \mathcal{F}_0 e^{-2\frac{(x-x_c)^2}{w_x^2}} e^{-2\frac{(y-y_c)^2}{w_y^2}}, \tag{3.3}$$

where x_c (y_c) and w_x (w_y) are the center and $1/e^2$ radius of the beam in the x (y) coordinate, respectively. The total energy incident on a power meter is

$$U = \int_{-\infty}^{\infty} dx \int_{-\infty}^{\infty} dy \mathcal{F}(x, y). \tag{3.4}$$

If, however, a knife-edge blocks the portion of the beam for which $x > x_k$ from reaching the power meter, then the measured energy is

$$U(x_k) = \int_{-\infty}^{x_k} dx \int_{-\infty}^{\infty} dy \mathcal{F}(x, y) = 0.5\sqrt{\pi} w_y \mathcal{F}_0 \text{erf}\left(\frac{\sqrt{2}(x_k - x_c)}{w_x}\right). \tag{3.5}$$

The energy as a function of x_k was measured using a power meter, and was then fit to Eq. 3.5 to recover the width of the beam in the x direction (a constant term is added to Eq. 3.5 during fitting to account for an offset in the power meter). By orienting the knife-edge to travel in the y direction, w_y was determined in the same fashion.

A knife-edge measurement of the beam profile before the focusing mirror is shown in Figs. 3.5 and 3.6 (x and y directions, respectively). The fit values of the beam width were $w_x = 4.18 \pm 0.08$ mm and $w_y = 4.29 \pm 0.05$ mm.

After the beam radius was measured, the beam divergence was able to be measured. Using Eq. 3.2 with $f = 1.5$ m and $\lambda_0 = 807$ nm and $w_m = w_x$, the predicted beam waist is $w_f^{DL} = 92$ μm. The uncertainty in f is $\sim 10\%$ [86], which is a considerably larger fraction than the relative uncertainties in the wavelength and beam radius; therefore, a 10% uncertainty in focal length corresponds to a 10% uncertainty in beam waist.

It was observed by eye that the brightest spot of the focus was about 1.6 m from the curved mirror. To find the beam waist, it was necessary to take many

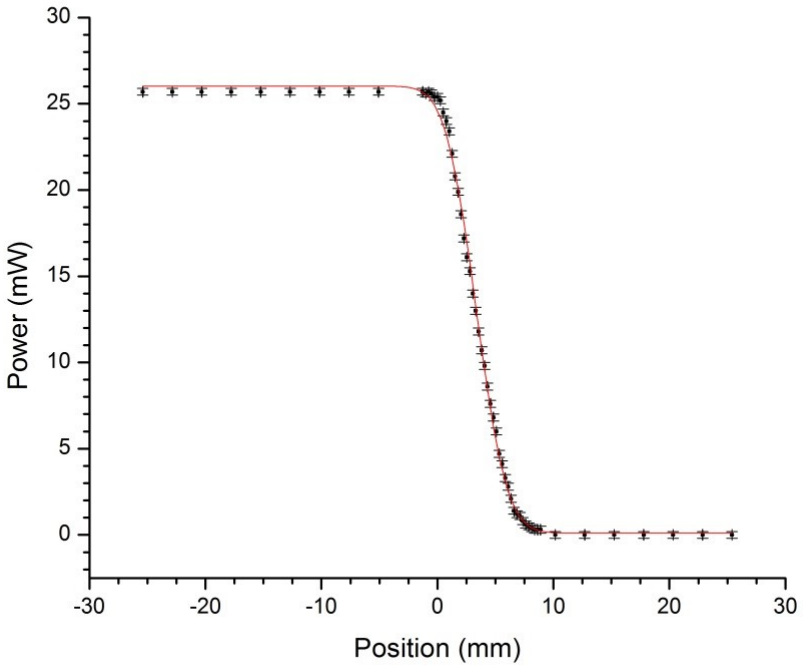

Fig. 3.5: Transmitted beam power vs. knife-edge position for horizontal knife-edge travel, taken before the focusing mirror. The data were fit to Eq. 3.5 (red solid curve) to determine the beam width, $w_x = 4.18 \pm 0.08$ mm.

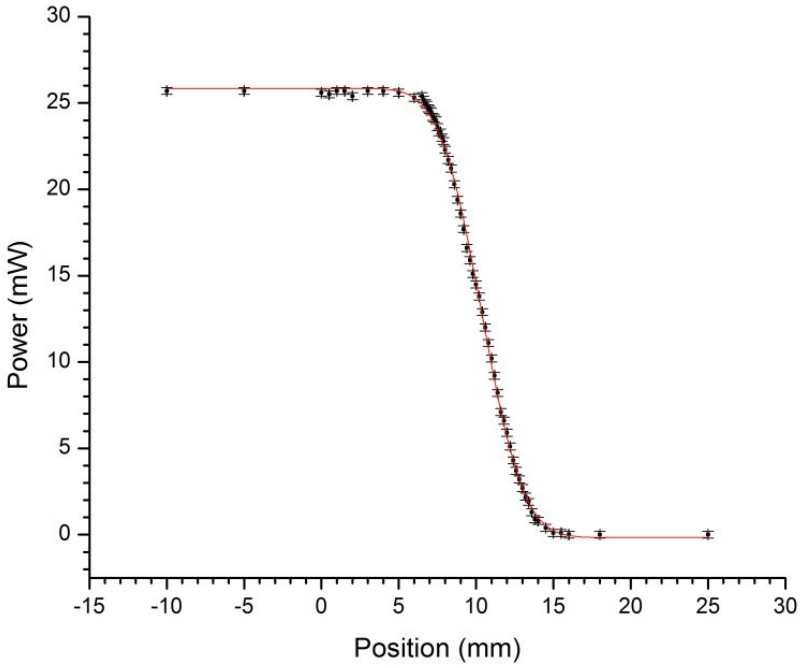

Fig. 3.6: Same as Fig. 3.5, but for vertical knife-edge travel. A fit of the data to Eq. 3.5 (red solid curve) yielded a beam width of $w_y = 4.29 \pm 0.05$ mm.

measurements of beam radius at different distances from the focus, $w(z)$, and fit to

$$w(z) = w_f\sqrt{1 + \left(\frac{z - z_c}{z_R}\right)^2}, \tag{3.6}$$

where w_f is the beam waist, z_c is the position of the focus and $z_R = \pi w_f^2/\lambda_0$ is the Rayleigh length. In order to fit the data to Eq. 3.6 accurately, beam radii must be measured over at least $2z_R$, centered at z_c. For the diffraction-limited beam waist of 92 μm, the Rayleigh length is $\sim$ 3.3 cm. If the beam divergence is not diffraction-limited, the Rayleigh range will be even larger. With this in mind, 14 knife-edges were taken of the beam, in 0.5-inch (1.27 cm) increments, over a range of 7 inches (18 cm). The uncertainty in the position was 0.1 inches (0.25 cm).

Knife-edging was done in the same ways as the unfocused beam (only in the x direction). The resolution of the translation stage used in knife-edge measurements was 0.001 inches (25.4 μm). The recovered beam radius as a function of position (the mirror was located at $z = 0$ is shown in Fig. 3.7. The red dotted line is a fit to Eq. 3.6. The recovered parameters from this fit are $w_f = 143.6 \pm 3.7\mu$m and $z_R = 3.27 \pm 0.28$ inches (83.1 ± 7.1 mm). Also, the focal length of the mirror was measured to be 64.30 ± 0.19 inches (1633 ± 7 mm). One can use z_R to confirm the measurement of of w_f. For the value of z_R given above and $\lambda_0 = 807$ nm,

$$w_f = \sqrt{\frac{\lambda_0 z_R}{\pi}} = 146.3\mu\text{m}, \tag{3.7}$$

in good agreement with the measured value. The measured beam waist is $\sim$1.5 times the predicted beam waist. Therefore, Eq. 3.2 must be modified to

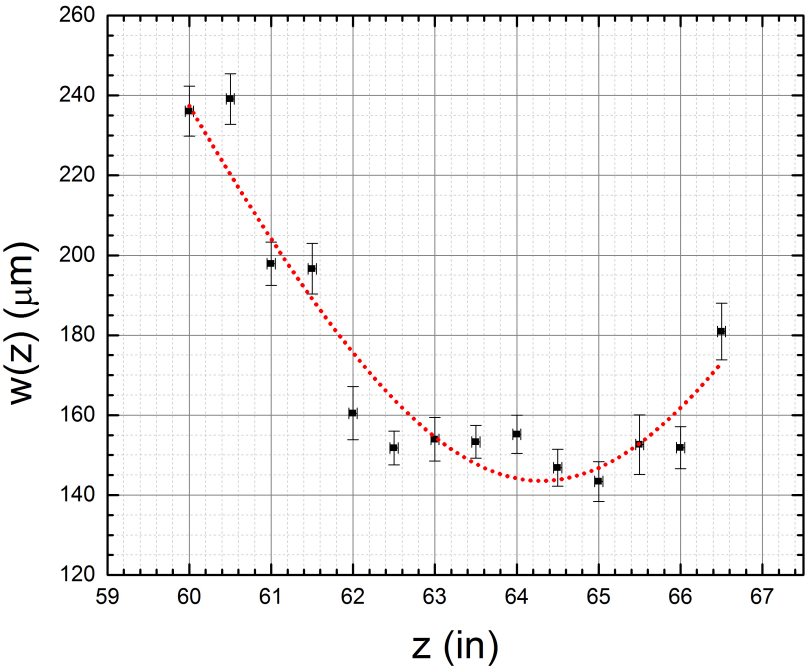

Fig. 3.7: Fit value of beam width, $w(z)$, vs knife-edge position z. The focusing mirror is taken to be at position $z = 0$. The data were fit to Eq. 3.6 (red dotted curve), giving $z_R = 83.1 \pm 7.1$ mm, $w_f = 143.6 \pm 3.8\mu$m, and $z_c = 1633 \pm 7$ mm.

$$w_f \simeq 1.5\frac{f\lambda_0}{\pi w_m}. \tag{3.8}$$

If the beam waist w_f is known, along with the beam average power P_{avg}, laser repetition rate f_{rep}, and pulse duration Δt_{FWHM}, the peak intensity of the pulse can be found,

$$I = \frac{2P_{avg}\mathcal{T}}{\pi w_f^2 \Delta t_{FWHM} f_{rep}}, \tag{3.9}$$

where $\mathcal{T}$ is the transmittance of the vacuum chamber entrance window (92%) [36,86]. Equation 3.9 is only valid for TL pulses. A determination of the maximum intensity of non-TL pulses is made in Sec. 3.3.3.

3.2 Pulse shapers

The pulses produced by the Spitfire–referred to as *input pulses* in this work – were near-transform limited[1]. In order to probe QuI in ionization, these input pulses must be shaped into twin-peaked pulses. This section describes the two ways in which TPPs were produced.

3.2.1 Spatial light modulator

The first way that input pulses were shaped to produce twin-peaked pulses was with frequency-domain pulse shaper (PS) which used a spatial light modulator (SLM). A TPP produced with the PS will be referred to as a TPP_{PS} in this work.

[1] This will be confirmed in Sec. 3.3.1

The PS leverages a major advantage in ultrafast pulse shaping – that the complex electric field of the pulse can be fully described as a function of *either* time or frequency, and that the two functions are related through a Fourier transform. In other words, for a desired complex field $E(t)$, the corresponding field in frequency space is

$$\tilde{E}(\omega) = \mathrm{F}[E(t)] \equiv \frac{1}{\sqrt{2\pi}} \int_{-\infty}^{\infty} E(t) e^{i\omega t} dt, \tag{3.10}$$

where $\omega = 2\pi\nu$ is the angular frequency and F is the Fourier transform operator. For a TPP as defined in Eq. 2.3, the frequency-domain field is calculated from Eq. 3.10 to be

$$\begin{aligned} \tilde{E}_{TPP}(\omega) = \frac{E_0 e^{i\theta_1}}{\sqrt{2\pi}} \Bigg[& \Delta t \pi \mathrm{sech}\left(\frac{\pi \Delta t}{2}(\omega - \omega_0)\right) \\ & + \Delta t \pi e^{i\Delta\phi} e^{-i(\omega-\omega_0)\tau} \mathrm{sech}\left(\frac{\pi \Delta t}{2}(\omega - \omega_0)\right) \Bigg], \end{aligned} \tag{3.11}$$

which can be simplified in several ways. The definitions $\tilde{E}_0 = \frac{E_0 \Delta t \pi}{\sqrt{2\pi}}$ and $\Delta\omega = \Delta\omega_{FWHM}/1.76 = \frac{2}{\pi\Delta t}$ are useful. In addition, the hyperbolic secant term can be factored out, which leads to

$$\tilde{E}_{TPP}(\omega) = \tilde{E}_0 e^{i\theta_1} \mathrm{sech}\left(\frac{\omega - \omega_0}{\Delta\omega}\right) \left[1 + e^{i(\Delta\phi - (\omega-\omega_0)\tau)}\right]. \tag{3.12}$$

The spectral intensity is

$$\begin{aligned}\tilde{I}_{TPP}(\omega) &\equiv |\tilde{E}_{TPP}(\omega)|^2 \\ &= \tilde{I}_0 \text{sech}^2\left(\frac{\omega-\omega_0}{\Delta\omega}\right)\cos^2\left(\frac{(\omega-\omega_0)\tau-\Delta\phi}{2}\right), \end{aligned} \tag{3.13}$$

where $\tilde{I}_0 \equiv 4\tilde{\mathcal{E}}_0^2$. The spectral intensity for four different TPPs with $\lambda_0 = 807$ nm ($\omega_0 = 2.34$ rad/fs), $\Delta\omega = 0.034$ rad/fs ($\Rightarrow \Delta\omega_{FWHM} = 0.060$ rad/fs, same as Fig. 3.4), and various combinations of τ and $\Delta\phi$ are plotted in Fig. 3.8. The spectral intensity profile consists of an envelope (the same envelope as the input pulse) with sinusoidal interference fringes. Because ω_0 and $\Delta\omega$ are fixed by the input pulse, τ and $\Delta\phi$ determine the period and phase of the fringes, respectively (see Fig. 3.8). A TPP can be produced if a device is able to modulate the intensity of the input pulse spectrum in this way. More generally, an arbitrary shaped pulse can be synthesized from the input pulse if a device exists that can change both the intensity ($\tilde{I}(\omega)$) and the phase ($\phi(\omega)$) of the frequency-domain input field.

One device that meets this requirement is an SLM. An SLM is an array of birefringent liquid crystal pixels, each with a voltage-controlled index of refraction for light polarized parallel to the crystal extraordinary axis (e-axis). Depending on the relative alignment of the light polarization and crystal axis, the phase or the polarization state of the input light can be altered [89]. There are three main modes of operation of an SLM, shown in Fig. 3.9 (taken from Ref. [89]).

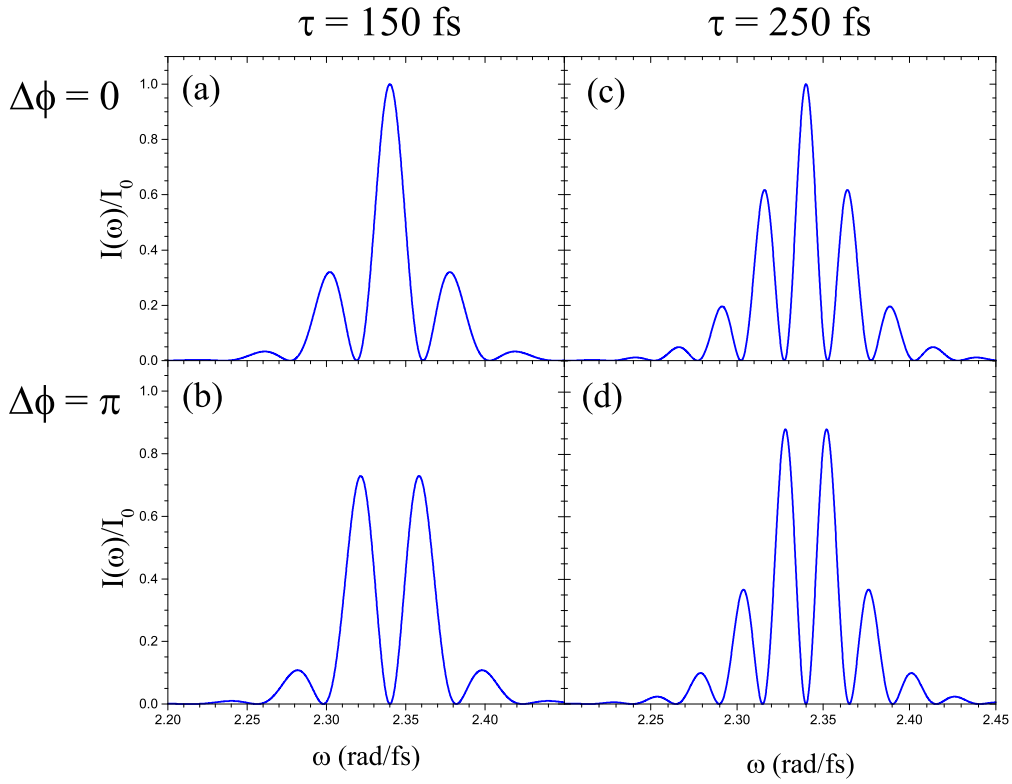

Fig. 3.8: Normalized spectral intensity $\tilde{I}_{TPP}(\omega)/\tilde{I}_0$ for TPPs with $\omega_0 = 2.34$ rad/fs, $\Delta\omega = 0.034$ rad/fs, which matches the input pulse shown in Fig. 3.4, and: (a) $\tau = 150$ fs, $\Delta\phi = 0$; (b) $\tau = 150$ fs, $\Delta\phi = \pi$; (c) $\tau = 250$ fs, $\Delta\phi = 0$; and (d) $\tau = 250$ fs, $\Delta\phi = \pi$.

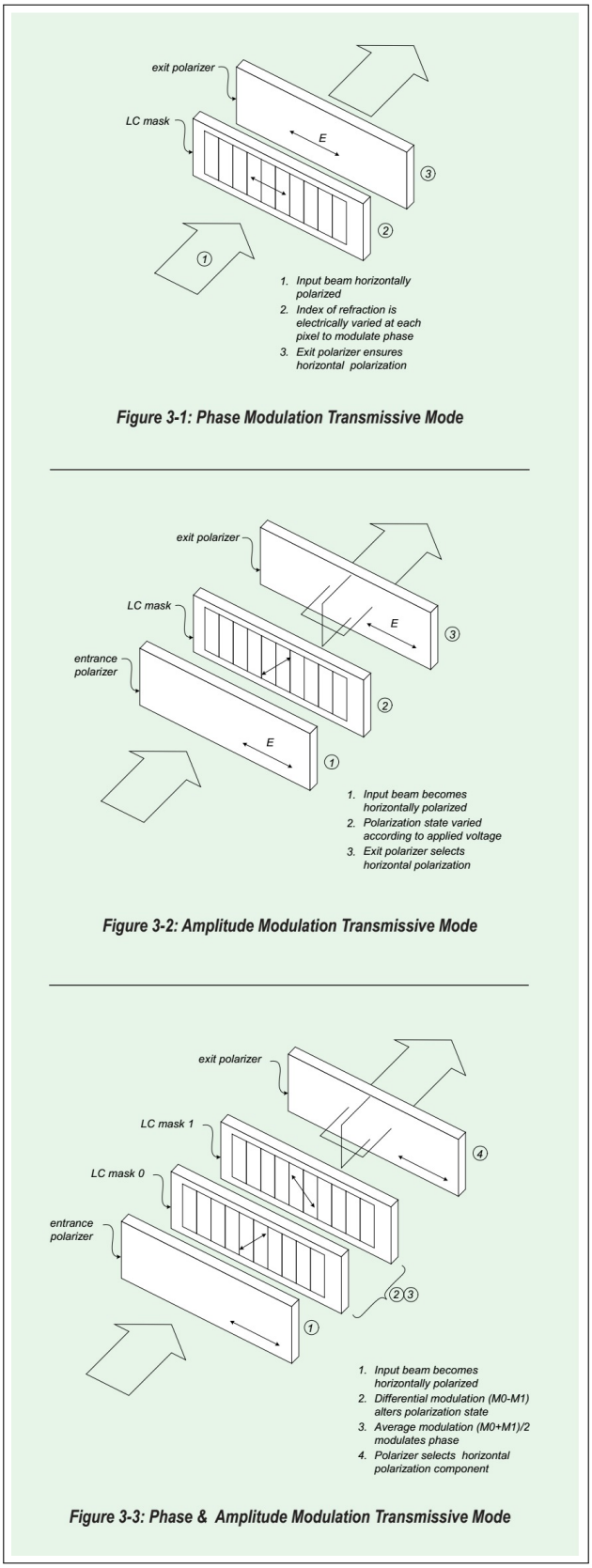

Fig. 3.9: Three operation modes of an SLM, taken from Ref. [89].

The first operation mode (top panel of Fig. 3.9) is for input light polarized parallel to the crystal e-axis. In this case, the SLM acts as a retarder, modifying the phase of the input light at each pixel. Light polarized along the ordinary axis (o-axis) is unaffected. By placing a polarizer before the SLM, o-axis light can be removed. If the input light has been spectrally dispersed (by, e.g., a diffraction grating), each pixel of the SLM will correspond to a particular frequency, and in this way $\phi(\omega)$ can be modified.

In the second operation mode (middle panel of Fig. 3.9), the e-axis of the crystals are oriented at 45° to the input light polarization. In this case, each pixel acts as a voltage-controlled waveplate, and the polarization state of the spectrally-dispersed input light can be changed as a function of frequency. An exit polarizer selects a single linear polarization. In this way, $I(\omega)$ can be modulated.

The third operation mode (bottom panel of Fig. 3.9) allows for simultaneous intensity and phase modulation, and is accomplished by placing two back-to-back arrays of liquid crystal pixels, with the e-axes oriented orthogonal to each other and both 45° to the input light polarization. The common mode variation of the pixels (i.e., the sum of the two modulations) modulates the phase of the input light, and the differential mode variation (the difference of the two modulations) rotates the polarization. The SLM used in these experiments, a Cambridge Research and Instrumentation SLM-128, uses the third operation mode, and consists of two sets of 128 liquid crystal pixels aligned horizontally in a one-dimensional array. The two arrays are referred to as the master and slave arrays.

A complete description of shaping ultrafast pulses with spatial light modula-

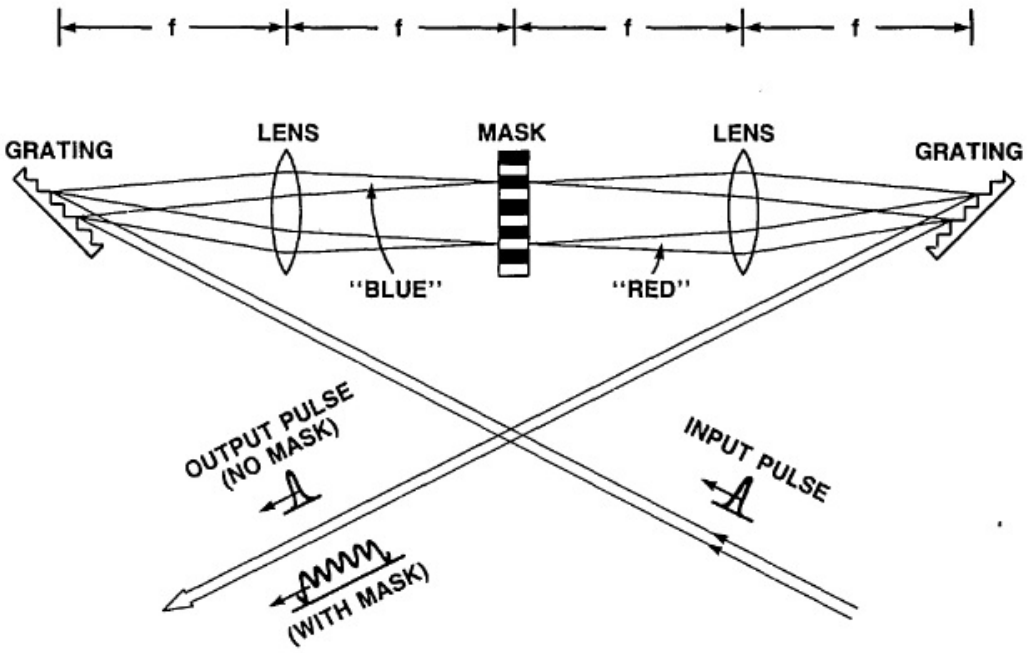

Fig. 3.10: Schematic of a $4f$ pulse shaper apparatus, taken from Ref. [90]. The first grating disperses the input pulse, which is then collimated by the first cylindrical lens. A spatial light modulator is placed at the MASK position to change the spectral intensity and phase of the input pulse. The output pulse spectrum is then recombined by a matched lens-grating pair. In the pulse shaper used in this thesis, cylindrical mirrors are used instead of lenses to collimate the beam, to reduce dispersion. Also, a mirror behind the mask reflects the beam back on itself, enabling only one mirror and grating to be used in the setup.

tors is given in Refs. [90, 91]. The PS was constructed by placing the SLM in the center of a grating-lens apparatus in a $4f$ geometry, pictured in Fig. 3.10 (taken from Ref. [90]). A $4f$ geometry PS consists of two gratings and two cylindrical lenses, where the distance between grating and lens is f, the focal length of the lens. The distance between the two lenses is $2f$, and the SLM is placed at the midpoint of the two lenses. In this way, the pulse spectra are spatially dispersed and collimated onto the face of the SLM, so that each pixel of the SLM corresponds to a different wavelength. This allows the intensity and phase to be adjusted at each wavelength increment. The spatial dispersion is undone by the second lens-grating pair. In practice, the matching of the pair of lenses and pair of gratings is difficult, as is the precise calibration of the distances between components. Because of this, most pulse shaping experiments (including the experiments here) use a folded-$4f$ geometry, where a mirror is placed on the back of the SLM to retro-reflect the beam; in this case, only one grating and one lens are needed. The pulse shaper used in this thesis uses a cylindrical mirror instead of a lens, to eliminate the dispersion caused by passage through the lens material.

In order to use the SLM for pulse shaping, its voltage response must be calibrated. Figure 3.11 shows the phase retardance of the SLM as a function of the applied voltage, from 0 to 4000 V. This retardance was calculated for a folded-$4f$ geometry, i.e., the light passes through the pixel arrays twice. The largest possible retardance of the SLM is approximately 8π. In the experiments, the working voltage range was about 850 V to 2500 V, which limits the phase retardance range to approximately 4π.

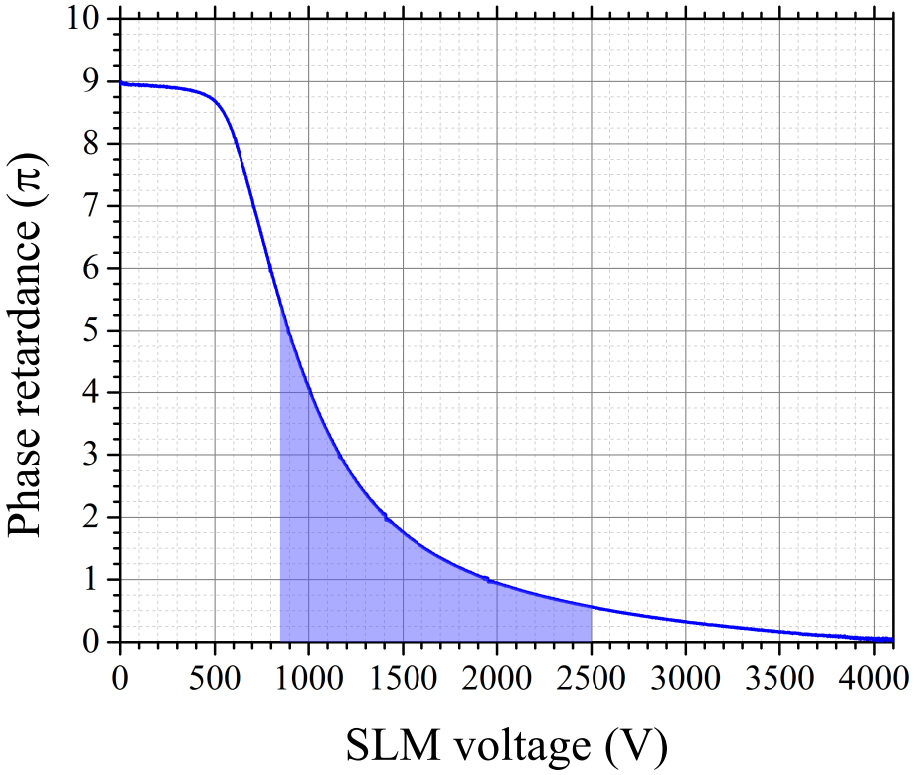

Fig. 3.11: Phase retardance (phase difference between extraordinary and ordinary light) vs SLM applied voltage. The typical operating voltage in the experiments is shown by the shaded area, 850 V to 2500 V.

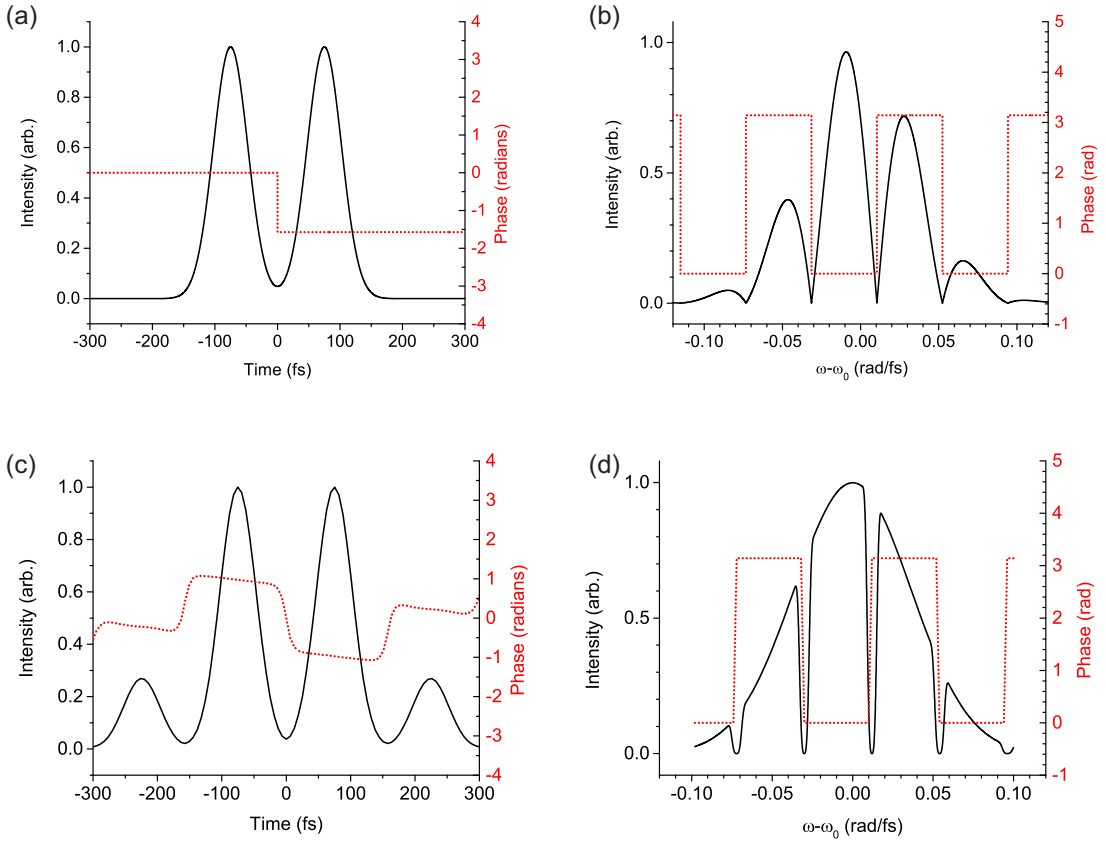

Fig. 3.12: Intensity (black solid) and phase (red dashed) of two TPPs, in the time and frequency domains. (a) Temporal profile of a TPP with $\tau = 150$ fs and $\Delta\phi = 0.5\pi$. (b) Spectral intensity and phase of the same TPP, obtained by performing a Fourier transform of the TPP in (a). (c) Temporal intensity and phase of an approximate TPP (referred to nonideal) with the same τ and $\Delta\phi$ as (a). The temporal field of this TPP was computed as a numerical inverse Fourier transform of (d). In (d), the $\cos^2$ variation in intensity seen in (b) is replaced by notches at the phase jumps in order to minimize energy loss through the spatial light modulator. The two main peaks in (c) combined contain about 75% of the total TPP energy.

One disadvantage of using the SLM to produce TPPs is that approximately half of the input pulse energy is absorbed by the SLM in order to create the fringes in frequency space. One way to circumvent this problem is to synthesize an approximate TPP by modifying the intensity mask. This is shown in Fig. 3.12. The mask shown in Fig. 3.12(d) consists of replacing the sinusoidal modulation with a series of notches, with the notches placed wherever $\cos^2\left(\frac{(\omega-\omega_0)\tau-\Delta\phi}{2}\right) = 0$. This creates a nonideal version of a TPP_{PS} (shown in Fig. 3.12(c)), so this mask will be referred to the nonideal mask. The ideal mask is shown in Fig. 3.12(b); it produces an ideal TPP (Fig. 3.12(a)). Use of the nonideal mask drastically reduces the amount of energy absorbed by the SLM. The nonideal TPP was found by performing a numerical inverse Fourier transform on the nonideal mask. The nonideal TPP has the same τ and $\Delta\phi$ as the ideal TPP, but small subordinate are present that are not present when using the ideal mask.

3.2.2 Mach-Zehnder interferometer

The second way that TPPs were produced from input pulses was with the Mach-Zehnder interferometer, which is diagrammed in Fig. 3.13. A TPP produced by the MZ will be referred to in this work as a TPP_{MZ}. The input pulse was split into two arms by a 50/50 beam splitter. Both of these arms traveled down a delay line and were recombined with a second 50/50 beam splitter. The retroreflecting mirror pair on one delay line was fixed, while the mirrors on the other were placed on a variable translation stage (Aerotech ALS130 linear motor stage). Upon recombination, the pair of pulses formed the TPP, and τ was varied by changing the position of the

variable arm translation stage. The setup of the MZ ensured that each arm traveled through one beam splitter and was reflected by the other. In this way the amount of group delay dispersion (GDD) accumulated by the two arms in the MZ was nearly equal, as long as the beam splitters were the same thickness and material. The nominal minimum step size of the stage was 10 nm, which caused a total change in the path length of the variable arm of the MZ of $\delta l = 20$ nm. This corresponds to a change in the delay between the two arms of $\delta\tau = 0.067$ fs. In other words, τ was ideally a linear function of the step number s, i.e.,

$$\tau(s) = \frac{k_0}{\omega_0} s + \tau_0, \tag{3.14}$$

where τ_0 is the TPP delay at $s = 0$ and k_0 is found by noting that $k_0 s = 2\pi$ when $s = 40.35$, i.e., the number of steps to travel one optical period (807 nm at 20 nm per step). This gives $k_0 = 0.157$ rad/step. Unfortunately, the translation stage used in the MZ took non-uniform steps, meaning that k_0 varied during the experiment. This variation in k_0 could be corrected after the experiment, using a procedure described in detail in Appendix A.

The post-correction step size can be verified in the MZ power interferometry. The power interferometry signal is a measurement of the TPP average power P as a function of τ. Optical interference between the two arms of the MZ will cause periodic oscillations in $P(\tau)$. These interference fringes will be largest when the pulses overlap ($\tau = 0$) and the oscillation envelope will decrease as $|\tau|$ increases. Before correction, the oscillation period was non-uniform (see Appendix A). The

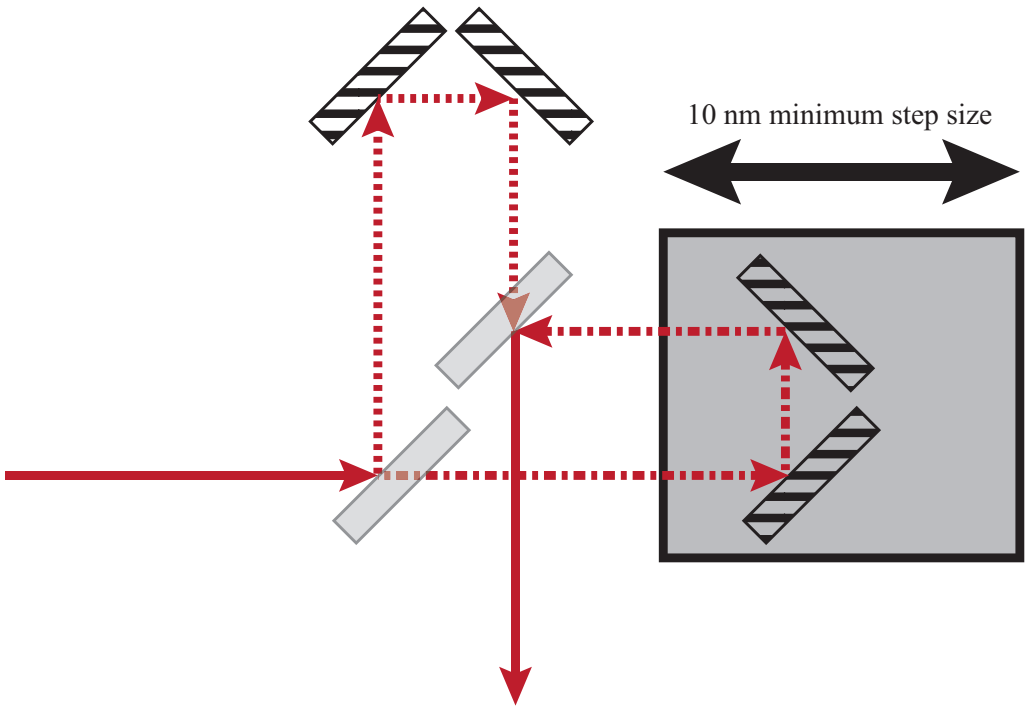

Fig. 3.13: Schematic of the Mach-Zehnder interferometer (MZ) used in these experiments. The translucent rectangles represent 50/50 beam splitters, and the hatched rectangles represent dielectric-coated mirrors. One of the mirror pairs in the MZ is mounted on a variable-delay translation stage with 10 nm resolution.

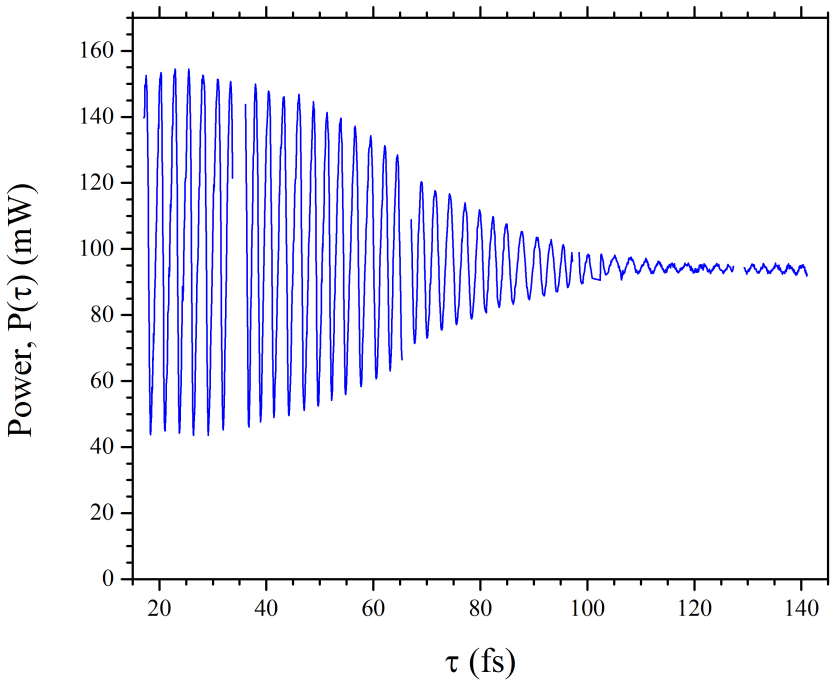

Fig. 3.14: TPP power P as a function of delay τ, after $\tau(s)$ has been calibrated using the procedure described in Appendix A. The appendix also addresses the four breaks in the signal, due to a jump in the translation stage every 500 steps.

power interferometry after the step-size correction is shown in Fig. 3.14, showing uniform, periodic oscillations, other than four breaks in the signal. These were due to jumps in the translation stage, that were also corrected for by the procedure in Appendix A. This indicates that the relative value of τ (i.e., the change in τ between each step) was well-determined.

3.3 Pulse measurement

Three measurement devices were used to characterize the pulses. The first was a spectrometer to record the spectra of the input and shaped pulses (i.e., Fig. 3.4). The spectrometer used was a Photon Control SPM-002. This spectrometer had a wavelength resolution of 0.189 nm. The second measurement device was a commercial Wizzler (from Fastlite Technologies), described in Sec. 3.3.1. It was suitable for characterization of the temporal intensity and phase of the input pulses and the individual arms of the MZ, i.e., near-TL pulses only. The Wizzler is not able to measure the intensity and phase of complex pulses accurately, which precluded measurement of the TPPs with this device. The third device was a home-built self-diffraction frequency-resolved optical gating (SD-FROG), which was used to characterize both the input pulses and the TPPs. The SD-FROG is described in Sec. 3.3.2. Section 3.3.3 describes how SD-FROG measurements can be used to find important parameters of complex pulses, e.g., τ and $\Delta\phi$ for a TPP.

3.3.1 Wizzler

The input pulses were measured with a Wizzler, which allows characterization of near-TL pulses through a process called self-referenced spectral interferometry (SRSI) [92, 93]. Briefly, the device works as follows: the pulse to be measured is first sent through a birefringent material to produce a time-delayed, polarization-rotated replica pulse. The main and replica pulses are both focused onto a cross-polarized wave (XPW) crystal [94, 95]. In the Wizzler, the XPW crystal is BaF_2.

For light polarized along the XPW crystal optical axis, an orthogonally-polarized XPW field with amplitude $E_{XPW}(t)$ is produced through a third-order nonlinear optical interaction; $E_{XPW}(t)$ is related to the input field amplitude $E(t)$ by

$$E_{XPW}(t) \propto |E(t)|^2 E(t). \tag{3.15}$$

Equation 3.15 shows that the XPW field is a replica of the input pulse filtered by the input pulse intensity. As a result, $E_{XPW}(t)$ is shorter in time and consequently has a broader spectrum than $E(t)$. This spectral broadening is reminiscent of self-phase modulation (SPM), and indeed Eq. 3.15 is similar to the equation describing SPM. The difference between the two is that SPM does not produce a rotated polarization, and can occur in isotropic media. In contrast, the XPW field is orthogonally-polarized to the input field and a nonisotropic medium is necessary.

In the Wizzler, the XPW crystal is rotated so that the main pulse produces an XPW signal but the replica pulse does not. After XPW generation, main pulse extinction is accomplished by a polarizer, so that only the time-delayed replica pulse and XPW pulse survive. These two pulses are measured using Fourier transform spectral interferometry (FTSI) [96, 97]. If the spectral phase of the XPW pulse is known, the spectral intensity and phase of the replica pulse (and, by a Fourier transform, the temporal intensity and phase) can be recovered from the interferogram. Because the XPW spectrum is much broader than the replica pulses, to a first approximation the XPW phase is 0. This approximation is only good if the spectral phase of the pulse to be measured is nearly constant, i.e., when the input

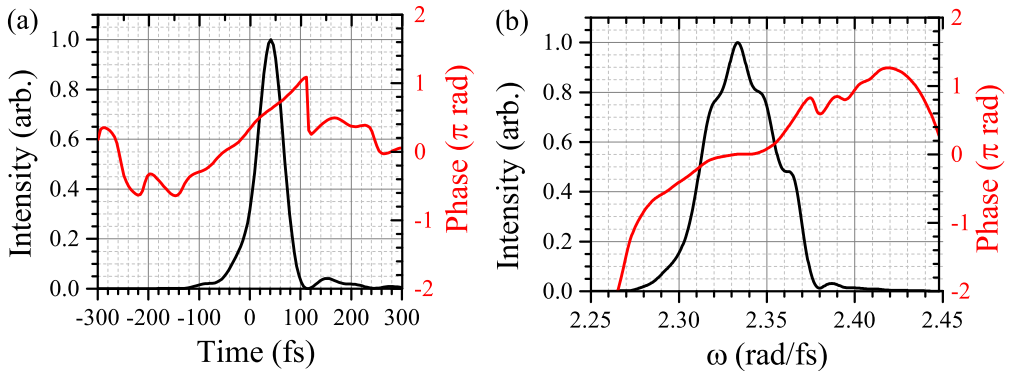

Fig. 3.15: Intensity (black) and phase (red) for a input pulse in the temporal (a) and frequency (b) domains, measured by the Wizzler.

pulse is near-TL. As such, the Wizzler is not able to measure TPPs or other shaped pulses.

The Wizzler-measured input pulse profile is shown in Fig. 3.15. The temporal intensity plot shows a small subordinate peak that arrives after the main pulse at $\tau \simeq 150$ fs; this subordinate peak is not unique to this measurement, but is quite robust, appearing in daily measurements from two separate pulse measurement devices (Wizzler and FROG, see Sec. 3.3.2) over a time period of four years (and before and after the laser was moved to a new building and realigned). The spectral profile of the pulse, in Fig. 3.15 gives a clue as to the origin of this subordinate peak. The spectral phase of the input pulse is not flat, indicating that the input pulse is chirped. In particular, the shape of the spectral phase roughly approximates a cubic function, indicating the presence of third-order chirp. Odd-order chirp is known to lead to pre- or post-pulses in the time domain with a π phase jump between the main pulse and the subordinate [98].

3.3.2 SD-FROG

One of the most successful methods developed to completely characterize ultrashort pulses is FROG, first developed in the early 1990s by Rick Trebino and coworkers [99]. The device, shown in Fig. 3.16, is in essence a spectrally-resolved autocorrelator. The pulse to be measured is divided in two by a 50/50 beam splitter. The two arms travel through delay lines, one of which has a variable translation stage with a resolution of $\sim$ 100 nm (0.67 fs). In the FROG measurements in this work, a step size of approximately 0.5 μm (3.3 fs) were used. The two arms are then focused and crossed onto a nonlinear optical element by a curved mirror. A nonlinear signal is produced by the pulses when they overlap spatially and temporally. Many different nonlinear effects have been employed in different FROG geometries. In this work, the nonlinear process used was self-diffraction, which occurs in any material with a $\chi^{(3)}$ nonlinearity (fused silica here). Due to the third-order nonlinearity, the two pulses change the index of refraction of the material. When the pulses overlap, the intensity-dependent index of refraction produces an effective grating inside the medium, and a portion of the incoming light is diffracted.

The spectrum of the nonlinear signal is measured as a function of the delay between the two arms. The resulting two-dimensional measurement, called an SD-FROG trace, is the light intensity as a function of both frequency and delay. An SD-FROG trace can also be calculated numerically for a given pulse intensity, $I(t)$, and phase, $\phi(t)$. An iterative process of comparing the experimentally-measured FROG trace with numerical reconstructions allows determination of $I(t)$ and $\phi(t)$;

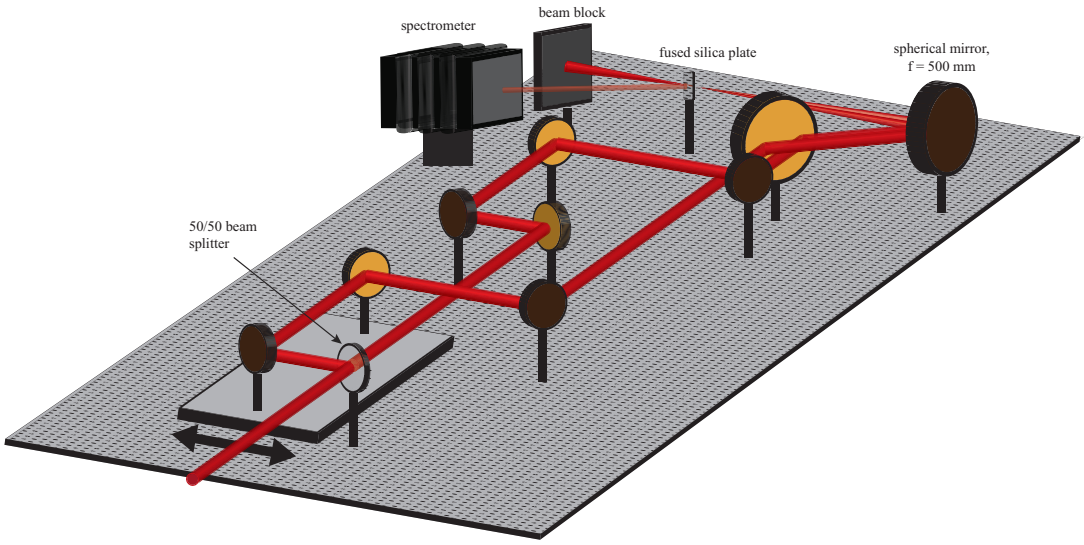

Fig. 3.16: Schematic of the self-diffraction frequency-resolved optical gating (SD-FROG) used in these experiments. All of the unlabeled optics in this figure are gold mirrors. The translation stage (light grey rectangle) had a minimum resolution of ~ 100 nm, corresponding to a temporal delay of 0.67 fs. Typically, a larger step size of 500 nm was used in the experiments.

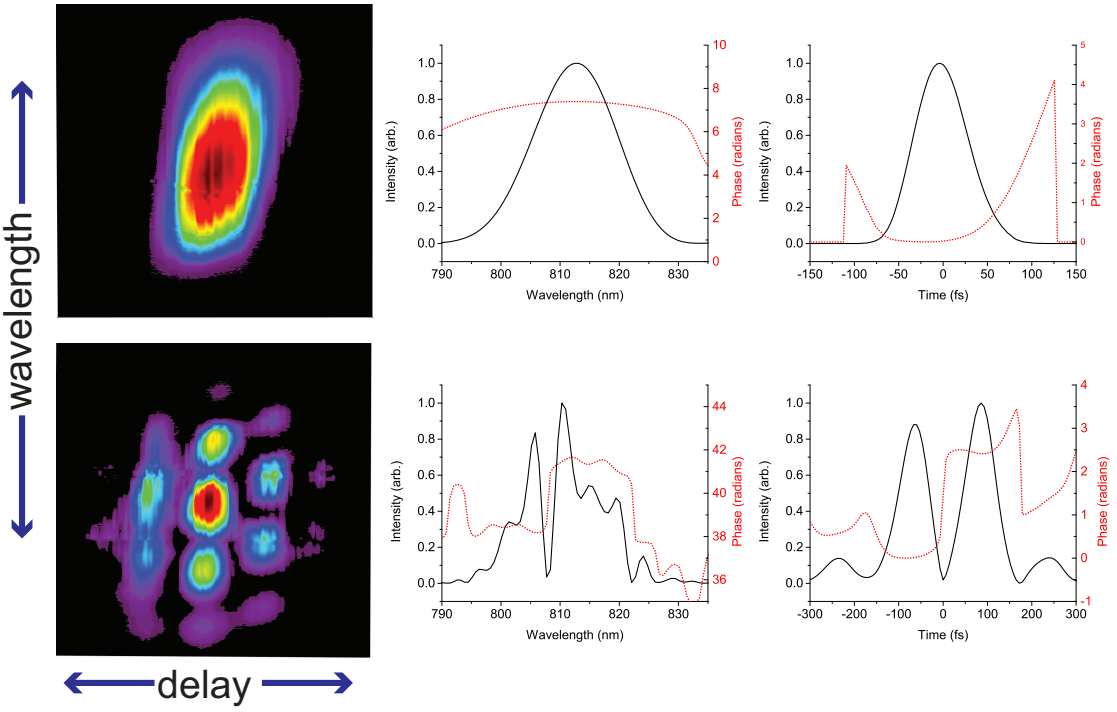

Fig. 3.17: SD-FROG traces (left column) and the corresponding reconstructed intensity and phase in both the spectral (middle) and temporal (right) domains, for a near-TL pulse (upper row) and a TPP produced by the SLM with a phase mask set for $\tau = 150$ fs, $\Delta\phi = -0.75\pi$ (lower row). The TPP was synthesized using an nonideal TPP mask, as described in Sec. 3.2.1.

the reconstructed solution is unique [98–100]. Figure 3.17 shows the measured SD-FROG traces, and the reconstructed intensity and phase in both the time and frequency domains, for two pulses–a near-TL pulse and a TPP. The TL pulse does not show the subordinate peak of the input pulse seen in Fig. 3.15(a) because the higher order spectral phase (Fig. 3.15(b)) was corrected by the PS prior to FROG measurement. The TPP was produced with the PS using the nonideal mask on the SLM (see Sec. 3.2.1 and Fig. 3.12), and as a result small subordinate peaks on the outside edges of the two main peaks were observed.

3.3.3 *Determination of shaped pulse characteristics*

The method for determining τ and $\Delta\phi$ is demonstrated in Fig. 3.18 using an example TPP from an experiment. First, the TPP intensity was fit to a double-Gaussian peak function, and the centers of the earlier and later peaks, t_1 and t_2 respectively, were determined. For the TPP in Fig. 3.18, $t_1 = -74.0(3)$ fs and $t_2 = 75.8(4)$ fs. One then finds that $\tau = t_2 - t_1 = 149.8(5)$ fs.

It should be noted that fitting the TPP intensity to a double-Gaussian is only a rough approximation of the TPP shape; a more thorough fit would be to a modified version Eq. 2.6 (sech^2 peaks) where the widths and heights of the two peaks are allowed to differ. The interference term in Eq. 2.6 can cause the peak locations to shift. This shift was measured (by performing both fits) to be as large as 10 fs, depending on $\Delta\phi$.

The phases of the earlier and later peaks, $\phi_1 = 4.79(6)$ rad and $\phi_2 = 8.01(14)$ rad, respectively, were found independently of τ by averaging the FROG-reconstructed phase $\phi(t)$ over the FWHM of each peak. These ranges are shown as solid blue curves in Fig. 3.18. The relative phase was calculated as $\Delta\phi = \phi_2 - \phi_1 = 1.03(5)\pi$ rad. The uncertainty in ϕ_1, ϕ_2 is the standard deviation of the phase over this range; in this way, the given uncertainty in $\Delta\phi$ was a rudimentary quantization of the chirp of the individual peaks.

It is also useful to determine the intensity of the TPPs. The intensity of TL pulses was derived in Sec. 3.1.3. For a non-TL pulse, the intensity can be determined from the FROG (or Wizzler) measurement, along with a measurement of the pulse

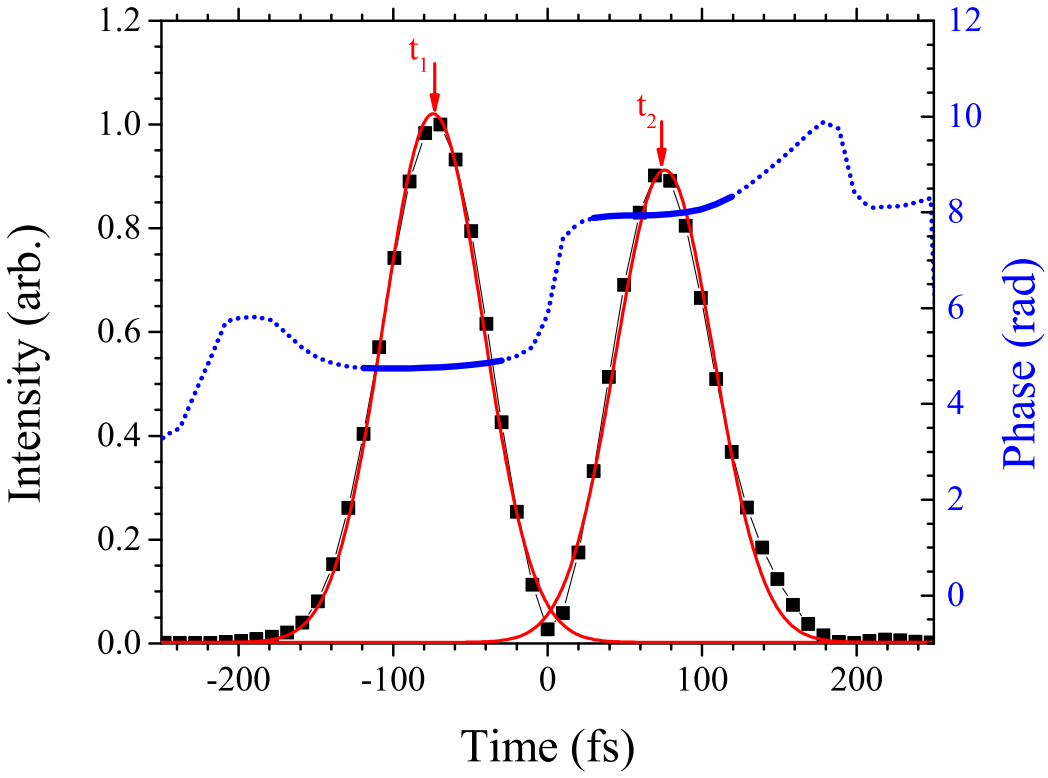

Fig. 3.18: SD-FROG reconstructed intensity $I(t)$ (black squares) and phase $\phi(t)$ (blue dotted curve) for a TPP, synthesized using the SLM with an ideal TPP mask (see Sec: 3.2.1). A fit of the TPP intensity to a double-Gaussian function is also shown (red solid curve). The center values of the earlier and later peaks, $t_1 = -74.0(3)$ fs and $t_2 = 75.8(4)$ fs, respectively, were used to find $\tau = t_2 - t_1 = 149.8(5)$ fs. The average phase of the earlier and later peak, $\Delta\phi_1 = 4.79(6)$ rad and $\Delta\phi_1 = 8.01(14)$ rad, respectively, were found by averaging $\phi(t)$ across the FWHM of each peak. These ranges are shown in solid blue.

energy. When a pulse (TPP or any arbitrary pulse shape) is measured by the SD-FROG or Wizzler, the reconstruction returns an intensity normalized so that the maximum intensity is unity. This normalized intensity will be referred to as $I_{FROG}(t)$. This intensity is proportional to the intensity in W/cm^2, $I(t)$, i.e.,

$$I_{FROG}(t) = \mathcal{C} I(t), \tag{3.16}$$

where $\mathcal{C}$ is the normalization constant. Finding $\mathcal{C}$, then, allows determination of the intensity. By integrating $I_{FROG}(t)$, one finds the area underneath the FROG-measured intensity curve,

$$A_{FROG} = \int_{-\infty}^{\infty} I_{FROG}(t) = \mathcal{C} \int_{-\infty}^{\infty} I(t). \tag{3.17}$$

The integral of intensity over all time is radiant fluence, $\mathcal{F}$, defined as energy per unit area. So, $\mathcal{C} = A_{FROG}/\mathcal{F}$, and

$$I(t) = \frac{\mathcal{F}}{A_{FROG}} I_{FROG}(t). \tag{3.18}$$

Because $I_{FROG}(t)$ and A_{FROG} are known, a determination of the pulse intensity can be made if the pulse fluence is known. The pulse fluence is

$$\mathcal{F} = U/A_{eff}, \tag{3.19}$$

where U is the pulse energy and $A_{eff} = \pi w^2/2$ is the effective mode area (i.e., the area of a top-hat beam with the same maximum intensity and total energy as the Gaussian beam, w is the beam radius at $1/e^2$ intensity.

The average power of the laser, P_{avg}, was measured before the vacuum chamber with a thermopile power meter (Newport 818P-015-19). The energy in each pulse at the focal spot is $U = P_{avg}\mathcal{T}/f_{rep}$, where f_{rep} is the repetition rate of the laser (1 kHz) and $\mathcal{T}$ is the transmittance of the vacuum chamber entrance window (92 %). The pulse fluence at the focus, when $w = w_f$, is then

$$\mathcal{F} = \frac{U}{A_{eff}} = \frac{2P_{avg}\mathcal{T}}{\pi w_f^2 f_{rep}}, \tag{3.20}$$

and combining Eqs. 3.18 and 3.20 gives

$$I(t) = \frac{2P_{avg}\mathcal{T}}{\pi w_f^2 f_{rep} A_{FROG}} I_{FROG}(t). \tag{3.21}$$

One can confirm this formula for intensities by investigating the appearance intensities of various charge states of xenon, which have been both calculated [101] and measured [102] previously. The measured appearance intensities for Xe^{2+} and Xe^{3+} found in Ref. [102] are $\sim 1.8 \cdot 10^{14}$ W/cm^2 and $\sim 3 \cdot 10^{14}$ W/cm^2, respectively.

Figure 3.19 shows the time of flight (TOF) mass spectrum (see Sec. 3.4) for an input pulse (i.e., a single pulse, not a TPP) with $P_{avg} = 21.9(5)$ mW. For this pulse, $A_{FROG} = 70.75$, and with $w_f = 7.2\mu$m (as determined in Sec. 3.4), $f_{rep} = 1000$ Hz, and $\mathcal{T} = 0.92$, one finds that this pulse has a maximum intensity (when $I_{FROG}(t) = 1$) of $3.34(1)\cdot 10^{14}$ W/cm^2, approximately the appearance intensity of Xe^{3+}. One can see in the mass spectrum a series of peaks corresponding to the various isotopes of Xe^+ and Xe^{2+}, but there is also a barely-perceptible Xe^{3+} signal, confirming that the determination of pulse intensity is correct.

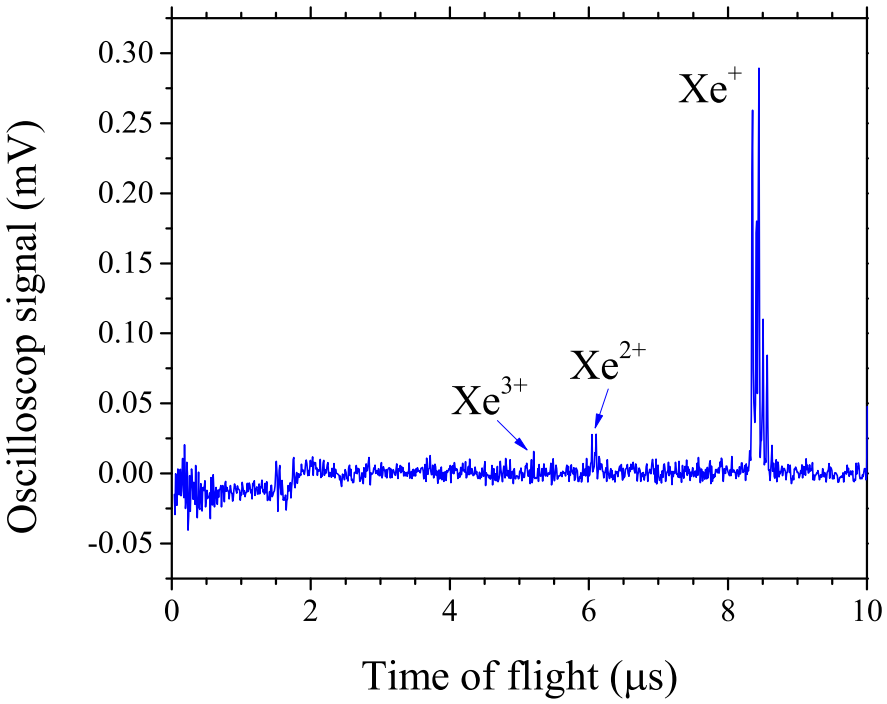

Fig. 3.19: Time of flight (TOF) mass spectrum for xenon, ionized with a pulse of $\sim$ 70 fs duration and an average laser power of 21.9(5) mW. This power corresponds to an intensity of $3.34(1) \cdot 10^{14}$ W/cm^2. The TOF peaks for Xe^+, Xe^{2+}, and Xe^{3+} are marked. The multiple-peaked structure for each charge state is due to the multiple stable isotopes of xenon; the relative heights of the peaks within each charge state were observed to agree with naturally-occurring isotopic abundances.

3.4 Ion measurement

After shaping and characterization, the pulses were sent into a ultrahigh vacuum chamber. The energy of the pulses could be changed immediately before entrance into the vacuum chamber with a rotatable half-wave plate and linear polarizer. A turbomolecular vacuum pump evacuated the chamber to a background

pressure of $\sim 3 \cdot 10^{-9}$ Torr, and the target gas (Xe or CO_2) was introduced through a variable leak valve up to an operating pressure between $7.5 \cdot 10^{-8}$ Torr and $1.0 \cdot 10^{-6}$ Torr, depending on the experiment. The exact pressure used will be specified in the description of each experiment's results. The pulses passed through a fused silica entrance window and hit a focusing mirror at the opposite end, where they were reflected and focused in the interaction region. The focal length of the lens was 75 mm, from which one can calculate the focal spot size using Eq. 3.8, giving $w_f = 7.2\mu$m.

The number of xenon ions emanating from the focal spot was measured using a TOF mass spectrometer, described in detail in Ref. [103]. A diagram of the TOF spectrometer is shown in Fig. 3.20. The spectrometer consists of three regions: the first acceleration region, the field-free drift region, and a second acceleration region. In the first acceleration region, a number of electrostatic rings (ERs) creates a uniform electric field $\mathcal{E}_a = (V_2 - V_1)/(d) = -V_1/(2d)$, where V_1 is the voltage applied to the ER1 (the ER closest to the field-free region) and d is the distance between ER1 and ER2. The voltages applied always obeyed the relation $V_1 = 2V_2$. In the experiment, the charged particles were born with some initial velocity due to kinetic energy release, but for atomic and molecular ions, this velocity was negligibly small compared to the final velocity due to acceleration in the field $\mathcal{E}_a$. Hence, it was assumed in this calculation that the particles started from rest (the case of nonzero initial velocity is considered in Ref. [103]). In this case, the time it takes a particle of mass m and charge q to traverse the acceleration region of the TOF is

$$t_a = \sqrt{\frac{2m}{-qV_1}}d \tag{3.22}$$

and the velocity of the particles at the end of the acceleration region is

$$v(t_a) = \sqrt{\frac{-qV_1}{2m}}. \tag{3.23}$$

One sees that the voltages applied to the grids must be negative in order to accelerate the (positively-charged) ions into the TOF mass spectrometer. In the field free region, there is no electric field, so the particles traverse this region with velocity $v(t_a)$. The time to traverse the field free region (of length d_{ff} is

$$t_{ff} = \frac{d_{ff}}{v(t_a)} = \sqrt{\frac{2m}{-qV_1}}d_{ff}. \tag{3.24}$$

In the second acceleration region, of length $d^{'}$, the particles accelerate through a field $\mathcal{E}_a^{'} = -V_{front}/d^{'}$, where V_{front} is the voltage applied to the front of the microchannel plate (MCP) detector and $d^{'}$ is the second acceleration region length. The initial velocity in this region is $v(t_a)$. One finds the total travel time in the second acceleration region to be

$$t_a^{'} = \sqrt{\frac{2m}{q}}d^{'}\left(\frac{\sqrt{-V_1/4} + \sqrt{-V_1/4 - V_{front}}}{V_{front}}\right). \tag{3.25}$$

The total flight time is t_{TOF} the sum of t_a, t_{ff}, and $t_a^{'}$,

$$t_{TOF} = \sqrt{\frac{2m}{q}}\left(\frac{d + d_{ff}}{\sqrt{-V_1}} + \frac{d^{'}\left(\sqrt{-V_1/4 - V_{front}} + \sqrt{-V_1/4}\right)}{V_{front}}\right). \tag{3.26}$$

The flight time depends only on the mass-to-charge ratio m/q of the particles and the applied voltages V_1, V_{front}. In these experiments, $V_1 = -2000$ V, $V_{front} = -300$ V, $d = 38.1$ mm, $d_{ff} = 140$ mm, and $d^{'} = 30$ mm.

At the end of the flight tube, the charges were amplified by the MCP, and TOF waveforms were subsequently captured with a 500 MHz digital oscilloscope (LeCroy 9350AM). One TOF waveform corresponded to one laser shot. Typically, 1000 waveforms were taken per data point. The temporal resolution of the spectrometer is 10 ns; for Xe^+ ions, with a mass of approximately 130 Daltons, the corresponding mass resolution is approximately 0.3 Daltons.

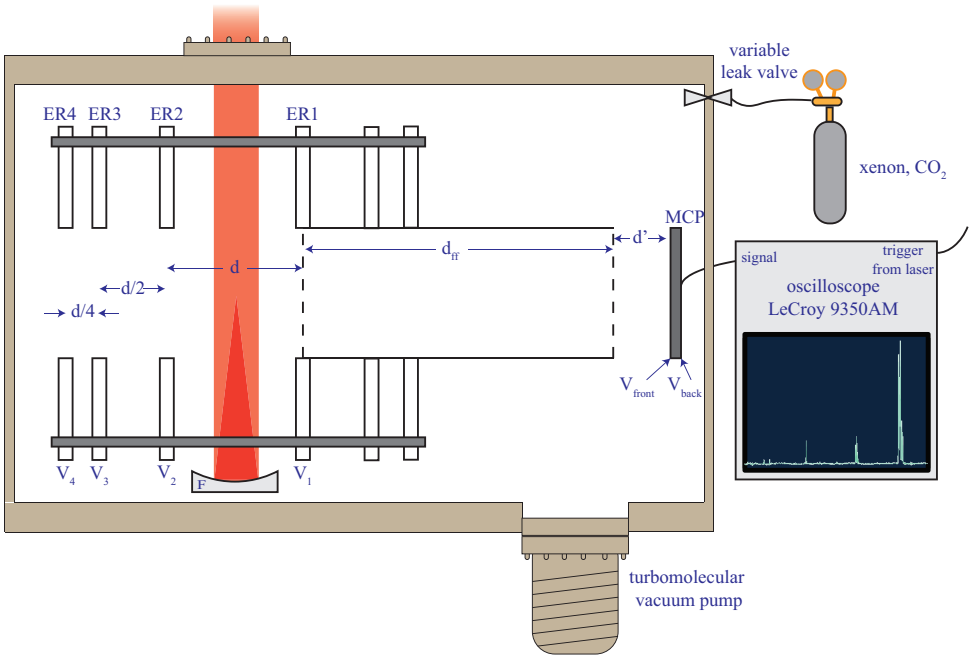

Fig. 3.20: Diagram (not to scale) of the vacuum chamber and TOF mass spectrometer. A turbomolecular pump evacuated the chamber and the target gas was introduced through a variable leak valve. The laser pulses passed through an entrance window into the chamber and struck a spherical mirror, F, with a focal length of 75 mm. The TOF spectrometer consists of a number of electrostatic rings (ER1 through ER4); two additional rings were not used in the experiment. The voltages applied to the rings were $V_1 = -2000$ V, $V_2 = V_1/2 = -1000$ V, $V_3 = V_1/4 = -500$ V, $V_4 = V_1/8 = -250$ V. The distances between two rings are labeled, $d = 38.1$ mm. This created a uniform electric field of $\mathcal{E}_a = V_1/(2d) = 26.2$ kV/m. Ion were accelerated to the right through a field-free drift region of length $d_{ff} = 140$ mm. After a second acceleration region of length $d^{'} = 30$ mm, the ion signal was amplified using a micro-channel plate (MCP) with front and back voltages $V_{front} = -300$ V and $V_{back} = -2300$ V. The amplified ions were then detected on an oscilloscope.

Chapter 4: Experiment 1, "Ions": Results and Discussion

In Sec. 1.3, two goals of the TPP ionization experiments were discussed: first, to determine the role that pulse trains with well-defined phases play in strong-field optimal control experiments, and second, to search for multiphoton QuI in strong-field ionization. The experiments described in this chapter are primarily concerned with the first goal, in the context of OI. The results of four representative TPP experiments will be presented and discussed. The experiments used TPPs synthesized from both the pulse shaper ($\mathrm{TPP_{PS}}$) and the Mach-Zehnder interferometer ($\mathrm{TPP_{MZ}}$) In each experiment, the target was Xe, which has an ionization potential of 12.13 eV. Therefore, eight 800 nm photons are required to reach the ionization threshold. The first experiment (Sec. 4.1) investigated ionization of Xe with a $\mathrm{TPP_{PS}}$ created using a nonideal mask as described in Sec. 3.2.1 and Fig. 3.12. The ion yield was measured as a function of $\Delta\phi$ for a fixed τ. The second experiment (Sec. 4.2) was similar to the first, except that an ideal mask was used to synthesize the TPPs. The third experiment measured the ionization of Xe vs τ for a $\mathrm{TPP_{MZ}}$, with a τ resolution of $\delta\tau = 0.67$ fs (Sec. 4.3). The experimental results were compared with two numerical simulations. The fourth experiment again used a $\mathrm{TPP_{MZ}}$ to ionize Xe, this time with a resolution of $\delta\tau \simeq 0.067$ fs (Sec. 4.4).

Originally, each successive experiment was viewed as an improvement on the previous one, in that the TPP phase could be controlled more precisely. While that is true, each experiment offered its own unique insight into the role of pulse trains in optimal control. The last experiment utilizes the most ideal (and well-known) TPP while the earliest experiment has considerable nonidealities in the TPP field. However, such nonidealities are common in optimal control experiments, which means that more direct comparison between the $\mathrm{TPP_{PS}}$ experiments with optimal control experiments is possible. This comparison will be done in Chap. 5.

4.1 TPP_{PS} produced with a nonideal mask

4.1.1 Results

The Xe^+ yield Y vs $\Delta\phi$ is plotted in Fig. 4.1(a). Xenon was ionized with a $\mathrm{TPP_{PS}}$ produced with a nonideal mask for three different values of τ (values are approximate): 140 fs, 150 fs, and 170 fs. Ion yields were calculated by integrating the composite TOF signal (sum of 1000 individual TOF waveforms) over all Xe^+ isotopes, then normalized so that the maximum yield is unity. The yields for 150 fs and 170 fs have been shifted for ease of viewing. Error bars for $\Delta\phi$ were determined as described in Sec. 3.3.3. The error bars in yield were found by measuring the yield from a sample pulse 10 times in a row. This was done for 13 different sample pulses at intensities between 0.3 and 0.8 $\mathrm{PW/cm^2}$ and was found to be $\sim 5\%$ at all intensities. As a result, 5% error bars are used in Fig. 4.1(a).

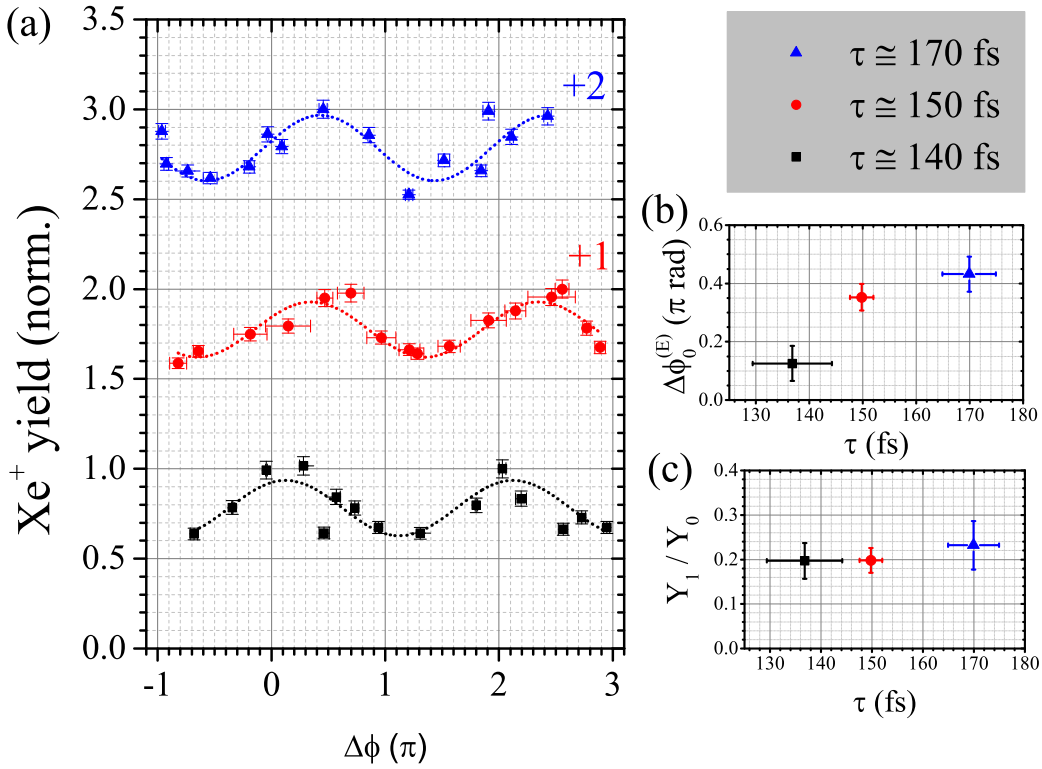

Fig. 4.1: (a) Yield of Xe^+ vs $\Delta\phi$ for a TPP_{PS} produced with a nonideal mask for three different set values of τ: 140 fs (black squares), 150 fs (red circles), and 170 fs (blue triangles). The 150 fs (170 fs) curve has been shifted by +1 (+2) for ease of viewing. The dotted lines on each plot are a fit of the data to Eq. 4.1. (b) The fit value of $\Delta\phi_0^{(E)}$ for the three data sets, vs τ. (c) Y_1/Y_0, calculated from the fit values of Y_1 and Y_0, vs τ.

All three runs were performed at a gas pressure of $7.5(1) \cdot 10^{-8}$ Torr. The TPP_{PS} energy was adjusted with the half-wave plate and polarizer combination so that the energy of the twin peaks was 91 μJ. This was the energy of the twin peaks *only*, without including additional energy from the small subordinate peaks that occurred as an artefact of the nonideal SLM mask (see Fig. 3.12). The subordinate

peaks had an energy between 5% and 20% of the twin peaks energy, so the total pulse energy was somewhere between 95 and 110 μJ. Each TPP_{PS} was measured with the SD-FROG to determine A_{FROG}. The maximum intensity of each TPP, denoted $I^{(max)}$, was calculated from Eq. 3.21. These intensities are shown in Fig. 4.2.

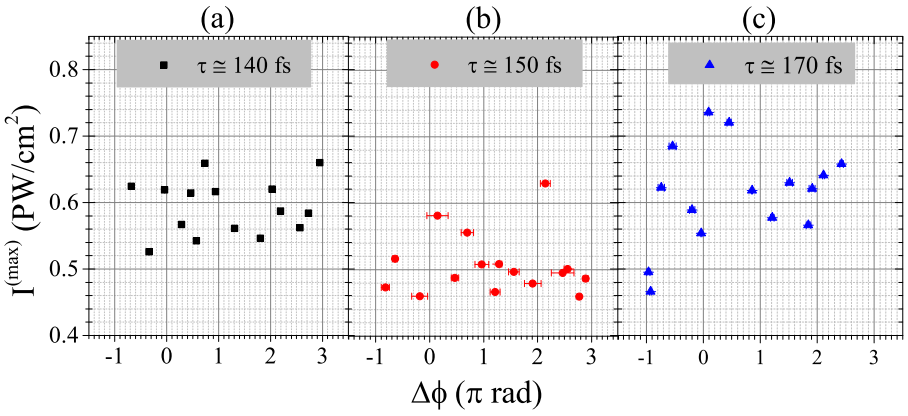

Fig. 4.2: The maximum intensity $I_{TPP}^{(max)}$ of each TPP_{PS} for the three runs shown in Fig. 4.1(a); (a) 140 fs, (b) 150 fs, and (c) 170 fs. The maximum intensity was determined from an SD-FROG measurement and Eq. 3.21.

4.1.2 Discussion

Most of the discussion of the SLM experiments will be deferred to Sec. 4.2, but there are a few observations that can be made from Fig. 4.1. First, all three of the plots oscillate periodically in $\Delta\phi$ with a period of 2π, indicative of OI. In fact, all are well-fit by a cosine function,

$$Y = Y_0 + Y_1 \cos\left(\Delta\phi - \Delta\phi_0^{(E)}\right), \tag{4.1}$$

where $\Delta\phi_0^{(E)}$ is the phase shift of the oscillation (the location of the yield maximum relative to $\Delta\phi = 0$). The "E" in this variable stands for "experimental"; it is used

to distinguish this phase shift from the phase shifts found in model calculations in Sec. 4.2.2. The fit curves are shown with the data in Fig. 4.1.

Figure 4.1(b) shows $\Delta\phi_0^{(E)}$ for the three values of τ. While the values of $\Delta\phi_0^{(E)}$ for $\tau = 150$ fs and 170 fs are close (within the fit uncertainty), it is clear that $\Delta\phi_0^{(E)}$ for $\tau = 140$ fs is different. The explanation of these phase shifts is deferred to Sec. 4.2.2.

The *visibility* of an oscillatory function is defined as follows:

$$\mathcal{V} = \frac{max - min}{max + min}, \tag{4.2}$$

where max and min are the maximum and minimum values of the function, respectively. In Eq. 4.1, $\mathcal{V} = Y_1/Y_0$. The visibilities for the three values of τ is plotted in Fig. 4.1(c). In contrast to $\Delta\phi_0^{(E)}$, the values of $\mathcal{V}$ are the same within the fit uncertainty, all approximately 0.2.

In this section, a quantification of OI will be presented that will be used in simulations in Secs. 4.2, 4.3, and 4.4 - namely, the relationship between the TPP maximum intensity $I^{(max)}$ and the ion yield. Equation 2.7 shows that $I^{(max)}$ varies periodically in $\Delta\phi$ due to OI (with a period of 2π). To lowest order (i.e., for a TL pulse), Y is a monotonically-increasing function of the pulse intensity, i.e., $Y \propto (I^{(max)})^m$, where m is positive. As described in Sec. 2.1, the value of m depends on the ionization regime as determined by the Keldysh parameter [7]. For 800 nm pulses with an intensity of $6 \cdot 10^{14}$ W/cm^2, $\gamma \simeq 0.4$, placing this experiment in the tunneling ionization regime [104]. Furthermore, at high intensities the corona of

Tab. 4.1: Visiblities of $I^{(max)}$, $(I^{(max)})^{3/2}$, and the fits of $Y(\Delta\phi)$ for different values of τ.

	$\tau \simeq 140$ fs	$\tau \simeq 150$ fs	$\tau \simeq 170$ fs
$I^{(max)}$	0.11	0.16	0.22
$(I^{(max)})^{3/2}$	0.17	0.23	0.33
Fit $Y(\Delta\phi)$	0.20(4)	0.20(3)	0.23(5)

the pulse is a significant contributor to ionization. Either multiphoton or tunneling ionization can occur, depending on where in the focus of the laser the atom was ionized. Eventually, this leads to $m = 3/2$ at very high intensities [59,60], but space charge effects due to the corona are present at lower intensities as well [10]. Based on the results in Ref. [10], $m = 3/2$ is expected in this experiment.

The numerical visibilities of $I^{(max)}$ were calculated using the data in Fig. 4.2 and Eq. 4.2, with max and min being the largest and smallest data points for each set, respectively. Visibilities for $I^{(max)}$ for the three runs are shown in Tab. 4.1, as are the visibilities of $(I^{(max)})^{3/2}$, which were found by raising the largest and smallest values of $I^{(max)}$ for each set to the 3/2 power. These visibilities are compared with the visibilities of the sinusoidal fits of the yield curves (as plotted in Fig. 4.1(c)). The reasonable agreement between visibilities for $(I^{(max)})^{3/2}$ and Y for the 140 fs and 150 fs experiments gives further evidence that the yield oscillations seen in the experiments are due to OI. The agreement is not as good for the 170 fs experiment; one possible explanation for this disagreement will be given later, in Sec. 4.2.2.

However, the variations in $I^{(max)}$ plotted in Fig. 4.2 are clearly not periodic (or at the least, the periodicity is much weaker than the periodicity of Y seen in

Fig. 4.1(a)). If Y oscillates periodically, then $Y \propto (I^{(max)})^{3/2}$ implies that $I^{(max)}$ will be periodic too. Why is this not observed?

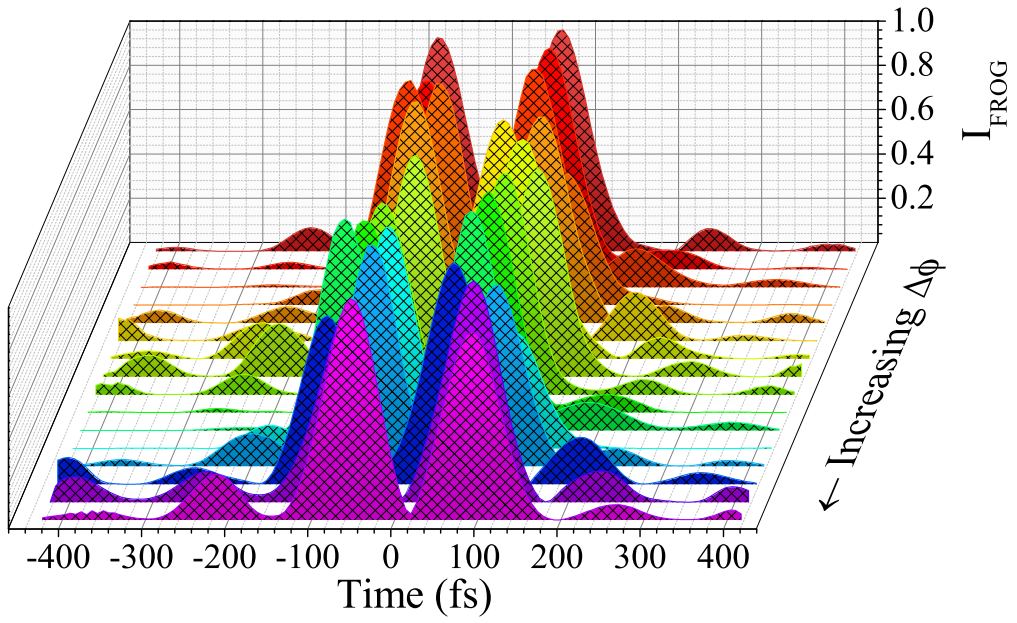

Fig. 4.3: Temporal intensity of every TPP used in the $\tau = 150$ fs PS experiment with a nonideal mask, reconstructed from an SD-FROG measurement.

It turns out that there is a considerable fluctuation in $I^{(max)}$ due to subordinate peaks. Figure 4.3 shows the SD-FROG traces of every TPP_{PS} in the $\tau = 150$ fs experiment. One clearly observes several subordinate peaks in each TPP_{PS}, the sizes and delays (relative to the main peaks) of the subordinate peaks are different for each TPP_{PS}. This variation in the subordinate peak size redistributes energy between the main peaks and the subordinates. Nominally, this was corrected in the experiment by demanding that the pulse energy of the twin peaks alone be fixed at 91 μJ, but this relies on an accurate determination of the size of the subordinate peaks. Unfortunately, such an accurate determination could not be made. Six SD-FROG measurement of the same TPP_{PS} (i.e., with the same mask applied to

the SLM) are shown in Fig. 4.4. The size of the subordinates varies substantially here as well. This variation in the size of the subordinates results in a variation in $I^{(max)}$. Furthermore, some of the subordinate peaks extended beyond the temporal range of the FROG measurement (notice that some of the subordinate peaks are cut off in Fig. 4.3), so this extra energy is unaccounted for. As such, it is possible that $I^{(max)}$ in this experiment *is* varying sinusoidally, but this sinusoidal variation is simply being masked by the variation in the subordinate peaks. In the interest of calculating $I^{(max)}$ more accurately, it is desirable to eliminate the subordinate peaks by making a TPP_{PS} using the ideal mask. This is done in the next section.

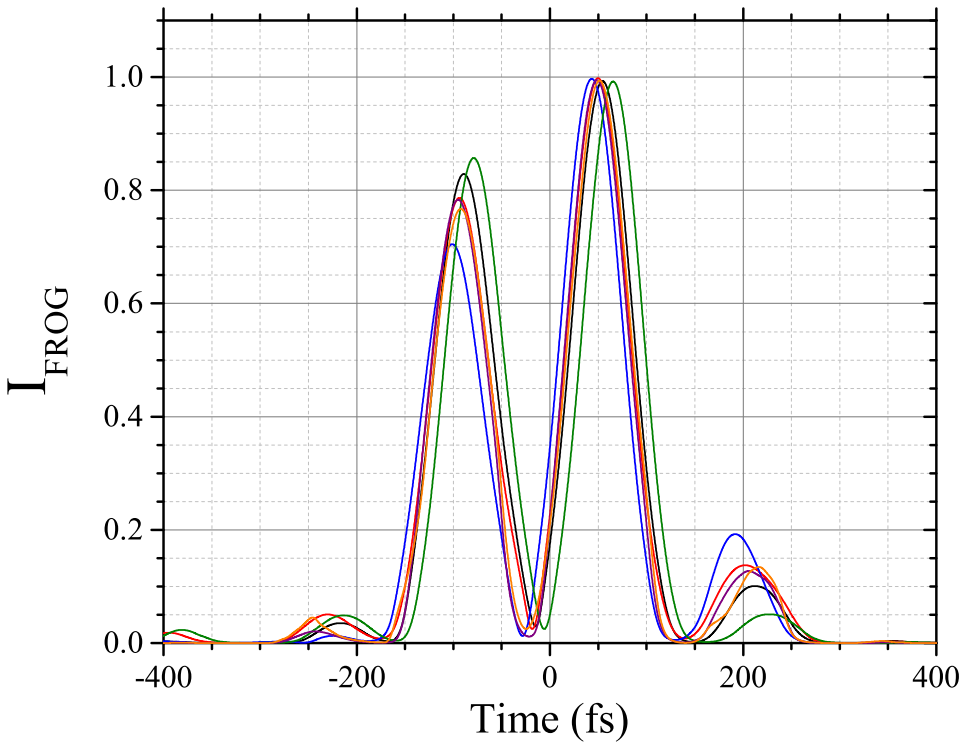

Fig. 4.4: Temporal intensity reconstructions of six SD-FROG measurements of the same TPP_{PS} (i.e., each TPP_{PS} was synthesized from the same, nonideal mask).)

4.2 TPP_{PS} produced with an ideal mask

4.2.1 Results

The Xe^+ yield vs $\Delta\phi$ for a TPP_{PS} with $\tau \simeq 150$ fs is shown in Fig. 4.5. Each TPP_{PS} was produced with an ideal TPP mask (see Fig. 3.12). The yield at each point was calculated by integrating the composite TOF signal (sum of 1000 TOF waveforms) over all Xe^+ isotopes, then normalized so that the maximum yield is unity.

The experiments were performed at a gas pressure of $4.0(1) \cdot 10^{-7}$ Torr. The TPP_{PS} energy was fixed at 40 μJ by adjusting the half-wave plate and polarizer combination. Each TPP_{PS} was measured with the SD-FROG to determine τ, $\Delta\phi$, and A_{FROG}. The FROG reconstructions of all 15 TPPs used in the 150 fs experiment are shown in Fig. 4.6, color-coded to match the colors of the data points in Fig. 4.5[1] Error bars for $\Delta\phi$ in Fig. 4.5 were determined as described in Sec. 3.3.3. Because these TPPs were created with the ideal mask, the energy of any residual subordinate peaks was negligible (as can be seen in Fig. 4.6). Minor alignment variations and variations in the SLM mask caused the relative energies of the two peaks to vary by about 10%.

[1] The maroon TPP_{PS}, 2nd column, 2nd row of Fig. 4.6, appears much rougher and noisier than every other TPP. This is an artefact of the FROG algorithm, which occasionally converges poorly on the true pulse profile due to the initial guess.

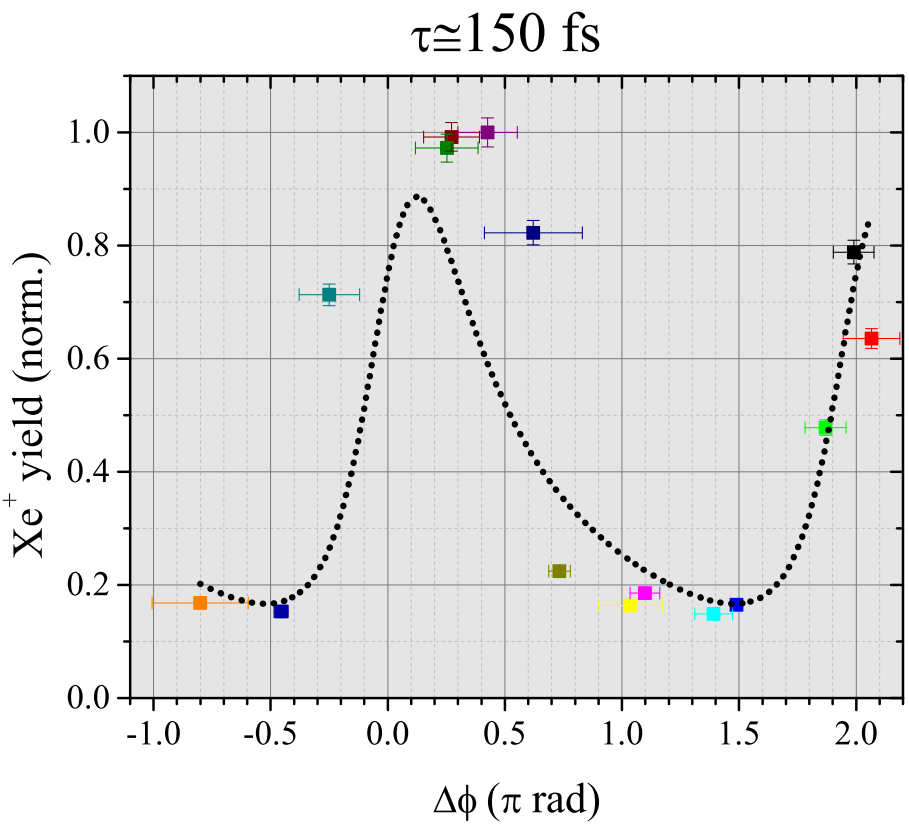

Fig. 4.5: The phase-dependent Xe^+ yield from a TPP_{PS} at $\tau = 150$ fs, summed over all Xe^+ isotopes, and captured from 1000 TOF waveforms. The colors of the data points match each point with its TPP_{PS} SD-FROG reconstruction shown in Fig. 4.6. The black dotted curve is the fit of the data to $Y \propto [I^{(max)}]^{3/2}$, where the TPP maximum intensity $I^{(max)}$ is calculated for $T = \tau/\Delta t = 3$ and assuming an input pulse with a pedestal, defined in Eq. 4.9 with $\beta = 0.23$ and $\phi_p = 1.17\pi$ (see Sec. 4.2.2).

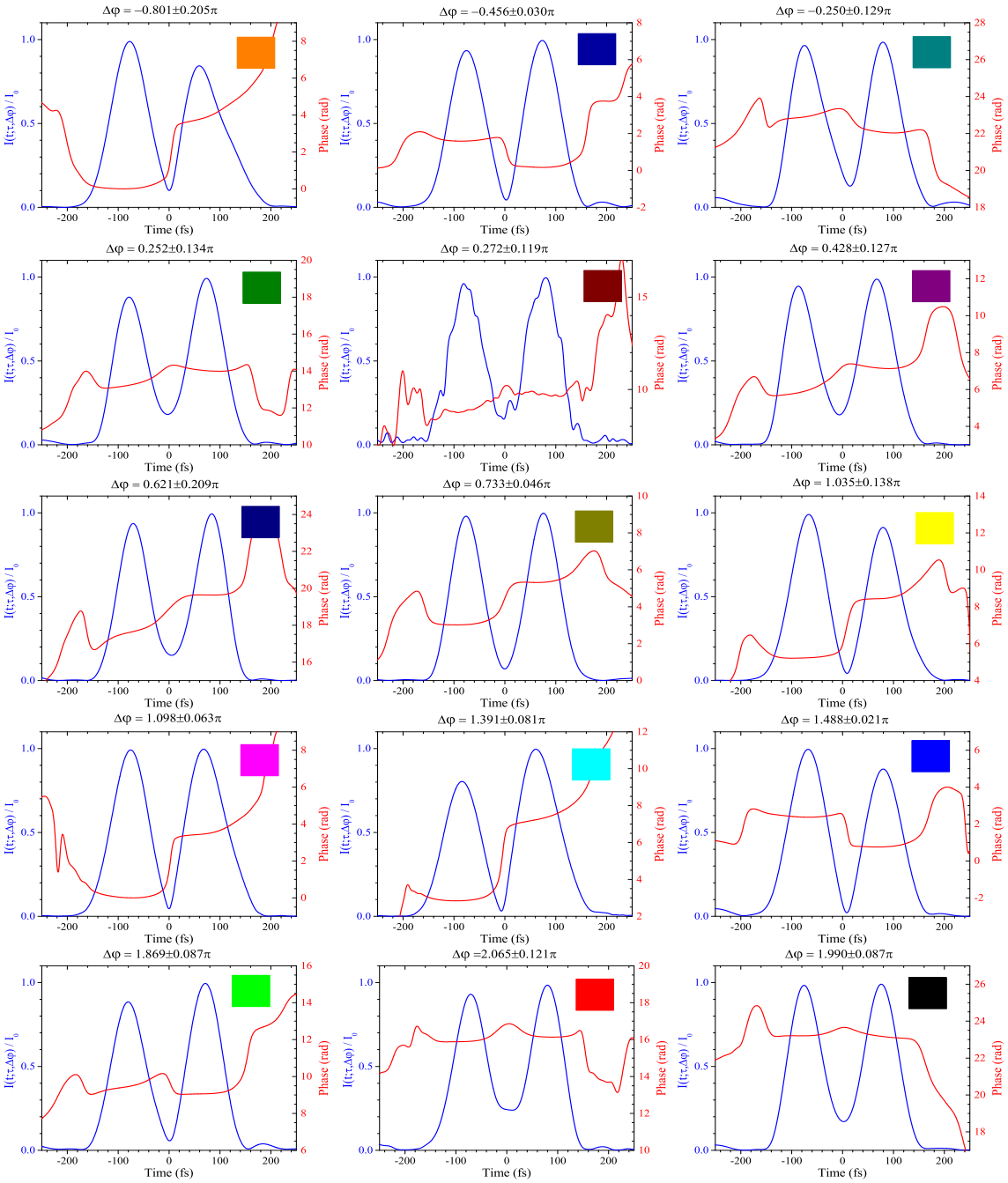

Fig. 4.6: SD-FROG reconstructions of the experimental TPP_{PS} intensity (blue) and phase (red) from the 150 fs, ideal mask experiment. The colored box in each plot can be used to match each reconstruction with a data point in Fig. 4.5. The plots are ordered by increasing $\Delta\phi$, from upper left to lower right.

Figure 4.7 shows Y as a function of intensity for a TL pulse of ~ 70 fs FWHM duration, normalized by the same factor as Fig. 4.5. Half of the points (shown as blue circles) are a composite TOF signal from 10,000 waveforms, the others (red triangles) are from 1000 waveforms. The standard deviation of Y, σ_Y, at each of the 10,000-waveform points was found by breaking up the 10,000 waveforms into ten groups of 1000 waveforms each. Figure 4.8 shows σ_Y vs Y for the 10,000 waveform points. One sees that σ_Y is approximately linear in Y, with a slope of 0.022(3) and an intercept of 0.004(1). From this linear fit, the error in the yields can be estimated. These errors are the error bars in Fig. 4.5 (recall that the data points in the TPP experiments were found by averaging 1000 waveforms).

4.2.2 Discussion

The results shown in Fig. 4.5 are qualitatively similar to Fig. 4.1. However, the absence of subordinate peaks on these TPPs (see Fig. 4.6) allows one to make more quantitative statements about the OI in these experiments. To that end, the focus of this discussion will be the two main issues introduced in Sec. 4.1.2.

The first of these issues is that the oscillations in Y are dominated by an oscillation at the optical period (2π). The modulation has a large visibility, $\mathcal{V}$ =0.74(3). This large visibility is perhaps unexpected, considering that the overlap between the two peaks is minimal at $\tau = 150$ fs. For example, consider a single sech^2 peak of a TPP with $\Delta t_{FWHM} \simeq 85$ fs, or $\Delta t = 50$ fs. At 150 fs away from the main peak, the intensity is approximately 1% of the intensity of the main peak.

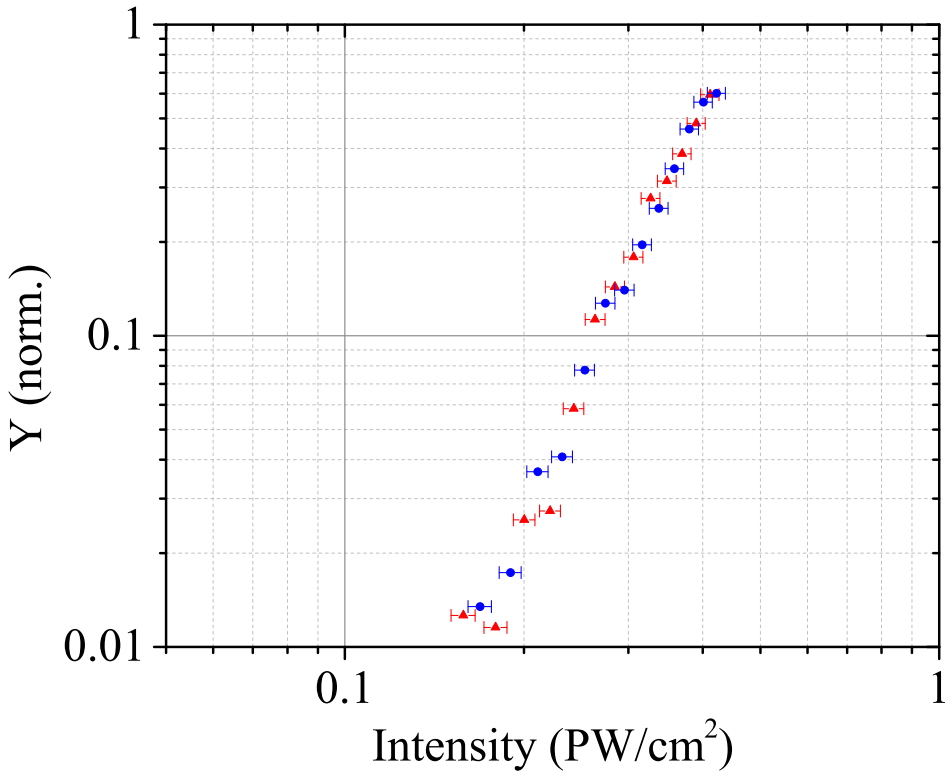

Fig. 4.7: Intensity-dependent Xe^+ yield Y from a near-TL pulse, displayed on a log-log scale. The yield has been normalized by the same factor as Fig. 4.5. Points represented by blue circles were found from an average of 10,000 waveforms; points represented by red triangles were found from an average of 1,000 waveforms.

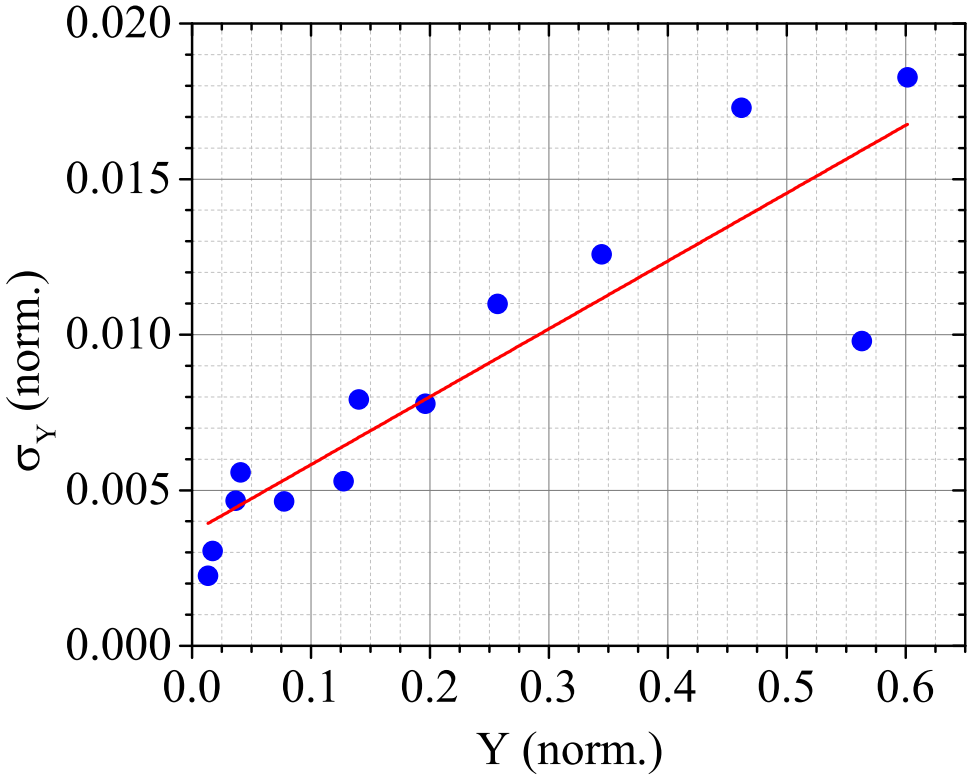

Fig. 4.8: (blue points) Standard deviation of ion yield σ_Y vs average yield Y. (red line) linear fit of σ_Y vs Y, which finds that $\sigma_Y = 0.022(3)Y + 0.004(1)$. This linear fit was used to estimate the yield error, producing the error bars shown in Fig. 4.5.

Second, the maximum Xe^+ yield does not occur at $\Delta\phi = 0$ in either experiment. One would naively expect the maximum yield to be at $\Delta\phi = 0$; the OI is constructive when the two pulses are in phase so the TPP intensity should be largest here. Recall from Sec. 4.1.2 that the value of $\Delta\phi$ where Y is maximal is notated $\Delta\phi_0^{(E)}$. In the 150 fs experiment, $\Delta\phi_0^{(E)} \simeq \pi/4$ rad (found by fitting the data in Fig. 4.5 to Eq. 4.1).

A discussion of the ion yield visibility and phase shift will be given below. In these discussions, a model of the TPP_{PS} maximum intensity will be developed.

Ion yield visibility

The deceptively large visibility in Y is partially due to an artificial change to the OI caused by fixing the TPP energy. Consider the intra-peak OI of an ideal TPP_{PS}—ideal in the sense that the TPP intensity I_{TPP} is given by Eq. 2.6. The pulse energy is

$$U_{TPP}(\tau, \Delta\phi) = A_{eff} \int_{pulse} I_{TPP}(\tau, \Delta\phi; t) dt, \tag{4.3}$$

where A_{eff} is the beam area (see Sec. 3.3.3). Evaluation of the integral over all time leads to

$$U_{TPP}(\tau, \Delta\phi) = U_0(1 + T\,\text{csch}(T)\cos(\Delta\phi)), \tag{4.4}$$

where $U_0 = 4A_{eff}I_0\Delta t$ ($\sim 40\mu$J) is the TPP energy as $\tau \to \infty$ (i.e., when the pulses do not overlap at all) and the definition of the *scaled peak separation* $T \equiv \tau/\Delta t$

has been introduced. In order to fix the TPP energy $U_{TPP}(\tau, \Delta\phi) = U_0$, one can multiply I_{TPP} by

$$f_{EC}(T, \Delta\phi) = (1 + T\text{csch}(T)\cos(\Delta\phi))^{-1}. \tag{4.5}$$

This is referred to as the energy correction term. The energy correction term was introduced in the experiment by adjusting the half-wave plate and polarizer combination. The maximum intensity can be found by evaluating $I_{TPP} \times f_{EC}$ at either $t = 0$ or $t = \tau$, which gives

$$I_{TPP}^{(max)}(T, \Delta\phi) = I_0 \frac{1 + \text{sech}^2(T) + 2\text{sech}(T)\cos(\Delta\phi)}{1 + T\text{csch}(T)\cos(\Delta\phi)}. \tag{4.6}$$

It is convenient to use the shortened form of this equation,

$$I_{TPP}^{(max)} = I_0 f_{OI} f_{EC}, \tag{4.7}$$

where

$$f_{OI}(T, \Delta\phi) = 1 + \text{sech}^2(T) + 2\text{sech}(T)\cos(\Delta\phi) \tag{4.8}$$

is the change in $I_{TPP}^{(max)}$ due to the OI of the two peaks (this Eq. 2.7, scaled by I_0). The individual peaks of the TPP have a width of $\Delta t \simeq 50$ fs, so $T \simeq 3$ in the $\tau = 150$ fs experiment and $T \simeq 5$ in the $\tau = 250$ fs experiment. Figure 4.9(b) shows how f_{OI} and f_{EC} vary with $\Delta\phi$ when $T = 3$. Also shown in Fig. 4.9(b) is $I_{TPP}^{(max)}/I_0$, as calculated from Eq. 4.7. The introduction of the energy correction was an attempt to cancel out the intensity fluctuations due to OI. While f_{EC} and f_{OI} oscillate out

of phase as intended, they have different oscillation amplitudes. Fixing the $\mathrm{TPP_{PS}}$ energy only partially eliminated intensity fluctuations due to OI. There remained a variation in $I_{TPP}^{(max)}/I_0$ of about 10% of its average value ($\mathcal{V} = 0.109$).

As described in Sec. 4.1.2, one expects that $Y \propto (I_{TPP}^{(max)})^{3/2}$ for pulses of intensity > 0.1 PW/cm^2 (see Ref. [10]). For a 40 μJ TPP and with $\Delta t = 50$ fs, $I_0 = 0.12$ PW/cm^2. The visibility of $I_{TPP}^{(max)}$ is 0.109, leading to visibility of $(I_{TPP}^{(max)})^{3/2}$ of 0.162. The visibility of $(I_{TPP}^{(max)})^{3/2}$ is much smaller than the visibility of the $\tau = 150$ fs experimental ion yield, $\mathcal{V} = 0.74(3)$. One way to increase $\mathcal{V}$ in the model is to decrease T (i.e., decrease τ or increase Δt). When T decreases, OI increases and so one expects a larger visibility. In order to determine if the uncertainty in T is large enough to explain this discrepancy in visibilities, the uncertainties in τ and Δt should be known.

From each FROG reconstruction shown in Fig. 4.6, τ and Δt for each peak were measured. These measurements were averaged to find $\tau = 148.8$ fs and $\Delta t = 44.9$ fs, with standard deviations $\sigma_\tau = 1.6$ fs and $\sigma_{\Delta t} = 5.7$ fs. From this, one can calculate that $T = 3.3(4)$. In order for the visibility of $(I_{TPP}^{(max)})^{3/2}$ to be 0.74, one requires that $T = 0.65$, more than 6σ away.

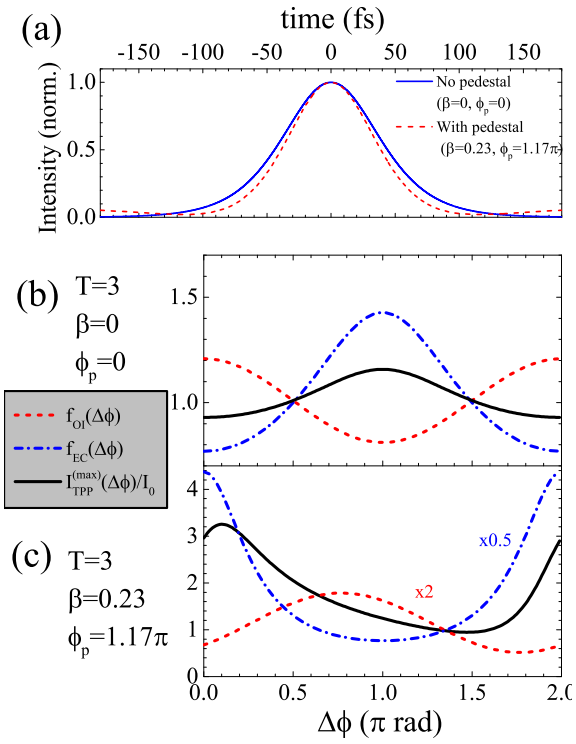

Fig. 4.9: (a) Intensity vs time of two model pulses: with (dashed red) and without (solid blue) a pedestal defined in Eq. 4.9 and $\beta = 0.23$, $\phi_p = 1.17\pi$. (b) I_{max}/I_0 (Eq. 4.7, solid black curve), f_{OI} (Eq. 4.8, dashed red curve), and f_{EC} (Eq. 4.5, dot-dashed blue curve) with no pedestal as a function of relative phase $\Delta\phi$, for $T \equiv \tau/\Delta t = 3$. (c) Same as (b) but with the pedestal, Eqs. 4.14 and 4.15. For ease of viewing, f_{OI} and f_{EC} have been multiplied by 2 and 0.5, respectively, in (c).

If, however, the OI was locally increased around $t = \tau$ without changing Δt, such a large visibility could occur. This could be done by changing the intensity of the wings while keeping Δt approximately the same. One way this could be achieved is by adding a long, weak pedestal to the pulse. Recall that the strength of OI follows the strength of the *electric field*, which goes as $\sqrt{I}$. So, for example, the intensity of a sech^2 pulse, $\Delta t = 50$ fs, at $t = 150$ fs is approximately 1% of the

peak intensity of the pulse. This means that the electric field amplitude at $t = 150$ fs is 10% of the peak electric field amplitude. If an added pedestal increases the intensity of the pulse to 2% of the peak intensity at $t = 150$ fs, the E-field amplitude increases to $\sim$ 15% of the peak. This example demonstrates that the strength of the OI is very sensitive to small changes in the shape of the wings of the pulse. This phenomenon will be explored more quantitatively in the next section.

Phase shift of yield response to $\Delta\phi$

As seen in Fig. 4.9(b), f_{OI} and f_{EC} oscillate out of phase, and peak at $\Delta\phi = 0$ and $\Delta\phi = \pi$ rad, respectively. These peak locations are independent of T, except in the limiting case $T = 0$ when f_{EC} diverges. The maximum intensity $I_{TPP}^{(max)}$ oscillates with either f_{OI} or f_{EC}, depending upon which of f_{OI}, f_{EC} is larger, with the crossover occuring at $T = 1.6$. For $T > 1.6$, $f_{OI} < f_{EC}$. The value of $\Delta\phi$ where $I_{TPP}^{(max)}$ is largest is referred to as $\Delta\phi_0^{(M)}$. In the 150 fs experiment, $T \simeq 3$, which means that $\Delta\phi_0^{(M)} = \pi$ rad. However, the peak ion yield is observed at $\Delta\phi_0^{(E)} \simeq \pi/4$ rad.

The discrepancy between $\Delta\phi_0^{(M)}$ and $\Delta\phi_0^{(E)}$ arises from the nonideality of the peaks of the TPP. Recall that $I_{TPP}^{(max)}$, and by extension $\Delta\phi_0^{(M)}$, are determined in the model by assuming perfect sech^2 peaks—that is, a TPP defined by Eq. 2.6. The real TPPs have deviations from this ideal case, and these modifications can be categorized into two groups. First, there are modifications that change the relative intensities and widths of the two peaks but maintain a sech^2 peak shape, referred to as proportional modifications. As can be seen in the derivation of f_{OI} and f_{EC}

in Sec. 4.2.2, modifications to the pulse heights and widths do not change the terms inside the cosine, so the period and phase of oscillation will be unaffected. As a result, proportional modifications will not change $\Delta\phi_0^{(M)}$. This would explain why even though the relative intensities and widths of the peaks fluctuating by about 10% (see Fig. 4.6), the periodic phase-dependent ionization yield modulation still appears.

The second class of modifications are pulse shape distortions, which change the shape of the individual peaks away from an ideal sech^2. Pulse shape distortions can be observed when trying to fit an ideal TPP to a FROG-reconstructed TPP, as can be seen in Fig. 4.10. In this figure, an experimentally-measured TPP_{PS} ($\Delta\phi \simeq \pi$ rad, yellow point in Figs. 4.5 and 4.6) was fit to Eq. 2.6 allowing for proportional modifications. The deviations between fit and experiment are small; however, it is straightforward to show that $\Delta\phi_0^{(M)}$ is quite sensitive to pulse shape distortions by considering a "toy" distortion model. The toy model adds a shape distortion to the peaks. It was already stated in the previous section that a pedestal can locally increase the OI to explain the abnormally large yield visibility in this experiment, so a pedestal is used here as the shape distortion. The pedestal is represented by a rectangular function, with a width of $10\Delta t$. The field of an input pulse with a pedestal is

$$E(t) = \mathcal{E}_0 e^{-i(\omega_0 t - \phi_1)} \left[\text{sech}\left(\frac{t}{\Delta t}\right) + \beta \Pi\left(\frac{t}{10\Delta t}\right) e^{i\phi_p} \right], \tag{4.9}$$

where ϕ_p is the relative phase between the pedestal and the main peak, β is the

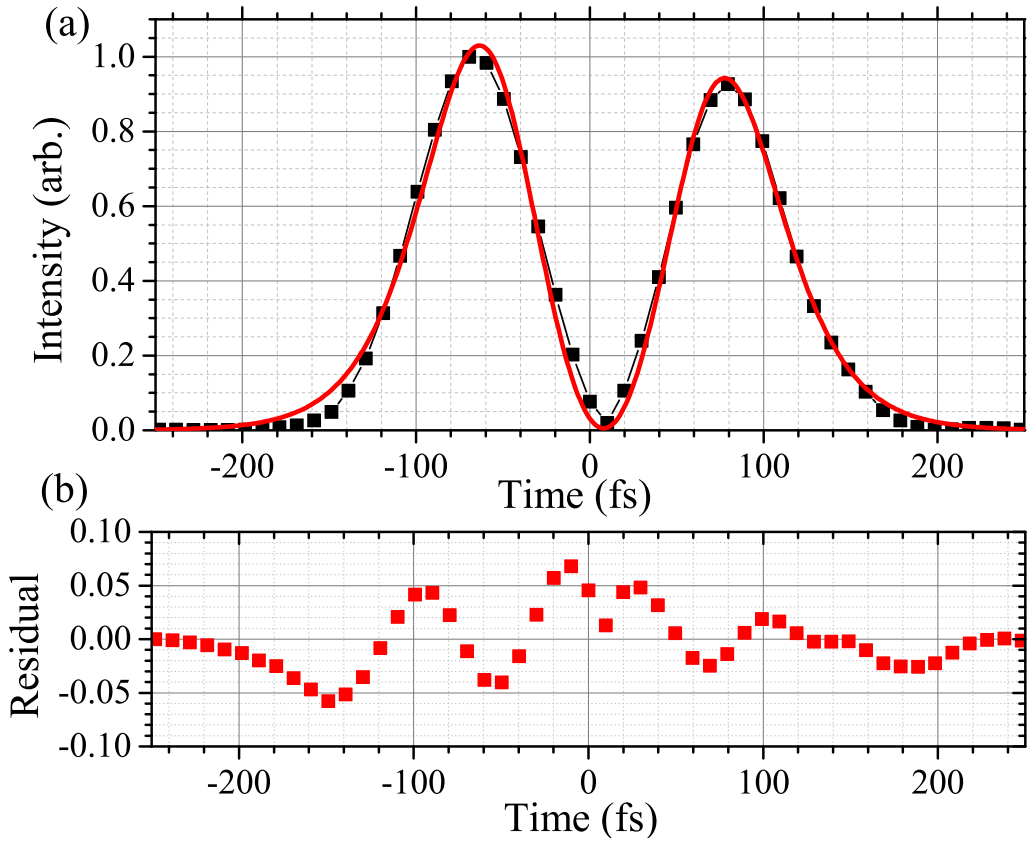

Fig. 4.10: (a) Temporal intensity of a FROG-reconstructed $\mathrm{TPP}_{\mathrm{PS}}$ (black squares) and a fit of this TPP to a model hyperbolic-secant TPP (red curve). The FROG-measured temporal phase for this TPP gave $\Delta\phi = 1.04\pi$, so this value was fixed in the fit. The fit is to Eq. 2.6 with proportional modulations added; i.e., the heights and widths of the two peaks were allowed to differ. The fit recovers widths for the first and second peaks, respectively, of $\Delta t_1 = 49.0(7)$ fs and $\Delta t_2 = 48.7(8)$ fs, and amplitudes $I_{01} = 1.35(2)$, $I_{02} = 1.27(2)$. (b) Residual (data − fit) of the fit shown in the upper panel.

ratio of the field amplitude of the pedestal to that of the main peak, and

$$\Pi\left(\frac{t}{10\Delta t}\right) = \begin{cases} 1, & |t| \leq 5\Delta t \\ \\ 0, & |t| > 5\Delta t \end{cases} \tag{4.10}$$

is a rectangular function. From this, one can find the TPP intensity,

$$\begin{aligned} I_{TPP}(\tau, \Delta\phi; t) = I_0 \Bigg\{ & \operatorname{sech}^2\left(\frac{t}{\Delta t}\right) + \operatorname{sech}^2\left(\frac{t-\tau}{\Delta t}\right) \\ & + 2\operatorname{sech}\left(\frac{t}{\Delta t}\right)\operatorname{sech}\left(\frac{t-\tau}{\Delta t}\right)\cos\left(\Delta\phi\right) \\ & + 2\beta\left[\left(\operatorname{sech}\left(\frac{t}{\Delta t}\right)\Pi\left(\frac{t}{10\Delta t}\right) + \operatorname{sech}\left(\frac{t-\tau}{\Delta t}\right)\Pi\left(\frac{t-\tau}{10\Delta t}\right)\right)\cos\left(\phi_p\right)\right. \\ & + \operatorname{sech}\left(\frac{t}{\Delta t}\right)\Pi\left(\frac{t-\tau}{10\Delta t}\right)\cos\left(\Delta\phi + \phi_p\right) \\ & \left. + \ \operatorname{sech}\left(\frac{t-\tau}{\Delta t}\right)\Pi\left(\frac{t}{10\Delta t}\right)\cos\left(\Delta\phi - \phi_p\right)\right]\Bigg\}, \end{aligned} \tag{4.11}$$

where all β^2 terms have been dropped. Following the same procedure as Sec. 4.2.2, one can find the pulse energy by integrating Eq. 4.11 over all time, finding

$$\begin{aligned} U_{TPP}(T, \Delta\phi) = U_0 \Big\{ & 1 + T\operatorname{csch}(T)\cos\left(\Delta\phi\right) \\ & + \beta\left[2\operatorname{gd}(5)\cos\left(\phi_p\right)\right. \\ & \left. + \ \left(\operatorname{gd}(5-T) + \operatorname{gd}(5+T)\right)\cos\left(\Delta\phi\right)\cos\left(\phi_p\right)\right]\Big\}, \end{aligned} \tag{4.12}$$

where the Gudermannian function,

$$\operatorname{gd}(x) = 2\tan^{-1}\left(\tanh\left(\frac{x}{2}\right)\right), \tag{4.13}$$

is used. As in Sec. 4.2.2, the energy is fixed at U_0 by multiplying Eq. 4.11 by $f_{EC} = U_0/U_{TPP}$. Then, $I_{TPP}^{(max)}(T, \Delta\phi)$ is found by evaluating $I_{TPP}(\tau, \Delta\phi; t = 0)$, again yielding $I_{TPP}^{(max)} = I_0 f_{OI} f_{EC}$ with

$$\begin{aligned} f_{OI}(T, \Delta\phi) = 1 &+ \text{sech}^2(T) + 2\text{sech}(T)\cos(\Delta\phi) \\ &+ 2\beta\left[(1 + \text{sech}(T))\cos(\phi_p)\right. \\ &+ \left.\cos(\Delta\phi + \phi_p) + \text{sech}(T)\cos(\Delta\phi - \phi_p)\right], \end{aligned} \tag{4.14}$$

$$\begin{aligned} f_{EC}(T, \Delta\phi) = \{1 &+ T\,\text{csch}(T)\cos(\Delta\phi) \\ &+ \beta\left[2\text{gd}(5)\cos(\phi_p)\right. \\ &+ \left.(\text{gd}(5 - T) + \text{gd}(5 + T))\cos(\Delta\phi)\cos(\phi_p)\right]\}^{-1}. \end{aligned} \tag{4.15}$$

In the case that $\beta = 0$, Eqs. 4.14 and 4.15 reduce to Eqs. 4.8 and 4.5, respectively.

It is important to emphasize that there are now terms that are phase-shifted by $\pm\phi_p$. So, the addition of a pedestal can introduce a phase shift of some sort into $I_{TPP}^{(max)}$. The experimental data in Fig. 4.5(a) was fit to $Y \propto (I_{TPP}^{(max)})^{3/2}$, where $I_{TPP}^{(max)}$ was computed using a pedestal with ϕ_p and β allowed to vary and $T = 3$. The dotted curve in Fig. 4.5(a) shows the result of the fit, using the fit values $\phi_p = 1.17(5)\pi$ rad, and $\beta = 0.23(2)$.

The effect of this pedestal on $I_{TPP}^{(max)}$ is shown in Fig. 4.9(c). With such a pedestal added, $\Delta\phi_0^{(M)} \simeq 0.1\pi$ rad, reasonably close to $\Delta\phi_0^{(E)}$ (within the $\Delta\phi$ error bars). Furthermore, the visibility in $I_{TPP}^{(max)}$ is 0.549, giving a visibility of $(I_{TPP}^{(max)})^{3/2}$

of 0.729. This matches the ion yield visibility in the 150 fs experiment ($\mathcal{V} = 0.74$). Input pulses with and without this pedestal are compared in Fig. 4.9(a), showing that the addition of the pedestal reduces the intensity on the wings of the pulse.

One potential issue with this fit is that $I_{TPP}^{(max)}$ was found by evaluating I_{TPP} at $t = 0$ fs. When there is no pedestal, both peaks have the same intensity for all $\Delta\phi$, but when a pedestal is added this is not necessarily the case. If the later peak has a higher intensity than the earlier peak this method of finding $I_{TPP}^{(max)}$ is not strictly correct. It is important to remember that the intent of this toy model was not to determine an exact pedestal electric field; rather, it was to show that *some* pedestal can introduce *some* phase shift in the phase response of $I_{TPP}^{(max)}$. That much has been made clear, but any further determination of the experimental pedestal is likely limited by the measurement uncertainty of the FROG.

This last observation from the paragraph above reinforces the conclusion first made at the end of Sec. 4.1.2—namely, that seemingly small features of a complex pulse can have a large effect on the ionization response. In the case of Sec. 4.1.2 the small feature was the subordinate peaks, while in this section, the small feature is the pedestal. Practitioners of optimal control experiments would do well to be mindful of the change in pulse intensity due to OI; however, knowledge of the pulse intensity is ultimately limited by the measurement device. Because these measurement devices typically rely on nonlinear optical effects (the SD-FROG, for example, uses a third-order nonlinearity), the sensitivity of such devices is nonlinear in the field amplitude, making low-intensity features of the pulses especially hard to detect.

One way to partially circumvent these issues in the current study is to make

TPPs from the MZ. As long as the intensity and phase of the *input* pulse is known, the intensity and phase of the TPP can be calculated. The input pulse is near-TL. Near-TL pulses have a higher intensity for a given pulse energy, so the SD-FROG measurement of these pulses is more accurate. The input pulses can also be measured by the Wizzler, giving an independent confirmation of the pulse shape. The MZ experiment also allows variation of $\Delta\phi$ over a longer range, albeit indirectly by changing τ. The combination of all these factors allows for a more deterministic way to change the TPP intensity. Investigation of the Xe ionization response to a TPP_{MZ} is the topic of Secs. 4.3 and 4.4.

4.3 TPP_{MZ}, resolution 0.67 fs

4.3.1 Results

The Xe^+ yield vs τ for a TPP_{MZ} is shown in Fig. 4.11(a). Each TPP_{MZ} was produced from the MZ, with a temporal resolution of 0.67 fs, in the range 50 fs $< \tau <$ 230 fs. The yield at each point was calculated by integrating the composite TOF waveform (corresponding to 1000 laser shots) over all Xe isotopes. The yield was normalized so that the yield as $\tau \to \infty$ was unity. The yield as $\tau \to \infty$ was found in practice by measuring the yield due to the two arms individually and adding them together.

The experiments were performed at a pressure of $4.0(1)\cdot10^{-7}$ Torr. The energy of the TPPs was adjusted so that the TPP energy as $\tau \to \infty = 40\mu$J. Due to an imbalance in the beam splitters within the MZ, the later peak had $\sim 89\%$ of the

energy of the earlier peak. A measurement of the spectrum and subsequent fitting to Eq. 3.13 allowed for a determination of τ. In order to determine the uncertainty in τ, a sample $\mathrm{TPP_{MZ}}$ spectrum was measured 1000 times, and τ was fit each time (at $\tau \simeq 150$ fs). The standard deviation in fit values of τ was 0.45 fs. The spectrum of each $\mathrm{TPP_{MZ}}$ during the experiment was measured once, so this standard deviation is taken to be the uncertainty in τ at each point. While this uncertainty is nearly as large as the step size, the uncertainty in $\delta\tau$, the change in τ between two steps, was much smaller, ~ 0.03 fs (see Sec. 3.2.2). Figure 4.11(b) and (c) show the results of two simulations: a numerical calculation of $I^{(max)}$, and a calculation of the ionization probability found by solving the time-dependent Schrödinger equation. Details of both simulations will be described in Sec. 4.3.2. The Fourier transforms of all three plots are given in Fig. 4.11(d).

The input pulses used to make the $\mathrm{TPP_{MZ}}$ were not TL; this was discussed in Sec. 3.3.1. A Wizzler measurement of the input pulse in this experiment is shown in Fig. 4.11(e). One clearly sees a small subordinate peak, arriving after the main peak at time $\tau_s \simeq 120$ fs.

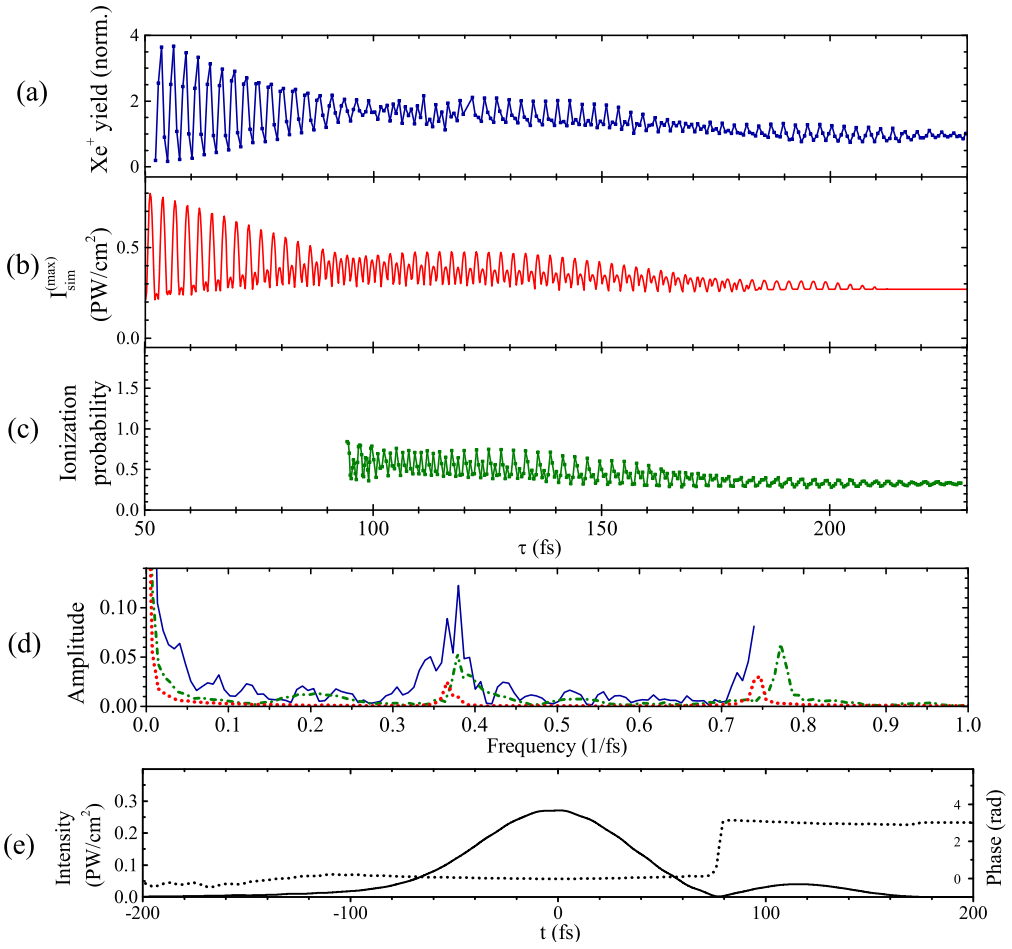

Fig. 4.11: (a) Xe^+ yield vs τ for a TPP_{MZ}, between 50 fs and 230 fs with a step size of 0.67 fs. The yield has been normalized so that the yield as $\tau \to \infty$ is unity. (b) Simulated TPP_{MZ} maximum intensity $I_{sim}^{(max)}$ vs τ (see Sec. 4.3.2). (c) Simulated ionization probability found by solving the time-dependent Schrödinger equation numerically (see Sec. 4.3.2). (d) Fourier transforms of (a) (solid blue), (b) (dotted red), and (c) (dash-dot green), all showing oscillations at the optical frequency ($\sim$ 0.375 fs^{-1}) and twice the optical frequency ($\sim$ 0.75 fs^{-1}). (e) $I(t)$ (solid) and $\phi(t)$ (dotted) SD-FROG reconstructions for the input pulse, as used in Eqs. 4.16 and 4.17.

4.3.2 Discussion

A clear oscillation at the optical period is seen in the Fig. 4.11(a), particularly for $\tau < 100$ fs. Based upon the results and discussion in Secs. 4.1 and 4.2, one concludes that this oscillation is due to OI between the peaks. The modulation visibility increases as the peaks are moved closer together as expected. Anomalous behavior occurs for $\tau > 100$ fs. In this discussion, two facets of the ionization in the range 100 fs $< \tau <$ 150 fs will be discussed. The first is the increase in the modulation envelope within this region, i.e., a revival of the yield visibility. The second is the appearance of an oscillation at twice the optical frequency, seen as smaller, secondary peaks in between the larger yield peaks in Fig. 4.11(a). The frequency doubling is also clearly seen by a peak at $2\nu_0$ in the Fourier transform spectrum. With a step size of 0.67 fs (4 points per optical cycle), oscillations at $2\nu_0$ are the highest frequencies that can be recovered in the Fourier spectrum.

Envelope modulation

The revival of the oscillation envelope between 100 fs and 150 fs is due to the nonideality of the input pulse. Due to the presence of the subordinate peak, the OI strength at $\tau = 120$ fs will be larger than at $\tau = 90$ fs, for example.

Following the procedure in Sec. 4.2.2, this hypothesis can be verified by calculating the maximum intensity of the TPP as a function of τ. In contrast to the SLM experiments, however, a significantly more accurate determination of $I^{(max)}$ can be made in the MZ experiments. The input pulse intensity $I(t)$ and phase $\phi(t)$ are

both known (shown in Fig. 4.11(e)). The MZ split this input pulse into two copies and recombined them with a time delay added. The only difference between the two peaks after recombination was that the later peak was less intense due to the imbalance of the MZ beam splitters. The imbalance is accounted for in the model by a scaling factor $\beta_{MZ} = 0.94$. The beam splitters could also add different amounts of spectral phase to the two arms, but this difference should be small due to the design of the MZ (see Sec. 3.2.2). Regardless, this difference will be nearly constant and so will not effect the τ dependent behavior of the ionization other than to add an overall phase shift to the data. As a result, this phase difference is ignored and the complex field and intensity of the TPP_{MZ} are

$$\mathcal{E}_{sim}(\tau, \Delta\phi; t) = \sqrt{\frac{2}{cn\epsilon_0}} e^{-i(\omega_0 t - \phi_1)} \Big[\sqrt{I(t)} e^{-i\phi(t)} + \beta_{MZ} \sqrt{I(t-\tau)} e^{-i\phi(t-\tau)} e^{i\Delta\phi} \Big] + \text{c.c.}, \tag{4.16}$$

$$I_{sim}(\tau, \Delta\phi; t) = \frac{cn\epsilon_0}{2} \left(\mathcal{E}_{sim}(\tau, \Delta\phi; t) \right)^2, \tag{4.17}$$

respectively. Both these functions were computed numerically using the input pulse in Fig. 4.11(e), and the maximum TPP intensity, denoted $I_{sim}^{(max)}$, was found as a function of τ. The result of this simulation is shown in Fig. 4.11(b). Just as with the experimental ion yield, the visibility of $I_{sim}^{(max)}(\tau)$ experiences a minimum around 100 fs and a revival between 100 fs and 150 fs. Frequency doubling is also observed in $I_{sim}^{(max)}(\tau)$, which will be discussed in Sec. 4.3.2.

The second simulation consisted of numerically solving the time-dependent

Schrödinger equation to calculate the ionization probability, using a TPP defined by Eq. 4.16 for the interaction potential [105]. The TDSE calculation was performed in momentum space where the photoelectrons have finite momenta and localized wave functions. For the calculations the time-dependent generalized pseudospectral method [106–108] was used, in which the electron wave function is discretized on an optimized momentum grid (depending on a single variable parameter) and propagated accurately using the split-operator scheme. The total ionization probability was calculated by projecting the post-interaction wave function onto the continuum states of the unperturbed Hamiltonian.

The TDSE simulation results are shown in Fig. 4.11(c). The calculation was not done for $\tau < 95$ fs, so the envelope visibility revival is not possible to see. However, the decay in visibility qualitatively matches the decay of the yield and $I_{sim}^{(max)}(\tau)$, and frequency doubling is also observed (see Sec. 4.3.2).

Finally, one may notice a secondary revival of the yield visibility around 200 fs, after a visibility minimum at $\tau \simeq 180$ fs. While this could be due to a second, even weaker subordinate peak (too weak to be detected in FROG or Wizzler measurements), it is likely that this revival is a sampling rate artefact due to the step size $\delta\tau = 0.67$ fs.

Frequency modulation

The modulation at the optical frequency ν_0 is well-described by OI; in this section the focus is on the oscillations at frequency $2\nu_0$. While an oscillation at $2\nu_0$ is consistent with two-photon QuI Mechanism I, similar to what is described

in Ref. [50], this is unlikely to be the cause of frequency doubling here. The first excited state in xenon requires more than five 800 nm photons to reach, so no two-photon transitions from the ground state at 800 nm are possible. Also, $I_{sim}^{(max)}$ and its Fourier transform (Fig. 4.11) show the same frequency doubling as the $\mathrm{TPP_{MZ}}$ spectra. Because $I_{sim}^{(max)}$ was calculated using OI alone, the frequency-doubling it exhibits can only be caused by OI.

Instead, the frequency doubling was likely caused by OI involving the subordinate peak. The subordinate peak, π rad out of phase with the main peak, causes a secondary OI that is out of phase with the primary OI, which is responsible for the frequency doubling in $I_{sim}^{(max)}$. This was recovered in the numerical model using the experimentally-measured input pulse (shown in Fig. 4.11(b)), but can also be seen analytically by modeling the input pulse field as a double-hyperbolic secant peak:

$$E(t) = \mathcal{E}_0 e^{-i\omega_0 t} e^{i\theta_1} \left[\mathrm{sech}\left(\frac{t}{\Delta t}\right) + \beta_s \mathrm{sech}\left(\frac{t-\tau_s}{\Delta t}\right) e^{i\omega_0 \tau_s} e^{i\phi'} \right], \tag{4.18}$$

where β_s is the ratio of the subordinate peak field amplitude to the main peak field amplitude, τ_s is the delay of the subordinate peak relative to the center of the main peak and $\theta_1 + \phi'$ is the CEP of the subordinate peak. All other variables are defined in Eq. 2.3. The widths of the main peak and subordinate peak are assumed to be equal. The subordinate peak is π out of phase with the main peak (see Fig. 4.11(e)); this means that $\omega_0 \tau_s + \phi' = \pi$. In this case, Eq. 4.18 simplifies to

$$E(t) = \mathcal{E}_0 e^{-i\omega_0 t} e^{i\theta_1} \left[\mathrm{sech}\left(\frac{t}{\Delta t}\right) - \beta_s \mathrm{sech}\left(\frac{t-\tau_s}{\Delta t}\right) \right]. \tag{4.19}$$

This model field (or rather, its intensity and phase) are compared with the experimentally-measured input pulse in Fig. 4.12 with the following parameter values: $\mathcal{E}_0 = 5.46 \cdot 10^{10}$ V/m, $\lambda_0 = 2\pi c/\omega_0 = 808$ nm, $\Delta t = 50$ fs, $\beta_s = 0.58$, and $\tau_s = 90$ fs. It is important to note that the tail of the subordinate peak is considerably longer than its experimental counterpart, so any OI for $\tau > 150$ will be magnified compared to the numerical model, where the TPP_{MZ} complex field is given by Eq. 4.16.

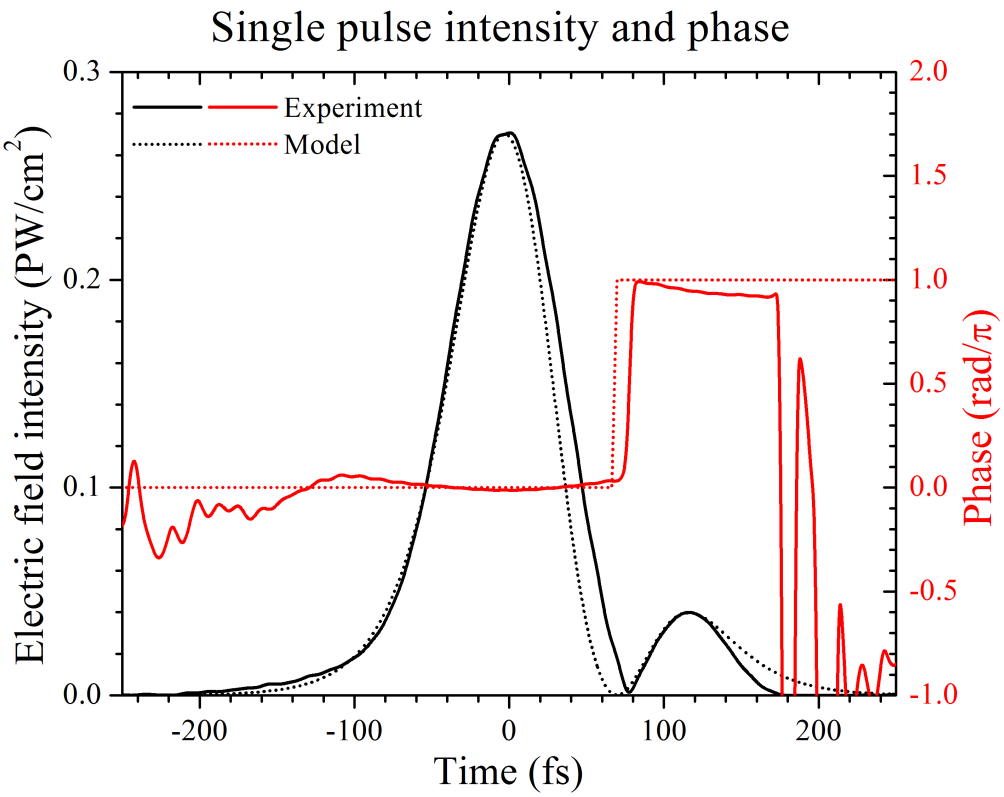

Fig. 4.12: Intensity (black) and phase (red) vs time for the experimentally-measured input pulse (solid) and a model pulse with a field given by Eq. 4.19 (dotted) with the following parameters: $\lambda_0 = 2\pi c/\omega_0 = 808$ nm, $\Delta t = 50$ fs, $\beta_s = 0.58$, and $\tau_s = 90$ fs.

The MZ produces a time-delayed copy of this input pulse. Therefore, the $\mathrm{TPP_{MZ}}$ field is

$$\begin{aligned} E_{TPP}(\tau;t) &= E(t) + \beta_{MZ}E(t-\tau) \\ &= \mathcal{E}_0 e^{-i\omega_0 t}e^{i\theta_1}\left[\mathrm{sech}\left(\frac{t}{\Delta t}\right) - \beta_s \mathrm{sech}\left(\frac{t-\tau_s}{\Delta t}\right)\right. \\ &\left. + \beta_{MZ}e^{i\omega_0\tau}\mathrm{sech}\left(\frac{t-\tau}{\Delta t}\right) - \beta_{MZ}\beta_s e^{i\omega_0\tau}\mathrm{sech}\left(\frac{t-\tau-\tau_s}{\Delta t}\right)\right]. \end{aligned} \tag{4.20}$$

The $\mathrm{TPP_{MZ}}$ intensity is proportional to the modulus-squared of the field, which will produce sixteen terms. It would be convenient to drop the smaller terms. However, with $\beta_{MZ}^2 = 0.89$ and $\beta_s^2 = 0.34$, it is not justifiable to drop even the order-$\beta_{MZ}^2\beta_s^2$ terms. Similarly, one may suggest to drop the cross term between the earlier main peak, centered at $t = 0$, and the subordinate peak, centered at $t = \tau + \tau_s$, but this term may be significant for delays of $\tau \simeq 0$ fs. With this in mind, every term was left in the TPP intensity, and so

$$
\begin{aligned}
\frac{I_{TPP}}{I_0} &= \mathrm{sech}^2\left(\frac{t}{\Delta t}\right) + \beta_s^2 \mathrm{sech}^2\left(\frac{t-\tau_s}{\Delta t}\right) \\
&+ \beta_{MZ}^2 \mathrm{sech}^2\left(\frac{t-\tau}{\Delta t}\right) + \beta_{MZ}^2\beta_s^2 \mathrm{sech}^2\left(\frac{t-\tau-\tau_s}{\Delta t}\right) \\
&- 2\beta_s\left[\mathrm{sech}\left(\frac{t}{\Delta t}\right)\mathrm{sech}\left(\frac{t-\tau_s}{\Delta t}\right) + \beta_{MZ}^2 \mathrm{sech}\left(\frac{t-\tau}{\Delta t}\right)\mathrm{sech}\left(\frac{t-\tau-\tau_s}{\Delta t}\right)\right] \\
&+ 2\beta_{MZ}\cos\left(\omega_0\tau\right)\left[\mathrm{sech}\left(\frac{t}{\Delta t}\right)\mathrm{sech}\left(\frac{t-\tau}{\Delta t}\right)\right. \\
&\left.+\beta_s^2 \mathrm{sech}\left(\frac{t-\tau_s}{\Delta t}\right)\mathrm{sech}\left(\frac{t-\tau-\tau_s}{\Delta t}\right)\right] \\
&- 2\beta_{MZ}\beta_s\cos\left(\omega_0\tau\right)\left[\mathrm{sech}\left(\frac{t}{\Delta t}\right)\mathrm{sech}\left(\frac{t-\tau-\tau_s}{\Delta t}\right)\right. \\
&\left.+\mathrm{sech}\left(\frac{t-\tau_s}{\Delta t}\right)\mathrm{sech}\left(\frac{t-\tau}{\Delta t}\right)\right]. \qquad (4.21)
\end{aligned}
$$

Equation 4.21 is a long and cumbersome, but it can be broken apart into manageable pieces. The first two lines are the four individual peak profiles (the non-interfering terms). The third line is the interference between a main peak and its own subordinate peak. Because the main peak and its subordinate are always π out of phase, this interference does not modulate in τ and is always destructive (hence the minus sign at the beginning of this line). This destructive interference can be seen in Fig. 4.12 for the input pulse as the intensity drops to zero between the main peak and the subordinate peak.

The final four lines is where the modulating, τ-dependent interference occurs. The fourth line is the interference of the two main peaks. This term is the largest interference term when τ is small. This term will be referred to as the *dominant interference term*. The fifth line is the interference between the two subordinate peaks.

The sixth and seventh lines are the out-of-phase (note the minus sign again) cross-interference terms, between one main peak and the other's subordinate peak. When $\tau \simeq \tau_s$, the seventh line—the interference between the later main peak and earlier subordinate peak—can be larger than the dominant interference term, depending on τ_s and β_s. This term will be referred to as the *subdominant interference term*.

The behavior of Eq. 4.21 for five different values of τ is shown in Fig. 4.13. The five plots are for $\tau \simeq 150$ fs, within one optical period (2.67 fs). When the two main peaks are in phase, the intensity of the earlier main peak will increase due to the constructive dominant interference term. At the same time, the intensity of the later main peak will decrease due to the destructive subdominant interference term. So, the earlier peak intensity will be larger than the later peak intensity. Conversely, if the main peaks are π out of phase the later peak intensity will be the greater of the two. This switching back and forth is what leads to the frequency doubling for 100 fs $\leq \tau \leq$ 150 fs.

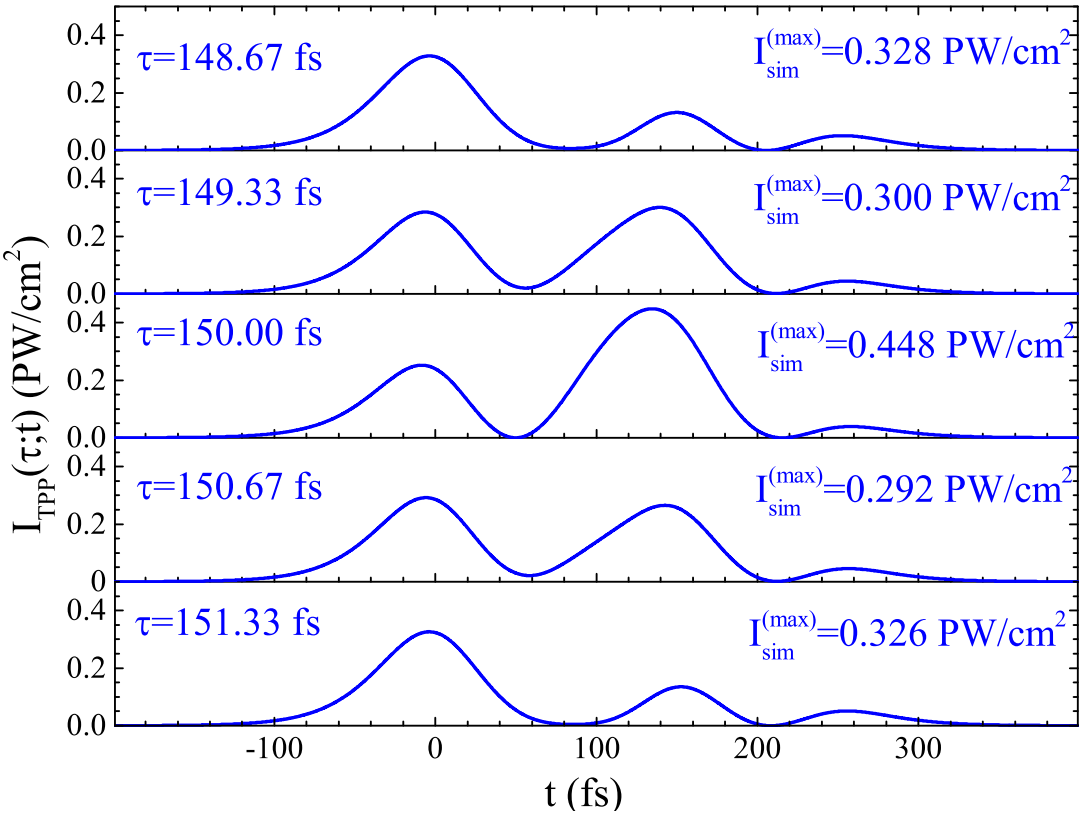

Fig. 4.13: $I_{TPP}(\tau;t)$ for five different simulated TPPs with different values of τ over one optical period near $\tau = 150$ fs, showing how the out-of-phase OI with the subordinate peak can cause a frequency doubling. All five TPPs have the following parameters: $\lambda_0 = 2\pi c/\omega_0 = 810$ nm, $\Delta t = 45.5$ fs, $\beta_s = 0.58$, and $\tau_s = 90$ fs. When the earlier peak is largest, the later peak is smallest, and vice-versa. The overall maximum intensity thus undergoes two oscillations per optical period.

4.4 TPP_{MZ}, resolution 0.067 fs

4.4.1 Results

One may note from the previous three experiments that the resolutions in $\Delta\phi$ and τ (Sec. 4.3) are too coarse to see QuI from a ground-state ionization. Recall

that eight photons at 800 nm are required to ionize Xe from the ground state. Quantum interference between the two wavepackets produced by a ground-state ionization would therefore have an oscillation period of $8\nu_0$, eight oscillations per optical period. In order to resolve this oscillation, at least sixteen points per optical period must be sampled. The SLM experiments in Secs. 4.1 and 4.2 had a phase resolution of $\sim \pi/4$, eight points per optical period. The MZ experiment in Sec. 4.3 had a temporal resolution of 0.67 fs, four points per optical period. None of these experiments have the necessary resolution.

Such a high resolution was not deemed important in order to compare this experiment with optimal control experiments, because of resolution limitations of the SLM. Consider as an example the SLM used in these experiments, with 128 pixels. The range of wavelengths admitted into the SLM during the experiment was 784 to 828 nm, giving a resolution of 0.344 nm/pixel. Using Eq. 3.13, one can extract a resolution in τ, which depends on τ. At $\tau = 150$ fs, the resolution is ~ 3.5 fs, greater than one optical period. The corresponding $\Delta\phi$ resolution at this value of τ is better, $\pi/10$, but this phase resolution gets worse as τ increases (and the fringe spacing correspondingly decreases). For more details, see Appendix B.

Nevertheless, it would be desirable to see if QuI plays a role in ionization from a TPP beyond the resolution typically used in optimal control experiments. Fortunately, the temporal resolution of the MZ experiment can be increased to 0.067 fs per step. The translation stage takes uneven steps at this resolution, but this can be post-corrected in the data analysis (see Sec. 3.2.2). The high-resolution Xe^+ yield vs τ for a TPP_{MZ} is shown in Fig. 4.14(a). Ion yields were measured over the

range 17 fs $< \tau <$ 140 fs. The yield at each point was calculated in the same way as Sec. 4.3, by integrating the composite TOF signal corresponding to 1000 laser shots over all Xe isotopes. The yield was normalized so that $Y(\tau \to \infty) = 1$. The Fourier transform of the region 98 fs $\leq \tau \leq$ 127 fs is shown in Fig. 4.14(b).

The experiments were performed at a pressure of $4.0(1) \cdot 10^{-7}$ Torr. The energy of the TPPs was adjusted so that the TPP energy approached 40 μJ as $\tau \to \infty$. The same beam splitter imbalance as in Sec. 4.3 was present, so the later peak had $\sim$ 89% of the energy (and peak intensity) of the earlier peak. The method to determine τ is described in Sec. 3.2.2. The input pulse had a subordinate peak, just as in Sec. 4.3.

4.4.2 Discussion

One can see in Fig. 4.14 clear oscillations at the optical frequency (throughout) and twice the optical frequency (for $\tau >$ 100 fs). No higher-frequency oscillations are clearly visible. The QuI oscillation amplitude must be larger than the noise present in the data in order to be visible in this experiment. In the Fourier transform data shown in Fig. 4.14(b), we estimated the noise in the normalized yield to be approximately 10% of the OI oscillation amplitude at $\tau \simeq$ 140 fs. This puts an upper limit of the QuI amplitude at 10% of the OI amplitude. This approximate 10% limit was found at other values of τ as well. So, while QuI could still be occurring in these experiments, it is at best a small contributor to the ionization when compared with OI.

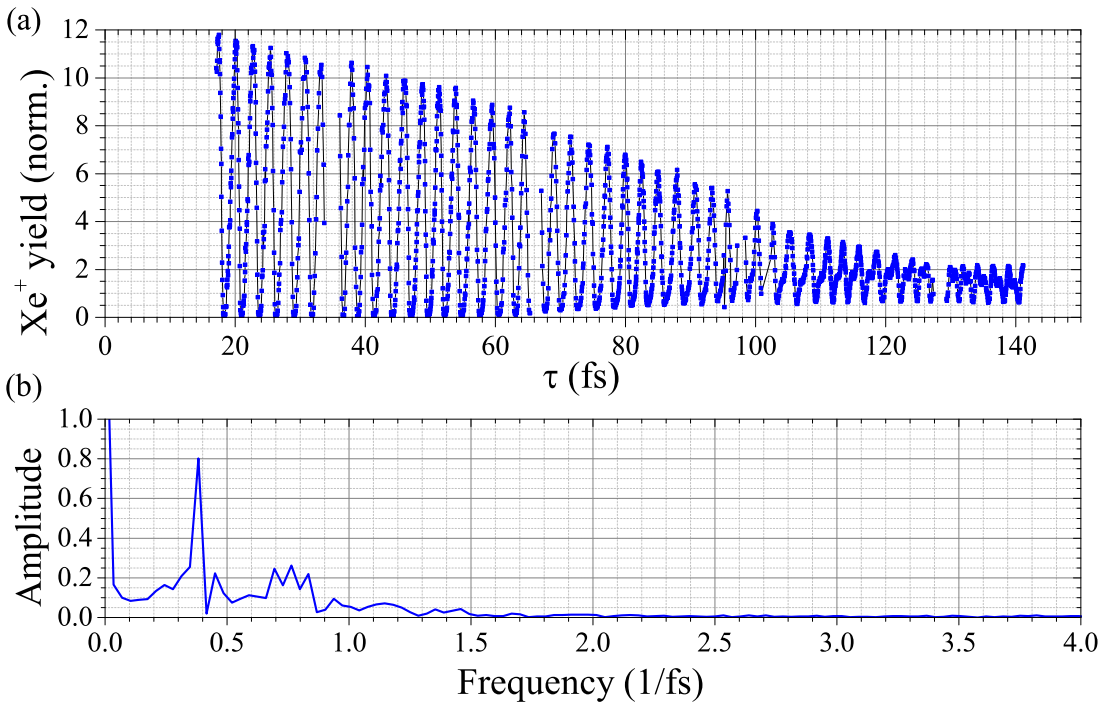

Fig. 4.14: (a) Xe^+ yield vs τ for a TPP_{MZ}, with a τ resolution of 0.067 fs. The data were collected in five different sections and τ was recovered as discussed in Sec. 3.2.2. The yield has been normalized so that the yield as $\tau \to \infty$ approaches unity. (b) Fourier transform of the fourth section, 98 fs $\leq \tau \leq$ 127 fs. Oscillations at ~ 0.375 fs^{-1} (the optical frequency) and ~ 0.75 fs^{-1} (twice the optical frequency) are visible, but higher frequencies are not clearly visible in these data.

Chapter 5: Experiment 1, "Ions": Applications to Optimal Control

A common theme emerged in the discussions of the "Ions" experiments in Chap. 4 – small, subtle features of the pulse can have a profound effect on the ionization yield due to OI. In all four experiments discussed, the relative phase between peaks of a TPP was found to affect the ionization rate. In the experiment described in Sec. 4.1, the subordinate peaks found outside the TPP (a result of the nonideal SLM mask, see Fig. 3.12) led to an uncertainty in the $\mathrm{TPP_{PS}}$ intensity and consequently the Xe^+ yield. In the second experiment (Sec. 4.2), the subordinate peaks were eliminated using an ideal SLM mask. It was shown that a pedestal on the input pulse, which modified the intensity at the wings of the pulse, could change OI enough to produce anomalous results in the ion yield. Because many pulse-measurement schemes rely on nonlinear optical effects (both the SD-FROG and Wizzler use third-order nonlinearities), low-intensity features such as pedestals and subordinate peaks can be difficult to resolve in pulse reconstructions. Finally, it was shown in the MZ experiments in Secs. 4.3 and 4.4 that a subordinate peak on the *input* pulse can modify OI in a manner that produces frequency doubling in the yield response. This frequency doubling is suggestive of two-photon QuI at first glance, but was in fact a purely optical effect.

These findings have direct application to optimal control in the strong-field regime. Ionization often occurs in strong-field optimal control experiments, either as a side-effect or as a first step in the dynamics of interest. While discussion of how an optimal control pulse guides a system to its optimal final state typically focuses on dominant features of the pulse (e.g., peak widths, chirp, inter-peak delays), the results presented in Chap. 4 provide evidence that more subtle features can influence the control process just as dramatically.

The purpose of this chapter is to illustrate this claim in the context of a specific optimal control experiment, described in Ref. [28]. This experiment was performed in the same lab, but before the work presented in this thesis. The data and several figures in this chapter are taken from Ref. [28]. The goal of this control experiment was to find an OCP to maximize the bending vibration of CO_2 during strong-field dissociative ionization. A brief summary of the experiment and results, along with a discussion of how OI-induced intensity fluctuations can influence the bending amplitude, is given in Sec. 5.1. A summary of an experiment that probed the bending vibration induced by a TPP_{PS} as a function of $\Delta\phi$ is described in Sec. 5.2.

5.1 Optimal control experiment to maximize CO_2 bending vibration amplitude

A detailed description of the experiment can be found in Ref. [28]; only a brief summary is given here. Input pulses were first shaped by an SLM before being

sent into the vacuum chamber filled with CO_2 molecules at a pressure of 5×10^{-8} Torr. Images of the CO_2 fragment ions (C^{2+} and O^{2+}) were detected by a 4π image spectrometer, also called a velocity map imager (VMI), described in Chap. 7 and Refs. [103, 109]. Several GAs were run to maximize the bending amplitude of the CO_2^{6+} ion prior to dissociation.

In these GAs, the pulse was represented by a number of *genes* – independent pulse parameters. Because the 128-pixel SLM was used to shape the pulses, there were at most 128 genes used to describe a pulse – each gene could have a value between 0 and 4π (see Sec. 3.2.1), encoded with 12-bit resolution. One finds that $\sim 1.5 \times 10^{364}$ pulse shapes were possible using this pulse shaper, demonstrating that the search space needed to be restricted somehow to hope for convergence on the optimal pulse.

Two types of GAs were run. The first was a restricted GA, where the input pulse was only changed by changing the coefficients of a 5th order polynomial expansion of the spectral phase of the pulse. The pulse measurement devices employed in this work were not sensitive to zeroth-order (constant) phase, and the first-order (linear) spectral phase only produces a temporal shift of the entire pulse [98]. As such, the restricted GA only consisted of four genes, the 2nd, 3rd, 4th, and 5th-order coefficients in the Taylor expansion of the spectral phase.

The second GA used a *quasi-unrestricted* parameter space. The pixels were allowed to vary independently, but a few restrictions were made to limit the search space. First, each group of four pixels were locked to the same value, making an effective 32 pixel pulse shaper. Second, the 12-bit resolution was reduced, to 20

steps between 0 and 2π rad. Third, the variation of a particular gene (i.e., the variation of a particular pixel's phase) was limited by a Gaussian cost functional; in the quasi-unrestricted GAs in this work, the variation of a particular gene from generation to generation was limited to $\sim \pi/4$ rad.

Because the molecular axis was aligned with the laser polarization direction in the experiment (alignment was performed concurrently with ionization by the OCP), the bending motion caused the carbon atom to move perpendicular to the polarization axis. As a result, the GAs sought to maximize the length of the C^{2+} lobe in the ion images. The length of the C^{2+} lobe was referred to as the fitness.

Four GA solutions were reported, two restricted [28] and two quasi-unrestricted [110]; the four solutions are shown in Fig. 5.1. Also shown are the phase-reversed pulses of the restricted-GA solutions (i.e., pulses created with $\phi(\omega) \rightarrow -\phi(\omega)$ in the mask; with all other parameters unchanged). The GA solutions were found when the best fitness did not change or decreased between successive generation of the algorithm; this took approximately 40 generations for each experiment. All GA solutions appear as trains of pulses, with nearly-flat phases across each peak and locked phases between peaks. Peaks 1 and 2 are labeled on each plot The relative phase between peaks 1 and 2 is $\Delta\phi_{12} = \phi_2 - \phi_1$. The inter-peak delay is τ_{12}.

Once the OCPs were found, statistical analysis was performed on the images using several techniques – image labeling [111], selective averaging [112], and coincidence imaging [113] – which all require each image frame to contain one and only one laser shot. The distribution of bending angles was approximately Gaussian (see the inset of Fig. 5.2). The CO_2 bond angle is defined as θ_b, and the bending

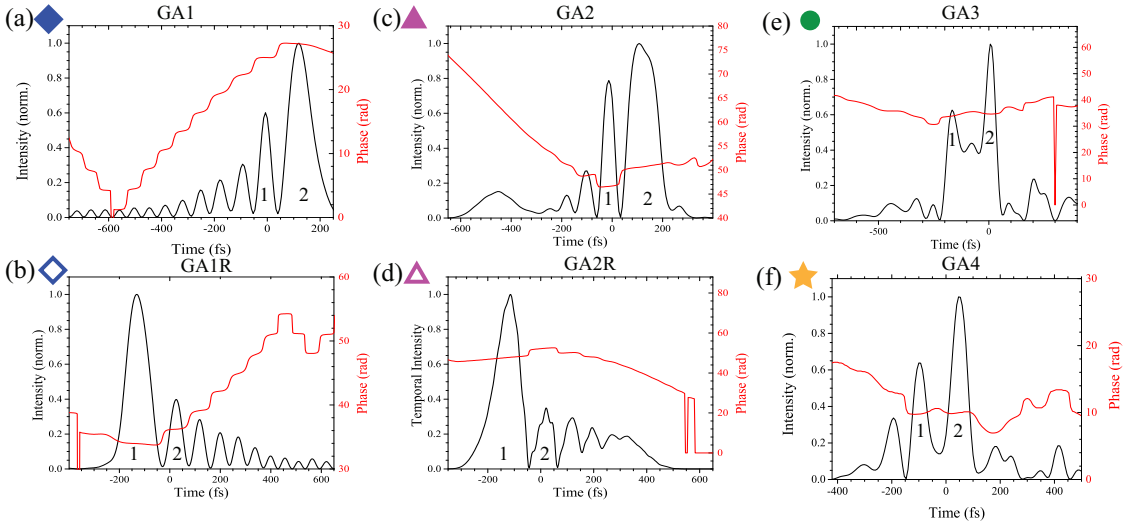

Fig. 5.1: SD-FROG reconstructions of the temporal intensity (black) and phase (red) of the four optimal control pulses: (a) and (c) are the restricted-GA solutions, GA2 and GA2, found in Ref. [28], (b) and (d) are their phase-reversed counterparts (i.e. the spectral intensity is unchanged but the spectral phase $\phi(\omega) \rightarrow -\phi(\omega)$), GA1R and GA2R, and (e) and (f) are the unrestricted-GA solutions, GA3 and GA4. Peaks 1 and 2 for each pulse are labeled. The relative phase between peaks 1 and 2 is $\Delta\phi_{12} = \phi_2 - \phi_1$.

Tab. 5.1: Pulse parameters for the four GA pulses and two phase-reversed pulses shown in Fig. 5.1. The two intensities are of the first and second peaks, each labeled in Fig. 5.1. The overall maximum intensity of each pulse is in bold. $\Delta\phi_{12}$ and τ_{12} is the relative phase and delay between peaks 1 and 2, respectively.

Pulse name	$\Delta_{1/2}\theta_b$ (degrees)	I_1 (PW/cm^2)	I_2 (PW/cm^2)	$\Delta\phi_{12}$ (π rad)	τ_{12} (fs)
GA1	34.9	0.44	**0.74**	0.70	126.7
GA1R	23.6	**0.72**	0.29	0.70	160.0
GA2	37.3	0.44	**0.56**	1.27	120.0
GA2R	29.1	**0.68**	0.24	1.46	133.3
GA3	28.0	0.30	**0.48**	0.22	173.3
GA4	21.0	0.37	**0.57**	0.06	146.7

angle is defined as $\Delta\theta_b = 180° - \theta_b$. These angles are shown in Fig. 5.2. The half width at half maximum (HWHM) of the bending angle distribution is $\Delta_{1/2}\theta_b$. Also in Fig. 5.2, $\Delta_{1/2}\theta_b$ is plotted as a function of the effective intensity (i.e., the intensity of the largest peak) of the two restricted-GA solutions and their phase-reversed counterparts (Fig. 5.1, colors and symbols can be matched between figures). Finally, in Fig. 5.2, $\Delta_{1/2}\theta_b$ is plotted as a function of the measured intensity for TL pulses with intensities between 10^{15} W/cm^2 and $2.5{\cdot}10^{15}$ W/cm^2. It is clear in Fig. 5.2 that the GA pulses also enhance the dissociative ionization because signals are observed at effective intensities below where signals from a TL pulse can be observed, i.e., $\leq 10^{15}$ W/cm^2. The characteristics of the GA pulses and phase-reversed counterparts (intensities, inter-peak delays, relative phases, and bending angles) are given in Tab. 5.1.

The first comment about Fig. 5.2 concerns the dependence of $\Delta_{1/2}\theta_b$ on I for TL pulses. Namely, $\Delta_{1/2}\theta_b$ decreases monotonically from 10^{15} W/cm^2 to $2 \cdot 10^{15}$ W/cm^2. The reasons for this intensity dependence appear to be linked to the intensity-dependent conformal bending of ionic potential surfaces as discussed in Ref. [28]. Both restricted GA OCPs enhance the bending compared to TL pulses, which is consistent the effective intensities being lower. However, the bending due to an OCP is also enhanced compared to its phase-reversed counterpart, which nominally has the same intensity as the OCP. The two GA pulses are similar in that the most intense peak is the last one, while the phase-reversed pulses have the most intense peak arrive first. The conclusion reached in Ref. [28] is that the earlier, weak peaks partially populate a bent state of the CO_2^{2+} molecular ion that increases the bending vibration amplitude; when the most intense peak arrives first, the molecule dissociates before this state is sufficiently populated.

However, it is also possible that the GA pulses and their phase-reversed counterparts did not truly have the same intensity. In Sec. 4.1.2, it was shown that a small pedestal significantly changed OI between a pair of pulses; with such a pedestal, two pulses with a relative phase $\Delta\phi$ did not have the same peak intensity as two pulses with a relative phase of $-\Delta\phi$ in general. Consequently, if such a pedestal were present in this optimal control experiment, the OCP peaks may have different intensities than their phase-reversed counterparts, even if the energies of the two pulses were the same. Such a discrepancy may not be detectable in the FROG reconstructions of the OCPs, depending on the size of the pedestal.

A pedestal is unlikely to have been the only "knob" with which the bending

vibration was controlled; however, it highlights the need to consider purely optical effects carefully, alongside the field-system dynamics, when discussing strong-field optimal control experiments. This example also highlights an advantage learning algorithm-based optimal control experiments have over manual manipulation—the learning algorithm can access regions of the control landscape (in this example, the pulse pedestal) that are not easily accessible to measurement instrumentation.

One can also investigate the bending response as a function of relative phase for the GA pulses, to check if they also exhibit periodic behavior in $\Delta\phi$ (because there are many different relative phases in each GA pulse, and because the intensities vary so much between pulses, this is unlikely). The bending angle $\Delta_{1/2}\theta_b$ and maximum intensity vs $\Delta\phi_{12}$ response of the four GA pulses and two phase-reversed pulses is shown in Fig. 5.3. It is difficult to tell if the bending from the GA pulses exhibits a periodic response in $\Delta\phi_{12}$ with only four points over $\sim 1.2\pi$ rad. If this is a periodic response, the two phase-reversed pulses are outliers. There is no discernible phase-dependent response in $I^{(max)}(\Delta\phi)$, which is no surprise as $\Delta\phi_{12}$ does not influence the intensity directly as it does in the case of a TPP.

The quasi-unrestricted GA pulses induced a lower bending amplitude than the restricted GA pulses. This is likely due to the GA not converging during the experiment, as the search space in the quasi-unrestricted GA was much larger than the restricted GA.

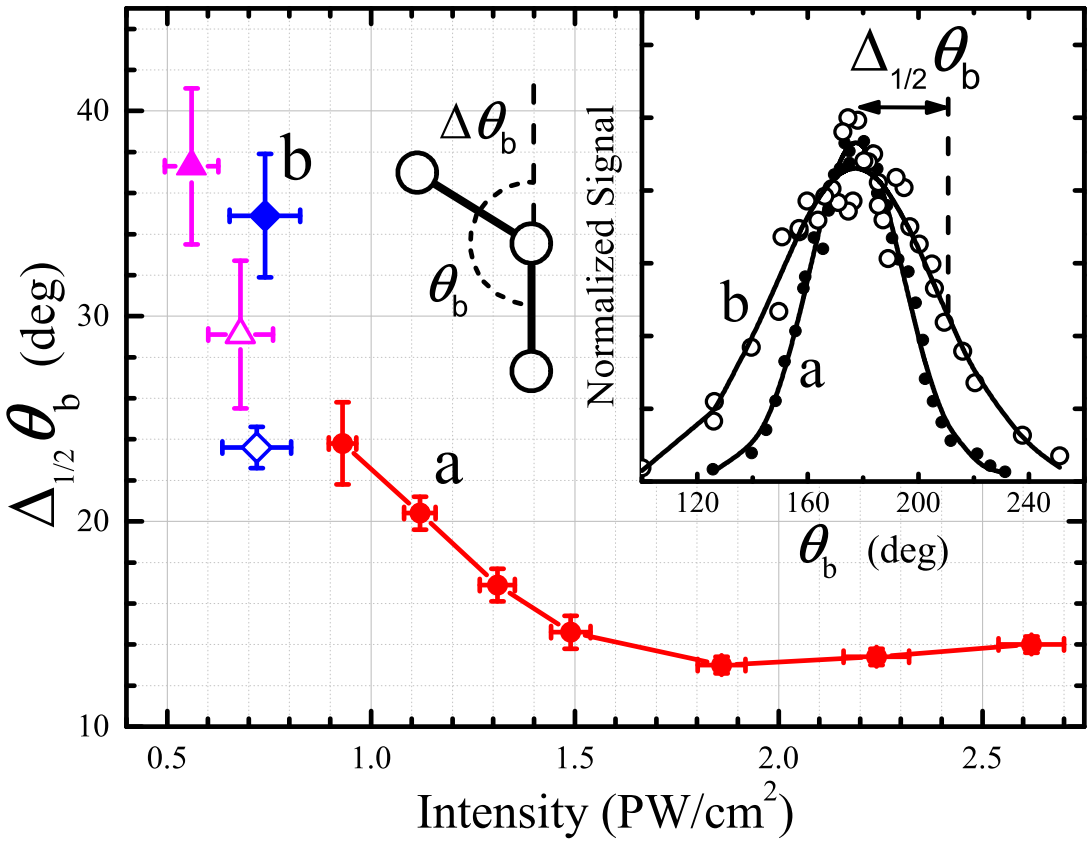

Fig. 5.2: (Modified from Fig. 3 of Ref. [28]) CO_2 bending vibration amplitude half width $\Delta_{1/2}\theta_b$ vs intensity for a TL pulse (red circles) and four shaped pulses: the two optimal control pulses (filled diamond and triangle) and their phase-reversed counterparts (hollow diamond and triangle). The data point symbols for the shaped pulses can be matched to the symbols in Fig. 5.1. (Inset) Bond angle distributions for the two pulses a and b, noted in the main plot. The cartoon to the left defines the bond angle θ_b and the bending angle $\Delta\theta_b$.

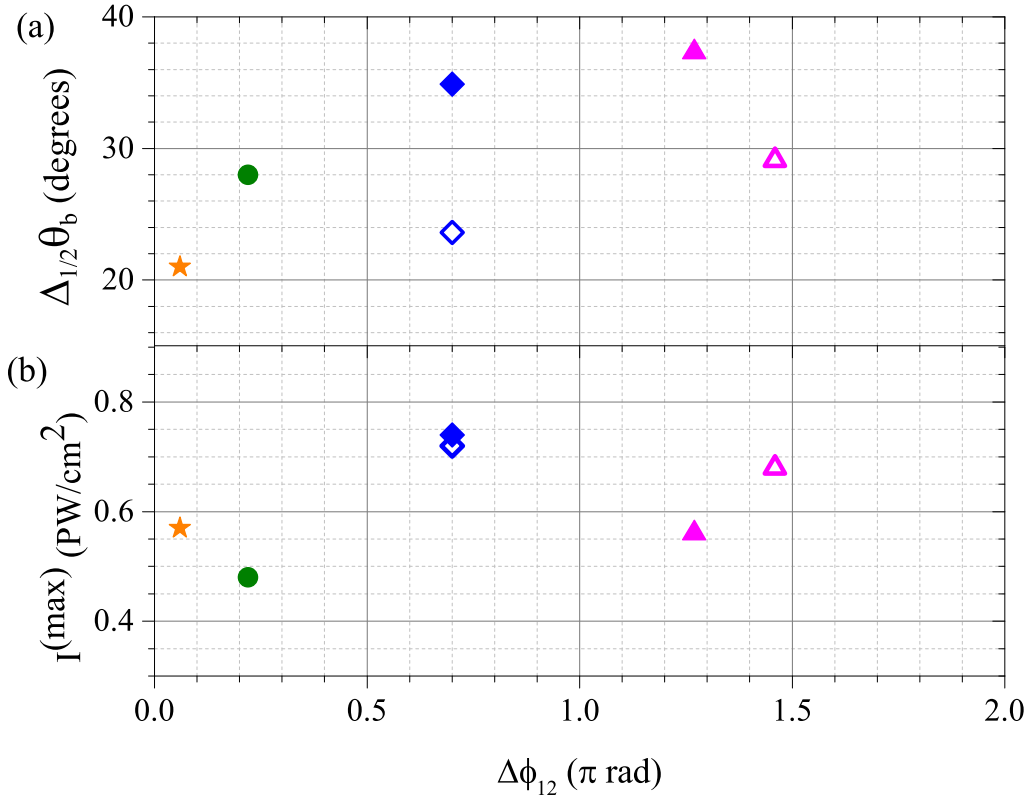

Fig. 5.3: (a) CO_2 bending amplitude half width $\Delta_{1/2}\theta_b$ vs $\Delta\phi_{12}$ for the GA pulses: restricted-GA pulses (filled diamond and triangle), their phase-reversed counterparts (hollow diamond and triangle) and the quasi-unrestricted GA pulses (filled circle and star). The data point symbols for the shaped pulses can be matched to the symbols in Fig. 5.1. (b) Maximum intensity $I^{(max)}$ vs $\Delta\phi_{12}$ for the same six pulses.

5.2 *Response of CO_2 bending amplitude to a TPP_{PS}*

To demonstrate further the role of OI in this strong-field optimal control experiment, an additional experiment was performed in which CO_2 bending was probed with a TPP_{PS}. In the experiment, a TPP_{PS} with variable $\Delta\phi$, at several different values of τ, was formed with a nonideal mask in the same manner as Sec. 4.1. The energy of the twin peaks (not including subordinate peaks) was fixed at 80 μJ by the half-wave plate/polarizer combination. After synthesis of the TPP_{PS}, the detection of fragment ions and data analysis on bending of the CO_2^{6+} molecular ion was done in the same way as Sec. 5.1. The maximum intensity of each TPP_{PS} was determined from SD-FROG measurements (see Sec. 3.3.3).

Figure 5.4(a) shows the bending angle HWHM $\Delta_{1/2}\theta_b$ vs $\Delta\phi$ for $\tau = 140$ fs. The TPP maximum intensity $I^{(max)}$ vs $\Delta\phi$ is shown in Fig. 5.4(b). Both are seen to oscillate periodically; the red solid curves are cosine fits meant to guide the eye.

One first notices the phase shift in the oscillations of $\Delta_{1/2}\theta_b$ and $I^{(max)}$, which can be seen by comparing the cosine fit curves. Based on the data for a TL pulse shown in Fig. 5.2, it is expected that $\Delta_{1/2}\theta_b$ will be largest when $I^{(max)}$ is smallest and vice versa; in other words, the two oscillations should be offset by π rad. Instead, the two oscillations are $\sim \pi/2$ rad out of phase. A similar observation was discussed in Sec. 4.1.2, and it was shown there that so-called shape distortions (modeled as a pedestal) can introduce a phase shift into the intensity modulations. For reasons discussed in Sec. 4.1.2, this phase shift is difficult to determine due to limitations in the pulse measurement devices.

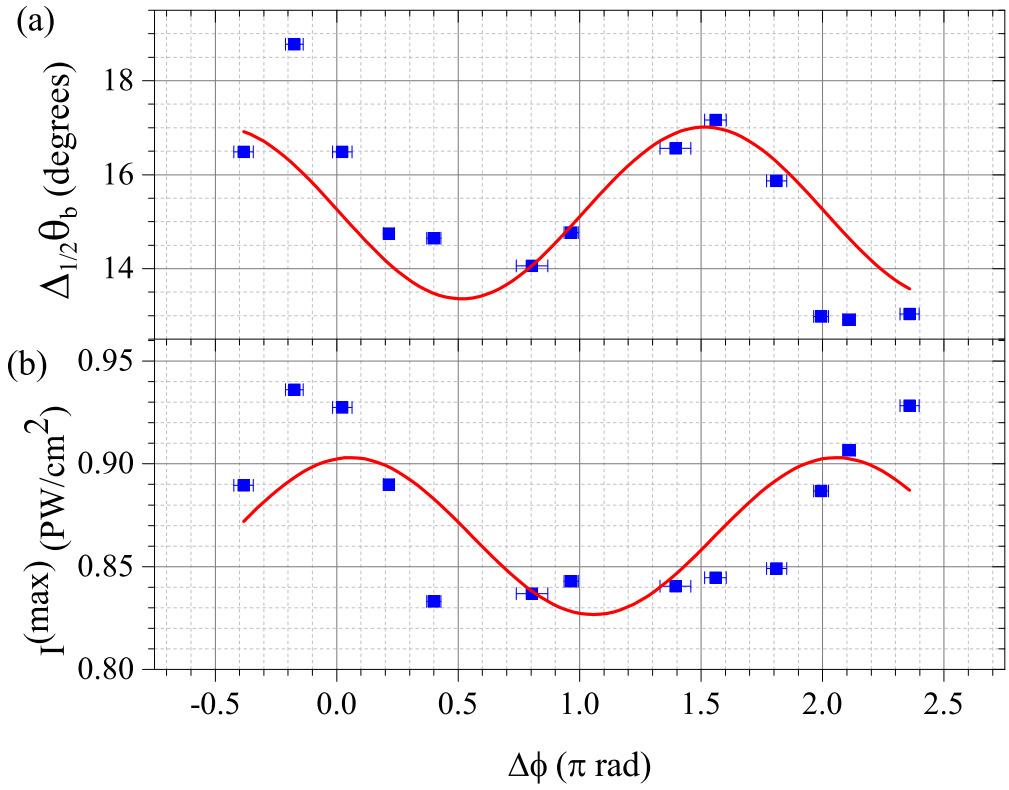

Fig. 5.4: (a) Bending angle half width $\Delta_{1/2}\theta_b$ vs $\Delta\phi$ for a TPP_{PS} produced with a nonideal mask and $\tau = 140$ fs. (b) Maximum intensity $I^{(max)}$ vs $\Delta\phi$ for the same TPPs. The experimental data is shown as blue squares, while the red curves are cosine fits of the data meant to guide the eye.

It is also worth commenting on the $\Delta_{1/2}\theta_b$ and $I^{(max)}$ oscillation amplitude (or, equivalently, the visibility as defined in Eq. 4.2). As can be seen in Fig. 5.4, $I^{(max)}$ varies by approximately 0.1 PW/cm^2 over the course of the experiment, between $\sim$ 0.84 PW/cm^2 and $\sim$ 0.94 PW/cm^2. The bending HWHM $\Delta_{1/2}\theta_b$ changes by approximately 4 degrees over the course of the experiment. This change in $\Delta_{1/2}\theta_b$ is compared with the change in $\Delta_{1/2}\theta_b$ from a TL pulse across the same intensities. The slope of the TL response shown in Fig. 5.2 around 0.9 PW/cm^2 is approximately

-20 degrees per PW/cm^2, so a change in intensity between 0.84 PW/cm^2 and 0.94 PW/cm^2 will change the bending HWHM by ~ 2 degrees. This is somewhat smaller than is observed in the TPP experiment. In addition, the range of $\Delta_{1/2}\theta_b$ is different in the TPP and TL experiments (13-17 degrees and 22-24 degrees, respectively). While it is unknown what the cause of this discrepancy is, it is not surprising that a change in the pulse shape changes the bending response. Specifically, it was shown in Ref. [28] that the bending response of CO_2 (i.e., $\Delta_{1/2}\theta_b$ variation) from a 100 fs single pulse was different than the response from a TL, 50 fs pulse.

Taking all of the above comments into consideration, the conclusion drawn from this experiment can only be based on the order-of-magnitude bending variation. The nonidealities of shaped pulses prevent a more quantitative comparison between $\Delta_{1/2}\theta_b$ and $I^{(max)}$ from being made. The change in $\Delta_{1/2}\theta_b$ seen in Fig. 5.4 is *roughly* what would be expected from intensity variations alone. Therefore, one concludes that any field-system dynamics present in this experiment are likely masked by the TPP intensity variation due to OI.

Chapter 6: Theory of Quantum Interference

None of the "Ions" experiments described in Chap. 4 showed any evidence of QuI. It is possible that τ-dependent oscillations due to QuI were present, but were being obscured by OI and experimental noise. Thus, it is desirable to have a model calculation that would predict the relative strengths of OI and QuI in the "Ions" experiments. A model of multiphoton ionization, treated using time-dependent perturbation theory (TDPT), is presented in this chapter. In Sec. 6.1, the photoelectron yield, as a function of both energy and τ, will be derived for the case of a two-photon ionization. The model is generalized to an m-photon transition in Sec. 6.2, and results of a calculation for $m = 8$ are presented. The model results show two sets of interference fringes with two distinct oscillation periods: the optical period t_{opt} (indicative of OI), and $t_{opt}/8$ (indicative of QuI Mechanism III). This model, while illustrative of the combined effects of OI and QuI in an experiment, has a limited applicability to the experiments in Chap. 4 because these experiments were performed in the strong-field regime. The extent to which the model calculation in Sec. 6.1 and 6.2 can be generalized to strong-field ionization is discussed in Sec. 6.3.

6.1 Two-photon QuI in the perturbative regime

The perturbation theory model for two-photon QuI presented in this section is similar to the derivation in Ref. [50]. The model atom is shown in Fig. 6.1. The model considers two-photon, non-resonant excitation to a collection of final states $|c\rangle$ from a single initial (ground) state $|i\rangle$. No photons are transferred to the non-resonant intermediate states $|m\rangle$. The energy difference between a given final state $|c\rangle$ and the initial state is $\hbar\omega_c$. Therefore, for any intermediate state $|m\rangle$, $\omega_c = \omega_{cm} + \omega_{mi}$. The central frequency of the laser is chosen to be close (within the spectral width) to half the energy difference between the final states and initial states; that is, $|2\omega_0 - \omega_c| \leq \Delta\omega$, where $\Delta\omega$ is defined in Eq. 3.12.

Following the procedure of Ref. [114], the transition amplitude to a final state $|c\rangle$ under second-order TDPT is

$$A_2(t,\omega_c) = \left(-\frac{i}{\hbar}\right)^2 \sum_m \int_{-\infty}^{t} dt' \int_{-\infty}^{t'} dt'' e^{i\omega_{cm}t'} V_{cm}(t') e^{i\omega_{mi}t''} V_{mi}(t''), \tag{6.1}$$

where $V_{ab}(t) = \langle a|V(t)|b\rangle$ and $V(t)$ is the time-dependent interaction potential. The dependence of A_2 on ω_c has been made explicit in anticipation of converting the discrete set of final states $|c\rangle$ into a continuum. In this model $V(t) = \mathcal{E}_{TPP}(\tau;t)\hat{\mathbf{z}}\cdot\mathbf{r}$, where $\mathcal{E}_{TPP}$ is defined in Eq. 2.3 and $\hat{\mathbf{z}}$ is the laser polarization direction (as in Sec. 4.3, this model assumes without loss of generality that the CEPs of both peaks are equal, i.e., $\theta_1 = \theta_2$). The time-dependent portion of the TPP electric field $\mathcal{E}_{TPP}$ can be pulled out of the matrix elements giving

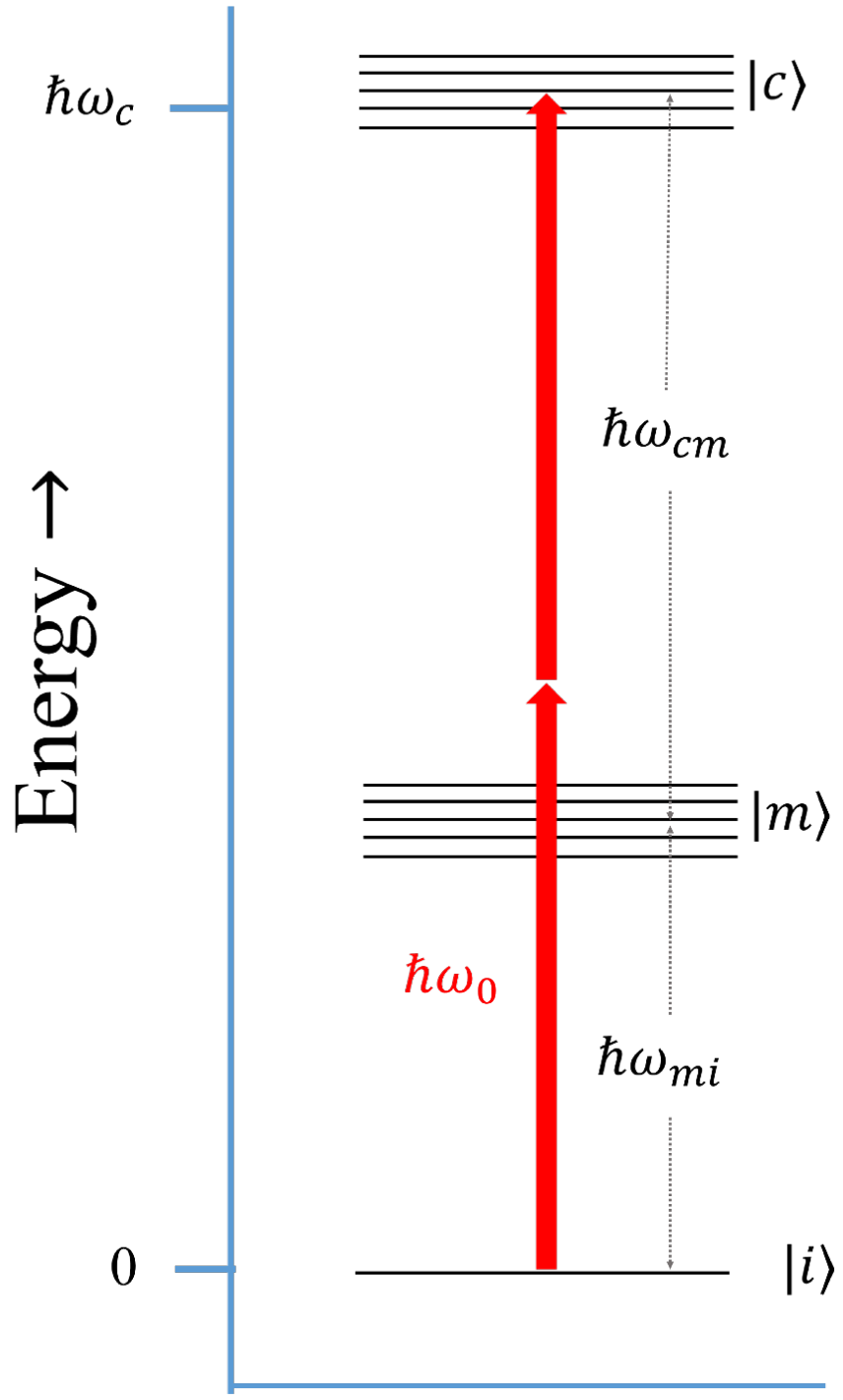

Fig. 6.1: Model atom used in the second-order time-dependent perturbation theory calculation. States labels and energies are defined in the text.

$$A_2(\tau;t,\omega_c) = -\frac{1}{\hbar^2}\sum_m \int_{-\infty}^{t} dt' \int_{-\infty}^{t'} dt'' e^{i\omega_{cm}t'} \mathcal{E}_{TPP}(\tau;t') e^{i\omega_{mi}t''} \mathcal{E}_{TPP}(\tau;t'') \times \langle c|\hat{\mathbf{z}}\cdot\mathbf{r}'|m\rangle\langle m|\hat{\mathbf{z}}\cdot\mathbf{r}''|i\rangle, \tag{6.2}$$

where the parameterization of A_2 on τ has now been made explicit. The integral with respect to t'' can be integrated by parts:

$$\int_{-\infty}^{t'} dt'' e^{i\omega_{mi}t''} \mathcal{E}_{TPP}(\tau;t'') = \left[\mathcal{E}_{TPP}(\tau;t'')\frac{1}{i\omega_{mi}} e^{i\omega_{mi}t''}\right]_{-\infty}^{t'} - \int_{-\infty}^{t'} dt'' \frac{1}{\omega_{mi}} e^{i\omega_{mi}t''} \frac{d\mathcal{E}_{TPP}(\tau;t'')}{dt''}. \tag{6.3}$$

When evaluating this integral with E_{TPP} given by Eq. 2.3, one finds that the second term of Eq. 6.3 vanishes, as does the first term evaluated at $t'' \to -\infty$, giving

$$\int_{-\infty}^{t'} dt'' e^{i\omega_{mi}t''} \mathcal{E}_{TPP}(\tau;t'') = \mathcal{E}_{TPP}(\tau;t')\frac{1}{i\omega_{mi}} e^{i\omega_{mi}t'}. \tag{6.4}$$

Substituting the right-hand side of Eq. 6.4 back into Eq. 6.2 results in

$$A_2(\tau;t,\omega_c) = -\frac{1}{\hbar^2}\sum_m \int_{-\infty}^{t} dt' e^{i\omega_{cm}t'} \left[\mathcal{E}_{TPP}(\tau;t')\right]^2 \frac{1}{i\omega_{mi}} e^{i\omega_{mi}t'} \times \langle c|\hat{\mathbf{z}}\cdot\mathbf{r}'|m\rangle\langle m|\hat{\mathbf{z}}\cdot\mathbf{r}''|i\rangle. \tag{6.5}$$

One can further simplify Eq. 6.5 by separating the time-dependent term from the time-independent dipole matrix elements. Keeping in mind that $\omega_{cm} + \omega_{mi} = \omega_c$, one finds that

$$A_2(\tau; t, \omega_c) = \frac{i}{\hbar} \int_{-\infty}^{t} dt' e^{i\omega_c t'} \left[\mathcal{E}_{TPP}(\tau; t')\right]^2 a_2, \tag{6.6}$$

where

$$a_2 \equiv \sum_m \frac{1}{\hbar\omega_{mi}} \langle c|\hat{\mathbf{z}} \cdot \mathbf{r}'|m\rangle\langle m|\hat{\mathbf{z}} \cdot \mathbf{r}''|i\rangle \tag{6.7}$$

is assumed to be independent of ω_c. The transition amplitude long after the ionization is found by evaluating Eq. 6.6 as $t \to \infty$, giving

$$A_2(\tau; \omega_c) = \frac{i}{\hbar} \tilde{\mathcal{E}}^2_{TPP}(\tau; \omega_c) a_2, \tag{6.8}$$

where

$$\tilde{\mathcal{E}}^2_{TPP}(\tau; \omega_c) = \int_{-\infty}^{\infty} dt e^{i\omega_c t} \left[\mathcal{E}_{TPP}(\tau; t)\right]^2 \tag{6.9}$$

is the Fourier transform of the *square* of the electric field. The energy-resolved photoelectron yield is

$$Y_2(\tau; \omega_c) = |A_2(\tau; \omega_c)|^2. \tag{6.10}$$

6.2 Generalization to m-photon QuI

The generalization of the model in Sec. 6.1 to an arbitrary number of photons m requires the use of mth order time-dependent perturbation theory. The setup of the model atom is similar to that shown in Fig. 6.1. Ionization again proceeds from an initial (ground) state $|i\rangle$ to a collection of final states $|c\rangle$ via an m-photon

transition. It turns out that the result found in Eq. 6.8 generalizes in the expected way; namely,

$$A_m(\tau;\omega_c) = \frac{i}{\hbar}\tilde{\mathcal{E}}^m_{TPP}(\tau;\omega_c)a_m, \tag{6.11}$$

where

$$\tilde{\mathcal{E}}^m_{TPP}(\tau;\omega_c) = \int_{-\infty}^{\infty} dt e^{i\omega_c t}\left[\mathcal{E}_{TPP}(\tau;t)\right]^m, \tag{6.12}$$

is the Fourier transform of the mth power of the electric field. The term a_m is a generalization of a_2 to include m dipole transitions; it is time-independent and, like a_2, assumed to be independent of ω_c. The energy-resolved photoelectron yield is

$$Y_m(\tau;\omega_c) = |A_m(\tau;\omega_c)|^2. \tag{6.13}$$

Figure 6.2 shows Y_m, referred to as the photoelectron spectrum (PES), as a function of τ and electron energy $\hbar\omega_c - I_p$, where I_p is the ionization potential of the atom. The following parameter values were used in the calculation: $\omega_0 = 2.35$ rad/fs, $\Delta t = 45$ fs, $m = 8$, $I_p = 12.13$ eV, and 150 fs $< \tau <$ 160 fs. The full code for the calculation, written in MATLAB, is provided in Appendix C.

Immediately obvious in Fig. 6.2 is the presence of two sets of interference fringes, with different time scales. There are slow oscillations, separated by $t_{opt} = 2.7$ fs, that correspond to OI. But, faster fringes indicative of QuI are also present. The fast fringe period is ~ 0.33 fs $= t_{opt}/8$. The energy width of the envelope (slow oscillations, ~ 0.05 eV) is determined by the spectral width of the laser field. All of

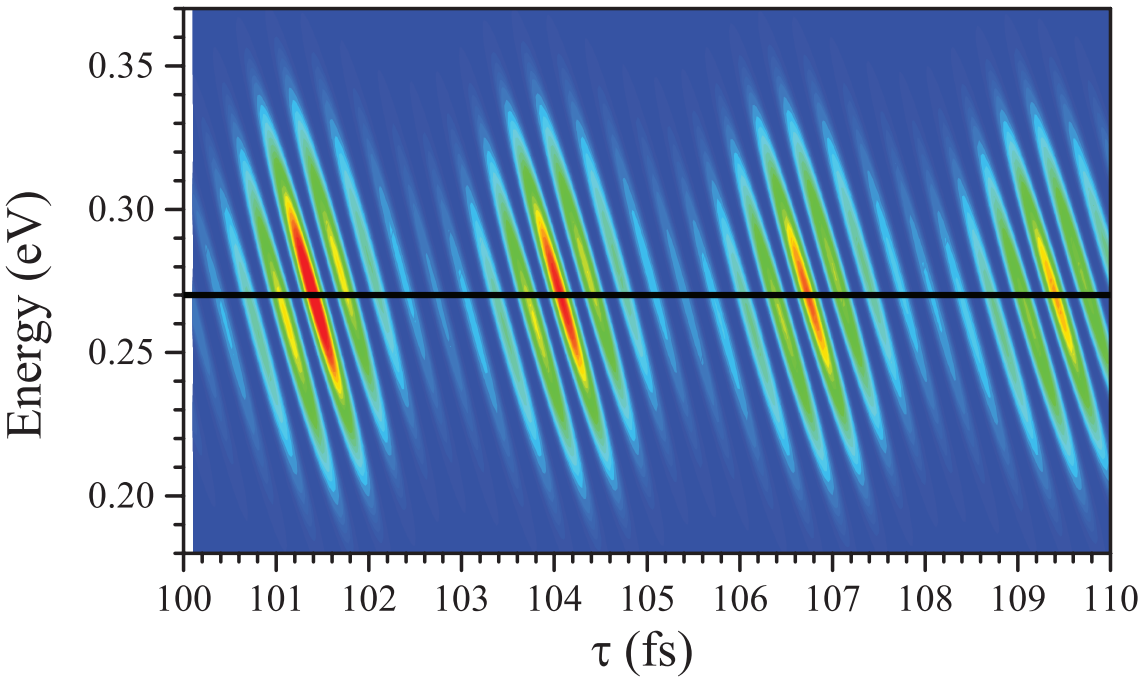

Fig. 6.2: Calculated energy- and τ-resolved photoelectron yield $Y_m(\tau; \hbar\omega_c - I_p)$, for the following model parameters: $\omega_0 = 2.35$ rad/fs ($\lambda_0 = 800$ nm), $\Delta t = 45$ fs, $m = 8$, and $I_p = 12.13$ eV. The black line indicates the single-energy yield vs. τ, which is shown in Fig. 6.3.

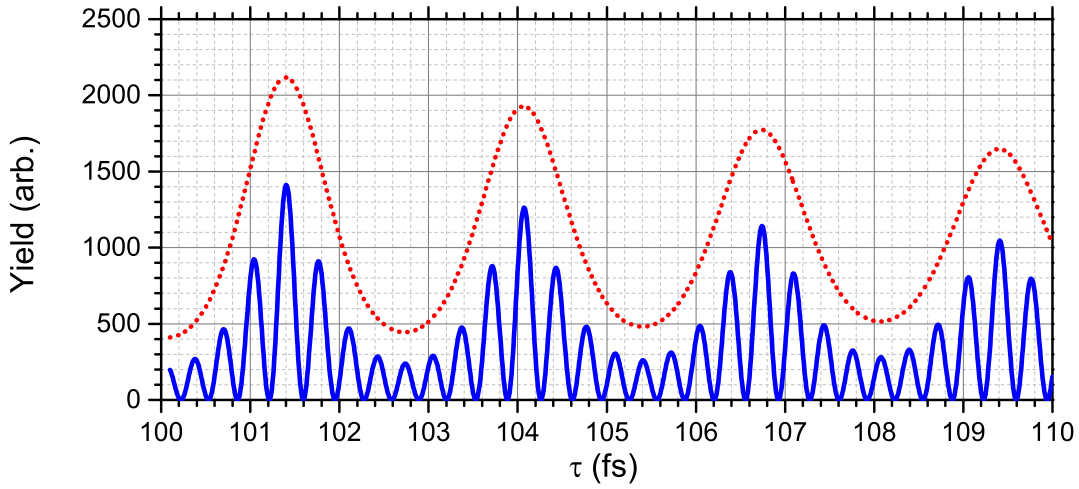

Fig. 6.3: τ-dependent photoelectron yield at a single energy (0.27 eV, blue solid curve, indicated by the horizontal black line in Fig. 6.2) and for all energies (red dotted curve), found by integrating the energy-dependent photoelectron yield shown in Fig. 6.2. The total electron yield has been divided by 10 to allow viewing alongside the single-energy yield.

the fringes are slanted, with a slope equal to $\hbar\omega_0/\tau$. Therefore, as τ increases, the fringes become more and more slanted.

An initially surprising feature of this calculation is illustrated in Fig. 6.3, which compares the electron yield at one particular energy (in this case, 0.27 eV $= 8\hbar\omega_0 - I_p$) with the total electron yield, found by integrating $Y_8(\tau; \hbar\omega_c - I_p)$ over all energies. The fast-oscillating fringes are only present in the single-energy yield; QuI is not observed in the total electron yield. The reason for this vanishing of QuI in total electron yields will be discussed in more detail in Sec. 6.3.2; for now, one concludes from this model that an energy-resolved photoelectron measurement is needed to see evidence of QuI in resonance-free atomic ionization.

6.3 Comments on strong-field QuI

It is not immediately clear that the results of the calculations in Secs. 6.1 and 6.2 are applicable to the experiments described in Chaps. 3, 4, and 5, because all of these experiments were performed in the strong-field regime. The Keldysh parameter γ [7] for these experiments was between 0.4 and 0.6, indicating that tunneling ionization played a major role in all of the experiments. Furthermore, the large laser intensities leads to a shift in bound state energies and the ionization potential due to the ac Stark effect and ponderomotive energy. As such, a perturbative, multiphoton model may not accurately describe the physics of these strong field experiments.

In order to determine the applicability of Secs. 6.1 and 6.2 to strong-field experiments, two significant questions must be addressed:

- Do QuI effects appear in PES calculations when using linearly-polarized, strong-field TPPs? Here, QuI effects refer to fringes in the PES with a time scale commensurate with the energy spacing between the ground state and final continuum states of the system. In the weak field limit, this energy spacing was $m\hbar\omega_0$, giving a QuI fringe period of $1/m$ times the optical period.

- In these strong-field QuI models, do the fast QuI fringes vanish when computing the total electron yield by integrating the PES? This was a major conclusion in Sec. 6.2 and, if it carries over to the strong-field case, provides a compelling explanation as to why QuI was not seen in the "Ions" experiments.

These two questions will be addressed in Secs. 6.3.1 and 6.3.2 respectively.

6.3.1 QuI in strong-field models

Some qualitative comments can be made about QuI at higher intensities, particularly concerning the ac Stark effect [115, 116] and ponderomotive energy. The ac Stark effect causes an upward shift in the ionization threshold of an atom, relative to the ground state. The ground-state shift due to the ac Stark effect can typically be neglected[1]. This shifting of the ionization threshold is given by the intensity-dependent ponderomotive energy $U_p(I)$ (see. Eq. 2.2).

The electron after ionization experiences a force due to the ponderomotive energy, which is related to the oscillation of the free electron in a periodic electromagnetic wave. This force is called the ponderomotive force $\mathbf{F}_p$,

$$\mathbf{F}_p = -\nabla U_p = -\frac{e^2}{4m\omega_0^2}\nabla\left(E^2\right), \tag{6.14}$$

where E is the electric field of the laser. One can see from Eq. 6.14 that the ponderomotive force points in the direction towards lower laser intensity (recall $I \propto E^2$), meaning that the electron gets pushed away from the focus after ionization. This leads to an increase in the velocity of the electron after ionization. In this way, the kinetic energy of the electron changes. The added energy is at most $U_p(I^{(max)})$, which occurs when the electron is ionized at the peak value of the laser intensity (the center of the focus). Because the laser intensity varies in both space and time, any energy between $U_p(0) = 0$ and $U_p(I^{(max)})$ is possible, depending on where and

[1] Note that, if the initial state in the experiment is *not* the ground state, then the Stark shift of the initial state may not be neglected in general.

when the electron is ionized.

For a typical TPP used in Chap. 3, $I^{(max)} \simeq 3 \times 10^{14}$ W/cm^2. One finds that for this intensity, $U_p = 17.9$ eV, larger than $I_p = 12.13$ eV in xenon. Each electron gains additional energy due to the ponderomotive force, depending on where and when the pulse is ionized. The electron measurement does not discriminate the positions and times of electron origin, leading to a washing out of the QuI fringes due to the ponderomotive energy. The energy scale of the QuI fringes is rather small (fringe spacing in Fig. 6.2 is ~ 0.04 eV, for example), which implies that the necessary intensities are much lower than used in Chap. 4. For example, $U_p < 0.04$ eV requires that $I_{max} < 7 \times 10^{11}$ W/cm^2.

Clearly, a strong-field version of the QuI model of Secs. 6.1 and 6.2 needs to be developed. Several strong-field ionization theories have been developed, including PPT theory, named after the authors Perelomov, Popov, and Terent'ev [8], and ADK theory, after the authors Ammosov, Delone, and Krainov [9]. Of the two, PPT is applicable for all ω and γ while ADK is only applicable for $\gamma << 1$ [56, 117, 118].

Some recent works have found quantum-mechanical interferences within the strong-field regime. Theoretical simulations of ionization from a single, linearly-polarized pulse based on ADK theory have found inter-cycle wavepacket interferences [119, 120], while works in both theory [121, 122] and experiment [123] have described inter-pulse interference effects using circularly-polarized TPPs. Notably, none of these works considered a linearly-polarized TPP. Past experimental results that did investigate QuI from a linearly-polarized TPP [50,80] were performed in the weak-field regime, $\gamma >> 1$. Quantum interference like that described in Refs. [50,80]

and Secs. 6.1 and 6.2 has not been confirmed to exist in the strong-field regime.

6.3.2 Absence of QuI in total electron yields

Even if QuI fringes were not washed out by ponderomotive shifts, there is a compelling reason to believe that no QuI fringes will be visible in the total ion signals measured in the "Ions" experiments. As mentioned briefly in Chap. 2, QuI can be considered a temporal analogue of a Young's double slit experiment, with the two peaks of the TPP representing the two slits. In this section, this double-slit analogy will be explored in more detail to explain from another viewpoint the vanishing of QuI in the total ion signal seen in Fig. 6.3. In the double-slit analogy, the slit spacing is represented in the TPP experiments by the relative phase $\Delta\phi$ (directly in the SLM experiments and indirectly, through τ, in the MZ experiments and the calculations in Secs. 6.1 and 6.2). Ionization of an electron corresponds to a photon or massive particle passing through the double slit apparatus. In the classic double slit experiment, there is ambiguity as to which slit the particle passed through. In the TPP ionization experiment, there is an ambiguity as to which peak was responsible for producing the electron.

In a traditional double slit experiment, the particles pile up on the screen at different locations with the minima and maxima determined by the relative phase after passing through the slits. The angular intensity pattern on the detector is

$$I(\theta) = 4I_0 \left(\frac{\sin\left(\pi d \sin\theta/\lambda\right)}{\pi d \sin\theta/\lambda} \right)^2 \cos^2\left(\frac{\pi a \sin\theta}{\lambda} \right), \tag{6.15}$$

where I_0 is the peak intensity, d is the slit separation, a is the slit width, and λ

is the wavelength of light. The total number of particles on the detector is found by integrating Eq. 6.15 from $\theta = -\pi/2$ to $\theta = \pi/2$. This is difficult to integrate analytically but can be readily performed numerically. In a numerical integration with $a = 20\mu$m, $\lambda = 800$ nm, and 50 μm $< d <$ 200 μm, one finds that the integrated signal varies by less than 0.230% of the average value over this range of d. The *total number of particles* on the detector does not depend on the slit spacing d.

In the TPP ionization experiments, the energy distribution of the electrons is analogous to the spatial pattern of the particles in the double slit experiment. Consequently, the *total number of electrons* produced by the TPP should not change due to QuI, but only due to a change in the "throughput" of the TPP (i.e., the pulse intensity via OI).

It is important to note the limits of this analogy; particularly, it only holds if the transition is to an open channel as in QuI Mechanism III (described in Sec. 2.4.3). In Ref. [50], modulation of the total ion yield due to QuI is observed and clearly differentiated from OI, but this is because the QuI that was observed was Mechanisms I and II, occurring in transitions to bound states. Mechanism I involved populating a single energy state in the atom, so it is similar to the single-energy case shown in Fig. 6.3. In an open channel experiment, like that done in Ref. [80], QuI Mechanism III-induced modulation in the total electron/ion yield will not occur. While the total electron yield is seen to change with changing TPP relative phase in Ref. [80], it only does so because the two peaks of the TPPs were closely separated, so OI was likely making a substantial contribution to the ionization dynamics. However, QuI could still appear in an open channel experiment via Mechanisms I and II involving

intermediate states.

6.3.3 Design of a strong-field QuI experiment

There is a notable void in the current literature on quantum-mechanical interferences in ionization; quantum interference probed by linearly-polarized TPPs in the strong-field regime has, to the author's knowledge, not been investigated in either theory or experiment. The double-slit analogy described in Sec. 6.3.2, coupled with the results shown in Figs. 6.2 and 6.3, demonstrates that an energy-resolved photoelectron experiment is necessary to see evidence of QuI Mechanism III. The energy of a photoelectron is connected with the location of a particle on the screen in the double-slit analogy, so an energy-resolved measurement is akin to recording the interference pattern on the screen rather than counting up all particles. The experiment to search for QuI could be modified from the high-resolution MZ experiment described in Sec. 4.4, by replacing the TOF ion detection with an energy-resolved photoelectron detector. Some salient design points of this proposed experiment are:

- In order to differentiate QuI from OI effectively, a multiphoton ionization (at least two photons) is required so that the oscillation periods of QuI and OI are consequently differentiable. Xenon satisfies this requirement. The more photons that are required, the smaller the period of QuI becomes, making its observation more difficult.

- Ideally, the target system should have no intermediate resonances, so that QuI Mechanism III can be investigated independently–Mechanisms I and II would

produce competing signals.

- The TPP intensity should be low enough that the ponderomotive energy is lower ($< 25\%$) of the QuI fringe spacing, to prevent a blurring of the QuI fringes due to the ac Stark effect.

- The experiment employs a linearly polarized TPP, with parallel polarization of the peaks[2].

The current experimental setup does not allow detection of electrons from pulses with an intensity below $\sim 10^{13}$ W/cm^2, likely precluding observation of QuI due to ac Stark shifts. Nevertheless, there is still much to be learned from an energy-resolved TPP experiment. The design and preliminary results of such an experiment is the focus of Chaps. 7 and 8.

[2] While rotating the polarization of one of the peaks of the TPP would eliminate OI, this is not ideal because the photoelectron angular distributions may have limited overlap. Selection rules may cause the two peaks to ionize to two different sets of final states, in which case the quantum interference will break down as there is full knowledge of which peak produced a given photoelectron. While QuI can also occur in ionization from circularly-polarized light, that investigation is not in the scope of this thesis.

Chapter 7: Experiment 2, "Electrons": Experimental Setup

This chapter describes the apparatus used in the second set of experiments, referred to as the "Electrons" experiments. The experiments were designed in accordance with the requirements listed in Sec. 6.3.3. A high-level schematic of the experimental setup is shown in Fig. 7.1. Synthesis of TPPs is the topic of Sec. 7.1. Many of the techniques described in Chap. 3 are used here. One new technique discussed in this section is the generation of a $\mathrm{TPP}_{\mathrm{MZ}}$ at 400 nm.

Generating TPPs at 400 nm allowed the pulse intensity to be lowered, because the ionization rates for these experiments were higher (four-photon ionization is a lower-order process than eight-photon ionization). Furthermore, decreasing the wavelength by a factor of two lowers the ponderomotive energy by a factor of four for a fixed intensity (see Eq. 2.2).

In these experiments, up to thirty minutes was required to produce a statistically-significant electron energy distribution plot. During this time, τ can change due to drifting of the MZ translation stage. A method, described in Sec. 7.2, was devised to post-sort the data based on the measured τ.

The biggest difference between the "Ions" experiments of Chap. 3 and the "Electrons" experiments of this chapter is the charged particle detection scheme.

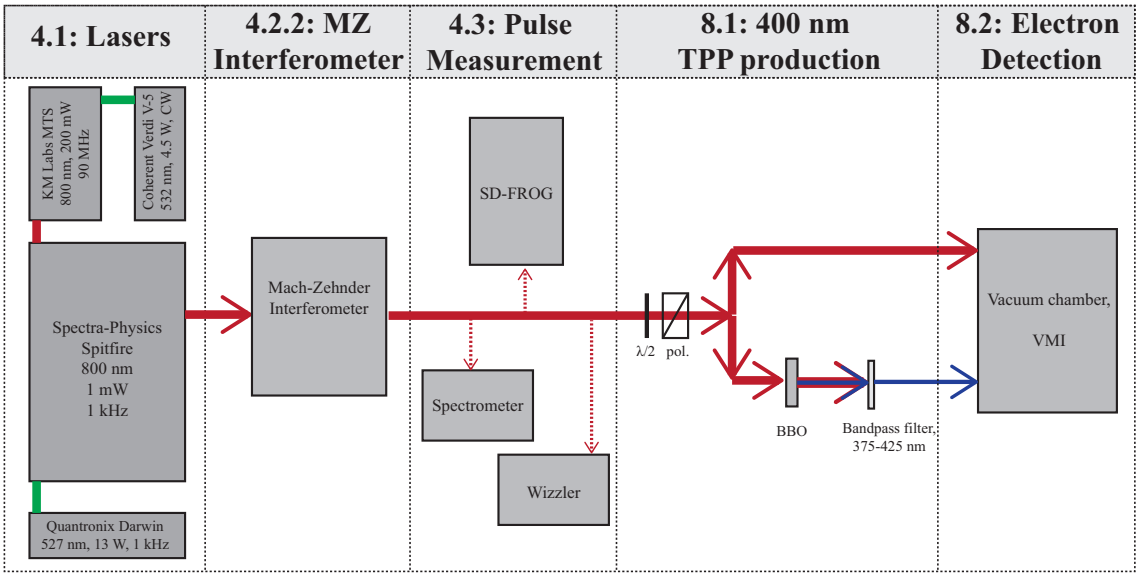

Fig. 7.1: High-level schematic of the "Electrons" experiments. The relevant sections that describe the apparatus are given in the upper headings. Much of the TPP generation and characterization is covered in Chap. 3, while energy-resolved electron detection is the subject of this chapter.

A velocity map imager (VMI) was used in the "Electrons" experiments, that will be described in Sec. 7.3. The analysis of the VMI data to recover energy- and angle-resolved electron distributions is the topic of Sec. 7.4.

7.1 TPP generation

The synthesis of the TPPs used in the "Electrons" experiments follows very closely the techniques of the "Ions" experiments. Every TPP used in the "Electrons" experiments was a TPP_{MZ}. In these experiments, τ was variable in steps of approximately 0.067 fs. Input pulse parameters were measured as in Sec. 3.1.3. The input pulses had a satellite peak, the same as discussed in Sec. 3.3.1. The

TPP energy varied at each point due to OI. The Wizzler (Sec. 3.3.1) and SD-FROG (Sec. 3.3.2) were used to measure the input pulses and TPPs, respectively. The TPP parameters τ, $\Delta\phi$, and I_{max} were measured as described in Sec. 3.3.3.

After TPP_{MZ} generation, experiments were performed investigating ionization from both 800 nm and 400 nm TPPs. A 400 nm TPP_{MZ} was generated directly from an 800 nm TPP_{MZ} using second harmonic generation (SHG) from a beta barium borate (BBO) crystal of 5 mm diameter and 0.5 mm thickness. The 800 nm TPP_{MZ} was focused onto the face of the BBO crystal with a lens of $\sim$ 1 m focal length. The BBO was placed $\sim$ 30 mm before the focal point to lower the intensity of the 800 nm beam (while still making the beam small enough to fit within the clear aperture of the crystal). The 800 nm TPP_{MZ} energy was adjusted prior to the first lens with the waveplate/polarizer combination, allowing indirect adjustment of the 400 nm TPP_{MZ} pulse energy.

The SHG efficiency, defined as

$$\eta_{BBO} = U_{400}/U_{800} \tag{7.1}$$

where U_{800} is the energy of the input 800 nm pulse and U_{400} is the energy of the 400 nm output pulse, increases as the BBO thickness increases, but this increase in efficiency comes at a cost. The phase-matching bandwidth, i.e., the range of frequencies that can be converted by SHG, decreases with increasing crystal thickness. Furthermore, a thicker crystal introduces more chirp, increasing the pulse duration. The temporal characteristics of frequency-doubled pulses has previously been

studied both experimentally and theoretically [124, 125]. In Ref. [125] particularly, it was shown that for frequency-doubling from a 0.5 mm thick BBO crystal, the temporal profile of the 400 nm pulse is unchanged from the 800 nm input pulse so long for an input pulse maximum intensity between 7 and 150 GW/cm^2 (even for moderately-chirped pulses). A crystal with 0.5 mm thickness was used in this work; this crystal was sufficient to double the input, 800 nm pulses ($\eta_{BBO} \leq 0.1$) and was not expected (based on Ref. [125]) to have broadened the temporal profile of a 70 fs input pulse.

Once the 400 nm pulse was produced, the TPP pulse parameters (i.e., pulse duration, maximum intensity, τ) were estimated from FROG and Wizzler measurements of the 800 nm TPPs (assuming, as stated above, that the temporal profile of the 400 nm pulse was identical to the 800 nm pulse). After frequency doubling, the 800 nm component was filtered out using a pair of mirrors with a high reflectance (>99%) between 375 and 425 nm and a low reflectance (<2%) around 800 nm. Two reflections off of these mirrors reduces the 800 nm pulse energy to 4×10^{-4} times the initial energy.

7.2 Phase tagging procedure

For several of the "Electrons" experimental runs, the laser intensity was relatively low ($\simeq 10^{13}$ W/cm^2), and consequently very few electrons were produced (approximately ten electrons per 1000 laser pulses). Consequently, exposure times as long as 30 minutes per point were necessary. Over this time, τ tended to drift

due to motion of the MZ translation stage. This can be observed by monitoring the TPP spectrum during the course of the experiment. Recall that changing τ causes the period and phase of the fringes in $\tilde{I}_{TPP}(\omega)$ to change (see Fig. 3.8 for an example). The variation in the TPP spectrum over the course of a six-hour experiment is shown in Fig. 7.2. During this experiment, the translation stage was nominally held at a fixed position for the entire six hours. The spectrum was measured once per second. The shifting of the fringes (about 1.5 fringe periods) indicates that τ changed by ~ 4 fs over six hours, or 0.01 fs per minute. The expected QuI fringe period for xenon is $t_{opt}/8 = 0.37$ fs. The drift in the stage will sweep over one entire QuI fringe in 37 minutes, and it can be seen in Fig. 7.2 that the stage drift can be significantly faster at some times. It is desirable, therefore, to correct for this stage drift.

The way the drift was corrected was by post-sorting the data based on τ (or, equivalently, phase). During the experiment, an electron image (Sec. 7.3) and a TPP spectrum were collected simultaneously (one each per second). The spectrum was fit to Eq. 3.13, with all parameters other than $\Delta\phi$ fixed. Although τ also changes the fringe period, this change is negligible in this case and is therefore ignored in the fit (the fringe spacing is 14.5 nm when $\tau = 150$ fs and 14.1 nm when $\tau = 154$ fs, see Appendix B for more details). One of these fits is shown in Fig. 7.3. The recovered phase is shown as a function of image number (20,700 images in total) in Fig. 7.4. One finds that $\Delta\phi$ changed by about 3π over the course of the experiment, in line with the previous observation that the change in τ was ~ 1.5 optical periods. This 3π range was then divided up into 60 bins, with a uniform bin width of $\pi/20$

radians. The spectra were sorted by phase into these bins. Because one electron image was collected for each spectrum measurement, these images could be tagged by their phase and sorted into bins. In this way, a composite electron image was built for each bin, containing only electrons that came from TPPs with the same $\Delta\phi$ (within a range of $\pi/20$ rad).

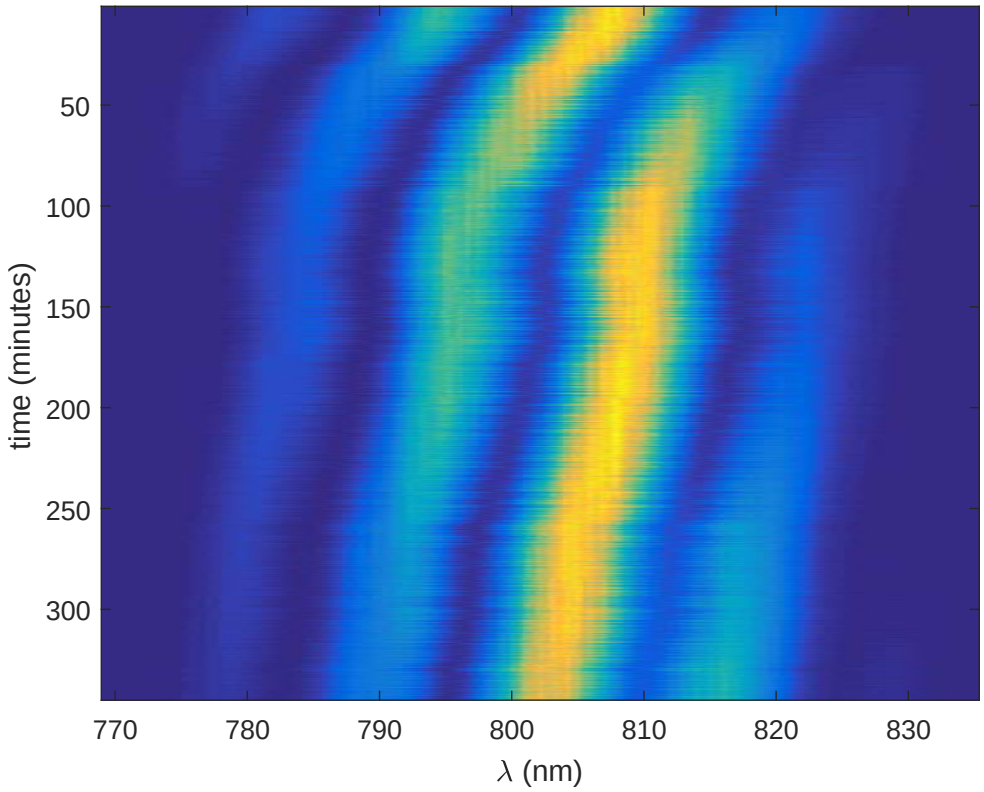

Fig. 7.2: Normalized TPP spectrum (color map, blue is minimum and yellow is maximum) as a function of λ and time. The spectral data were collected once per second, and each spectrum measurement matched with a single, 1-second electron image (see Sec. 7.3). The wavelength spacing between fringes in this figure is $\Delta\lambda \simeq 11.9$ nm.

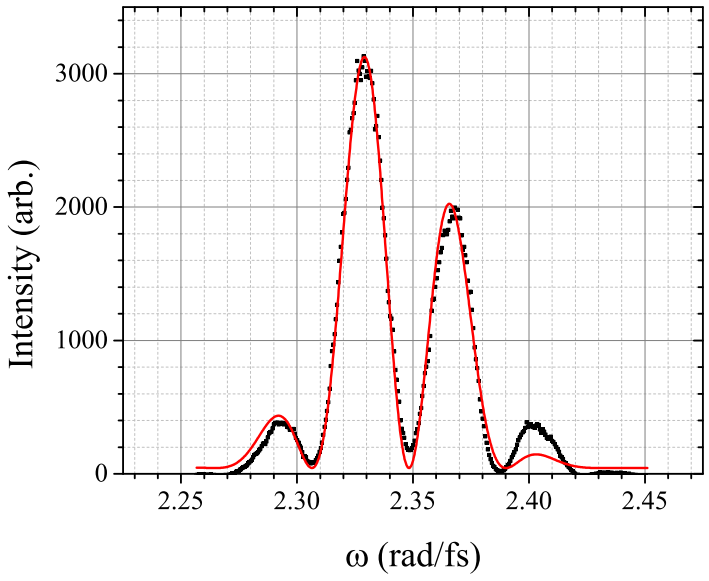

Fig. 7.3: A fit of an example TPP spectrum to Eq. 3.13, with the following parameters fixed: $\omega_0 = 2.34$ rad/fs ($\lambda_0 = 806nm$), $\Delta\omega = 0.035$ rad/fs, $\tau = 150.2$ fs. The result of the fit finds $\Delta\phi = 0.74(1)\pi$ rad.

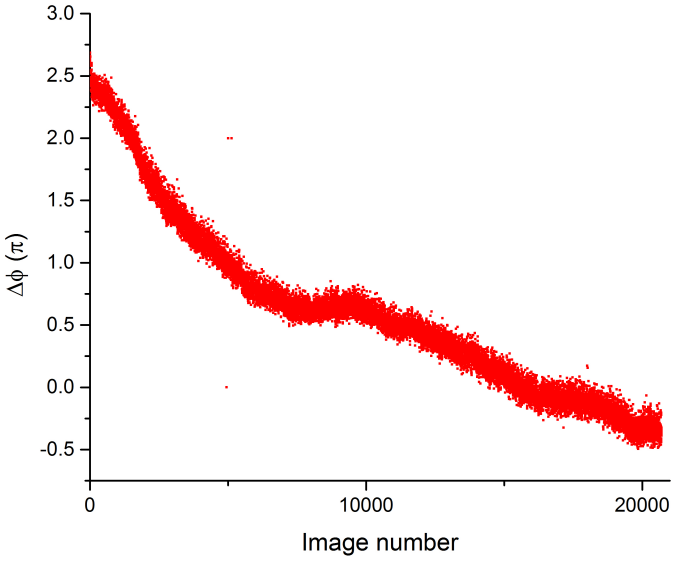

Fig. 7.4: Fit value of $\Delta\phi$ vs image number for the spectra shown in Fig. 7.2.

7.3 Velocity map imager

Detection of electron energies was accomplished with a VMI. In a VMI, the position of electrons on a two-dimensional detector is measured, which gives information on the electron velocity (and consequently energy). A charged particle imagers was initially developed by Chandler and coworkers [126] to detect molecular ions from photodissociation. Helm and coworkers [127] constructed a similar device to detect photoelectrons. Eppink and coworkers [128] improved the design of these detectors with an electrostatic lens to improve the energy resolution. The VMI used in this work is similar to that discussed in Ref. [127], and is shown schematically in Fig. 7.5. A complete description of the VMI used in this work is given in Ref. [129]. In Sec. 7.3.1, an qualitative description of the VMI will be given. The trajectory of electrons in the VMI will be calculated in Sec. 7.3.2.

7.3.1 General description

The VMI is located inside a vacuum chamber, filled to an operating pressure (typically 10^{-6} Torr) of a target gas. The TPPs enter the vacuum chamber through a window and are focused by a spherical mirror (the same setup as described in Sec. 3.4. The coordinate axes are defined as follows: the x-axis is the laser propagation direction ($\mathbf{k} \propto \hat{\mathbf{x}}$). The laser is polarized along the z-axis, ($\mathbf{E}_{TPP} \propto \hat{\mathbf{z}}$). The y-axis is perpendicular to these two, and forms a line between the laser-matter interaction region (the position of the laser focus, the origin in Fig. 7.5) and the center of the MCP detector.

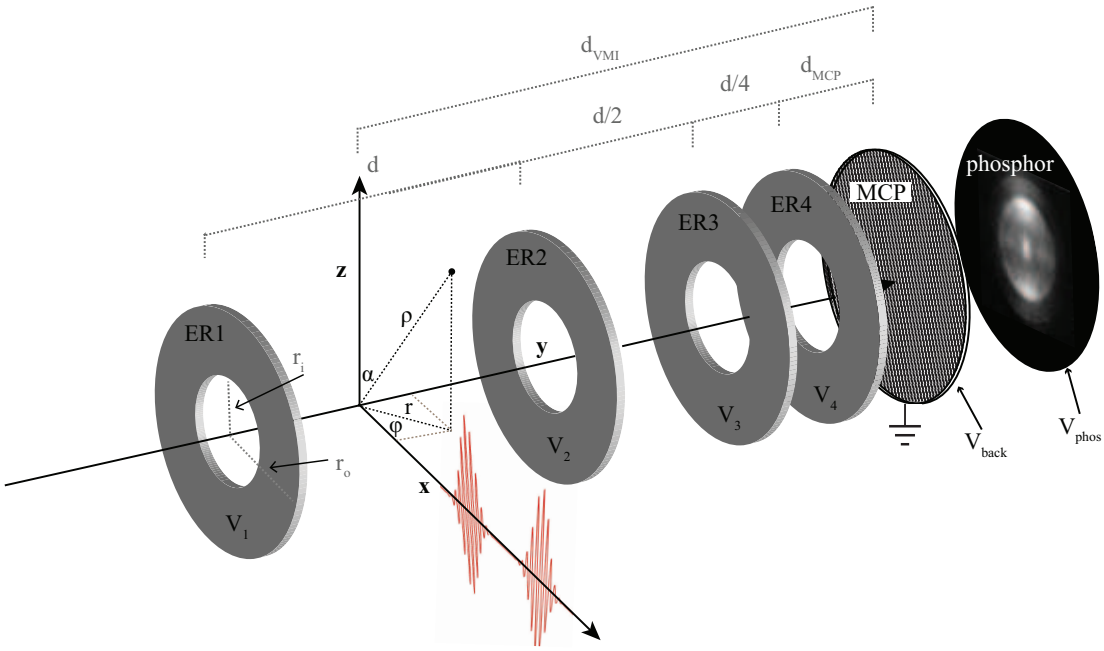

Fig. 7.5: A schematic of the velocity map imager (VMI) used in this work (not to scale). The voltages on each electrostatic ring (ER) were variable, but obeyed the relation $V_1 = 2V_2 = 4V_3 = 8V_4$. Typical values for the microchannel plate (MCP) and phosphor voltages were $V_{back} = 2000$ V and $V_{phos} = 4200$ V, respectively. The distances were $d = 38.1$ mm, $d_{MCP} = 9.7$ mm, $r_o = 62.7$ mm, and $r_i = 20.5$ mm. The MCP and phosphor (one assembly) had a quality diameter of 40 mm. Standard cylindrical and spherical coordinates are used in this chapter and Chap. 8, with the definitions of the angles given here.

A series of electrostatic rings (ERs) provide an approximately-uniform electric field in the VMI (in the $\pm\hat{\mathbf{y}}$ direction). The distances between ER j and $j+1$ is $d/2^{j-1}$, where $j = 1, 2, 3$ and $d = 38.1(3)$mm (1.5 inches). The distance between ER4 and the MCP is $d_{MCP} = 9.7(3)$ mm. The total distance between the interaction region and the MCP is $d_{VMI} = 1.25d + d_{MCP}$. The voltages applied to the ERs vary based on the experiment, but the relative voltages always obey the relation $V_{j+1} = V_j/2^j$ for $j = 1, 2, 3$. If the ERs are approximated as infinite sheets, this leads to a uniform electric field inside the VMI of $\boldsymbol{\mathcal{E}}_{VMI} = V_1/(2d)\hat{\mathbf{y}}$, $\mathcal{E}_{VMI} \equiv |\boldsymbol{\mathcal{E}}_{VMI}|$. In order for an electron to travel towards the MCP (a force in the $+\hat{\mathbf{y}}$ direction), the voltages applied to the grids must be negative.

The ERs were not infinite sheets, so edging and other effects lead to a nonuniform electric field. The electric field was calculated, using the true dimensions of the ERs, with the ion trajectory modeling program SIMION [130]. The y component of the electric field, $\boldsymbol{\mathcal{E}}_{VMI} \cdot \hat{\mathbf{y}}$, vs y for $V_1 = -2000$ V, $V_2 = -1000$ V, $V_3 = -500$ V, and $V_4 = -250$ V is shown in Fig. 7.6 (blue curve). The simulated electric field is always less than the "infinite-sheet" electric field for this setup, 26.2 V/mm.

SIMION can also be used to iteratively optimize the ER voltages for a uniform electric field. A SIMION optimization was run to minimize the electric field deviation from 24 V/mm. The optimization succeeded in reducing the field fluctuations, as can be seen in Fig. 7.6 (red curve), and recovered the following ER voltages: $V_1 = -2111.8$ V, $V_2 = -1133.2$ V, $V_3 = -569.9$ V, and $V_4 = -270.8$ V.

The electron signal is amplified by an MCP, which is grounded on the front surface and at a potential $V_{back} \simeq +2000$ V on the back surface. The gain of the

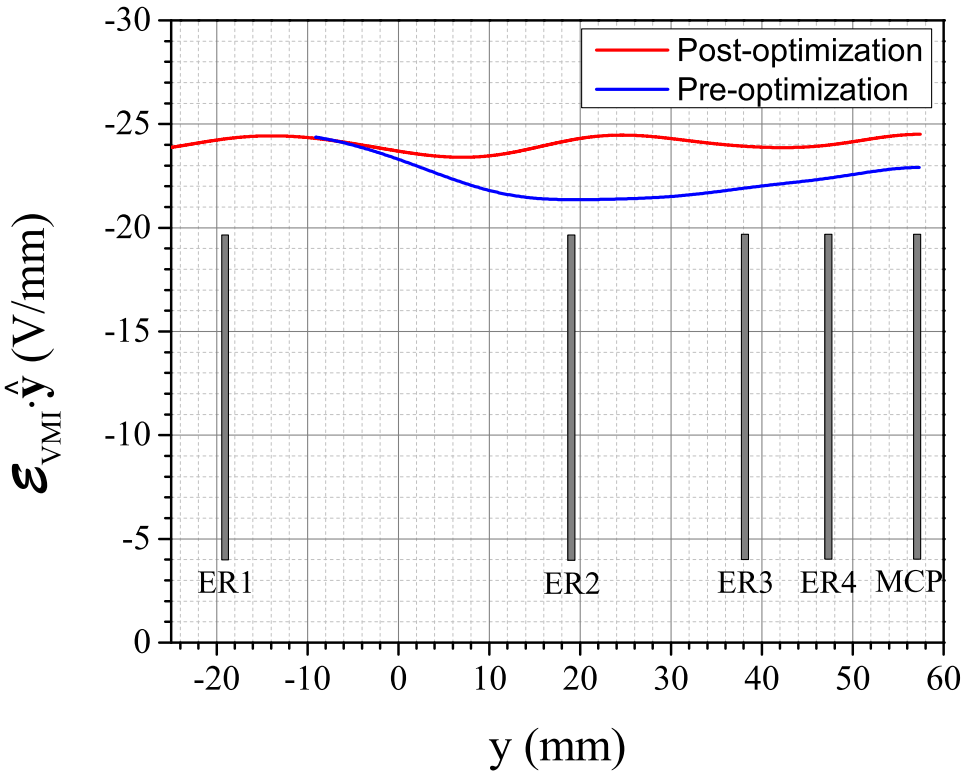

Fig. 7.6: SIMION-simulated electric field in the y direction (electron travel direction, see Fig. 7.5) vs y, for two sets of electrostatic ring voltages: before optimization (blue, $V_1 = -2000$ V, $V_2 = -1000$ V, $V_3 = -500$ V, and $V_4 = -250$ V), and after optimization (red, $V_1 = -2111.8$ V, $V_2 = -1133.2$ V, $V_3 = -569.9$ V, and $V_4 = -270.8$ V). The interaction region is at $y = 0$. The locations of the electrostatic rings and the microchannel plate are included for reference.

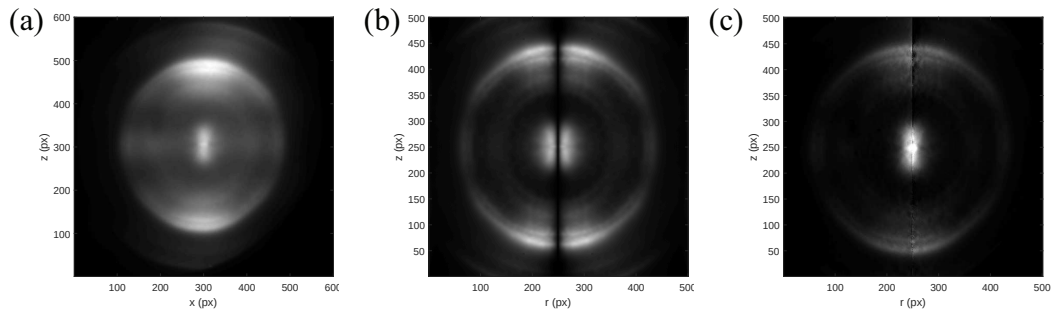

Fig. 7.7: (a) Example electron image from ionization of xenon atoms, collected over 60,000 laser shots and using a 400 nm, near-TL pulse, with an intensity of $3.4(3)\times10^{14}$ W/cm^2. (b) Abel inversion of (a), using the BASEX inversion algorithm implemented by a home-built MATLAB code (see Appendix D). (c) Abel inversion of (a), using the BASEX inversion algorithm implemented by the PyAbel project [131].

MCP is approximately 10^7 at a bias voltage of 2400 V. The amplified signal then proceeds to a phosphor screen (phosphor type P20), which converts the electric signal into light. This light is detected by means of a CCD camera (Andor Apogee Alta U47+). An example image collected over 60,000 laser shots, from a near-TL pulse (not a TPP) with an intensity of $3.4(3)\times10^{14}$ W/cm^2, is shown in Fig. 7.7(a).

7.3.2 Electron trajectory in VMI

The trajectory of an electron in the VMI can be calculated using kinematics. In addition to Cartesian coordinates, standard cylindrical and spherical coordinate systems are used, i.e., $r^2 = x^2+y^2$, azimuthal angle $\tan(\varphi) = y/x$, $\rho^2 = x^2+y^2+z^2 = r^2+z^2$, and polar angle $\tan(\alpha) = r/z$. For the polar angle, α is used instead of the more common θ to distinguish this angle from the pulse CEP (as in Eq. 2.4). Cylindrical coordinates will not be referred to here, but will be used in Sec. 7.4. It

is assumed that the electron is created at the origin with an initial velocity,

$$\begin{aligned}\mathbf{v}_0 &= v_0 \sin\alpha\cos\varphi\hat{\mathbf{x}} + v_0 \sin\alpha\sin\varphi\hat{\mathbf{y}} + v_0\cos\alpha\hat{\mathbf{z}} \\ &\equiv v_{0x}\hat{\mathbf{x}} + v_{0y}\hat{\mathbf{y}} + v_{0z}\hat{\mathbf{z}},\end{aligned} \tag{7.2}$$

where

$$v_0 = \sqrt{\frac{2U_0}{m_e}} \tag{7.3}$$

is the magnitude of the initial velocity, U_0 is the initial electron energy, and m_e is the electron mass. The electrons experience a force due to the static field, $\mathbf{F} = -e\boldsymbol{\mathcal{E}}_{VMI}$, where e is the elementary charge. The time it takes to travel from the interaction region to the MCP detector t_{VMI} is found from the kinematic equation

$$d_{VMI} = -\frac{e\mathcal{E}_{VMI}}{2m_e}t_{VMI}^2 + v_{0y}t_{VMI}, \tag{7.4}$$

which has the solution

$$t_{VMI} = -\frac{m_e}{e\mathcal{E}_{VMI}}\left[\sqrt{v_{0y}^2 - \frac{2e\mathcal{E}_{VMI}d_{VMI}}{m_e}} - v_{0y}\right]. \tag{7.5}$$

Because the electric field in the $\hat{\mathbf{x}}$ and $\hat{\mathbf{z}}$ directions is assumed to be 0, the distance that the electron travels in these directions is given by

$$x\left(t_{VMI}\right) = v_{0x}t_{VMI} \text{ and } z\left(t_{VMI}\right) = v_{0z}t_{VMI}. \tag{7.6}$$

A few specific examples, corresponding to electrons with different ejection angles, will be considered here. The first example is the case in which the electron is

ejected in the $\hat{\mathbf{z}}$-direction, $\alpha = 0$. In this case, $v_{0y} = 0$, and by combining Eqs. 7.3, 7.5, and 7.6, one finds that

$$z\left(t_{VMI}\right) = 2\sqrt{\frac{U_0 d_{VMI}}{-e\mathcal{E}_{VMI}}}, \tag{7.7}$$

which shows that the position the electron lands on the MCP goes as $\sqrt{U_0}$. For electrons ejected at an arbitrary angle, $U_0 \propto \rho^2$ to lowest order.

The second example considers two electrons (labeled 1 and 2) ejected at 45 degrees off of the z-axis, one in the $+\hat{\mathbf{y}}$ direction and the other in the $-\hat{\mathbf{y}}$ direction: $\varphi_1 = \pi/2$ rad, $\alpha_1 = \pi/4$ rad; and $\varphi_2 = 3\pi/2$ rad, $\alpha_2 = \pi/4$ rad. Both electrons have the same initial energy U_0. In this case, Eq. 7.2 gives

$$\mathbf{v}_{0,1} = \sqrt{\frac{U_0}{m_e}}(\hat{\mathbf{y}} + \hat{\mathbf{z}}) \text{ and } \mathbf{v}_{0,2} = \sqrt{\frac{U_0}{m_e}}(-\hat{\mathbf{y}} + \hat{\mathbf{z}}). \tag{7.8}$$

The two electrons have the same energy and the same initial velocity in the $\hat{\mathbf{z}}$ direction; consequently, one would like for these two electrons to hit the detector at the same z. However, the increased flight time of the backwards-ejected electron (electron 2) means that its final z position will be larger than the forwards-ejected electron (electron 1). The purpose of this example is to determine how large this difference is. As such, values of initial energy ($U_0 = 10$ eV) and voltage ($V_1 = -500$ V) were chosen to maximize this difference under accessible experimental conditions. Most electrons in this work have energy < 10 eV and no grid potential lower (less negative) than $V_1 = -500$ V was used. The flight time is calculated from Eq. 7.5,

$$t_{VMI,j} = -\frac{m_e}{e\mathcal{E}_{VMI}}\left[\sqrt{\frac{U_0 - 2e\mathcal{E}_{VMI}d_{VMI}}{m_e}} + (-1)^j\sqrt{\frac{U_0}{m_e}}\right], \tag{7.9}$$

for $j = 1, 2$. The z position of the particles on the detector is then calculated from Eq. 7.6. The difference of z position is

$$\Delta z = z(t_{VMI,2}) - z(t_{VMI,1}) = -\frac{2U_0}{e\mathcal{E}_{VMI}} = -\frac{4U_0 d}{eV_1}. \tag{7.10}$$

For the choices $U_0 = 10$ eV and $V_1 = -500$ V, $z(t_{VMI,1}) = 11.8$ mm, $z(t_{VMI,1}) = 14.8$ mm, and $\Delta z = 3.0$ mm. The diameter of the phosphor screen is 40 mm, so this represents a significant deviation. To illustrate this, consider a third electron (electron 3), ejected at the same angle as electron 1, but with a different initial energy. In order for electron 3 to land at the same final z position as electron 2, the initial energy of electron 3 must be 17 eV.

Most electrons measured in the following studies are less than 10 eV, but even for a 1 eV electron (a typical electron energy for a threshold ionization), the Eq. 7.10 gives a 0.3 mm discrepancy in final position. An electron 3 as described above would need an additional 0.16 eV of energy to account for this discrepancy.

7.4 Image analysis

In this section, the method for determining a (potentially angle-resolved) electron energy distribution from a VMI image such as that shown in Fig. 7.7(a) is described. Sec. 7.4.1 describes the Abel inversion method implemented in this work, and Sec. 7.4.2 describes how the spatial distribution of the electrons is converted to

an energy distribution.

7.4.1 *Abel inversion*

To lowest order, $U_0 \propto \rho^2$. This assumes the electrons were all created in exactly the same location and in the presence of zero applied field. The real size of the laser focus (Rayleigh length $z_R \simeq 100\mu$m) and the presence of the applied field will cause deviations from this lowest-order solution. Regardless, one would like to determine the full three-dimensional distribution of electrons at the detector $Y(x, y, z)$. What is measured on the detector is only a projection of $Y(x, y, z)$ onto the xz plane. It was shown by Niels Abel that the full three-dimensional solution is recoverable if it obeys cylindrical symmetry [1], i.e., $Y(x, y, z) = Y(r, z)$ [132]. In this case, $Y(r, z)$ and its xz projection $P(x, z)$ are related by the Abel integral,

$$P(x,z) = 2\int_{|x|}^{\infty} \frac{rY(r,z)}{\sqrt{r^2 - x^2}} dr, \tag{7.11}$$

from which a determination of $Y(r, z)$ can be made by computing the inverse Abel transform,

$$Y(r,z) = -\frac{1}{\pi}\int_{r}^{\infty} \frac{1}{\sqrt{x^2 - r^2}} \frac{dP(x,z)}{dx} dx. \tag{7.12}$$

This integro-differential equation is difficult to use directly because it has singularities. Also, when applied to an experimental measurement, the noise in the data is amplified by the numerical differentiation. Several methods of Abel inversion have

[1] It is important to note that this is not strictly true in the VMI experiments, as was demonstrated in the second example of Sec. 7.3.2.

been proposed [133–135]; the most commonly-used method (and the method used in this work) is the basis-set expansion (BASEX) method developed by Dribinski and coworkers [136]. The BASEX method represents $Y(r,z)$ as an expansion of a set of K basis functions $f_k(r,z)$:

$$Y(r,z) = \sum_{k=0}^{K-1} \mathbf{C}_k f_k(r,z). \tag{7.13}$$

Finding $Y(r,z)$ is equivalent in this construction to finding the coefficient matrix $\mathbf{C}$. It is shown in Ref. [136] that $\mathbf{C}$ can be calculated for a suitable choice of basis functions (namely, for any set of basis functions which are all analytically integrable). Implementation of BASEX Abel inversion was accomplished via a home-built MATLAB code, and was compared to an open-source code available in Python (the PyAbel project, see Ref. [131]). The MATLAB code used in the inversion is shown in Appendix D. Figure 7.7(b) and (c) show the BASEX Abel inversion results $Y(r,z)$ for both the MATLAB and PyAbel inversion implementations, respectively. Both implementations have distortions along the z axis. These distortions are inherent to the BASEX method and are acknowledged in Ref. [136]. Because the PyAbel inversion implementation gives a smaller z-axis distortions than the home-built MATLAB code, it was used to invert the experimental data.

7.4.2 Finding angle-resolved energy distributions from Abel-inverted images

From $Y(r,z)$, the energy distribution can be found – recall that $U \propto \rho^2 = r^2 + z^2$. First, the position distribution in spherical coordinates was found by transforming from r, z to ρ, α. For a general distribution of two variables x and y, called

$g(x, y)$ a transformation to new variables u and v and distribution $h(u, v)$ is given by

$$h(u, v) = g[x(u, v), y(u, v)]|J|, \tag{7.14}$$

where

$$J = \begin{vmatrix} \frac{\partial x}{\partial u} & \frac{\partial x}{\partial v} \\ \frac{\partial y}{\partial u} & \frac{\partial y}{\partial v} \end{vmatrix} \tag{7.15}$$

is the Jacobian [137]. For transformation from cylindrical coordinates to spherical coordinates, $|J| = \rho$.

Once $Y(\rho, \alpha)$ has been found, conversion to an angle-resolved energy distribution $Y(U, \alpha)$ can be done by reapplying Eq. 7.14. In this case, $|J| \propto \sqrt{U}$. Figure 7.8 shows $Y(\rho, \alpha)$ and $Y(U, \alpha)$ that are found from the $Y(r, z)$ shown in Fig. 7.7(c). The conversion from ρ to energy in this figure set the energy of the first above-threshold ionization (ATI) peak (the largest feature at $\rho = 192$ pixels) to 3.1 eV (the energy of one 400 nm photon). A weak second ATI peak is observed at ~ 6.2 eV as expected. In images where multiple ATI peaks are visible, conversion from ρ to energy was accomplished by setting the energy between the first and second ATI peaks to be the photon energy (either 1.55 eV for 800 nm photons or 3.10 eV for 400 nm photons).

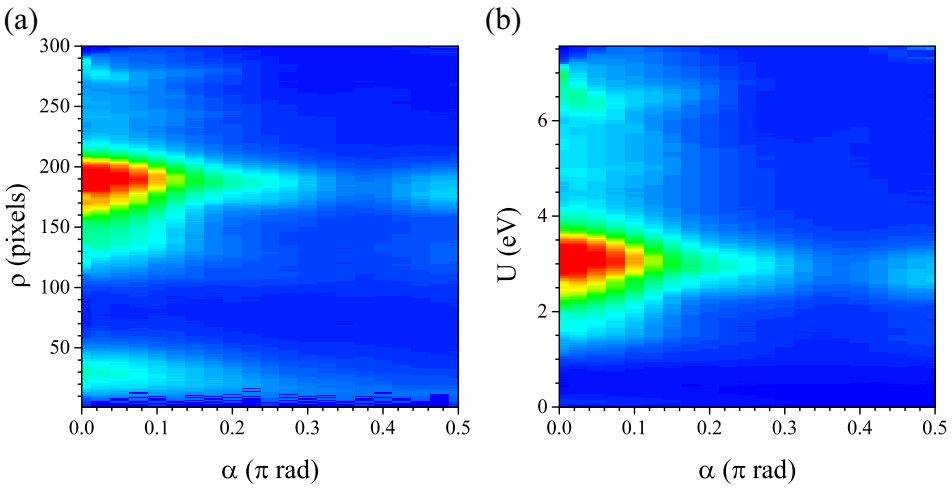

Fig. 7.8: (a) $Y(\rho, \alpha)$, calculated from the Abel-inverted $Y(r, z)$ shown in Fig. 7.7(c). (b) $Y(U, \alpha)$ for the same Abel-inverted image.

Chapter 8: Experiment 2, "Electrons": Results and Discussion

In this chapter, the results of several "Electrons" experiments are presented and discussed. These experiments were primarily concerned with answering the second question stated in Sec. 1.3: can quantum interference be observed in strong-field ionization from a TPP? A representative collection of experiments were performed in which selected experimental parameters were varied. These include the laser intensity, laser wavelength (800 nm or 400 nm), and target gas (xenon or CO_2). In each experiment, the photoelectron energy distribution was measured as a function of τ, using a TPP_{MZ}. The parameters of each experiment presented in this chapter are given in Tab. 8.1.

Section 8.1 presents results of "Electrons" experiments conducted at the low intensities, $\sim 5 \times 10^{13}$ W/cm^2. The results of "Electrons" experiments at higher intensities ($\sim 3 \times 10^{14}$ W/cm^2) are shown for 800 nm TPPs in Sec. 8.2 and for 400 nm TPPs in Sec. 8.3.

Tab. 8.1: Parameters of the "Electrons" experiments discussed in this chapter. [a]Low-intensity experiments were performed at the lowest intensity at which electrons could be detected, corresponding to ~ 0.01 detected electrons per laser shot. High-intensity experiments were performed at intensities comparable to the "Ions" experiments of Chap. 4. [b]Nominal value. [c]Indicates whether the phase-tagging procedure described in Sec. 7.2 was used to determine $\Delta\phi$ for the experiment. If the phase-tagging procedure was used, the electron yield was found across only one optical period, and plotted as a function of $\Delta\phi$. If not, the electron yield was measured across multiple optical periods, and the yield was plotted as a function of τ. [d]Nominal intensity, calculated from Eq. 3.9. [e]Ponderomotive energy, Eq. 2.2 using the larger of the fixed/variable arm intensities. [f]Keldysh parameter, Eq. 2.1.

Section	Figures	Intensity range[a]	λ_0 (nm)	Target	τ (fs)[b]	Phase tagging[c]	Fixed arm intensity (W/cm^2)[d]	Variable arm intensity (W/cm^2)[d]	U_p (eV)[e]	γ[f]
8.1.1	8.1, 8.2, 8.3	Low	400	Xe	150	Yes	5×10^{13}	7×10^{13}	1.0	2.4
8.1.2	8.4, 8.5, 8.6	Low	400	CO_2	200	Yes	3×10^{13}	4×10^{13}	0.6	3.4
8.2.1	8.7(a), 8.8(a)	High	800	Xe	70 - 78	No	1.8×10^{14}	1.9×10^{14}	11.4	0.7
8.2.2	8.7(b), 8.8(b), 8.9	High	800	CO_2	250	Yes	1.3×10^{14}	1.5×10^{14}	9.0	0.9
8.3.1	8.10(a), 8.11(a)	High	400	Xe	75 - 85	No	3.3×10^{14}	3.1×10^{14}	4.9	1.1
8.3.2	8.10(b), 8.11(b), 8.13	High	400	CO_2	200	Yes	1.7×10^{14}	1.9×10^{14}	2.8	1.6

8.1 Low-intensity experiments

8.1.1 Xenon

Results

Figures 8.1, 8.2, and 8.3 show the results of the low-intensity "Electrons" experiment in xenon. The gas pressure in the vacuum chamber was $1.0(1) \times 10^{-6}$ Torr. The TPP was produced with the MZ at 800 nm with $\tau \simeq 150$ fs, and converted to 400 nm via SHG. The nominal intensities of each pulse of the 400 nm TPP were 5×10^{13} and 7×10^{13} W/cm^2, for the fixed and variable arms of the MZ, respectively. These intensities correspond to ponderomotive energies of 0.7 and 1.0 eV. Electrons were measured in the VMI using the following voltages: $V_1 = -500$ V, $V_{back} = 2020$ V, $V_{phos} = 4000$ V (see Sec. 7.3 for a description of these voltages). The experiment consisted of 22,500 one-second exposures that were sorted by $\Delta\phi$ into bins of width $\pi/20$ rad using the phase tagging procedure (Sec. 7.2).

An example Abel-inverted electron image from one of the phase bins is shown in Fig. 8.1. The intensity was low enough that only threshold electrons produced from multiphoton ionization appeared. A 400 nm photon has an energy of 3.1 eV; the ionization potential of xenon, 12.13 eV, means that four photons were required to ionize and that ejected photoelectrons had a average energy of 0.27 eV. The maximum point of the electron energy distribution was set to be 0.27 eV; the corresponding radius $\rho = 41$ pixels is marked on Fig. 8.1 as a red dot (at $z = 41$ pixels, $r = 0$ pixels). This treatment ignores the possible added ponderomotive energy.

The photoelectron yield as a function of energy and $\Delta\phi$ is shown in Fig. 8.2(a). Recall that the $\Delta\phi$ recovered from phase tagging is for the 800 nm TPP, i.e. $\omega_0 \simeq 2.35$ rad/fs in Eq. 2.4. The 400 nm TPP oscillates twice as fast, so this experiment (and all subsequent experiments) ran over a range of 4π rad for the 400 nm TPP. The single energy electron yield at 0.27 eV is shown in Fig. 8.2(b), found from a lineout of Fig. 8.2(a) (the black horizontal line in the figure). The Fourier transform of (b) is shown in (c).

It is important to note that when the phase tagging procedure of Sec. 7.2 is employed, not every composite image is made from the same number of exposures in general. The yields were all normalized to a one-second exposure, but if some of the images were generated from a particularly small number of exposures, poor statistics could distort the results presented above. The nominal minimum electron detection rate in this experiment was 0.01 electrons per laser shot (10 electrons per one-second exposure). The total exposure time vs $\Delta\phi$ for this experiment is shown in Fig. 8.3. Higher exposure times correspond to lower statistical uncertainties. One finds that all but one point had exposure times of more than 200 seconds (200,000 laser shots, at least 2000 electrons detected). Therefore, the exposure times were all long enough to achieve statistically-significant results, but this was not true for all of the "Electrons" experiments which used phase tagging.

Discussion

The electron yield variations seen in Fig. 8.2 are dominated by an oscillation at the 800 nm optical period; the yield is maximum at $\Delta\phi = 0$ and $\Delta\phi = 2\pi$ rad and

is lower between these two maxima. While at first glance it might be surprising that the oscillation is at the 800 nm optical period when the ionizing TPP has $\lambda_0 = 400$ nm, this is expected due to how the 400 nm TPP was generated. The TPP is first made at 800 nm and then converted to 400 nm via SHG; therefore, OI at 800 nm is responsible for changing the maximum intensity of the TPP. We the TPPs made directly from a 400 nm input pulse, the OI would reflect the 400 nm optical period. Such an approach has not yet been implemented.

There is a small increase in the electron yield at $\Delta\phi \simeq 1.15\pi$ rad, which is most likely due to the satellite peak, for the same reasons as discussed in Sec. 4.3.2. The single energy, 0.27 eV yield shown in Fig. 8.2(b) shows the oscillations at both the optical frequency and twice the optical frequency, but no higher-frequency oscillations are visible. The results of this experiment show no evidence of QuI; the modulations are consistent with OI alone.

Also of some interest is the apparent energy shift of the threshold electrons, depending on the relative phase at which they were ionized. The electron yield peak near $\Delta\phi = 1.15\pi$ rad occurs at a slightly higher energy than the electron peaks at $\Delta\phi = 0$ and 2π rad. The TPP intensity which causes the ionization at $\Delta\phi = 1.15\pi$ rad is lower than the intensity at 0 or 2π rad. Intensity-dependent shifts in the photoelectron energy due to the ac Stark effect are well-documented in the literature, see Refs. [116, 138, 139] for example.

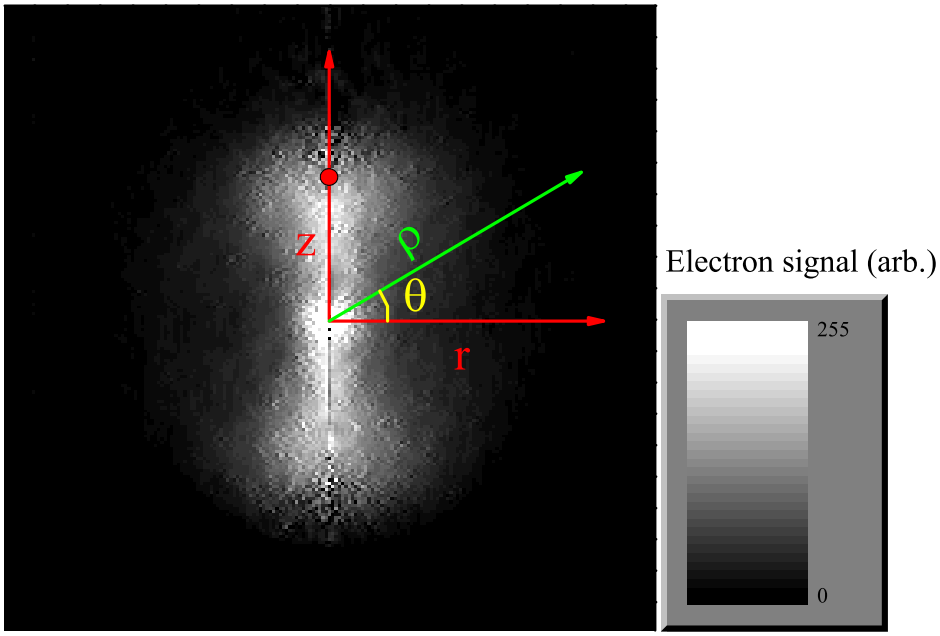

Fig. 8.1: Example Abel-inverted photoelectron image from the low-intensity "Electrons" experiment in xenon. The Abel inverted image gives the photoelectron yield (grayscale) as a function of r and z, both measured in pixels. The total image size is 200x200 pixels.

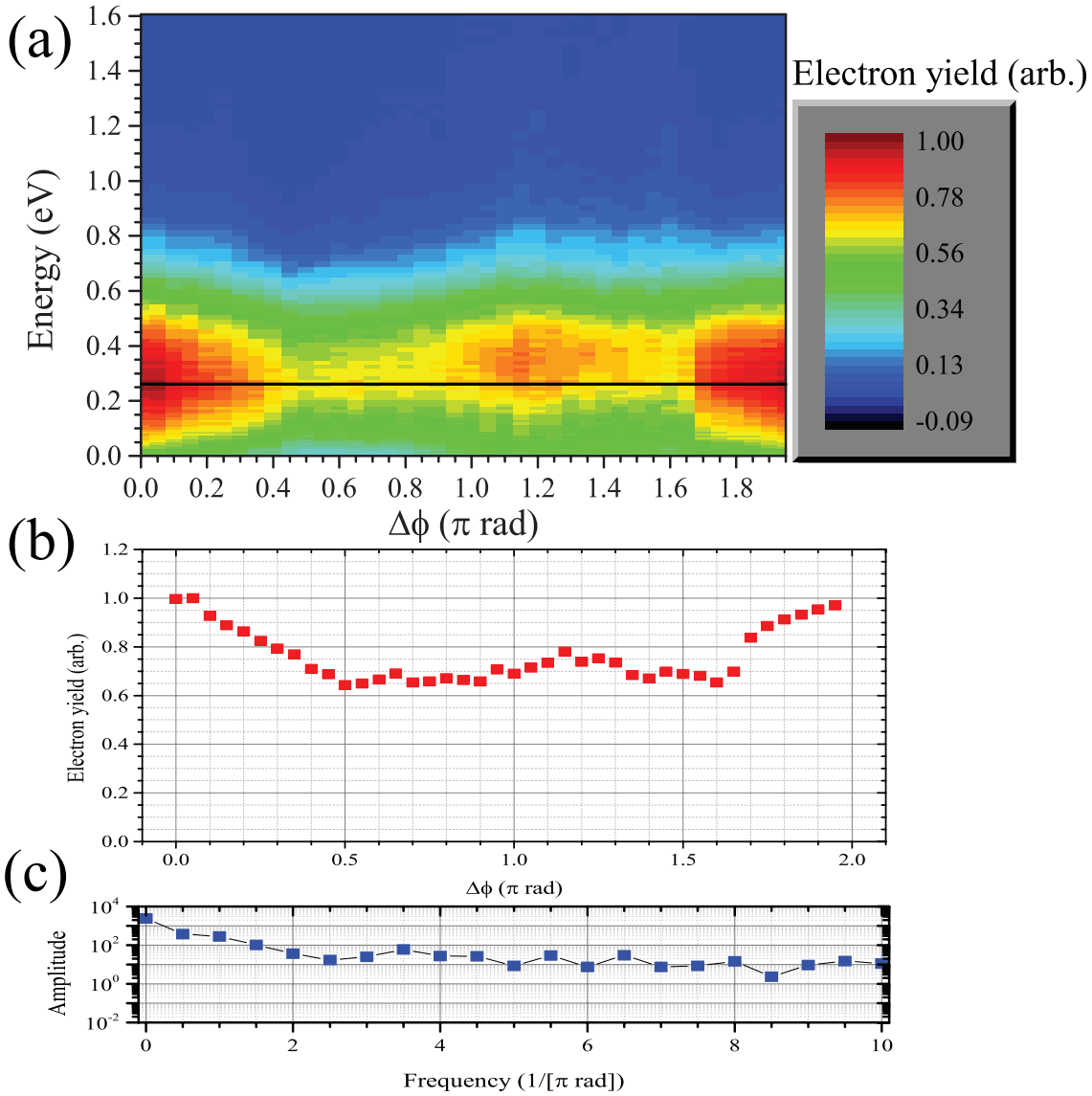

Fig. 8.2: (a) Normalized electron yield (colormap) vs electron energy and $\Delta\phi$, for the low-intensity "Electrons" experiment in xenon, at $\tau \simeq 150$ fs. (b) Yield of 0.27 eV electrons vs $\Delta\phi$ for the same experiment, found from a lineout of (a) at 0.27 eV (indicated by the black horizontal line in (a)). (c) Fourier transform of (b).

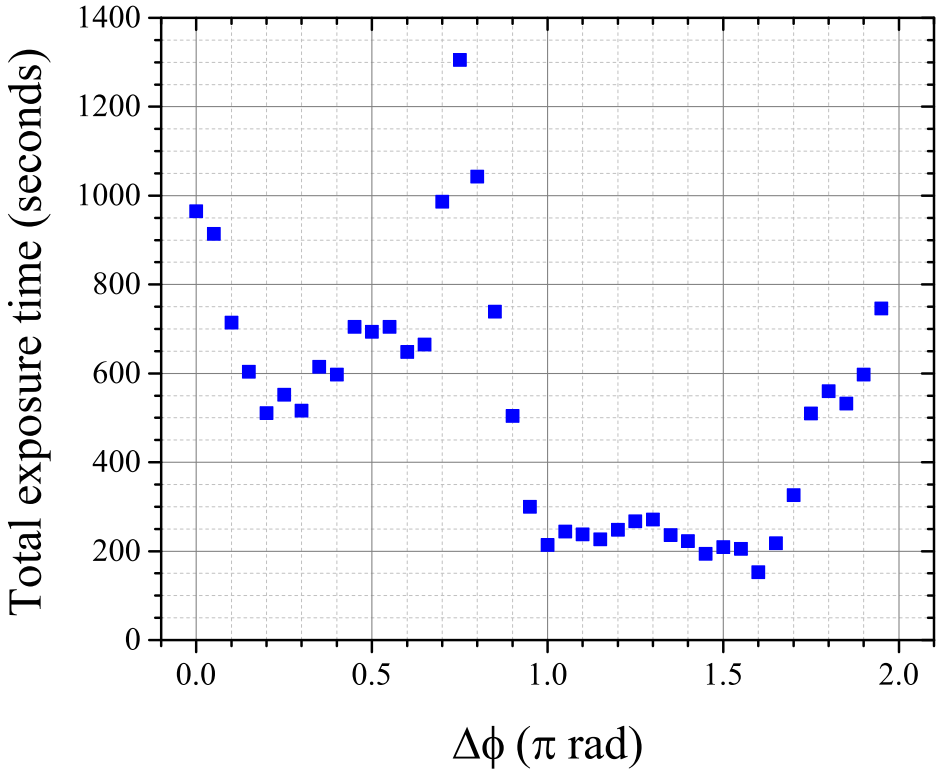

Fig. 8.3: Total exposure time in the composite electron image vs $\Delta\phi$ for the experiment shown in Fig. 8.2. The total number of laser shots contributing to each image is 1000 times the exposure time in seconds.

8.1.2 CO_2

Results

In addition to xenon, a low-intensity "Electrons" experiment was performed in CO_2. In this experiment, the gas pressure in the vacuum chamber was $1.0(1) \times 10^{-6}$ Torr. The TPP was produced with the MZ at 800 nm with $\tau \simeq 200$ fs, and then converted to 400 nm via SHG. The nominal intensities of the single-arms of the 400 nm TPP were 3×10^{13} and 4×10^{13} W/cm^2, for the fixed and variable arms of the MZ, respectively. These intensities correspond to ponderomotive energies of 0.5 and 0.6 eV. Electrons were collected with the VMI using the following voltages: $V_1 = -1050$ V, $V_{back} = 2020$ V, $V_{phos} = 4200$ V. The experiment consisted of 24,000 one-second exposures that were sorted by $\Delta\phi$ into bins of width $\pi/20$ rad using the phase tagging procedure (Sec. 7.2). An example Abel-inverted electron image of one of the phase bins is shown in Fig. 8.4.

The photoelectron spectra vs $\Delta\phi$ are shown in Fig. 8.5(a). The ionization potential of CO_2 is 13.77 eV, meaning five photons at 400 nm (3.1 eV per photon) were required to ionize. The excess electron energy after ionization was 1.73 eV in this case, ignoring the ponderomotive energy as before. The peak of the electron energy distribution in Fig. 8.5(a) was set to be 1.73 eV. Fig. 8.5(b) is the single-energy electron yield vs $\Delta\phi$ found from a lineout of (a) at 1.73 eV. The Fourier transform of Fig. 8.5(b) is shown in Fig. 8.5(c).

Figure 8.6 shows the total exposure time vs $\Delta\phi$ for this experiment. In contrast to the xenon experiment (Fig. 8.3), there are several values of $\Delta\phi$ for which the total

exposure time was less than 100 seconds (100,000 laser shots). In particular, the composite image at $\Delta\phi = 0$ consists of only 27 seconds of exposure, 27,000 laser shots or only about 300 electrons. The image at $\Delta\phi = 0.05\pi$ rad was from a 91 second exposure. These two points are have a surprising high yield which can be observed in Fig. 8.5(a) and (b), but this is probably due to poor statistics from a short exposure time. Other noisy points (like, for example, 1.2π and 0.45π rad) can also be explained in the same way.

Discussion

As with the xenon experiment, the phase-dependent electron yield shows a dominant oscillation at the 800 nm optical frequency, but no higher-frequency oscillations due to QuI are visible. The results are consistent with OI alone. In this experiment, the frequency-doubling effect is not visible. While the input pulse still had a subordinate peak, the large TPP delay, 200 fs, likely means that frequency doubling does not occur (consult the "Ions" experiments, e.g., Fig. 4.11(a) at $\tau = 200$ fs to confirm this).

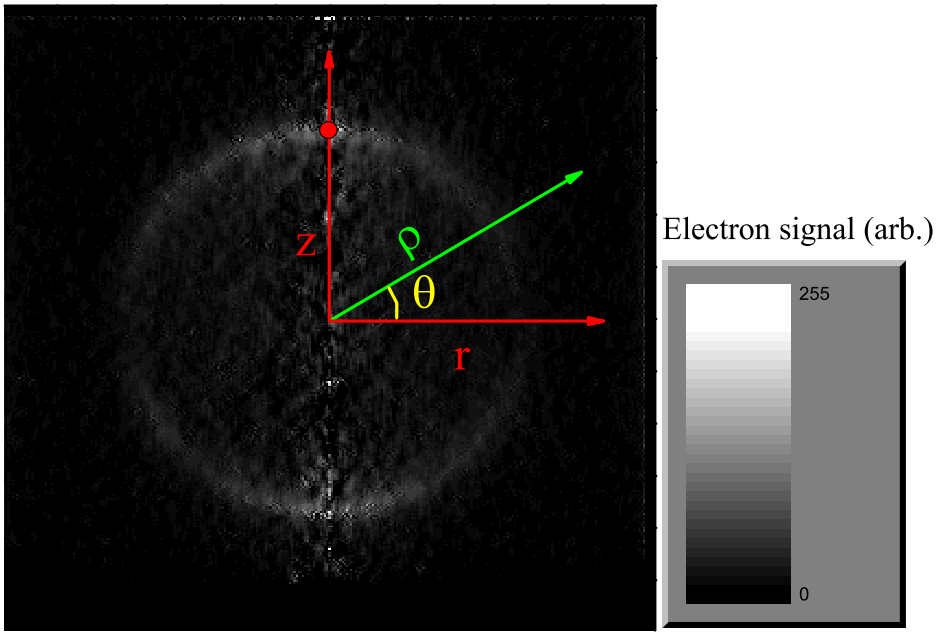

Fig. 8.4: Example Abel-inverted photoelectron image from the low-intensity "Electrons" experiment in CO_2. The Abel inverted image gives the photoelectron yield (grayscale) as a function of r and z, both measured in pixels. The total image size is 300x300 pixels.

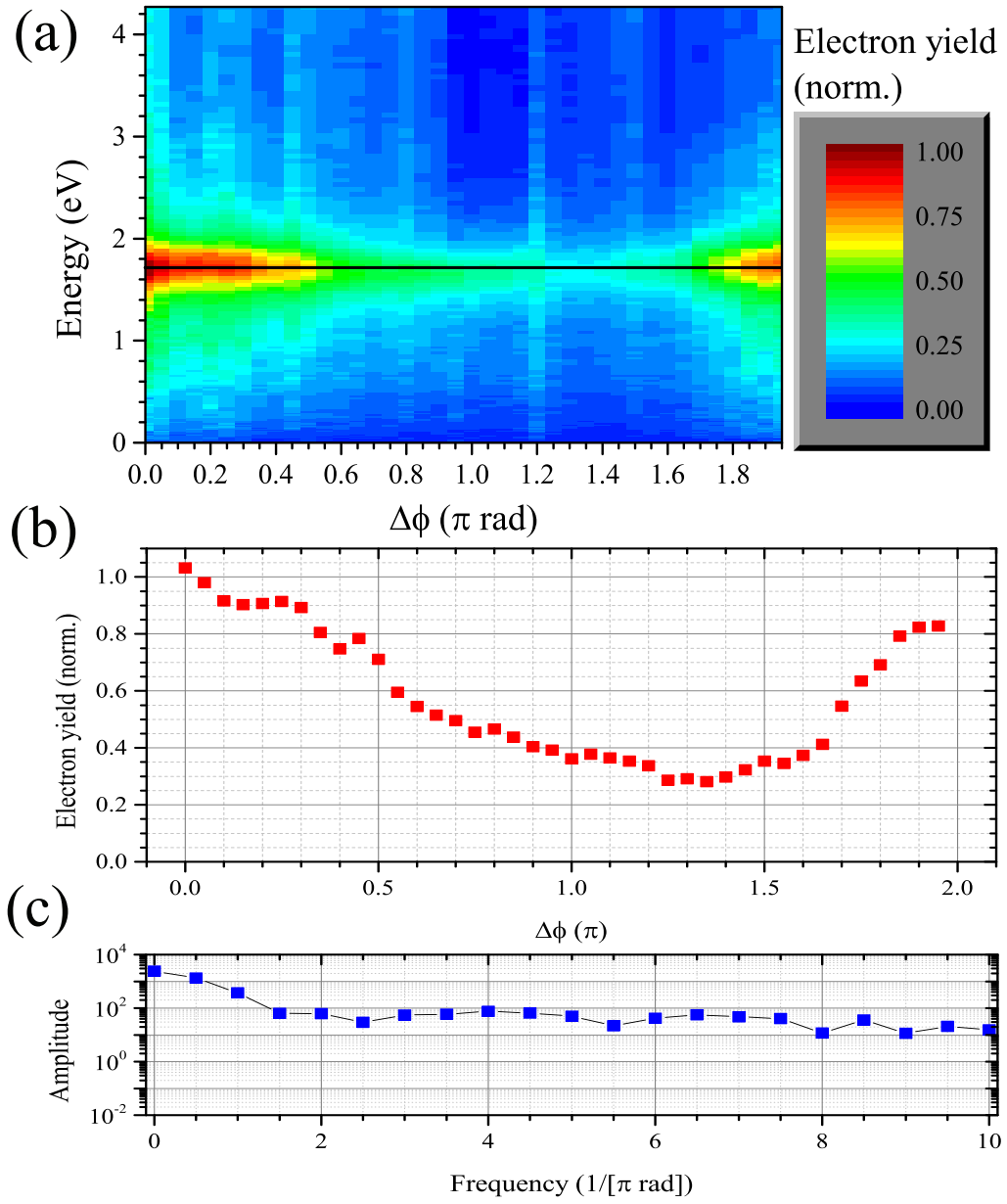

Fig. 8.5: (a) Electron yield (colormap) vs electron energy and $\Delta\phi$, for the low-intensity "Electrons" experiment in CO_2. (b) Yield of 1.73 eV electrons vs $\Delta\phi$ for the same experiment, found from a lineout of (a) at 1.73 eV. (c) Fourier transform of (b).

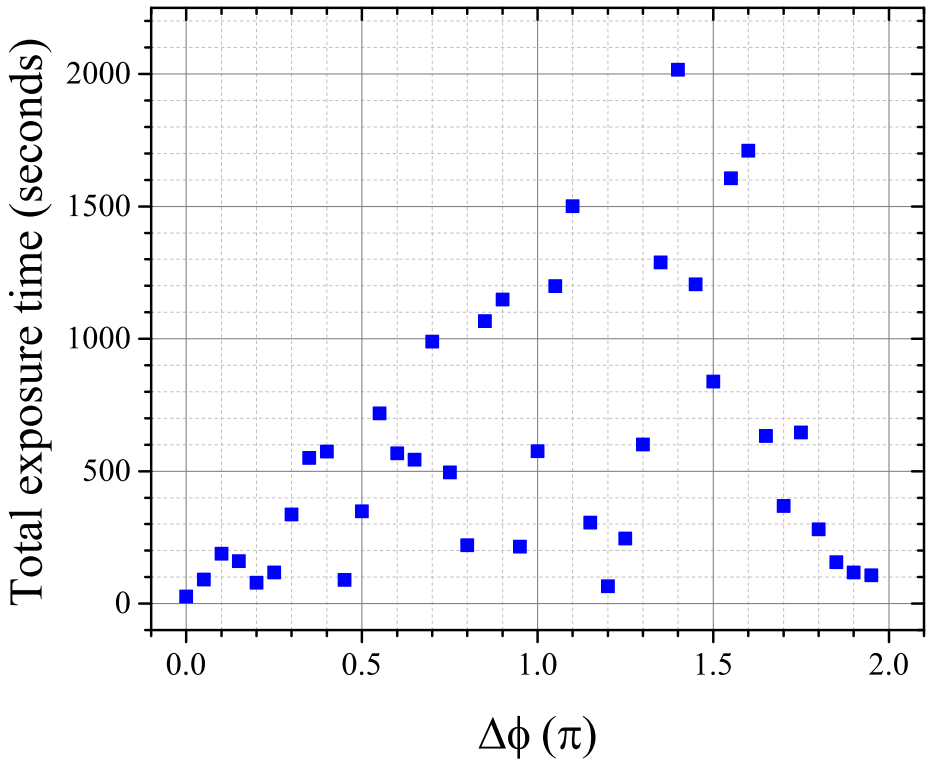

Fig. 8.6: Total exposure time in the composite electron image vs $\Delta\phi$ for the experiment shown in Fig. 8.5. The total number of laser shots contributing to each image is 1000 times the exposure time in seconds.

8.2 High-intensity experiments, 800 nm TPP

The results from the high-intensity, 800 nm experiments in both Xe and CO_2 are shown together in Figs. 8.7 and 8.8, to allow direct comparison between the results in both target species. The parameters, results, and conclusions of the Xe and CO_2 experiments will be discussed separately in Sec. 8.2.1 and 8.2.2, respectively.

8.2.1 Xenon

Results

In this experiment, the gas pressure in the vacuum chamber was $1.0(1) \times 10^{-6}$ Torr. The TPP was produced with the MZ at 800 nm. The nominal intensities of the single-arms of the TPP were 1.8×10^{14} and 1.9×10^{14} W/cm^2, for the fixed and variable arms of the MZ, respectively. These intensities correspond to ponderomotive energies of 10.8 and 11.4 eV. Electrons were measured in the VMI using the following voltages: $V_1 = -1200$ V, $V_{back} = 2050$ V, $V_{phos} = 4100$ V. During the experiment, τ was changed in steps of 0.067 fs, over 125 steps, for a total travel of 8.375 fs, between approximately 70 and 78 fs. At each step, electrons were collected on the VMI for eight seconds. The procedure described in Appendix A was used to determine τ at each point.

An example phase-tagged, Abel-inverted electron image is shown in Fig. 8.7(a). Above-threshold ionization is characterized by a series of well-separated energy peaks in the photoelectron spectrum. The Keldysh parameter for this experiment, $\gamma \simeq 0.7$, indicates that multiphoton and tunneling ionization are mixing. As such, individual,

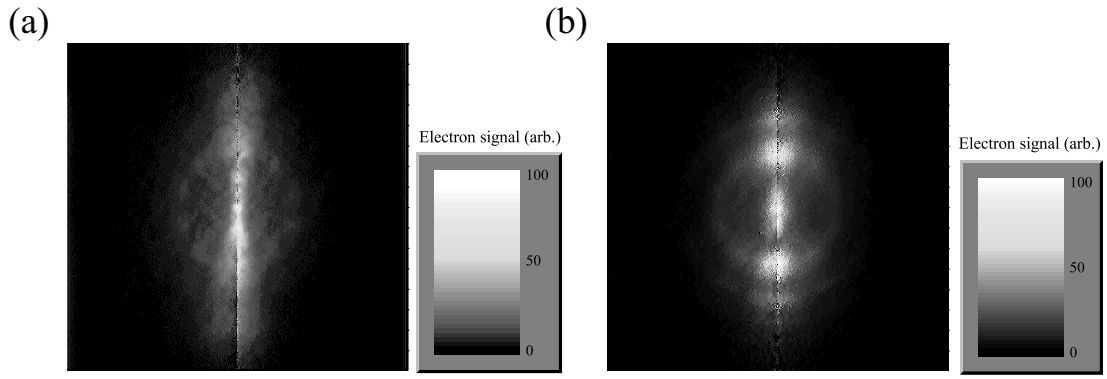

Fig. 8.7: Example Abel-inverted photoelectron images from high-intensity, 800 nm "Electrons" experiments in (a) xenon and (b) carbon dioxide. The image sizes are (a) 400x400 pixels and (b) 400x400 pixels

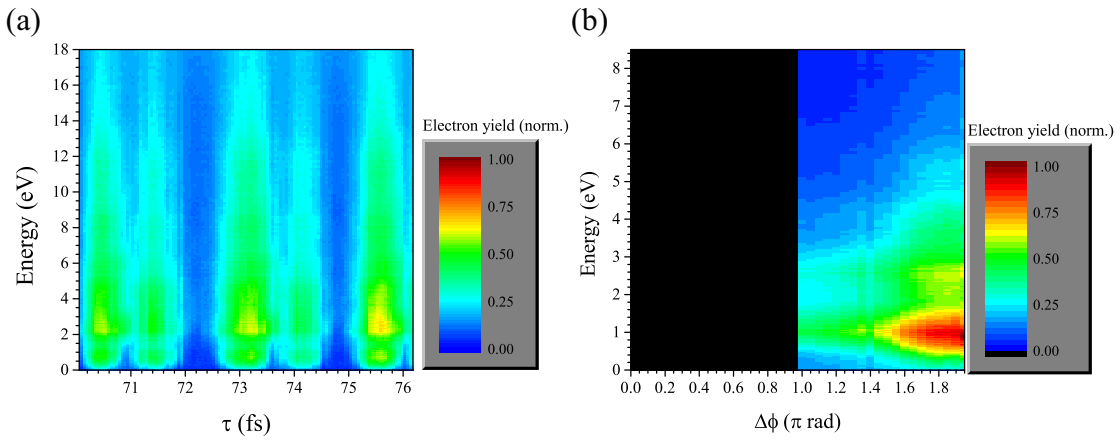

Fig. 8.8: Phase-dependent photoelectron spectra for the high-intensity, 800 nm "Electrons" experiment in (a) xenon and (b) carbon dioxide. In (a), phase tagging was not employed and the electron yields are plotted as a function of τ. In (b), phase tagging was employed and the yields are plotted as a function of $\Delta\phi$, for $\tau \simeq 250fs$.

well-separated ATI peaks do not appear in the VMI image. The ATI peaks have been blurred together into a pair of "jets" extending outwards from the center of the image, a signature of tunneling ionization. The electrons have a strong preference to be ejected along the polarization axis of the laser in the tunneling ionization regime. Some remnants of MPI and ATI are visible; for example, the faint ring structure is likely due to first ATI electrons. The photoelectron energy distribution as a function of τ is shown in Fig. 8.8(a). The same as in Fig. 8.7(a), the discrete energy structure of ATI is not observed, and instead a continuum of electron energies extending from nearly 0 up to 20 eV is observed.

Discussion

The τ-dependent, energy-resolved electron yields shown in Fig. 8.8(a) show a strong oscillation at the optical frequency. No oscillations at higher frequencies are present. Although the input pulse had a subordinate peak, it did not play a role in modulating I_{max} at $\tau \simeq 70fs$, as can be seen in Fig. 4.11(b). The results of this experiment are consistent with OI alone.

The maximum photoelectron energy observed in the experiment (approximately 20 eV) was much higher than the ponderomotive energy listed above and in Tab. 8.1. However, that ponderomotive energy was calculated using a single pulse, while the maximum intensity of the TPP changes substantially due to OI. One finds by consulting Fig. 4.11(b) that $I_{max}(\tau = 70\text{fs}) \simeq 2I_0$ when the two peaks of the TPP are in phase and constructively interfere, where I_0 is the maximum intensity of the input pulse. This will increase the ponderomotive energy by a factor of two

as well, so one expects a maximum electron energy of approximately 2×11.4 eV $= 22.8$ eV when there is constructive OI. This prediction is in agreement with the experimental observations.

8.2.2 CO_2

Results

Figures 8.7(b) and 8.8(b) show the results of the high-intensity "Electrons" experiment at 800 nm in CO_2. The gas pressure in the vacuum chamber was $9.4(1) \times 10^{-7}$ Torr. The TPP was produced with the MZ at 800 nm. The nominal intensities of the single-arms of the TPP were 1.3×10^{14} and 1.5×10^{14} W/cm^2, for the fixed and variable arms of the MZ, respectively. These intensities correspond to ponderomotive energies of 7.8 and 9.0 eV. Electrons were collected with the VMI using the following voltages: $V_1 = -1250$ V, $V_{back} = 2020$ V, $V_{phos} = 4500$ V. Although this experiment was done at higher intensities than the CO_2 experiment described in Sec. 8.1.2, the electron yield was still low enough that the phase-tagging procedure had to be employed. The experiment was run at $\tau \simeq 250$ fs. A total of 1800 exposures of ten-second duration were collected and post-sorted by $\Delta\phi$ into bins of width $\pi/20$ rad.

An example Abel-inverted electron image from one of the phase bins is shown in Fig. 8.7(b). In contrast to the high-intensity xenon experiment in Fig. 8.7(a), well-separated energy peaks corresponding to above-threshold ionization are observed. The center spot on the image corresponds to threshold electrons; two outer rings are

visible, corresponding to first ATI and second ATI electrons. The ionization energy of CO_2 is 13.77 eV. The absorption of nine 800 nm photons adds 13.95 eV of energy to the molecule, resulting in an emitted electron with an energy of 0.18 eV.

The photoelectron energy distribution as a function of $\Delta\phi$ is shown in Fig. 8.8(b). The energies were calibrated by imposing that the energy difference between the first and second ATI peaks was equal to the 800 nm photon energy, 1.55 eV.

Figure 8.9 shows the total exposure time vs $\Delta\phi$ for this experiment. Due to the minimal drift of the MZ stage during this experiment, TPPs were only produced with $\Delta\phi$ between π and 2π rad. Over this range, the exposure time was very nonuniform, although most points (17 out of 20) had a total exposure time in excess of 200 seconds.

Discussion

As in all of the previously-discussed experiments, the energy-resolved electron yields shown in Fig. 8.8(b) oscillate periodically at the optical frequency, without any visible higher-frequency oscillations. An oscillation at twice the optical frequency is not observed; as in Sec. 8.1.2, the large value of τ, 250 fs, in this experiment means that the subordinate peak has minimal effect on the ionization dynamics.

In contrast to the 800 nm, high intensity experiment in xenon (Sec. 8.2.1), the photoelectron spectra shows clearly-resolved energy peaks corresponding to ATI. This is expected, as the Keldysh parameter in this experiment, $\gamma = 0.9$, is higher than the xenon experiment, and implies that MPI still plays a significant role in the ionization of CO_2. All of the observed dynamics are consistent with OI alone.

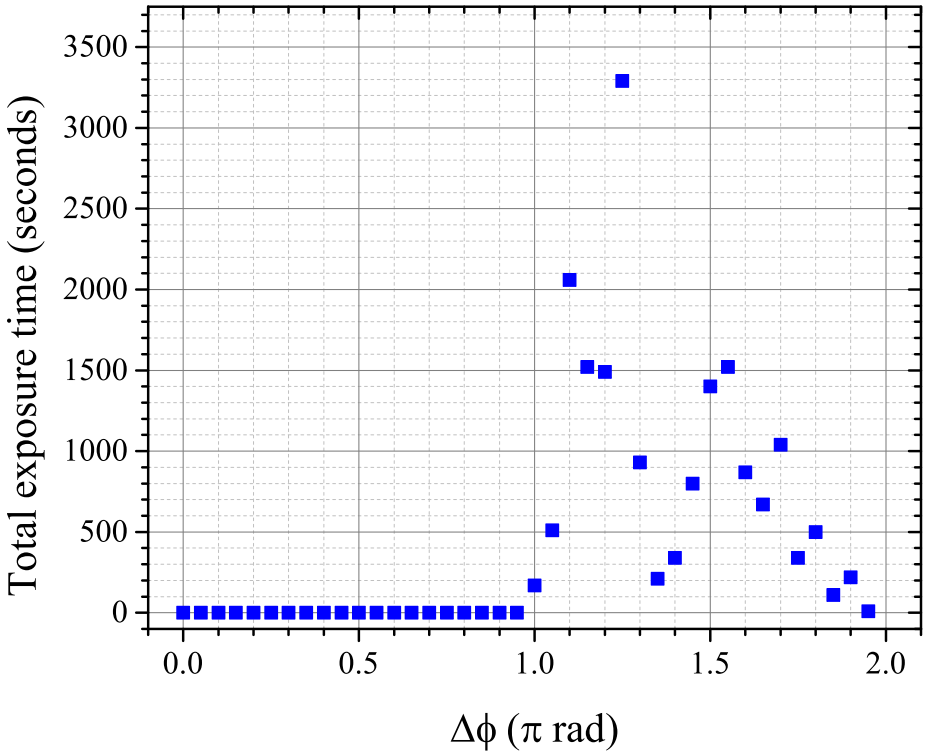

Fig. 8.9: Total exposure time in the composite electron image vs $\Delta\phi$ for the experiment shown in Fig. 8.8(b). The total number of laser shots contributing to each image is 1000 times the exposure time in seconds.

8.3 High-intensity experiments, 400 nm TPP

The results from the high-intensity, 400 nm experiments in both Xe and CO_2 are shown together in Figs. 8.10 and 8.11, to allow direct comparison between the results in both target species. The parameters, results, and conclusions of the Xe and CO_2 experiments will be discussed separately in Sec. 8.3.1 and 8.3.2, respectively.

8.3.1 Xenon

Results

Figures 8.10(a) and 8.11(a) show the results of the high-intensity "Electrons" experiment at 400 nm in xenon. The gas pressure in the vacuum chamber was $9.7(1) \times 10^{-7}$ Torr. The TPP was produced with the MZ at 800 nm, then frequency doubled. The nominal intensities of the single-arms of the TPP were 3.3×10^{14} and 3.1×10^{14} W/cm^2, for the fixed and variable arms of the MZ, respectively. These intensities correspond to ponderomotive energies of 4.9 and 4.6 eV. Electrons were measured in the VMI using the following voltages: $V_1 = -1000$ V, $V_{back} = 2050$ V, $V_{phos} = 4100$ V. During the experiment, τ was changed in steps of 0.067 fs, over 1250 steps, for a total travel of 83.75 fs, between approximately 70 and 155 fs. At each step, electrons were collected on the VMI for five seconds. The procedure described in Appendix A was used to determine τ at each point.

An example phase-tagged, Abel-inverted electron image is shown in Fig. 8.10(a). Reducing the wavelength by a factor of two reduces U_p by a factor of four, and γ by a factor of two, meaning that in contrast to Sec. 8.2.1, MPI and ATI dominate in

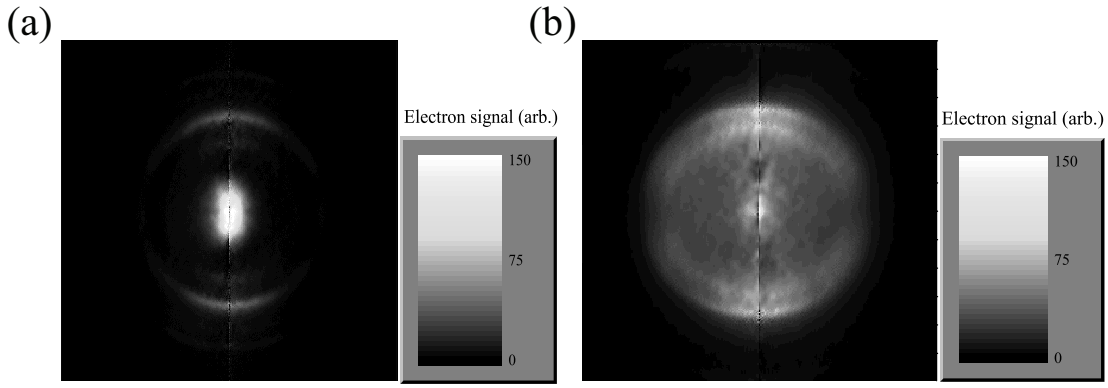

Fig. 8.10: Example Abel-inverted photoelectron images from high-intensity, 400 nm "Electrons" experiments in (a) xenon and (b) carbon dioxide. The image sizes are (a) 500x500 pixels and (b) 300x300 pixels

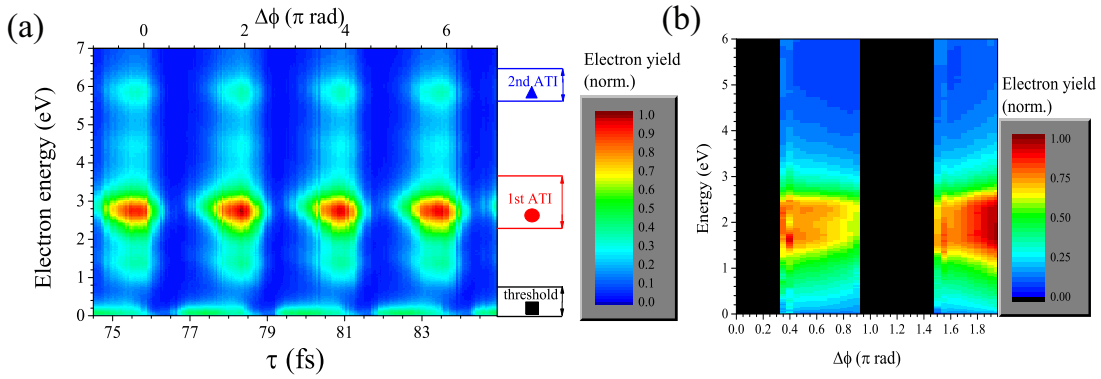

Fig. 8.11: Phase-dependent photoelectron spectra for the high-intensity, 400 nm "Electrons" experiment in (a) xenon and (b) carbon dioxide. In (a), phase tagging was not employed and the electron yields are plotted as a function of τ. A relatively large range of τ was able to be scanned. In (b), phase tagging was employed and the yields are plotted as a function of $\Delta\phi$, for $\tau \simeq 200fs$. Due to the phase-tagging procedure, only a range of 2π rad was able to be scanned.

this experiment (even at the higher intensities used here). Individual, well-separated ATI peaks appear in the VMI image. Threshold electrons appear at the center spot of the image; rings corresponding to first and second ATI electrons are visible. The energy-dependent photoelectron yield as a function of τ is shown in Fig. 8.11(a), for a range of τ between approximately 75 and 85 fs. The energy scale was calibrated by imposing that the energy difference between the first and second ATI peaks was equal to a single photon energy at 400 nm, 3.1 eV.

Discussion

As in all previous experiments, the τ-dependent, energy-resolved electron yields shown in Fig. 8.11(a) show a strong oscillation at the 800 nm optical frequency. No oscillations at higher frequencies are present. The subordinate peak OI is negligible at $\tau \simeq 70$ fs (see Fig. 4.11(b)), so an oscillation at twice the optical frequency is not observed.

Beyond OI, there are a few notable phenomena in the energy-resolved yields. First, there are two weak intermediate peaks, one halfway between the threshold and first ATI peaks (approximately 1.5 eV) and one halfway between the first and second ATI peaks (approximately 4.5 eV). These peaks are believed to be due to the absorption or stimulated emission of an 800 nm photon during the ionization process. As described in Sec. 7.1, the 800 nm beam was filtered out from the 400 nm beam after SHG with a pair of dichroic mirrors with a reflectance of <0.2% at 800 nm. This means that the 800 nm pulse energy is reduced by a factor of $0.002^2 = 4 \times 10^{-6}$. The nominal intensity of the 800 nm pulse (one peak of the

TPP) used to generate the 400 nm TPP in this experiment was 50 μJ; the residual 800 nm energy was therefore approximately 0.2 nJ. This corresponds to a focal intensity of $\sim 3 \times 10^9$ W/cm^2 – too low to ionize the target gas sufficiently by itself, but possibly high enough to enable the absorption of emission of an 800 nm photon after ionization by the 400 nm TPP.

The second observation is that the threshold electrons have a shift in phase (equivalently, τ) compared to the ATI electrons. This can be seen most directly in Fig. 8.12, which plots the yield vs τ for threshold, first ATI, and second ATI electrons. The yields were calculated by integrating Fig. 8.11(a) over the energy ranges indicated to the left of the figure. The phase shifts of the three yield curves were found by fitting each to a sinusoid. The two ATI peaks were found to oscillate in phase with each other within the fitting uncertainty; the phase shift between the threshold and first ATI peaks, on the other hand, was found to be $0.63 \pm 0.28\pi$ rad.

This phase shift was found to be quite robust, appearing in several experiments over the course of many weeks. Additional experiments were performed in which a piece of borosilicate glass was introduced into the beam path. The thickness of the glass was varied by rotating the glass in the beam path. The wavelength-dependent index of refraction of borosilicate introduced a thickness-dependent phase shift between the 400 nm and 800 nm beams, but had no effect on the phase shift between threshold and ATI peaks observed in the experiment. The origin of this phase shift is currently unknown, and further experiments are necessary to explain it.

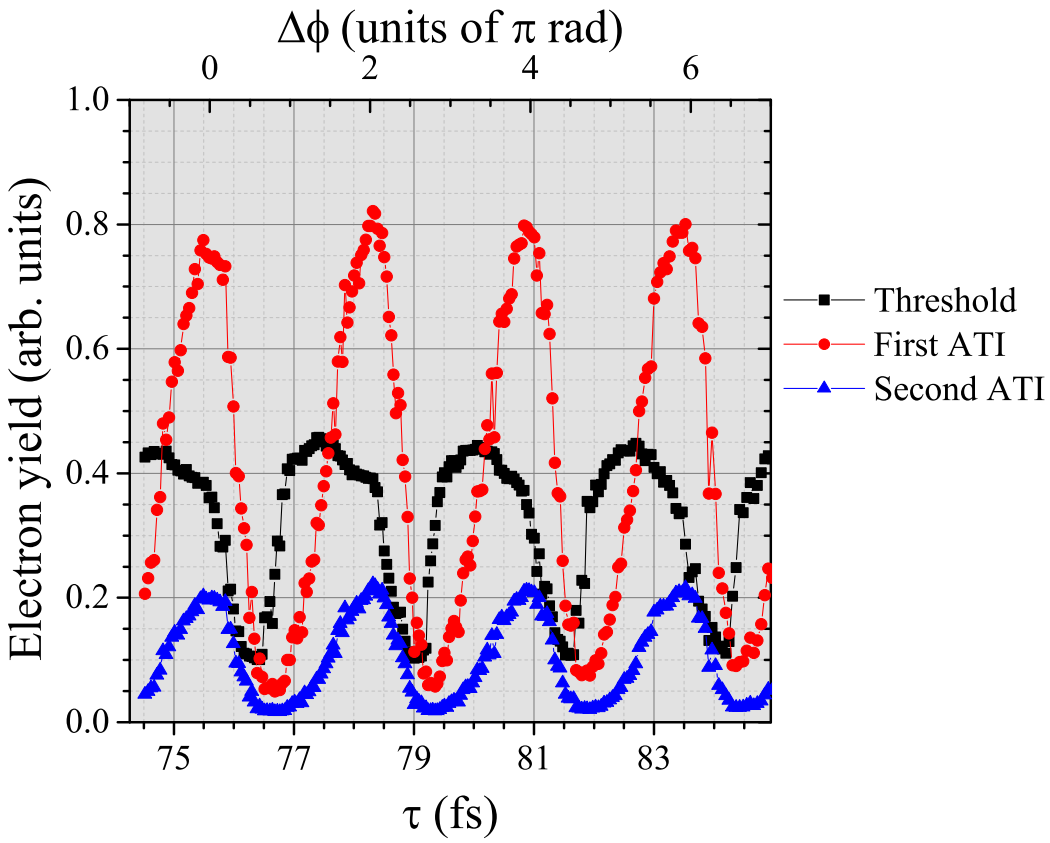

Fig. 8.12: Electron yield (arbitrary units) vs τ for the high intensity, 400 nm "Electrons" experiment in xenon, between approximately 75 and 85 fs. Yields of threshold (black squares), first ATI (red circles) and second ATI (blue triangles) electrons are plotted separately. These yields were computed by integrating the energy dependent yields in Fig. 8.11(a) over the corresponding energy ranges given to the right of that figure.

8.3.2 CO_2

Results

Figures 8.10(b) and 8.11(b) show the results of the high-intensity "Electrons" experiment at 400 nm in CO_2. The gas pressure in the vacuum chamber was $1.0(1) \times 10^{-6}$ Torr. The TPP was produced with the MZ at 800 nm and converted to 400 nm via SHG in the BBO crystal. The nominal intensities of the single arms of the TPP were 1.7×10^{14} and 1.9×10^{14} W/cm^2, for the fixed and variable arms of the MZ, respectively. These intensities correspond to ponderomotive energies of 2.5 and 2.8 eV. Electrons were measured in the VMI using the following voltages: $V_1 = -1050$ V, $V_{back} = 2020$ V, $V_{phos} = 4200$ V. Although this experiment was done at higher intensities than the CO_2 experiment described in Sec. 8.1.2, the electron yield was still low enough that the phase-tagging procedure had to be employed. The experiment was run at $\tau \simeq 200$ fs. A total of 12,000 exposures, each of one-second duration were collected and post-sorted by $\Delta\phi$ into bins of width $\pi/20$ rad.

An example Abel-inverted electron image from one of the phase bins is shown in Fig. 8.7(b). Only one energy peak is observed in this image, most likely corresponding to threshold electrons. The energy of the threshold electrons is estimated by recalling that five 400 nm photons are required to ionize CO_2, imparting 15.5 eV of energy. The ionization energy of CO_2 is 13.77 eV, meaning that emitted photoelectrons have an excess energy of 1.73 eV, ignoring additional energy due to pondoromotive shifts. The photoelectron energy distribution as a function of $\Delta\phi$ is shown in Fig. 8.11(b). The energy scale was set by imposing that the center energy

of the electron peak was 1.73 eV.

Figure 8.13 shows the total exposure time vs $\Delta\phi$ for this experiment. Only two small ranges of $\Delta\phi$ were ever produced by the MZ in the experiment, leaving significant holes in the data of Fig. 8.11(b). Most points in these two ranges (15 out of 17) had a total exposure time in excess of 200 seconds.

Discussion

As in all of the previously-discussed experiments, the energy-resolved electron yields shown in Fig. 8.11(b) oscillate periodically at the optical frequency, without any visible higher-frequency oscillations. As in Secs. 8.1.2 and 8.2.2, the large value of τ means that oscillations at twice the optical frequency are not clearly observed. All of the dynamics observed in this experiment are consistent with OI alone. Because no ATI electrons were observed, it cannot be determined if an anomalous phase shift (see Sec. 8.3.1) appears between threshold and ATI electrons in CO_2 as well, or if this phenomenon is unique to xenon.

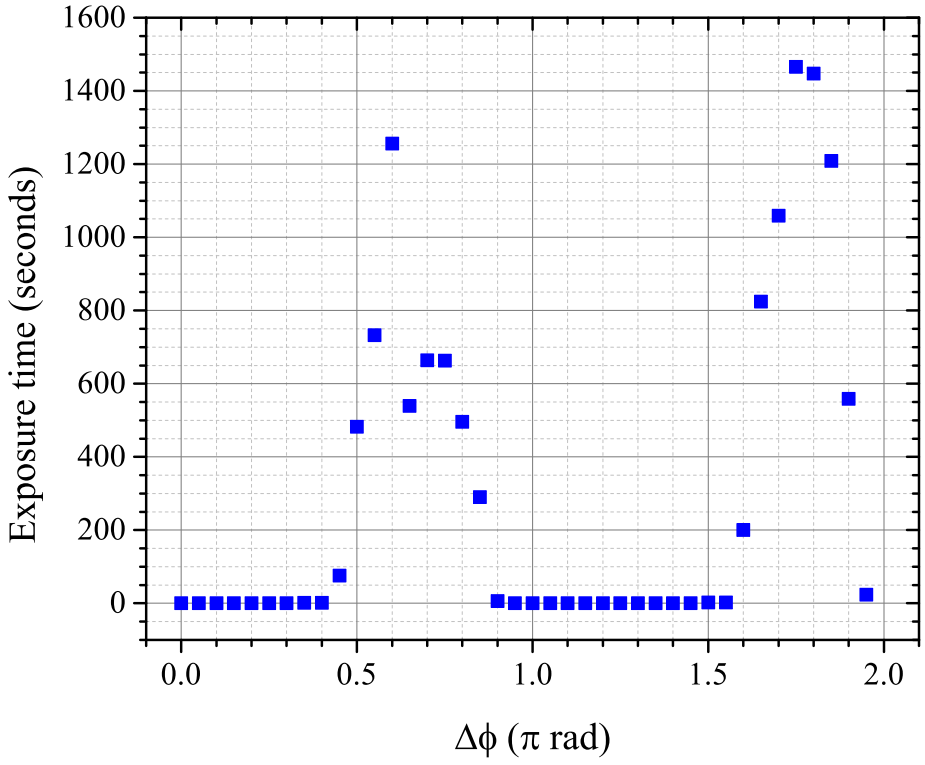

Fig. 8.13: Total exposure time in the composite electron image vs $\Delta\phi$ for the experiment shown in Fig. 8.11(b). The total number of laser shots contributing to each image is 1000 times the exposure time in seconds.

Chapter 9: Experiment 2, "Electrons": Proposals for a Future Experiment

In this chapter, an experiment is proposed which will enable the observation of QuI in multiphoton ionization to the continuum. The laser intensity in the "Electrons" experiments was far too high to enable clear, unambiguous observation of QuI; the ponderomotive energy in all of these experiments was much larger than the expected QuI fringe spacing. As described in Chap. 6, the ponderomotive energy should be below 0.1 eV to allow for observation of QuI, and an ponderomotive energy < 0.01 eV is preferable.

However, if one lowers the intensity in the experiment so that the ponderomotive energy is this small (this requires intensities on the order of 10^{11} W/cm^2 for an eight-photon ionization), no electrons are visible. Therefore, a target with a significantly higher ionization probability needs to be found. Rubidium is an attractive target to investigate QuI, because its low ionization energy (4.18 eV) enables three-photon ionization at 800 nm. Furthermore, there is an intermediate resonance at 800 nm which can be leveraged to increase ionization rates further. Section 9.1 determines the ionization rate of Rb from the ground state using an 800 nm laser with an intensity of 1.65×10^{11} W/cm^2. This rate is shown to compare favorably with the

ionization rates of the low intensity "Electrons" experiments discussed in Sec. 8.1. In Sec. 9.2, an experimental design is proposed in which QuI could be probed in Rb, taking advantage of the resonant intermediate states to further increase ionization rates.

9.1 Rubidium ionization rates

The m-photon ionization rate is

$$W^{(m)} = \frac{\sigma^{(m)} I^m}{(\hbar\omega_0)^m}, \tag{9.1}$$

where $\sigma^{(m)}$ (units of $\mathrm{m}^{2m}\mathrm{s}^{m-1}$) is the m-photon generalized cross section, I is the laser intensity, and ω_0 is the central frequency of the laser. Assuming a top-hat laser pulse of duration Δt, the total ionization probability during interaction with the laser pulse is

$$p^{(m)} = W^{(m)} \Delta t. \tag{9.2}$$

For a more general pulse shape, the time-dependent intensity should be used in Eq. 9.1 and $W^{(m)}$ must be integrated over the pulse duration to find the ion yield; Eq. 9.2 is sufficient for the order-of-magnitude estimations needed here.

The wavelength-dependent three-photon ionization cross section, $\sigma^{(3)}$, was calculated using the single-active-electron Herman-Skillman potential [140], and is shown in Fig. 9.1. At 800 nm, $\sigma^{(3)} = 2.9810 \times 10^{-79}$ $\mathrm{cm}^6\mathrm{s}^2$. The maximum allowable laser intensity for the proposed experiment can be computed from the equation for

the ponderomotive energy, Eq. 2.2, assuming an upper limit of $U_p = 0.01$ eV. One finds $I = 1.65 \times 10^{11}$ W/cm^2. Using these values for $\sigma^{(3)}$ and I, Eq. 9.1 is used to find $W^{(3)} = 9.08 \times 10^{10}$ s^{-1}.

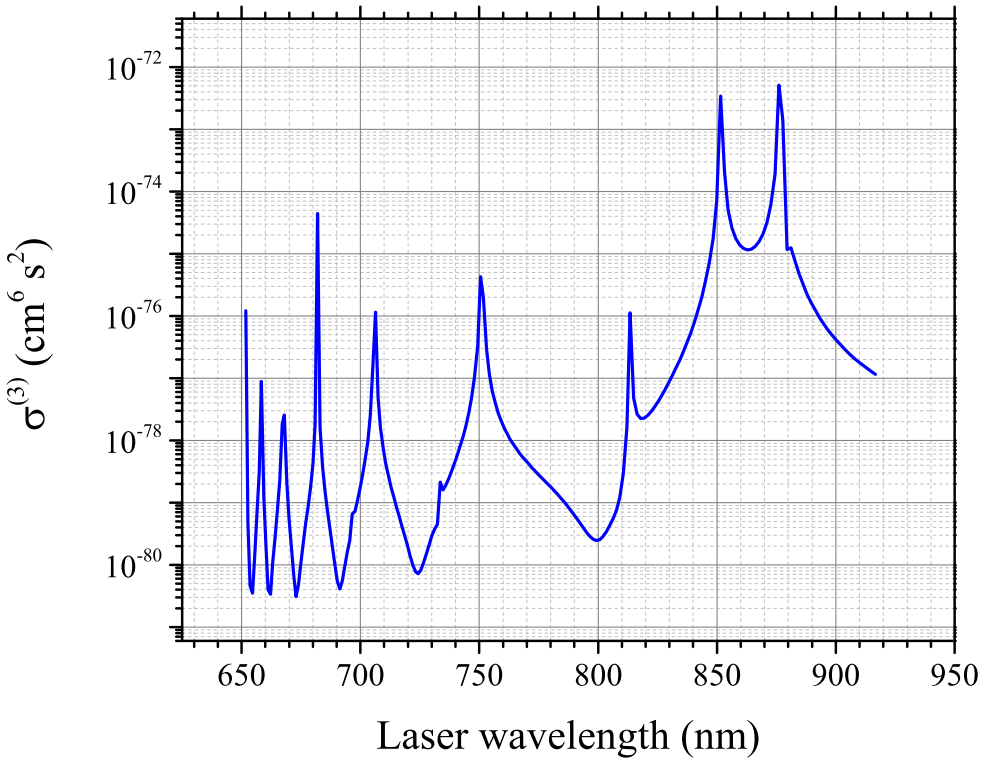

Fig. 9.1: Three-photon generalized cross section $\sigma^{(3)}$ vs laser wavelength, for ionization from the Rb $5s_{1/2}$ state [140].

If a single pulse is used to ionize, $\tau \simeq 75$ fs. If a TPP is used, $\tau \simeq 150$ fs as long as the peaks are well separated (by at least the FWHM of a single pulse). This gives $p^{(3)} \simeq 0.005$ for a single pulse and $p^{(3)} \simeq 0.01$ for a TPP. Due to OI, $p^{(3)}$ for a TPP will change if τ changes.

In the following, this estimated ionization probability will be compared to the

ionization probability observed in previous experiments. The number of electrons in the low intensity "Electrons" experiments (Sec. 8.1) was no fewer than 0.01 electron per laser shot, or 10 electrons per one second exposure. Assuming a typical quantum efficiency (QE) of 50% for the MCP (Ref. [141] gives a 50-85% QE for detection of electrons with an MCP), 0.02 electrons are produced per laser shot.

The focal spot size ($1/e^2$ radius) was $\sim$ 5 μm, with a Rayleigh length of $\sim$ 200μm. The interaction volume is estimated to be a cylinder of this radius and height, a volume of 1.6×10^{-14} m^3. Experimental pressures were approximately 1.0×10^{-6} Torr. Using the ideal gas law, one finds that approximately 15 atoms were in the interaction volume during the experiment. The production of 0.02 electrons per laser shot out of 15 target atoms corresponds to an ionization probability of $p^{(4,5)} = 0.0013$ (superscript $(4, 5)$ because the experiment involved a four-photon ionization of xenon or a five-photon ionization of CO_2 with the 400 nm TPP).

Therefore, one concludes that the ionization rates predicted in rubidium at $\sim 10^{11}$ W/cm^2 are comparable to, or perhaps larger than, those found in the low intensity "Electrons" experiments in xenon. Furthermore, the Rb atom density will likely be higher than in the xenon experiment due to the gas jet geometry that will likely be employed (see below). This will further increase the electron yield per laser shot. In conclusion, it appears that a QuI experiment in rubidium at laser intensities of $\sim 10^{11}$ W/cm^2 is feasible.

9.2 Rubidium experiment proposal

The energy level diagram of neutral rubidium (Rb I) is given in Fig. 9.2 [142], with some relevant states labeled. The ground state, spectroscopic notation $5^2S_{1/2}$, is at 4.18 eV (33 691 cm^{-1}) below the Rb II limit (i.e., the ionization threshold). A pair of closely-spaced intermediate excited states, the $5^2P_{1/2}$ and $5^2P_{3/2}$ states, are 1.56 eV (12 579 cm^{-1}) and 1.59 eV (12 817 cm^{-1}) above the ground state, respectively.

In the proposed experiment, Rb atoms are injected into the target chamber using a gas jet. A π pulse interacts with the Rb $5^2S_{1/2}$ state and populates either the $5^2P_{1/2}$ or $5^2P_{3/2}$ state (the resonant laser wavelengths are 795.1 nm and 780.3 nm, respectively). After this, an 800 nm TPP (identical to that described in the experiments of this work except at an intensity of 10^{11} W/cm^2) interacts with the excited state population. The absorption of two photons is sufficient to ionize, and the emitted photoelectrons will have a kinetic energy of $\sim$ 0.5 eV. Quantum interference Mechanism III occurs in the transition from the bound intermediate state to the continuum, and can be observed in the photoelectron energy spectra using the VMI. Because this QuI is due to a two-photon transition, it is clearly differentiated from OI, unlike Ref. [80]. The electron energy distribution for variable τ can be calculated using the procedure described in Chap. 6.

The ionization rates from these excited states are likely higher than the three-photon ionization rate from the $5^2S_{1/2}$ state calculated in Sec. 9.1, so the laser intensity and the ponderomotive energy can be kept low in this experiment. In fact, the

two-photon ionization rate, while not calculated fully in this work, can be estimated with help from Ref. [143]; for the case of a hydrogenic atom, an approximation of the two-photon cross section $\sigma^{[2]}$ gives

$$\sigma^{[2]} \simeq \left(1.572 \times 10^{-45}\right) I g_2 \lambda^6 \quad \left(\mathrm{cm}^2\right), \tag{9.3}$$

where λ is given in nm, I is in W/cm^2, and $g_2 \simeq 0.4$ is the two-photon Gaunt factor [144]. For $\lambda = 800$ nm and a laser intensity of 1.65×10^{11} W/cm^2, $\sigma^{[2]} \simeq 2.72 \times 10^{-17}$ cm^2. The total ionization rate is $W = \sigma^{[2]} F$, where $F = I/(\hbar\omega_0)$ is the photon flux. One finds in this case that $W = 1.8 \times 10^{13}$ s^{-1}, substantially higher than the three-photon ionization rate calculated in Sec. 9.1. A calculation of the ionization rate of Rb from the $5^2\mathrm{P}_{1/2}$ and $5^2\mathrm{P}_{3/2}$ states, similar to Sec. 9.1, should be done to confirm this prediction.

Following the procedure of Ref. [145], the generalized Rabi frequency for a transition between states i and j is

$$\Omega_{i\to j} = \frac{1}{\sqrt{2} t_{i\to j}} \tag{9.4}$$

when pumped with a laser at the saturation intensity

$$I_{sat} = \frac{c\epsilon_0 \hbar^2}{4 d_{i\to j}^2 t_{i\to j}^2}, \tag{9.5}$$

where $t_{i\to j}$ is the transition lifetime, c is the speed of light in vacuum, ϵ_0 is the vacuum permittivity, and $d_{i\to j}$ is the transition dipole moment. The values of the parameters for both transitions are given in Ref. [145] and are summarized in Tab. 9.1.

Tab. 9.1: Optical properties of the transitions from the $5^2S_{1/2}$ state to the $5^2P_{1/2}$ and $5^2P_{3/2}$ excited states in rubidium.

Transition	$t_{i\to j}$ (ns)	$d_{i\to j}$ (C m)	I_{sat} (mW/cm^2)	$\Omega_{i\to j}$ (s^{-1})
$5^2S_{1/2} \to 5^2P_{1/2}$	27.70(4)	$2.537(3)\times10^{-29}$	1.49	25.53(4)
$5^2S_{1/2} \to 5^2P_{3/2}$	26.24(4)	$3.584(4)\times10^{-29}$	0.83	26.95(4)

A laser pulse at intensity I_{sat}, applied for a time $t = \pi/\Omega_{i\to j}$, will transfer all of the population from the ground state to the excited state (a π pulse, so called because it rotates the electron population by an angle of π on the Bloch sphere). This time is 0.123 μs for the transition to the $5^2P_{1/2}$ state and 0.117 μs for the transition to the $5^2P_{3/2}$ state.

This experiment has promise to unambiguously detect QuI Mechanism III for the first time; the experimental design can also be modified to open up other avenues of research. For example, if the duration of the preparatory pulse is changed so that it is no longer a π pulse, a superposition state between the ground and excited states will be created. The TPP interacts with this superposition, which will change the ionization yield and possibly the energy distribution of the ejected photoelectrons. In this way, QuI Mechanisms I and III can be investigated simultaneously. If both the $5^2P_{1/2}$ and $5^2P_{3/2}$ are initially populated, Mechanisms I, II, and III could all be investigated simultaneously.

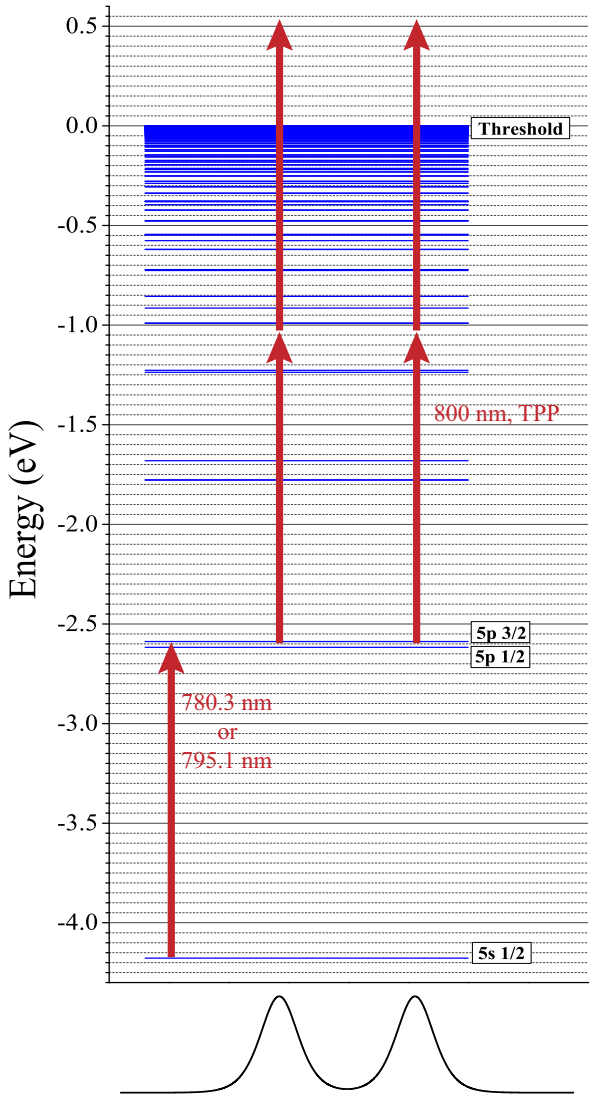

Fig. 9.2: Energy level diagram of rubidium, taken from Ref. [142]. The energy levels are shown as blue horizontal lines. The relevant states for the proposed experiment are labeled, the ground state, $5^2S_{1/2}$, and the first two excited states $5^2P_{1/2}$ and $5^2P_{3/2}$. In the proposed experiment, a long, comparatively weak laser pulse transfers the population of the ground state to one of the two excited states. Then, a TPP at 800 nm interacts with the excited state to ionize. Quantum interference Mechanism III occurs in the electron transition to the continuum. The photoelectron energy distribution can be predicted using the calculations in Chap. 6.

Chapter 10: Conclusions

In Chap. 1, the two questions that form the basis of this dissertation were posed:

- Question 1: What role does the relative phase play in controlling ionization from a TPP, and how does this in turn influence more complicated molecular dynamics?
- Question 2: Can quantum interference be observed in strong-field ionization from a TPP?

The answers given by this dissertation to these two questions will be given below.

Question 1

The first question was motivated by the results in strong-field optimal control of CO_2 Coulomb explosion dynamics [28], and was answered by the "Ions" experiments [82]. The optimal control experiments of this group consistently recovered phase-locked pulse trains as solutions (as did several other experiments [46–49]). Like many optimal control experiments, these experiments all relied on ionization as the first step in the dynamics, illustrating the need to fully understand the influence of pulse trains on ionization.

The most direct way that ionization yields can change under the influence of a phase-locked TPP is due to the changing intensity of the TPP via OI. Quantum interference, on the other hand, can change total ionization yields when the ionization proceeds through a resonant intermediate state as in Ref. [50] (QuI Mechanisms I and II), but it was shown in Chap. 6 that only OI is responsible for changing the ion yield when there are no intermediate resonances. However, in strong-field ionization, states are dynamically shifted into resonance by the ac Stark effect (Freeman resonances [57, 58]), and so the possibility remained open that QuI Mechanisms I and II could play a role in strong-field ionization.

The "Ions" experiments of Chaps. 3 and 4 explored the roles of OI and QuI in ionization of xenon atoms using an experimental setup similar to the previous work of Ref. [28]. It was found that OI was the dominant effect which governed the change in ionization yield as the relative phase or delay between peaks of the TPP was changed; QuI, if present, played a minor role. An upper limit on the relative strength of QuI was found to be 10% that of OI by comparing the OI oscillation amplitude to the experimental noise.

Although QuI was found to not play a role in ionization dynamics, OI was found to influence the ionization in surprising ways, due to imperfections in the pulse shape. In the experiments in which the TPP was made with a $4f$ pulse shaper, it was found that the presence of a pedestal can cause an anomalously large oscillation in the ion yield vs $\Delta\phi$, even when the peaks of the TPP appear well separated. This was because the pedestal locally increased the strength of OI, causing larger fluctuations in intensity. A pedestal was also found to have the

potential to phase-shift the ion yield oscillations away from the expected ion yield maxima at $\Delta\phi = 0$ or π. The experiments in which the TPP was made with a Mach-Zehnder interferometer showed that when the input pulse had an out-of-phase subordinate peak, the corresponding out-of-phase OI led to an oscillation in the ion yield at twice the optical frequency. Such an oscillation could be due to a two-photon QuI Mechanism I, but a calculation of the TPP maximum intensity vs τ showed that this frequency doubling was purely an optical effect. Both pedestals and subordinate peaks are common in ultrafast pulses, and so great care must be taken to characterize pulses and account for pulse imperfections in optimal control experiments.

Finally, it was shown that an intensity-driven analysis is consistent with the results of CO_2 bending dynamics described in Ref. [28]. It was well known that a lower laser intensity corresponded to reduced bending amplitude when using a TL pulse. Further experiments using a TPP found that the bending amplitude oscillated periodically with $\Delta\phi$, consistent with a change in laser intensity due to OI. More quantitative analysis was found to not be possible due to the significant TPP imperfections (pedestals and subordinate peaks) present in this experiment.

Question 2

The perturbation theory calculation in Chap. 6 found that an energy-resolved electron measurement is necessary to see QuI Mechanism III, involving nonresonant transitions to the ionic continuum. Quantum interference can be imagined as a temporal analogue of a double slit experiment, with the TPP delay τ representing

the slit spacing. While changing the slit spacing in a double slit experiment changes the interference pattern on the detector, it does not change the total throughput of the slits; similarly, changing τ will change the energy structure of the emitted photoelectrons but will not change the total number of electrons emitted, except by changing the "single-slit" throughput via OI.

This realization motivated the "Electrons" experiments. The "Electrons" experiments used a velocity map imager to detect the spatial distribution of electron after ionization with a TPP, which was converted to an energy distribution using an Abel inversion. The goal of the "Electrons" experiments was to observe QuI in multiphoton transitions to the continuum. Although QuI in continuum transitions was observed in Ref. [80], this ionization was a single-photon ionization, meaning that OI and QuI had the same period and were difficult to separate in the experimental results. A multiphoton ionization removes this ambiguity, but necessitates higher laser intensities.

"Electrons" experiments were performed at various intensities, using both 800 nm and 400 nm TPPs with target species xenon and CO_2. None of the experiments showed evidence of QuI, likely due to the substantial ponderomotive energy resulting from the high laser intensities (at least 10^{13} W/cm^2). It was found that the laser intensity must to be lowered to $\sim 10^{11}$ W/cm^2 to reduce the ponderomotive energy to $\sim$ 0.01 eV, the approximate energy spacing of QuI fringes. Unfortunately, at these intensities, too few xenon atoms or CO_2 molecules were ionized to be able to perform the experiment.

The dissertation ended by proposing an experiment that should allow one to

see QuI in multiphoton ionization, using rubidium atoms prepared in the $5^2P_{1/2}$ or $5^2P_{3/2}$ excited states as the target species. This target requires two photons at 800 nm to ionize, which give significantly higher ionization rates and therefore allows the experiment to be performed at lower intensities.

In summary, this dissertation found that OI plays a significant role in optimal control experiments that use ionization as an intermediate step, by changing the intensity of the shaped pulse. Small imperfections in the pulse can cause surprisingly large changes to the OI, and resultant ionization yield. Furthermore, an experiment was proposed and developed that enables the first unambiguous detection of quantum interference in multiphoton ionization from a pair of phase-locked pulses.

Appendix A: Correction of Non-uniform Step Size in the Translation Stage

This appendix describes how the non-uniform step size of the Aerotech ALS-130 translation stage was corrected after the MZ experiments so that the relationship between step number s and TPP delay τ was well-known.

The ideal relationship between s and τ is given by Eq. 3.14. For the case where the step size is uniform, k_0 is a constant in Eq. 3.14, 0.157 rad/step in the case of 20 nm steps.

The step size in the MZ experiments was not uniform, however. This was most clearly demonstrated by measuring the power interferometry of the MZ. The power interferometry signal is a measurement of the TPP average power P as a function of the stage step number s. If each step $s = 20$ nm, then the period of the power interference fringes should be 40.35 steps, the number of steps it takes to change the path length of the variable arm by one laser wavelength ($\lambda_0 = 807$ nm).

The power interferometry observed in the experiment is shown in Fig. A.1, showing that the period of the power interference fringes drifts. Correction of the non-uniform step size proceeds as follows. First, the oscillatory portion of the power interferometry signal in Fig. A.1 is isolated by subtracting a baseline from P (the

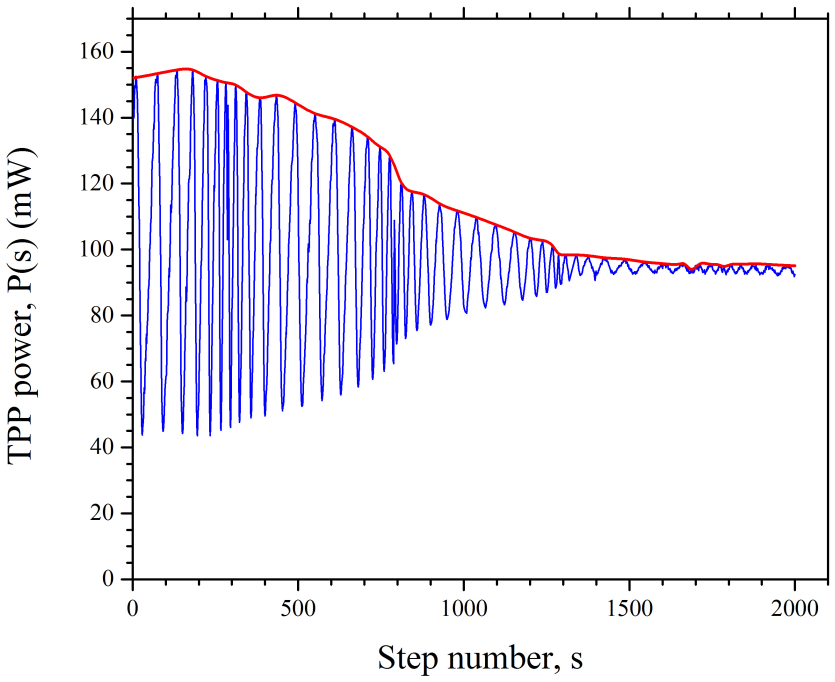

Fig. A.1: Twin-peaked pulse power P as a function of the translation stage step number s, shown in blue. Each step was nominally 20 nm. The non-uniform period of the power interference fringes means that the stage was not taking uniform step sizes throughout the experiment. The envelope of the power oscillations is shown in red.

baseline is $P(|\tau| \to \infty)$, 93.75 mW in this case), and then dividing by the envelope. The envelope is shown as a red curve in Fig. A.1. This normalized power, labeled as $\mathcal{P}$, is shown in Fig. A.2. One requires that $\mathcal{P}$ be a uniform, sinusoidal curve, but there are two main deviations from this shape. The first is the previously mentioned frequency drift. The second is that there are several breaks in the fringes (at steps 287, 789, 1285, and 1784–approximately every 500 steps). There is also considerable noise for $s > 1300$, due to the small oscillation amplitude when the peaks of the TPP are well-separated. The data in Fig. A.2 were split up into five individual sections around the four break points. The second section, between steps 287 and 788, is shown in Fig. A.3. Then, each of the five data sections was fit to the expected sinusoidal power interference function:

$$\mathcal{P}(s) = \mathcal{P}_0 + \mathcal{P}_1 \cos\left(\omega_0 \tau(s)\right), \tag{A.1}$$

where $\mathcal{P}_1 \simeq 1$ is the oscillation amplitude and $\mathcal{P}_0 \simeq 0$ is the baseline. Due to the stage drift, $\tau(s)$ must be modified from Eq. 3.14 in the following way:

$$\tau(s) = \frac{k_0}{\omega_0}\left[s + \Delta s \cos\left(\bar{k}s + \alpha\right)\right] + \tau_0, \tag{A.2}$$

where $\bar{k}$ and α determine the period and the phase shift of the stage drift, respectively, and Δs gives the modulation strength of the drift (the larger Δs is, the larger the difference between minimum and maximum step size). Each of the five sections was fit to Eq. A.1 using $\tau(s)$ as defined in Eq. A.2. The values of the fitting parameters for each section are shown in Tab. A.1, and these values determine the

relationship between step number s and TPP delay τ. The relationship $\tau(s)$ is shown in Fig. A.4; the corrected power interferometry signal $P(\tau)$ was previously shown in the main text, Fig. 3.14. It can be seen that upon application of this correction, the power interferometry fringes become much more uniform as expected. It should further be noted that the fit of the data in Fig. A.3 will only give a τ_0 value modulo the optical period of the laser. As a result, τ_0 for each section was artificially shifted to line up the five different sections and keep the τ separation between interference peaks equal to $2\pi j/\omega_0$, where j is an integer.

This correction procedure was applied to the "Ions" experiment using the high-resolution MZ stage, Sec. 4.4, from which the data in this appendix was taken. The same procedure was used for the "Electrons" experiments in which phase-tagging (Sec. 7.2) was not used: these were the high-intensity "Electrons" experiments in xenon at 800 nm (Sec. 8.2.1) and 400 nm (Sec. 8.3.1).

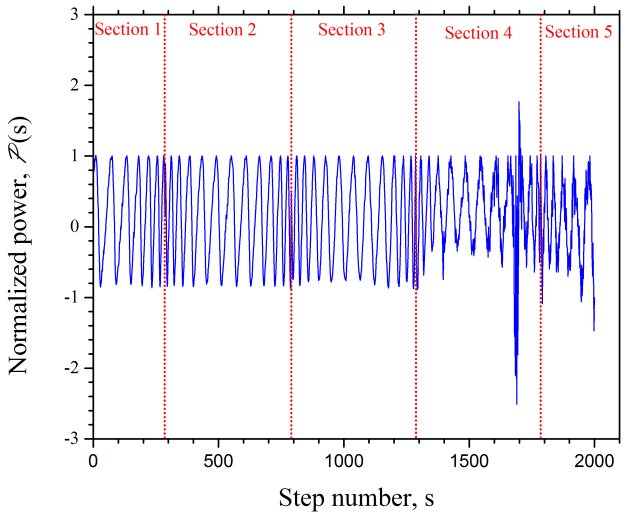

Fig. A.2: Normalized twin-peaked pulse power $\mathcal{P}$, found by subtracting the baseline ($P(\tau \to \infty)$) and dividing by the envelope shown in Fig. A.1, vs step number s. Because of breaks in the data, $\mathcal{P}$ was divided up into five sections as indicated.

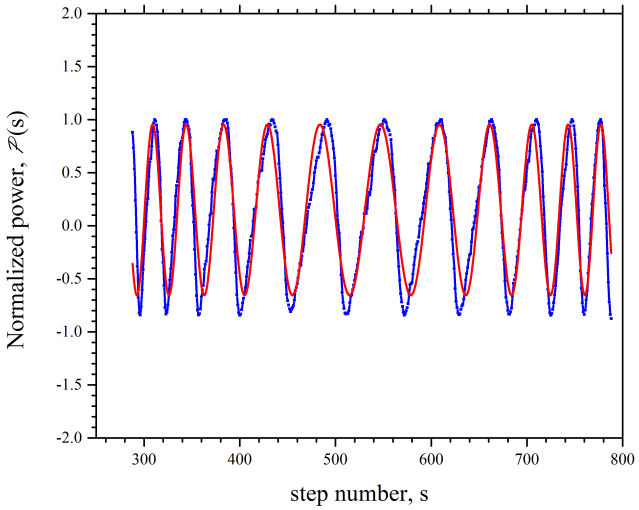

Fig. A.3: Section 2 from Fig. A.2 (blue points), showing the period drift of the power interference fringes. The data were fit to Eq. A.1, using $\tau(s)$ as defined in Eq. A.2. The parameters of the fit for this section and the others are given in Tab. A.1.

Tab. A.1: fitted values of the parameters in Eqs. A.1 and A.2, for each of the five section of the data shown in Fig. A.1. [a]The delay shift τ_0 was not fit but was rather added post-fit to line all of the sections up with each other in the corrected data shown in Fig. 3.14. [b]The fit on section 5 was not successful, so the fit values for section 4 were used to correct section 5 data.

Section	$\mathcal{P}_0$	$\mathcal{P}_1$	k_0 (rad/step)	Δs (steps)	$\bar{k}$ (rad/step)	α (rad)	τ_0 (fs)[a]
1	0.16(1)	0.83(3)	0.228(3)	77(3)	0.0074(2)	1.08(4)	13.5
2	0.15(1)	0.80(4)	0.1547(6)	39.2(5)	0.00950(8)	2.73(5)	15.35
3	0.12(1)	0.84(7)	0.1726(3)	49.8(2)	0.00856(4)	5.22(4)	6
4	0.71(5)	1.5(5)	0.1405(5)	30.5(5)	0.0116(1)	2.6(1)	21.1
5[b]	0.71	1.5	0.1405	30.5	0.0116	2.6	21.5

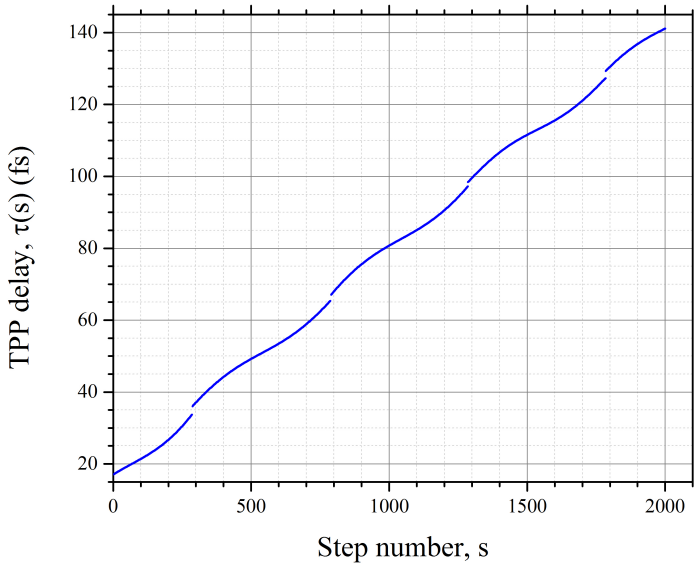

Fig. A.4: Recovered $\tau(s)$ for the five sections, constructed using the values in Tab. A.1 and Eq. A.2.

Appendix B: Temporal Resolution of Pulse Shaping and Measurement Devices

Several devices were used to shape and characterize the ultrafast pulses, described in Chap. 3. In this Appendix, the τ resolution of three of these devices – the spectrometer, the SD-FROG, and the SLM – will be derived. The Wizzler cannot measure complicated pulses including TPPs, so its temporal resolution is not considered here.

B.1 Derivation of τ resolution

First, it is helpful to define some of the terminology that will be used in this section. In both TPP synthesis and measurement, τ is determined by the fringe spacing in the TPP spectrum. An example TPP spectrum, $\tilde{I}_{TPP}(\omega)$, is shown in Fig. B.1. The fringe spacing in frequency space is labeled $\delta\omega \simeq 0.025$. One can determine τ by fitting $\tilde{I}_{TPP}(\omega)$ to Eq. 3.13; alternatively, one finds from Eq. 3.13 that τ can be determined directly from $\delta\omega$, namely,

$$\tau\delta\omega = 2\pi. \tag{B.1}$$

For the TPP in Fig. B.1, $\tau \simeq 250$ fs. Clearly, the τ resolution is related to the

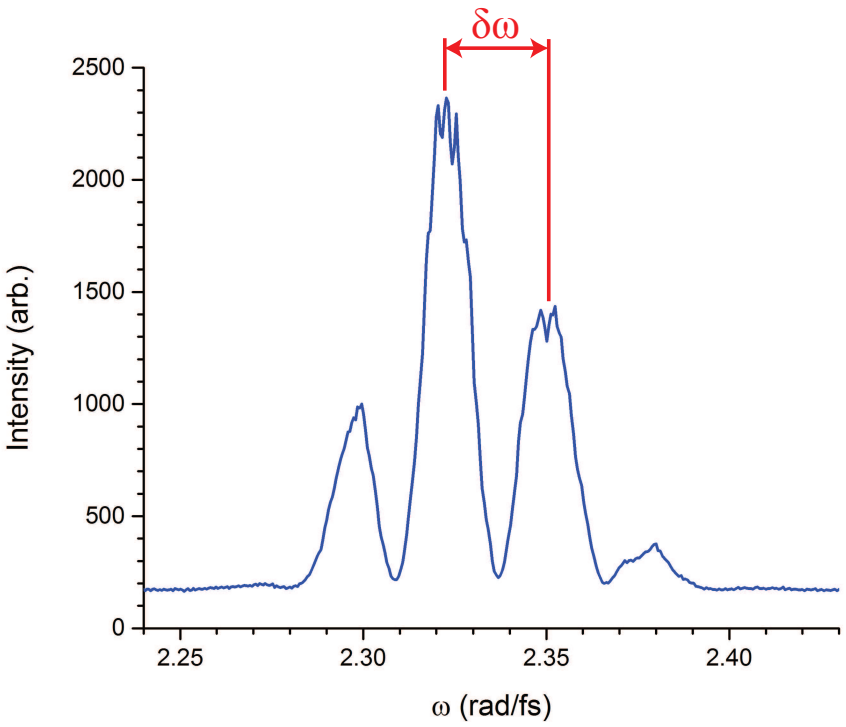

Fig. B.1: Example TPP spectrum $\tilde{I}_{TPP}(\omega)$, with the fringe spacing $\delta\omega$ labeled.

angular frequency resolution.

The three devices used to shape and measure TPPs in this work do not have a uniform angular frequency resolution, instead having a uniform wavelength resolution. The wavelength is related to the frequency by

$$\omega = \frac{2\pi c}{\lambda}, \tag{B.2}$$

which one differentiates to find

$$|\delta\omega| = \frac{2\pi c}{\lambda^2}\delta\lambda, \tag{B.3}$$

where $\delta\lambda$ is the fringe spacing in wavelength. In this equation, $\delta\omega$ is negative. However, the fringe spacing is by definition positive, so the absolute value is taken here. Substitution of Eq. B.3 into Eq. B.1 gives

$$\tau = \frac{\lambda^2}{\delta\lambda c}. \tag{B.4}$$

One wishes to answer the following question: how much does τ change when the fringe spacing $\delta\lambda$ changes by some amount? The change in fringe spacing will be called $\delta(\delta\lambda)$, the corresponding change in τ is $\delta\tau$. One further differentiation of Eq. B.4 allows one to determine $\delta\tau$ (with an absolute value taken for the same reason as in Eq. B.3):

$$\begin{aligned} |\delta\tau| &= \frac{\lambda^2}{\delta\lambda^2 c}\delta(\delta\lambda) \\ &= \frac{\tau^2 c}{\lambda^2}\delta(\delta\lambda). \end{aligned} \tag{B.5}$$

B.2 Spectrometer

The spectrometer used in this work consisted of 3447 pixels evenly spaced between 350 nm and 1000 nm. This gives a wavelength resolution of 0.189 nm/px. If two measured TPPs have fringe spacings that differ by less than this resolution, then the spectrometer cannot uniquely differentiate the two values of τ. Sub-pixel centroiding could increase this resolution but is not employed in this dissertation. As an example, for $\tau = 150$ fs, $\lambda = 807$ nm, and $\delta(\delta\lambda) = 0.189$ nm, Eq. B.5 finds that $\delta\tau = 1.96$ fs. So, for example, a measurement using the spectrometer cannot differentiate between a TPP with $\tau = 150$ fs and one with $\tau = 151.5$ fs. The temporal resolution as a function of τ for $\lambda = 807$ nm is given in Fig. B.2.

B.3 SD-FROG

The SD-FROG does not detect the fundamental pulse spectrum, but instead detects the spectrum of the beam produced by a nonlinear effect (self-diffraction, see Sec. 3.3.2). However, the self-diffraction spectrum also consists of fringes with the same fringe spacing as the fundamental spectrum, which means that the temporal resolution of the FROG is also given by Eq. B.5, where $\delta(\delta\lambda)$ is the wavelength resolution of the spectrometer used to detect the SD signal. This spectrometer had 747 pixels, spaced evenly between 768 and 837 nm, for a wavelength resolution of 0.092 nm/px. This gives $\delta\tau = 0.95$ fs when $\tau = 150$ fs and $\lambda = 807$ nm. The temporal resolution as a function of τ for $\lambda = 807$ nm is given in Fig. B.2.

B.4 Spatial Light Modulator

In the SLM, the input pulse is spectrally dispersed across the liquid crystal arrays, which consist of 128 pixels (see Sec. 3.2.1). To make a TPP, the spectral fringes shown in Fig. B.1 are imprinted onto the input pulse. This means that once again, the temporal resolution can be found from Eq. B.5, where $\delta(\delta\lambda)$ is the wavelength resolution of the SLM liquid crystal array. The range of wavelengths that were incident on the SLM face varied slightly from experiment to experiment; a representative experiment is considered here, where the first pixel corresponded to light at 784 nm and the last pixel corresponded to light at 828 nm. The wavelengths within this range were evenly distributed across the 128 pixel array, giving a wavelength resolution of 0.344 nm/px. This gives $\delta\tau = 3.57$ fs when $\tau = 150$ fs and $\lambda = 807$ nm. The temporal resolution as a function of τ for $\lambda = 807$ nm is given in Fig. B.2.

The temporal resolution is much better at lower values of τ for all three devices, however there is a lower limit in determining τ using the fringe spacing. For the 800 nm pulses used in this work $\Delta\lambda_{FWHM} \simeq 20$ nm. When $\tau \simeq 100$ fs, one finds that the fringe spacing $\delta\lambda \simeq 20$ nm. In this case, there is only one fringe underneath the pulse envelope and so the fringe spacing can not be determined in the experiment. As such, this method of determining τ is not useful when $\tau < 100$ fs.

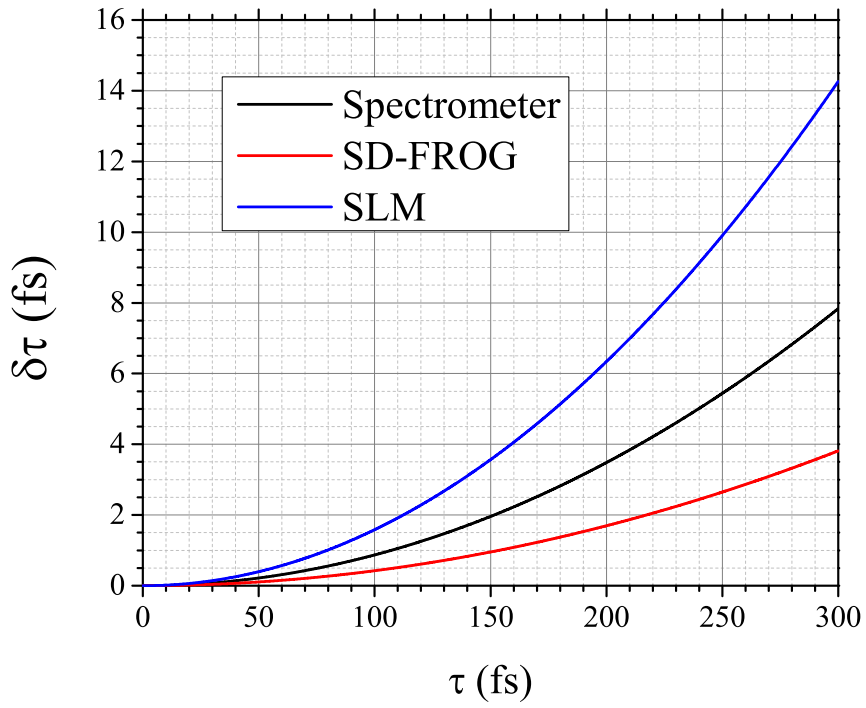

Fig. B.2: Inter-peak delay resolution $\delta\tau$ vs τ for the three TPP synthesis/measurement devices: The spectrometer (black), the SD-FROG (red), and the SLM (blue).

Appendix C: MATLAB Code for QuI Model

The following program, written in MATLAB, computes the ionization yield for an eight-photon ionization from a TPP numerically, using time-dependent perturbation theory as described in Sec. 6.2.

```
%QuantumInterferenceModel.m
%Author:  Davy Foote
%Version:  1.1
%Date:  March 28, 2016


clear, clc
close all


%This program calculates the photoelectron
%spectrum as a function of both tau and electron energy.
%The photoelectron spectrum (PES) is found for an n-photon
%ionization by finding the Fourier transform of the nth
%power of the electric field.


lambda0=800; %central wavelength of the laser, in nm
FWHM=80; %pulse width, in fs
E0=1; %Peak electric field of first pulse
beta=1; %ratio of second/first peak electric field
phi12=0; %relative pulse CEP, in rad
n=8; %multiphoton order
hbar=6.626E-34/(2*pi); %reduced Planck's constant
```

```
tau=100.1:0.01:110; %TPP delay, in fs
t=-99.9:0.1:350; %time in fs


deltaT=0.568*FWHM;
omega0=2*pi*299.79/lambda0;
deltaOmega=4/deltaT;
%omegaC is the range of energies over which the ionization
%yield is calculated.
omegaC=n*omega0-4*deltaOmega:0.05*deltaOmega:n*omega0+4*deltaOmega;


%Initialize array for the nth power of electric field
Integrand=zeros(length(tau),length(t),length(omegaC));


%Initialize array for the multiphoton transition amplitude
An=zeros(length(tau),length(omegaC));


for i=1:length(tau)
    %Initialize the array for the TPP electric field
     ETPP=zeros(1,length(t));


    %Print the running step number
    fprintf('%04.1f percent', 100*i/length(tau));


    for j=1:length(t)
        %Compute the TPP electric field
         ETPP(j)=E0*exp(-1i*omega0*t(j))*(sech(t(j)/deltaT)^2
        +beta*sech((t(j)-tau(i))/deltaT)^2
        *exp(1i*omega0*tau(i))*exp(1i*phi12))
        +E0*exp(1i*omega0*t(j))*(sech(t(j)/deltaT)^2
        +beta*sech((t(j)-tau(i))/deltaT)^2
        *exp(-1i*omega0*tau(i))*exp(1i*phi12));
    end


    for j=1:length(t)
```

```
          %Compute the integrand
          for k=1:length(omegaC)
               Integrand(i,j,k)=(1/sqrt(2*pi))
               *(ETPP(j)^n)*exp(1i*omegaC(k)*t(j));
          end
     end


     %Integrate the integrand to get An
     for k=1:length(omegaC)
          An(i,k)=trapz(t,Integrand(i,:,k));
     end
     clear ETPP
     fprintf('\b\b\b\b\b\b\b\b\b\b\b\b');
end


fprintf('\b\b\b\n Done!  \n\n');
clear i
clear j
clear k


%Compute the photoelectron spectrum, |An|^2
PES=abs(An).^2;


%convert from frequency to energy (eV)
U=(hbar*omegaC*1E15)/1.602E-19;


%Ionization potential of xenon in eV
IP=12.13;


%plot the photoelectron spectrum as a function of electron
%energy, U-IP, and tau.

figure, imagesc(U-IP,tau,PES);
```

Appendix D: MATLAB Code for BASEX Abel Inversion

The following program, written in MATLAB, implements the BASEX Abel inversion algorithm described in Sec. 7.4.1 and Ref. [136]. The program computes two matrices, `A` and `B`, such that `A`×`Im`×`B`=`C`, where `Im` is the original image and `C` is the expansion coefficient matrix (equivalent to the inverted image, see Eq. 7.13).

```
%AbelBASEX.m
%Author:  Davy Foote
%Version:  1.0
%Date:  August 23, 2016


clear, clc
close all


%First, declare the maximum size of the image to be inverted
imageSizeX = 501;
imageSizeZ = 501;


%Now, declare the size of the basis set in both r and z
Kx = 250;
Kz = 250;


%Other user parameters
q1 = 50; %regularization parameter for matrix A
q2 = 10; %regularization parameter for matrix B
sigma = 1; %basis function scaling parameter
```

```
x = round(-imageSizeX/2)+1:round(imageSizeX/2)-1;
z = round(-imageSizeZ/2)+1:round(imageSizeZ/2)-1;


%Define the two basis function transform matrices
X = zeros(Kx, imageSizeX);
Z = zeros(Kz, imageSizeZ);


%Now fill in the values of X
for i = 1:imageSizeX
      clc
      fprintf('Computing X: On step %i of %i \n', i, imageSizeX);
      for k = 0:Kx-1
           sum_tmp = 0;


           %step through l to compute the sum in the definition for
           %X_k^2(x/sigma)
           for l = 0:k^2


               %Each term in the sum is alpha_l/gamma_(k^2-l)*R_k^2(x/sigma)
               %We only need to add a term to the sum if x/sigma is close
               %to sqrt(k^2-l), so perform that check here.
                if abs(abs(x(i))/sigma-sqrt(k^2-l))<5


                    %Compute alpha
                    alpha_l = 1;
                    for a=1:l
                         alpha_l = alpha_l * (1-(1/(2*a)));
                    end


                    %Compute gamma.  The definition of gamma,
                    %gamma_a=(e/a)^a*a!, has problems for large a.
                    %To correct this, I took the log of gamma_a,
                    %added the two terms, and then exponentiated.
                    %ln(a!)  was found w/ Stirling's approximation.
                    %When a=0, this approximation fails, but
```

```
                    %gamma_a(0)=1 so I hard-coded it.


                    a=k^2-l;
                    if a==0
                         gamma_k2_l=1;
                    else
                         term1=a*log(exp(1)/a);
                         term2=a*log(a)-a+0.5*log(2*pi*a);
                         gamma_k2_l = exp(term1+term2);
                    end


                    %Add to the sum.  R_k^2(x/sigma) is the exponential.
                    sum_tmp = sum_tmp + exp(-2*(x(i)/sigma-sqrt(k^2-l))^2)
                    *(alpha_l)/(gamma_k2_l);
               end
          end


          %To find X_ki, I need to find gammaK_k^2.  I used the same
          %procedure as above to calculate this gamma.
          if k^2==0
               gamma_k2=1;
          else
               term1=k^2*log(exp(1)/k^2);
               term2=k^2*log(k^2)-k^2+0.5*log(2*pi*k^2);
               gamma_k2 = exp(term1+term2);
          end


          %Finally, write the value of gamma to X
          X(k+1,i) = 2*gamma_k2*sum_tmp;
     end
end


%Now compute A
A=(X*X'+q1^2*eye(Kx))\X;
```

```
%Now compute Z. Z is defined to be just rho_m(z_j), and according to
%the appendix of the BASEX paper, rho_m(z_j)=R_m^2(z_j/sigma)
for j=1:imageSizeZ
     clc
      fprintf('Computing Z: On step %i of %i\n', i, imageSizeZ);
      for m = 0:Kz-1


          %Similar check to x
          if abs(abs(z(j))/sigma-m)<5
               Z(m+1,j) = exp(-2*(z(j)/sigma-m)^2);
          end
     end
end


%Now compute B
B=Z'/(Z*Z'+q2^2*eye(Kz));


%The inverted image is C = A*ExampleImage*B;
```

Bibliography

[1] A. H. Zewail. The birth of molecules. *Scientific American*, 263:76–82, 1990.

[2] A. H. Zewail. Femtochemistry: Atomic-scale of the chemical bond using ultrafast lasers. In I. Grenthe, editor, *Nobel Lectures in Chemistry 1996-2000*. World Scientific, 2003.

[3] H. Rabitz. Shaped laser pulses as reagents. *Science*, 299(5606):525–527, 2003.

[4] H. Rabitz. Strong-arming molecular dynamics. *Science*, 314(5797):564–265, 2006.

[5] G. Mainfray and G. Manus. Multiphoton ionization of atoms. *Reports on Progress in Physics*, 54(10):1333, 1991.

[6] L. D. Landau and E. M. Lifshitz. *Quantum Mechanics*, chapter 10, pages 275–276. Pergamon, New York, 2 edition, 1965.

[7] L. V. Keldysh. Ionization in the field of a strong electromagnetic wave. *Soviet Physics JETP*, 20(5):1307–1314, 1965.

[8] A. M. Perelomov, V. S. Popov, and M. V. Terent'ev. Ionization of atoms in an alternating electromagnetic field. *Soviet Physics JETP*, 50:1393–1409, 1966.

[9] M. V. Ammosov, N. B. Delone, and V. P. Krainov. Tunnel ionization of complex atoms and of atomic ions in an alternating electromagnetic field. *Soviet Physics JETP*, 64(6):924–934, 1986.

[10] S. F. J. Larochelle, A. Talebpour, and S. L. Chin. Non-sequential multiple ionization of rare gas atoms in a Ti:sapphire laser field. *Journal of Physics B: Atomic, Molecular and Optical Physics*, 31(6):1201, 1998.

[11] J. L. Krause, K. J. Schafer, and K. C. Kulander. High-order harmonic generation from atoms and ions in the high intensity regime. *Physical Review Letters*, 68:3535–3538, 1992.

[12] P. B. Corkum. Plasma perspective on strong field multiphoton ionization. *Physical Review Letters*, 71:1994–1997, 1993.

[13] M. Lewenstein, Ph. Balcou, M. Yu. Ivanov, A. L'Huillier, and P. B. Corkum. Theory of high-harmonic generation by low-frequency laser fields. *Physical Review A*, 49:2117–2132, 1994.

[14] M. Hentschel, R. Kienberger, Ch. Spielmann, G. A. Reider, N. Milosevic, T. Brabec, P. Corkum, U. Heinzmann, M. Drescher, and F. Krausz. Attosecond metrology. *Nature*, 414:509–513, 2001.

[15] P. M. Paul, E. S. Toma, P. Breger, G. Mullot, F. Augé, Ph. Balcou, H. G. Muller, and P. Agostini. Observation of a train of attosecond pulses from high harmonic generation. *Science*, 292(5522):1689–1692, 2001.

[16] G. Sansone, E. Benedetti, F. Calegari, C. Vozzi, L. Avaldi, R. Flammini, L. Poletto, P. Villoresi, C. Altucci, R. Velotta, S. Stagira, S. De Silvestri, and M. Nisoli. Isolated single-cycle attosecond pulses. *Science*, 314(5798):443–446, 2006.

[17] F. Krausz and M. Ivanov. Attosecond physics. *Reviews of Modern Physics*, 81:163–234, 2009.

[18] National Research Council Committee on AMO2010. *Controlling the Quantum World: The Science of Atoms, Molecules, and Photons.* The National Academies Press, 2007.

[19] F. Légaré, K. F. Lee, I. V. Litvinyuk, P. W. Dooley, A. D. Bandrauk D. M. Villeneuve, and P. B. Corkum. Imaging the time-dependent structure of a molecule as it undergoes dynamics. *Physical Review A*, 72:052717, 2005.

[20] M. P. Minitti, J. M. Budarz, A. Kirrander, J. S. Robinson, D. Ratner, T. J. Lane, D. Zhu, J. M. Glownia, M. Kozina, H. T. Lemke, M. Sikorski, Y. Feng, S. Nelson, K. Saita, B. Stankus, T. Northey, J. B. Hastings, and P. M. Weber. Imaging molecular motion: Femtosecond x-ray scattering of an electrocyclic chemical reaction. *Physical Review Letters*, 114:255501, 2015.

[21] M. Centurion. Viewpoint: Making a molecular movie with x rays. *Physics*, 8(59), 2015.

[22] J. M. Glownia, A. Natan, J. P. Cryan, R. Hartsock, M. Kozina, M. P. Minitti, S. Nelson, J. Robinson, T. Sato, T. van Driel, G. Welch, C. Weninger, D. Zhu, and P. H. Bucksbaum. Self-referenced coherent diffraction x-ray movie of ångstrom- and femtosecond-scale atomic motion. *Physical Review Letters*, 117:153003, 2016.

[23] M. J. J. Vrakking. Viewpoint: Showtime for molecular movies. *Physics*, 9(112), 2016.

[24] R. J. Levis and H. A. Rabitz. Closing the loop on bond selective chemistry using tailored strong field laser pulses. *Journal of Physical Chemistry A*, 106(27):6427–6444, 2002.

[25] R. J. Levis, G. M. Menkir, and H. Rabitz. Selective bond dissociation and rearrangement with optimally tailored, strong-field laser pulses. *Science*, 292(5517):709–713, 2001.

[26] R. S. Judson and H. Rabitz. Teaching lasers to control molecules. *Physical Review Letters*, 68(10):1500–1503, 1992.

[27] W. S. Warren, H. Rabitz, and M. Dahleh. Coherent control of quantum dynamics: the dream is alive. *Science*, 259(5101):1581–1589, 1993.

[28] G.-Y. Chen, Z. W. Wang, and W. T. Hill, III. Adaptive control of the CO_2 bending vibration: Deciphering field-system dynamics. *Physical Review A*, 79:011401(R), 2009.

[29] S. Singha, Z. Hu, and R. J. Gordon. Closed-loop coherent control of electronic transitions in gallium arsenide. *Journal of Physical Chemistry A*, 115(23):6093–6101, 2011.

[30] F. Langhojer, D. Cardoza, M. Baertschy, and T. Weinacht. Gaining mechanistic insight from closed loop learning control: The importance of basis in searching the phase space. *Journal of Chemical Physics*, 122:014102, 2005.

[31] T. Bayer, M. Wollenhaupt, and T. Baumert. Strong-field control landscapes of coherent electronic excitation. *Journal of Physics B: Atomic, Molecular, and Optical Physics*, 41:074007, 2008.

[32] V. V. Lozovoy, X. Zhu, T. C. Gunaratne, D. Ahmasi Harris, J. C. Shane, and M. Dantus. Control of molecular fragmentation using shaped femtosecond pulses. *Journal of Physical Chemistry A*, 112:3789–3812, 2008.

[33] N. Schirmel, N. Reusch, P. Horsch, and K.-M. Weitzel. Formation of fragment ions (H^+, H_3^+, CH_3^+) from ethane in intense femtosecond laser felds – from understanding to control. *Faraday Discussions*, 163:461, 2013.

[34] I. Plesser, Z. Vager, and R. Naaman. Structure of C_3 as measured by the coulomb-explosion technique. *Physical Review Letters*, 56:1559–1562, 1986.

[35] Z. Vager, R. Naaman, and E. P. Kanter. Coulomb explosion imaging of small molecules. *Science*, 244(4903):426–431, 1989.

[36] A. E. Siegman. *Lasers*. University Science Books, Sausalito, California, 1986.

[37] W. S. Warren and Ahmed H. Zewail. Multiple phasecoherent laser pulses in optical spectroscopy. i. the technique and experimental applications. *The Journal of Chemical Physics*, 78(5):2279–2297, 1983.

[38] F. Spzno, M. Haner, and W.S. Warren. Spectroscopic demonstration of picosecond, phase-shifted laser multiple-pulse sequences. *Chemical Physics Letters*, 135(1):97 – 102, 1987.

[39] John T. Fourkas, William L. Wilson, G. Wäckerle, Amy E. Frost, and M. D. Fayer. Picosecond time-scale phase-related optical pulses: measurement of sodium optical coherence decay by observation of incoherent fluorescence. *J. Opt. Soc. Am. B*, 6(10):1905–1910, 1989.

[40] N. F. Scherer, A. J. Ruggiero, M. Du, and G. R. Fleming. Time resolved dynamics of isolated molecular systems studied with phaselocked femtosecond pulse pairs. *The Journal of Chemical Physics*, 93(1):856–857, 1990.

[41] M. Wollenhaupt, M. Krug, J. Köhler, T. Bayer, C. Sarpe-Tudoran, and T. Baumert. Photoelectron angular distributions from strong-field coherent electronic excitation. *Applied Physics B*, 95(2):245–259, 2009.

[42] P. Hockett, M. Wollenhaupt, and T. Baumert. Coherent control of photoelectron wavepacket angular interferograms. *Journal of Physics B: Atomic, Molecular and Optical Physics*, 48(21):214004, 2015.

[43] N. Kanda, T. Higuchi, H. Shimizu, K. Konishi, K. Yoshioka, and M. Kuwata-Gonokami. The vectorial control of magnetization by light. *Nature Communications*, 2(362):1–5, 2011.

[44] T. Hornung, R. Meier, R. de Vivie-Riedle, and M. Motzkus. Coherent control of the molecular four-wave-mixing response by phase and amplitude shaped pulses. *Chemical Physics*, 267(13):261 – 276, 2001.

[45] V. G. Nikiforov, A. G. Shmelev, G. M. Safiullin, and V. S. Lobkov. Coherent control of vibrational and rotational molecular motions using double-pulse optical kerr effect. *Chemical Physics Letters*, 592:196 – 199, 2014.

[46] T. Hornung, R. Meier, and M. Motzkus. Optimal control of molecular states in a learning loop parameterization in frequency and time domain. *Chemical Physics Letters*, 326:445–453, 2000.

[47] C. Daniel, J. Full, L. González, C. Lupulescu, J. Manz, A. Merli, S. Vajda, and L. Wöste. Deciphering the reaction dynamics underlying optimal control laser fields. *Science*, 299(5606):536–539, 2003.

[48] E. Papastathopoulos, M. Strehle, and G. Gerber. Optimal control of femtosecond multiphoton double ionization of atomic calcium. *Chemical Physics Letters*, 408(13):65 – 70, 2005.

[49] N. X. Truong, P. Hilse, S. Göde, A. Przystawik, T. Döppner, Th. Fennel, Th. Bornath, J. Tiggesbäumker, M. Schlanges, G. Gerber, and K. H. Meiwes-Broer. Optimal control of the strong-field ionization of silver clusters in helium droplets. *Physical Review A*, 81:013201, 2010.

[50] V. Blanchet, C. Nicole, M.-A. Bouchene, and B. Girard. Temporal coherent control in two-photon transitions: From optical interferences to quantum interferences. *Physical Review Letters*, 78(14):2716–2719, 1997.

[51] P. Lambropoulos. Topics on multiphoton processes in atoms. In D.R. Bates and B. Bederson, editors, *Topics on Multiphoton Processes in Atoms*, volume 12 of *Advances in Atomic and Molecular Physics*, pages 87 – 164. Academic Press, 1976.

[52] P. Lambropoulos. Mechanisms for multiple ionization of atoms by strong pulsed lasers. *Physical Review Letters*, 55:2141–2144, 1985.

[53] L. Pan, B. Sundaram, and L. Armstrong. Dressed-state perturbation theory for multiphoton ionization of atoms. *Journal of the Optical Society of America B*, 4(5):754–759, May 1987.

[54] J. H. Posthumus. The dynamics of small molecules in intense laser fields. *Reports on Progress in Physics*, 67(5):623, 2004.

[55] T. D. Scarborough, J. Strohaber, D. B. Foote, C. J. McAcy, and C. J. G. J. Uiterwaal. Ultrafast REMPI in benzene and the monohalobenzenes without the focal volume effect. *Physical Chemistry Chemical Physics*, 13:13783–13790, 2011.

[56] S. V. Popruzhenko. Keldysh theory of strong field ionization: history, applications, difficulties and perspectives. *Journal of Physics B: Atomic, Molecular and Optical Physics*, 47(20):204001, 2014.

[57] G. N. Gibson, R. R. Freeman, T. J. McIlrath, and H. G. Muller. Excitation and ionization dynamics in short-pulse multiphoton ionization. *Physical Review A*, 49:3870–3874, 1994.

[58] T. Marchenko, H. G. Muller, K. J. Schafer, and M. J. J. Vrakking. Wavelength dependence of photoelectron spectra in above-threshold ionization. *Journal of Physics B: Atomic, Molecular and Optical Physics*, 43(18):185001, 2010.

[59] S. Speiser and J. Jortner. The 3/2 power law for high order multiphoton processes. *Chemical Physics Letters*, 44(3):399 – 403, 1976.

[60] J. Strohaber and C. J. G. J. Uiterwaal. In situ measurement of three-dimensional ion densities in focused femtosecond pulses. *Physical Review Letters*, 100:023002, 2008.

[61] W. D. M. Lunden, P. Sándor, T. C. Weinacht, and T. Rozgonyi. Model for describing resonance-enhanced strong-field ionization with shaped ultrafast laser pulses. *Physical Review A*, 89:053403, 2014.

[62] A. M. Popov, O. V. Tikhonova, and E. A. Volkova. Strong-field atomic stabilization: numerical simulation and analytical modeling. *Journal of Physics B: Atomic, Molecular, and Optical Physics*, 36:R125–R165, 2003.

[63] M. Gavrila. Atomic stabilization in superintense laser fields. *Journal of Physics B: Atomic, Molecular, and Optical Physics*, 35:R147–R193, 2002.

[64] M. V. Fedorov, N. P. Poluektov, A. M. Popov, O. V. Tikhonova, V. Yu. Kharin, and E. A. Volkova. Interference stabiliation revisited. *IEEE Journal of Selected Topics in Quantum Electronics*, 18(1):42–53, 2012.

[65] M. Pont, N. R. Walet, M. Gavrila, and C. W. McCurdy. Dichotomy of the hydrogen atom in superintense, high-frequency laser fields. *Physical Review Letters*, 61(8):939–943, 1988.

[66] M. Pont and M. Gavrila. Stabilization of atomic hydrogen in superintense, high-frequency laser fields of circular polarization. *Physical Review Letters*, 65(19):2362–2365, 1990.

[67] R. R. Jones and P. H. Bucksbaum. Ionization suppression of Stark states in intense laser fields. *Physical Review Letters*, 67(23):3215–3218, 1991.

[68] L. D. Noordam, H. Stapelfeldt, D. I. Duncan, and T. F. Gallagher. Redistribution of Rydberg states by intense picosecond pulses. *Physical Review Letters*, 68(10):1496–1499, 1992.

[69] L. Roso-Franco, G. Orriols, and J. H. Eberly. Rydberg stabilization in a model atom with a flat quasicontinuum. *Laser Physics*, 2(5):741–746, 1992.

[70] R. R. Jones, D. W. Schumacher, and P. H. Bucksbaum. Population trapping in Kr and Xe in intense laser fields. *Physical Review A*, 47(1):R49–R52, 1993.

[71] M. P. deBoer, J. H. Hoogenraad, R. B. Vrijen, L. D. Noordam, and H. G. Muller. Indications of high-intensity adiabatic stabilization in neon. *Physical Review Letters*, 71(20):3263–3266, 1993.

[72] M. P. deBoer, J. H. Hoogenraad, R. B. Vrijen, R. C. Constantinescu, L. D. Noordam, and H. G. Muller. Adiabatic stabilization against ionization: An experimental study. *Physical Review A*, 50(5):4085–4098, 1994.

[73] D. W. Schumacher and P. H. Bucksbaum. Phase dependence of intense-field ionization. *Physical Review A*, 54(5):4271–4278, 1996.

[74] A. Talebpour, C.-Y. Chien, and S. L. Chin. Population trapping in rare gases. *Journal of Physics B*, 29:5725–5733, 1996.

[75] N. J. van Druten, R. C. Constantinescu, J. M. Schins, H. Nieuwenhuize, and H. G. Muller. Adiabatic stabilization: Observing the surviving population. *Physical Review A*, 55(1):622–629, 1997.

[76] N. P. Poluektov and M. V. Fedorov. Phase control of the degree of ionization of Rydberg atoms by a strong laser field. *Journal of Experimental and Theoretical Physics*, 90(5):794–804, 2000.

[77] M. Born and E. Wolf. *Principles of Optics*. Pergamon Press, Headington Hill Hall, Oxford, UK, 4 edition, 1970.

[78] I. A. Walmsley and C. Dorrer. Characterization of ultrashort electromagnetic pulses. *Advances in Optics and Photonics*, 1(2):308–437, 2009.

[79] C. Cohen-Tannoudji, J. Dupont-Roc, and G. Grynberg. *Atom-Photon Interactions*, chapter 1, pages 9–12. John Wiley and Sons, Inc., New York, 1992.

[80] M. Wollenhaupt, A. Assion, D. Liese, Ch. Sarpe-Tudoran, T. Baumert, S. Zamith, M. A. Bouchene, B. Girard, A. Flettner, U. Weichmann, and G. Gerber. Interferences of ultrashort free electron wave packets. *Physical Review Letters*, 89(17):173001, 2002.

[81] M.A. Bouchene, V. Blanchet, C. Nicole, N. Melikechi, B. Girard, H. Ruppe, S. Rutz, E. Schreiber, and L. Wöste. Temporal coherent control induced by wave packet interferences in one and two photon atomic transitions. *The European Physical Journal D - Atomic, Molecular, Optical and Plasma Physics*, 2(2):131–141, 1998.

[82] D. B. Foote, Y. Lin, L.-W. Pi, J. M. Ngoko Djiokap, A. F. Starace, and W. T. Hill III. Ionization enhancement and suppression by phase-locked ultrafast pulse pairs. *Phys. Rev. A*, 96:023425, 2017.

[83] Spectra-Physics, 1335 Terra Bella Avenue, Mountain View, CA 94043 USA. *Spitfire Pro User's Manual*, 8 2006.

[84] Coherent, 5100 Patrick Henry Drive, Santa Clara, CA 95054 USA. *Verdi V-2/V-5/V-6 Operator's Manual*.

[85] S. Yefet and A. Pe'er. A review of cavity design for Kerr lens mode-locked solid-state lasers. *Applied Sciences*, 3(4):694–724, 2013.

[86] K. Zhao. Ultrafast dynamics of small molecules in strong fields, 2005. Ph.D. Thesis.

[87] Kapteyn-Murnane Laboratories Inc., 4699 Nautilus Court S. 205, Boulder, CO 80301 USA. *Model MTS Mini Ti:Sapphire Laser Kit Instruction Manual*, 2 1993.

[88] Quantronix, 41 Research Way, East Setauket, NY 11733 USA. *Darwin-527 Operator's Manual*, 5 2006.

[89] Cambridge Research and Instrumentation, Inc., 35-B Cabot Road, Woburn, MA 01801 USA. *SLM Spatial Light Modulator User's Manual*, 11 2010.

[90] A. M. Weiner, J. P. Heritage, and E. M. Kirschner. High-resolution femtosecond pulse shaping. *Journal of the Optical Society of America B*, 5(8):1563–1572, 1988.

[91] M. M. Wefers and K. A. Nelson. Analysis of programmable ultrashort waveform generation using liquid-crystal spatial light modulators. *Journal of the Optical Society of America B*, 12(7):1343–1362, Jul 1995.

[92] FASTLITE, 1900 route des crêtes - Les Bouillides, Les Collines de Sophia, 0650 Valbonne, France. *Wizzler System Operating Manual V1.2 and 1.3*, 4 2012.

[93] T. Oksenhendler, S. Coudreau, N. Forget, V. Crozatier, S. Grabielle, R. Herzog, O. Gobert, and D. Kaplan. Self-referenced spectral interferometry. *Applied Physics B*, 99(1):7–12, 2010.

[94] N. Minkovski, S. M. Saltiel, G. I. Petrov, O. Albert, and J. Etchepare. Polarization rotation induced by cascaded third-order processes. *Optics Letters*, 27(22):2025–2027, Nov 2002.

[95] A. Jullien, O. Albert, G. Chériaux, J. Etchepare, S. Kourtev, N. Minkovski, and S. M. Saltiel. Nonlinear polarization rotation of elliptical light in cubic crystals, with application to cross-polarized wave generation. *Journal of the Optical Society of America B*, 22(12):2635–2641, Dec 2005.

[96] L. Lepetit, G. Chériaux, and M. Joffre. Linear techniques of phase measurement by femtosecond spectral interferometry for applications in spectroscopy. *Journal of the Optical Society of America B*, 12(12):2467–2474, 1995.

[97] C. Dorrer and M. Joffre. Characterization of the spectral phase of ultrashort light pulses. *Comptes Rendus de l'Acadmie des Sciences - Series IV - Physics*, 2(10):1415 – 1426, 2001.

[98] R. Trebino. *Frequency-Resolved Optical Gating: The Measurement of Ultrashort Laser Pulses*. Kluwer Academic Publishers, 101 Philip Drive, Assinippi Park, Norwell, Massachusetts 02061, 2000.

[99] D. J. Kane and R. Trebino. Characterization of arbitrary femtosecond pulses using frequency-resolved optical gating. *IEEE Journal of Quantum Electronics*, 29(2):571–579, 1993.

[100] R. Trebino, K. W. DeLong, D. N. Fittinghoff, J. N. Sweetser, M. A. Krumbügel, B. A. Richman, and D. J. Kane. Measuring ultrashort laser pulses in the time-frequency domain using frequency-resolved optical grating. *Review of Scientific Instruments*, 68(9):3277–3295, 1997.

[101] M. Brewczyk, K. Rzążewski, and C. W. Clark. Appearance intensities for multiply charged ions in a strong laser field. *Physical Review A*, 52:1468–1473, 1995.

[102] S. Augst, D. Strickland, D. D. Meyerhofer, S. L. Chin, and J. H. Eberly. Tunneling ionization of noble gases in a high-intensity laser field. *Physical Review Letters*, 63:2212–2215, 1989.

[103] K. Zhao, T. Colvin, W. T. Hill III, and G. Zhang. Deconvolving two-dimensional images of three-dimensional momentum trajectories. *Review of Scientific Instruments*, 73(8):3044–3050, 2002.

[104] S. L. Chin. From multiphoton to tunnel ionization. In S. H. Lin, A. A. Villaeys, and Y. Fujimura, editors, *Advances in multi-photon processes and spectroscopy*, volume 16, chapter 3, pages 249–271. World Scientific, 5 Toh Tuck Link, Singapore 596224, 2004.

[105] A. F. Starace, L.-W. Pi, and J. M. Ngoko Djiokap. Private communication.

[106] T. F. Jiang. Calculation of atomic hydrogen and its photoelectron spectra in momentum space. *Computer Physics Communications*, 178(8):571 – 577, 2008.

[107] Z. Zhou and S.-I. Chu. Precision calculation of above-threshold multiphoton ionization in intense short-wavelength laser fields: The momentum-space approach and time-dependent generalized pseudospectral method. *Physical Review A*, 83:013405, 2011.

[108] T.-F. Jiang, S.-D. Jheng, Y.-M. Lee, and Z.-Y. Su. Lande subtraction method with finite integration limits and application to strong-field problems. *Physical Review E*, 86:066702, Dec 2012.

[109] J. Zhu and W. T. Hill III. Momentum and correlation spectra following intense-field dissociative ionization of H_2. *Journal of the Optical Society of America B*, 14(9):2212–2220, Sep 1997.

[110] G.-Y. Chen, J. Lee, H. Jang, D. B. Foote, and W. T. Hill III. *Progress in Ultrafast Intense Laser Science XII*, pages 1–20. Springer International Publishing, Cham, 2015.

[111] K. Zhao, G. Zhang, and W. T. Hill III. Image labeling: a graphical interface to correlation in multiparticle ejection dynamics. *Optics Express*, 9(1):42–48, 2001.

[112] K. Zhao, G. Zhang, and W. T. Hill III. Strong-field dissociative ionization of a linear triatomic molecule: Relationship between coulomb-explosion energies and bond angle. *Physical Review A*, 68:063408, 2003.

[113] K. Zhao and W. T. Hill III. Ejection anisotropy in three-atom coulomb explosions. *Physical Review A*, 71:013412, 2005.

[114] J. J. Sakurai and J. Napolitano. *Modern Quantum Mechanics*, chapter 5, page 356. Addison Wesley, Boston, 2 edition, 2011.

[115] M. P. de Boer and H. G. Muller. Observation of large populations in excited states after short-pulse multiphoton ionization. *Physical Review Letters*, 68:2747–2750, 1992.

[116] H. G. Muller, A. Tip, and M. J. van der Wiel. Ponderomotive force and AC Stark shift in multiphoton ionisation. *Journal of Physics B: Atomic, Molecular, and Optical Physics*, 16:L679–L685, 1983.

[117] S. F. J. Larochelle, A. Talebpour, and S. L. Chin. Coulomb effect in multiphoton ionization of rare-gas atoms. *Journal of Physics B: Atomic, Molecular and Optical Physics*, 31(6):1215, 1998.

[118] V. S. Popov. Tunneling and above-barrier ionization of atoms in a laser radiation field. *Journal of Experimental and Theoretical Physics*, 91(1):48–66, 2000.

[119] M. Li, J.-W. Geng, H. Liu, Y. Deng, C. Wu, L.-Y. Peng, Q. Gong, and Y. Liu. Classical-quantum correspondence for above-threshold ionization. *Physical Review Letters*, 112:113002, Mar 2014.

[120] N. I. Shvetsov-Shilovski, M. Lein, L. B. Madsen, E. Räsänen, C. Lemell, J. Burgdörfer, D. G. Arbó, and K. Tőkési. Semiclassical two-step model for strong-field ionization. *Physical Review A*, 94:013415, 2016.

[121] J. M. Ngoko Djiokap, S. X. Hu, L. B. Madsen, N. L. Manakov, A. V. Meremianin, and A. F. Starace. Electron vortices in photoionization by circularly polarized attosecond pulses. *Physical Review Letters*, 115:113004, 2015.

[122] J. M. Ngoko Djiokap, A. V. Meremianin, N. L. Manakov, S. X. Hu, L. B. Madsen, and A. F. Starace. Multistart spiral electron vortices in ionization by circularly polarized uv pulses. *Physical Review A*, 94:013408, 2016.

[123] D. Pengel, S. Kerbstadt, D. Johannmeyer, L. Englert, T. Bayer, and M. Wollenhaupt. Electron vortices in femtosecond multiphoton ionization. *Physical Review Letters*, 118:053003, 2017.

[124] V. Krylov, A. Rebane, A. G. Kalintsev, H. Schwoerer, and U. P. Wild. Second-harmonic generation of amplified femtosecond ti:sapphire laser pulses. *Optical Letters*, 20(2):198–200, 1995.

[125] J.-Y. Zhang, J. Y. Huang, H. Wang, K. S. Wong, and G. K. Wong. Second-harmonic generation from regeneratively amplified femtosecond laser pulses in bbo and lbo crystals. *Journal of the Optical Society of America B*, 15(1):200–209, 1998.

[126] David W. Chandler and Paul L. Houston. Twodimensional imaging of state-selected photodissociation products detected by multiphoton ionization. *The Journal of Chemical Physics*, 87(2):1445–1447, 1987.

[127] H. Helm, N. Bjerre, M. J. Dyer, D. L. Huestis, and M. Saeed. Images of photoelectrons formed in intense laser fields. *Physical Review Letters*, 70:3221–3224, 1993.

[128] Andr T. J. B. Eppink and David H. Parker. Velocity map imaging of ions and electrons using electrostatic lenses: Application in photoelectron and photofragment ion imaging of molecular oxygen. *Review of Scientific Instruments*, 68(9):3477–3484, 1997.

[129] J. Zhu. Image-spectrometer for the analysis of the momentum spectra of energetic charges, 1997. Ph.D. Thesis.

[130] D. J. Manura and D. A. Dahl. *SIMION Version 8.0/8.1 User Manual*.

[131] D. D. Hickstein, R. Yurchak, D. Das, C.-Y. Shih, and S. T. Gibson. PyAbel (v0.7): A Python Package for Abel Transforms, March 2016.

[132] N. H. Abel. Auflsung einer mechanischen aufgabe. *Journal für die Reine und Angewandte Mathematik*, 1:153–157, 1826.

[133] E. W. Hansen and P.-L. Law. Recursive methods for computing the abel transform and its inverse. *Journal of the Optical Society of America A*, 2(4):510–520, 1985.

[134] C. J. Dasch. One-dimensional tomography: a comparison of abel, onion-peeling, and filtered backprojection methods. *Applied Optics*, 31(8):1146–1152, 1992.

[135] S. Ma, H. Gao, and L. Wu. Modified Fourier-Hankel method based on analysis of errors in Abel inversion using Fourier transform techniques. *Applied Optics*, 47(9):1350–1357, 2008.

[136] V. Dribinski, A. Ossadtchi, V. A. Mandelshtam, and H. Reisler. Reconstruction of Abel-transformable images: The Gaussian basis-set expansion Abel transform method. *Review of Scientific Instruments*, 73(7):2634–2642, 2002.

[137] G. B. Arfken, H. J. Weber, and F. E. Harris. *Mathematical Methods for Physicists*, chapter 23, page 1159. Academic Press, Oxford, UK, 7 edition, 2013.

[138] U. Johann, T. S. Luk, H. Egger, and C. K. Rhodes. Rare-gas electron-energy spectra produced by collision-free multiquantum processes. *Phys. Rev. A*, 34:1084–1103, 1986.

[139] T. J. McIlrath, P. H. Bucksbaum, R. R. Freeman, and M. Bashkansky. Above-threshold ionization processes in xenon and krypton. *Phys. Rev. A*, 35:4611–4623, 1987.

[140] L.-W. Pi and A. F. Starace. Private communication.

[141] J. Ladislas Wiza. Microchannel plate detectors. *Nuclear Instruments and Methods*, 162:587–601, 1979.

[142] C. E. Moore. *Atomic Energy Levels Volume II*. Circular of the National Bureau of Standards 467, 1952.

[143] F. H. M. Faisal. *Theory of Multiphoton Processes*, chapter 5, pages 92–95. Plenum Press, 233 Spring Street, New York, N.Y. 10013, 1987.

[144] W. Zernik and R. W. Klopfenstein. Two photon ionization of atomic hydrogen. *Journal of Mathematical Physics*, 6(2):262–270, 1965.

[145] D. A. Steck. Rubidium 87 D line data. *Theoretical Division (T-8), MS B285, Los Alamos National Laboratory*, 2003.